PACIFIC EARTHQUAKE ENGINEERING RESEARCH CENTER

Performance Evaluation of Innovative Steel Braced Frames

T. Y. Yang

Jack P. Moehle

and

Bozidar Stojadinovic

University of California, Berkeley

PEER 2009/103
AUGUST 2009

Performance Evaluation of Innovative Steel Braced Frames

T. Y. Yang
Department of Civil Engineering
University of British Columbia, Vancouver

Jack P. Moehle
Department of Civil and Environmental Engineering
University of California, Berkeley

Bozidar Stojadinovic
Department of Civil and Environmental Engineering
University of California, Berkeley

PEER Report 2009/103
Pacific Earthquake Engineering Research Center
College of Engineering
University of California, Berkeley

August 2009

ABSTRACT

Adoption of new structural systems is hampered by the lack of a comprehensive method to evaluate their seismic performance. This report introduces a seismic performance evaluation procedure and demonstrates its application for the suspended zipper braced frame. The performance evaluation procedure includes laboratory and computer simulations. The laboratory simulations may be necessary in cases where behavior of a structural system or its components is inadequately understood and therefore cannot be modeled confidently for computer simulation. By integrating the laboratory specimen behavior and computer models, the complete system performance can be simulated.

The suspended zipper braced frame configuration is similar to the inverted-V braced frame except that a vertical structural element, the zipper column, is added at the beam mid-span points from the second to the top story of the frame. In the event of severe earthquake shaking, the lower-story braces will buckle and create unbalanced vertical forces at mid span of the beams. The zipper columns will mobilize the beams and the braces above the story where buckling occurs, to resist the unbalanced vertical forces. Such action will force the entire system to be engaged to resist the earthquake loads, hence preventing concentration of inelastic action in one story.

Seismic performance evaluation of the suspended zipper braced frame is conducted in two phases. Hybrid and analytical models of the suspended zipper braced frame are developed and validated in the first phase. These models are based on new analysis and simulation tools developed within NSF's George E. Brown Jr. Network for Earthquake Engineering Simulation (NEES). A probabilistic seismic performance evaluation method is developed and used in the second phase to evaluate the seismic risk of the suspended zipper braced frame. This method is based on the Pacific Earthquake Engineering Research Center (PEER) probabilistic seismic performance-based evaluation framework. The seismic risk evaluation is limited to risk of repair cost in the present study, and does not include other performance measures that might be important, including downtime and collapse. The results of performance evaluation conducted using validated hybrid and analytical structural models provide information that can be used to demonstrate the relative merits of the suspended zipper braced frame structural system compared with conventionally braced frame systems.

ACKNOWLEDGMENTS

This work was supported in part by the National Science Foundation under award CMS-0324629, and by the Earthquake Engineering Research Centers Program under NSF Award Number EEC-9701568 through the Pacific Earthquake Engineering Research Center (PEER) under subaward Project ID: 2422006. Any opinions, findings, and conclusions or recommendations expressed in this material are those of the authors and do not necessarily reflect those of the National Science Foundation.

The design and evaluation of the suspended zipper braced frame was executed under the leadership of Professor R. Leon (Georgia Institute of Technology) in cooperation with Professor A. Reinhorn (University at Buffalo); Professor B. Shing (University of California, San Diego); Dr. C. S. Yang (Georgia Institute of Technology); Dr. M. Schachter (University at Buffalo); and Dr. E. Stauffer (University of Colorado, Boulder).

The hybrid simulation testing of the suspended zipper braced frame was successfully implemented with the contribution from Dr. A. Schellenberg (University of California, Berkeley) and the staff at the *nees@berkeley* laboratory, including D. Clyde, D. Peterson, Dr. S. Takhirov, W. Neighbour, D. McLam, J. Robles, and N. Knight.

The concepts of the performance-assessment implementation were developed in collaboration with Professors A. Der Kiureghian and M. Comerio (University of California, Berkeley) and C. Comartin (Comartin Associates). The fragility, repair method, and repair cost information were provided by the ATC-58 project team, including R. Bachman, C. Comartin, G. Hecksher, and Professor A. Whittaker (University at Buffalo).

CONTENTS

LIST OF FIGURES

LIST OF TABLES

1 Study Overview

1.1 INTRODUCTION

Traditional methods of investigating the performance of structural systems involve using either computational simulation of the structure or experimental testing of the structure in the laboratory, or both. The results of the performance evaluation are often presented in terms of the deformation and strength capacity of the structure. While such evaluations are useful in understanding the nonlinear behavior of the structure, they do not provide a performance metric that can be used by building owners/stakeholders to make a risk management decision. In this study the performance assessment methodology developed in the Pacific Earthquake Engineering Research Center (PEER) is used to evaluate the structural performance of a newly proposed structural framing system, the suspended zipper braced frame. The methodology consistently accounts for the inherent uncertainties in the earthquake hazards, structural responses, component damages, and repair actions to provide a fully probabilistic description of the total repair cost of the suspended zipper braced frame under earthquake ground shaking.

To properly model the structural responses, a series of analytical and experimental studies has been conducted to study the system response of the suspended zipper braced frame. First, the hysteresis behavior of the steel brace has been studied experimentally. The experimental data were used to calibrate an analytical brace model in the Open System for Earthquake Engineering Simulation (OpenSees 2006). The calibrated analytical brace model was then used in an OpenSees analytical model to evaluate the system response of the suspended zipper braced frame. Finally, a hybrid simulation test utilizing OpenSees has been conducted to verify the system response of the analytical simulation.

The merits of this study are that

1. The seismic performance of a newly proposed structural system, the suspended zipper braced frame, has been investigated.
2. A collaborative work involving multiple researchers at geographically distributed sites was conducted using facilities of the George E. Brown Network for Earthquake Engineering Simulation (NEES).
3. A hybrid simulation test utilizing OpenSees has been conducted. This hybrid simulation test, for the first time, accounts for the geometry and material nonlinearity in both the analytical and laboratory elements to study the system response of a complex structural system, in this case the suspended zipper braced frame.
4. A performance evaluation methodology has been proposed. The methodology consistently accounts for the inherent uncertainties in the ground motion, model, damage, and repair actions to compute a quantitative probabilistic description of the seismic risk of the structure. The methodology has been implemented in an end-to-end computer program that engineers can use to evaluate the structural performance of different structural framing systems.

The following subsections provide additional discussion on each of these four elements.

1.2 SUSPENDED ZIPPER BRACED FRAME

The zipper braced frame configuration (Fig. 1.1b) was first proposed by Khatib (Khatib et al. 1988). The frame has geometry similar to that of the conventional inverted-V braced frame (Fig. 1.1a), except that a vertical structural element, the zipper column, is added at the beam mid-span points from the second to the top story of the frame. Like other concentrically braced frames, the zipper braced frame is very effective in providing stiffness to limit the story drifts under lateral loading. However, in seismically active zones, for economical reasons, the design philosophy allows the structure to absorb and dissipate earthquake energy through yielding of the structure. Because the braces have the largest stiffness in the building, they attract the largest lateral load and may buckle under severe lateral loading. Conventional steel braces have lower compression capacity then tension capacity: thus, when the compression brace in the inverted-V subassembly buckles, the tension force in the other brace creates a large, unbalanced vertical force at the mid span of the beam. This creates a design challenge. The zipper braced frame is designed to resist the unbalanced vertical load using the zipper columns.

In the event of severe earthquake shaking, the compression brace in the first story of a zipper braced frame may buckle. This action will create an unbalanced vertical force at the mid span of the first-floor beam. The unbalanced vertical force will be transmitted to the mid span of the second-floor beam through the zipper column. This action will increase the compression force in the second-story brace and consequently may cause it to buckle. Under increasing lateral deformations, the unbalanced vertical force will be transmitted upward through the structure and may lead to a mechanism in which all compression braces are buckled and beam plastic hinges are activated. This will result in a highly desirable distribution of inelastic response along the height of the frame (Khatib et al. 1988). However, loss in structural stiffness may occur once the full-height zipper mechanism forms and the frame enters a softening response range.

The reduced lateral load capacity and softening in the force-deformation response of the zipper braced frame after a full plastic mechanism has formed limits the applicability of the zipper braced frame configuration. Leon and Yang (2003) therefore modified the conventional zipper braced frame by increasing the member sizes of the braces at selected stories along the frame height such that they remain elastic and prevent the formation of the complete zipper mechanism. This configuration is named the suspended zipper braced frame (Fig. 1.1c). The primary function of the zipper column is to transfer the unbalanced vertical force to the upper-story braces and to support the beams at mid span. Leon and Yang (2003) have shown that by providing the support at mid span of the beams, a reduction of the beam sizes can be achieved, which may save material and makes the suspended zipper braced frame more economical. This configuration also provides a clear force path and makes the capacity design for the frame structural members relatively straightforward. From the results of nonlinear static analyses (Leon and Yang 2005), it seems that the suspended zipper braced frame has a slightly larger strength and more ductility than the conventional zipper braced frame. The main disadvantage arises as the number of stories increases, and the magnitudes of the unbalanced vertical forces transmitted up to the top-story braces become very large, making the design of the top-story braces very difficult.

1.3 COLLABORATIVE RESEARCH ACTIVITY

A joint project involving the Georgia Institute of Technology, the University at Buffalo, the University of California, Berkeley, and the University of Colorado at Boulder was organized to evaluate the seismic performance of the suspended zipper braced frame. This collaborative effort comprised a number of experimental and analytical components. The University at Buffalo tested the suspended zipper braced frame on a shaking table, while the Georgia Institute of Technology tested the suspended zipper braced frame quasi-statically in their strong-wall laboratory. The University of California, Berkeley, and the University of Colorado at Boulder conducted hybrid simulation tests of the suspended zipper braced frame using different testing algorithms. All participants conducted a variety of analytical simulations of the suspended zipper braced frame.

1.4 HYBRID SIMULATION

Traditional methods for investigating the response of structures to external excitations involve using either pure computational analysis or pure experimental testing, or both. The experimental testing methods are further divided into quasi-static, pseudo-dynamic, and real-time testing methods. Real-time testing is usually the most realistic simulation of real earthquake loading but usually requires building the entire structure and testing it on the shaking table. In the case of complicated structural systems, this may make the testing relatively expensive. Furthermore, the experimental model is usually scaled down to match the shaking table capacity. The quasi-static test is a much simpler test to implement. With the appropriate boundary condition assumptions, larger structures can be decomposed into subassemblies that can be tested separately. However, traditional quasi-static test methods require a predetermined displacement loading history that is sometimes difficult to relate to the seismic demand for the structure (Shing and Mahin 1984). The pseudo-dynamic testing method improves the quasi-static test by using measured force feedback to adjust the applied displacement loading history and, thus, simulate the actual earthquake loading on the structure or a subassembly. However, the limitation of computer speed has, at the outset, restricted the pseudo-dynamic testing method to relatively simple structural models and slow testing rates. As computers became faster, and interface between servo-hydraulic hardware and controllers become more advanced, increasingly more complex structures and subassemblies have been tested (Magonette and Negro 1998; Mahin et al. 1989; Shin et al. 1996; Takanashi 1975; Takanashi and Nakashima 1987; and Tsai et al. 2004).

Hybrid simulation is a form of pseudo-dynamic testing in which the structure is partially represented physically in the laboratory, while the remainder of the structure is simulated using a computer. The physical portion of the hybrid model can be an assemblage of one or more physical models, while the analytical portion can be one or more numerical, consistently scaled, substructures. The equation of motion of the hybrid model is solved during a hybrid simulation test. The basis of the hybrid simulation method is the decomposition of the structural model into the components that are difficult to model analytically and are, thus, tested in the laboratory, while the rest of the structure is modeled simultaneously using a computer. The hybrid simulation method therefore provides a cost effective way to study structural system behavior. Furthermore, with the appropriate boundary conditions, hybrid simulations involving multiple subassemblies can be conducted to study larger and more complex structural system. The innovation presented in this work is the first implementation of the hybrid simulation method within the Open System for Earthquake Engineering Simulation (OpenSees 2006) to account for nonlinear material and geometry properties in both analytical and experimental elements to conduct local and distributed hybrid simulation tests.

1.5 PROBABILISTIC SEISMIC PERFORMANCE ASSESSMENT

The framework for performance-based assessment, developed by the Pacific Earthquake Engineering Research Center (PEER), provides the means to consistently account for the inherent uncertainties in ground motion, structural response, structural damage occurrence and distribution, and repair procedures and cost to give building owners/stakeholders performance metrics that can be used to make risk management decisions. A new method for generating consistent structural demand measures was developed to enable the application of the PEER framework to the seismic evaluation of the suspended zipper braced frame. The method samples the structural response from a few dynamic analyses and generates additional correlated response matrixes using functions of random variables. With the generated correlated response matrixes. the performance of the structural system was assessed using the Monte-Carlo simulation. An end-to-end computer implementation of the new method was used to conduct a comparative seismic performance assessment of a suspended zipper braced frame and an inverted-V braced frame.

1.6 TEST MODEL

A test model of the suspended zipper braced frame was designed according to the proposal by Yang (2006) to provide a common structure for the experimental and analytical investigations in the joint project. It was assumed that the model is located on site class D soil with mapped spectral accelerations at the short period and 1-sec period of 1.5 g and 0.6 g, respectively. The model was scaled using a length scale factor of 3 to fit the shaking table capacity at the University at Buffalo. The first-mode period and the spectral acceleration of the scaled model were calculated to be 0.22 sec and 1.0 g respectively. The design seismic weight for the 1/3-scale suspended zipper braced frame was estimated to be 40 kips at each floor level. Using IBC2000 (ICC 2000) with response modification coefficient (R) = 6 and occupancy importance factor (I_e) = 1.5, the seismic base shear was calculated to be 30 kips. Given this design demand, the size and weight constraints of the shaking table at the University at Buffalo, the final tested model was a 1/3-scale, two-dimensional, three-story, one-bay, suspended zipper braced frame as shown in Figure 1.1c. The member sizes of the test model are listed in Table 1.1.

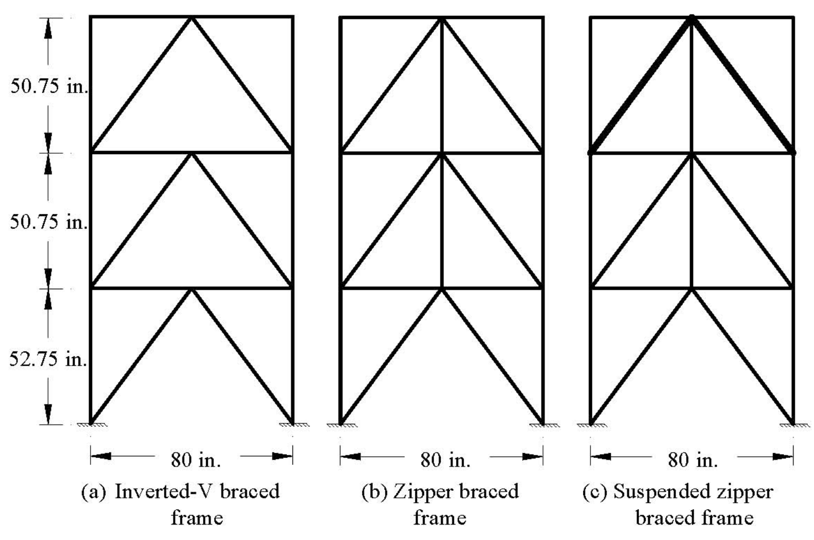

Fig. 1.1 Configurations of steel concentrically braced framing systems.

Table 1.1 Member sizes of 1/3-scale suspended zipper braced frame.

Story	Brace	Column	Beam	Zipper column
3	HSS 3x3x3/16	S4x9.5	S3x5.7	HSS2x2x3/16
2	HSS 2x2x1/8	S4x9.5	S5x10	HSS1.25x1.25x3/16
1	HSS 2x2x1/8	S4x9.5	S3x7.5	

1.7 RESEARCH OBJECTIVES

The research presented in this report has three objectives.

The first objective is to develop and calibrate a finite element model of the suspended zipper braced frame using OpenSees and to conduct a study of the system behavior of the suspended zipper braced frame. This computational simulation can demonstrate if the intended force redistribution in the system is, indeed, occurring in the suspended zipper braced frame.

The second objective is to implement the newly proposed hybrid simulation method (Schellenberg 2008) within the OpenSees framework and use it to conduct a hybrid simulation evaluation of the suspended zipper braced frame.

The third objective is to develop a methodology that efficiently implements the PEER probabilistic performance-based seismic evaluation of structural framing systems. Traditional performance evaluation of structural framing systems uses performance objectives defined in terms of structural response measures such as story drift or floor acceleration. While such response quantities are useful in providing indirect performance measures, many decision makers prefer performance metrics that more directly relate to business decisions, such as downtime and repair cost. The implementation of the PEER probabilistic performance-based seismic evaluation framework developed in this study will enable engineers to compute performance in terms of capital losses, and thereby help inform decisions about design levels within a risk management framework. This implementation will be used to evaluate the performance of the suspended zipper braced frame.

1.8 ORGANIZATION OF REPORT

Seismic performance evaluation of the suspended zipper braced frame is described in the following six chapters.

Chapter 2 presents an analytical and experimental study of a steel inverted-V braced subassembly under cyclic displacements. This chapter includes descriptions of the quasi-static test, the behavior of the inverted-V braced subassembly under inelastic cyclic displacements, and a description of a calibrated finite element model that can be used to model the nonlinear hysteretic behavior of steel hollow structural section (HSS) which buckles out of plane.

The analytical inverted-V braced subassembly model calibrated in Chapter 2 is used to simulate the system response of the suspended zipper braced frame under static and dynamic loading. The results, presented in Chapter 3, illustrate expected force redistribution in the system.

Chapter 4 describes a hybrid simulation test used to verify the system behavior of the suspended zipper braced frame. This chapter includes descriptions of the architecture of the hybrid simulation algorithm, the experimental setup, the solution algorithm, as well as experimental results and a comparison of those results with results obtained from pure analytical simulation. A new implementation of the hybrid simulation testing method within the OpenSees framework is presented in this chapter.

Chapter 5 describes the basis of the probabilistic performance-based seismic evaluation framework. A new method that enables a very efficient implementation of the framework, based on the use of correlation matrices to generate structural demand statistics using a Monte Carlo approach, is presented.

The performance-based assessment method developed in Chapter 5 is used to implement a computer tool for probabilistic performance-based evaluation of structural framing systems. This tool is used to evaluate the system performance of the suspended zipper braced frame and compare it with the seismic performance of the inverted-V braced frame. The description of the structural model, the ground motion used in the analysis, the system responses under the selected ground motions, and the repair cost simulation comparison between these two systems are presented in Chapter 6.

Chapter 7 presents a summary of research findings and conclusions and a list of topics for future research.

2 Analytical and Experimental Study of Steel Brace Hysteresis Behavior

2.1 INTRODUCTION

The nonlinear response of concentrically braced steel frames depends strongly on the brace hysteresis behavior. Hence, in order to effectively study the system response of the suspended zipper braced frame, using either computer-only or hybrid simulation, it is crucial to be able to model the force-deformation response of the inverted-V braced subassembly. This chapter summarizes the analytical and experimental studies of steel brace hysteresis behavior.

An inverted-V braced subassembly nominally identical to the first-story braces of the 1/3-scale suspended zipper braced frame, shown in Figure 1.1c, was tested quasi-statically at the *nees@berkeley* laboratory at the University of California, Berkeley. The results of the quasi-static test were used to calibrate a finite element model in OpenSees to generate the force-deformation response of steel hollow structural sections (HSS) that buckle out of plane. The analytical simulations were verified against the experimental data collected from the 1/3-scale inverted-V braced subassembly test and an independent quasi-static test conducted by Uriz (2005) to study the hysteresis response of a larger steel HSS (HSS6x6x3/8) brace under inelastic cyclic displacements.

2.2 EXPERIMENTAL EVALUATION OF STEEL HSS HYSTERESIS RESPONSE UNDER INELASTIC CYCLIC DISPLACEMENTS

An inverted-V braced subassembly was tested quasi-statically under well-known boundary conditions and cyclic displacement history with progressively increasing amplitude. The main purpose of the test was to calibrate a finite element model for HSS steel braces that buckle out of plane. The tested specimen was identical to the first-story braces of the 1/3-scale suspended zipper braced frame shown in Figure 1.1c and listed in Table 1.1.

Figure 2.1 shows a photograph of the inverted-V braced subassembly. Figure 2.2 shows the dimensions of the specimen and the locations where the brace deformations were recorded. According to the original design suggested by Yang (2006), the braces were connected to 0.375 in. gusset plates at both ends. A clear distance of 0.75 in. between the brace end and the gusset plate Whitmore line was provided to allow the brace to buckle out of plane. Table 2.1 shows a summary of the brace properties.

Table 2.1 Summary of brace properties.

Properties	Values
Shape	HSS2x2x1/8
Cross sectional area, A_g	0.84 in.^{2}
Brace length, L_b	66.2 in.
Minimum specified yield stress, F_y	46 ksi
Ratio of expected yield stress to minimum specified yield stress, R_y	1.3
Expected yield stress, $F_{ye} = R_y \times Fy$	59.8 ksi
Modulus of elasticity, E	25000 ksi
Ratio of post yield stiffness to modulus of elasticity, β	0.005

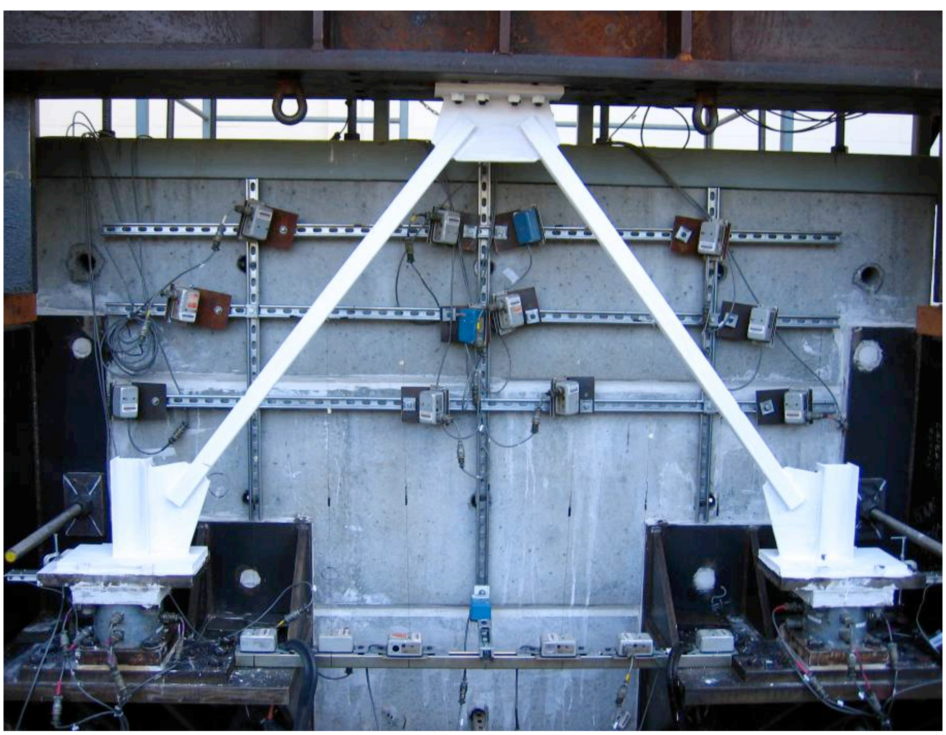

Fig. 2.1 Photograph of inverted-V braced subassembly.

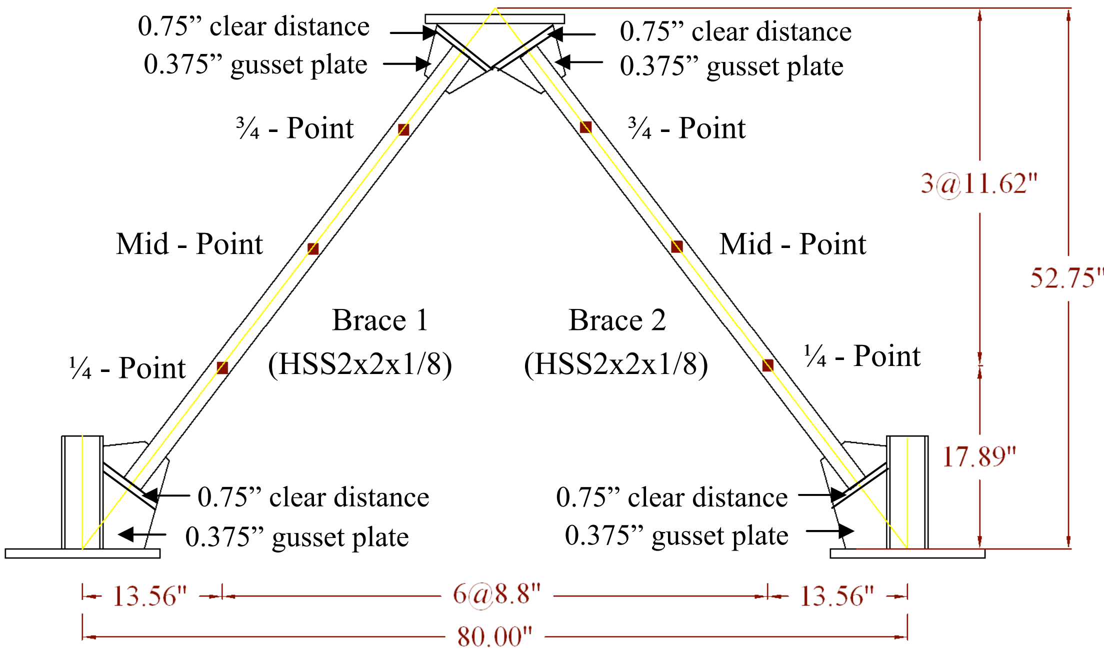

Fig. 2.2 Dimensions and measurement points of inverted-V braced subassembly.

2.2.1 Test Setup

Figure 2.3 shows a global view of the inverted-V braced subassembly test setup. The setup consisted of two dynamic actuators in the vertical direction, one dynamic actuator in the horizontal direction, and a guiding system to allow the intersection of the braces to move in-plane. The dimensions of the test setup are shown in Figure 2.4. Figure 2.5 shows the components of the test setup and the global coordinate system used to reference the degrees of freedom. The vertical dynamic actuators have a displacement capacity of ±21 in., a dynamic force capacity of ±150 kips, and a maximum velocity of 20 in./sec. The horizontal dynamic actuator has a displacement capacity of ±11 in., a dynamic force capacity of ±220 kips, and a maximum velocity of 20 in./sec.

Figure 2.6 shows the components and the degrees of freedom of the guiding system. The guiding system consists of a W14x283 middle section, with W27x235 sections welded on each end, and two 15″x22.5″x1.5″ steel plates welded at the bottom flange. The guiding system was restrained by the movement of the steel plates such that the three out-of-plane degrees of freedom are restrained, while the two translational and the rotational degrees of freedom in-plane are allowed. The plates were designed to move freely in the slots formed by the L4x4x3/4 steel angles on each side of the plates. Because the guiding system was designed to minimize any interference to in-plane motion, a small 1/16 in. gap was provided between the steel plates and guiding slots formed by the steel angles.

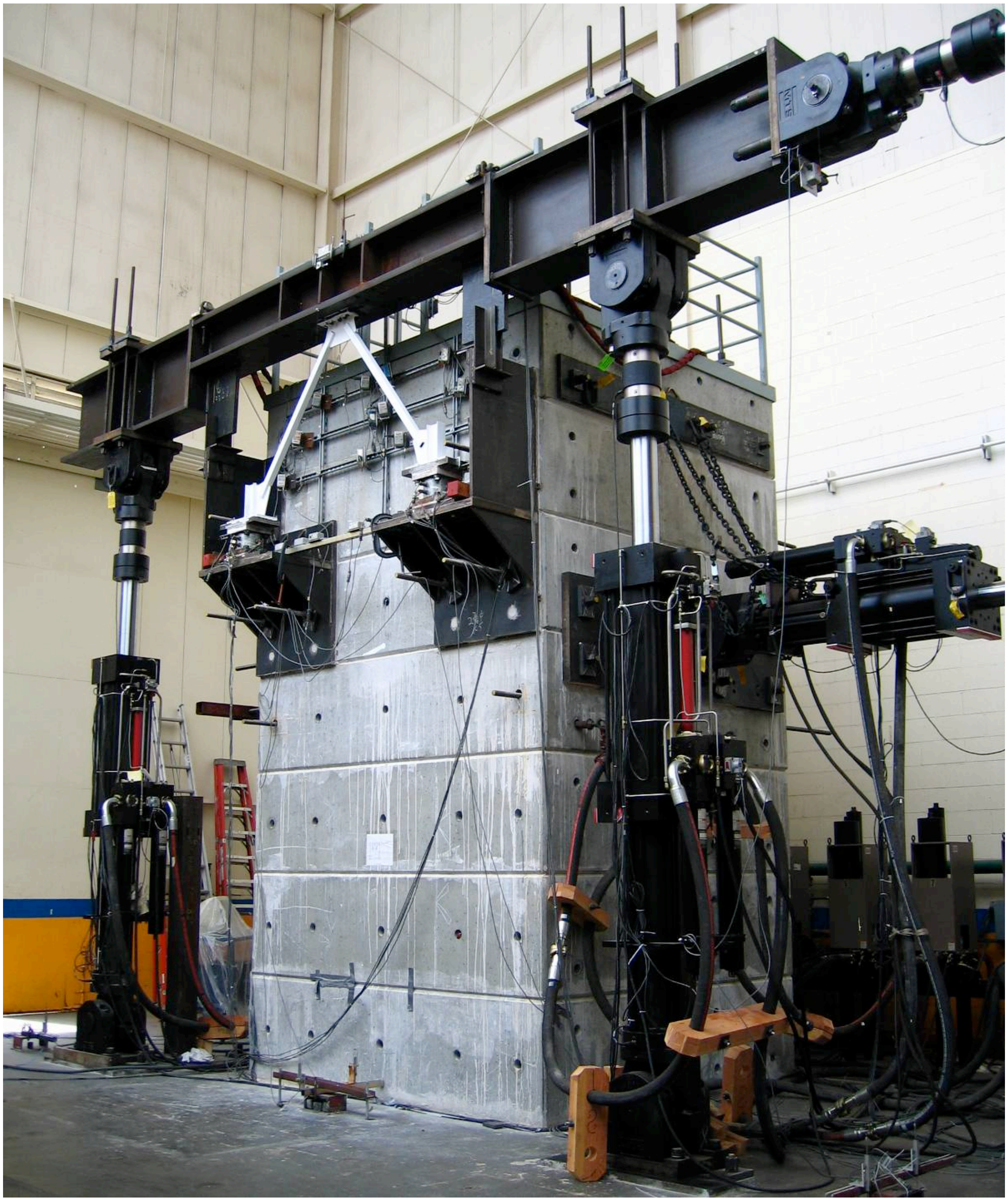

Fig. 2.3 Inverted-V braced subassembly test setup at *nees@berkeley*.

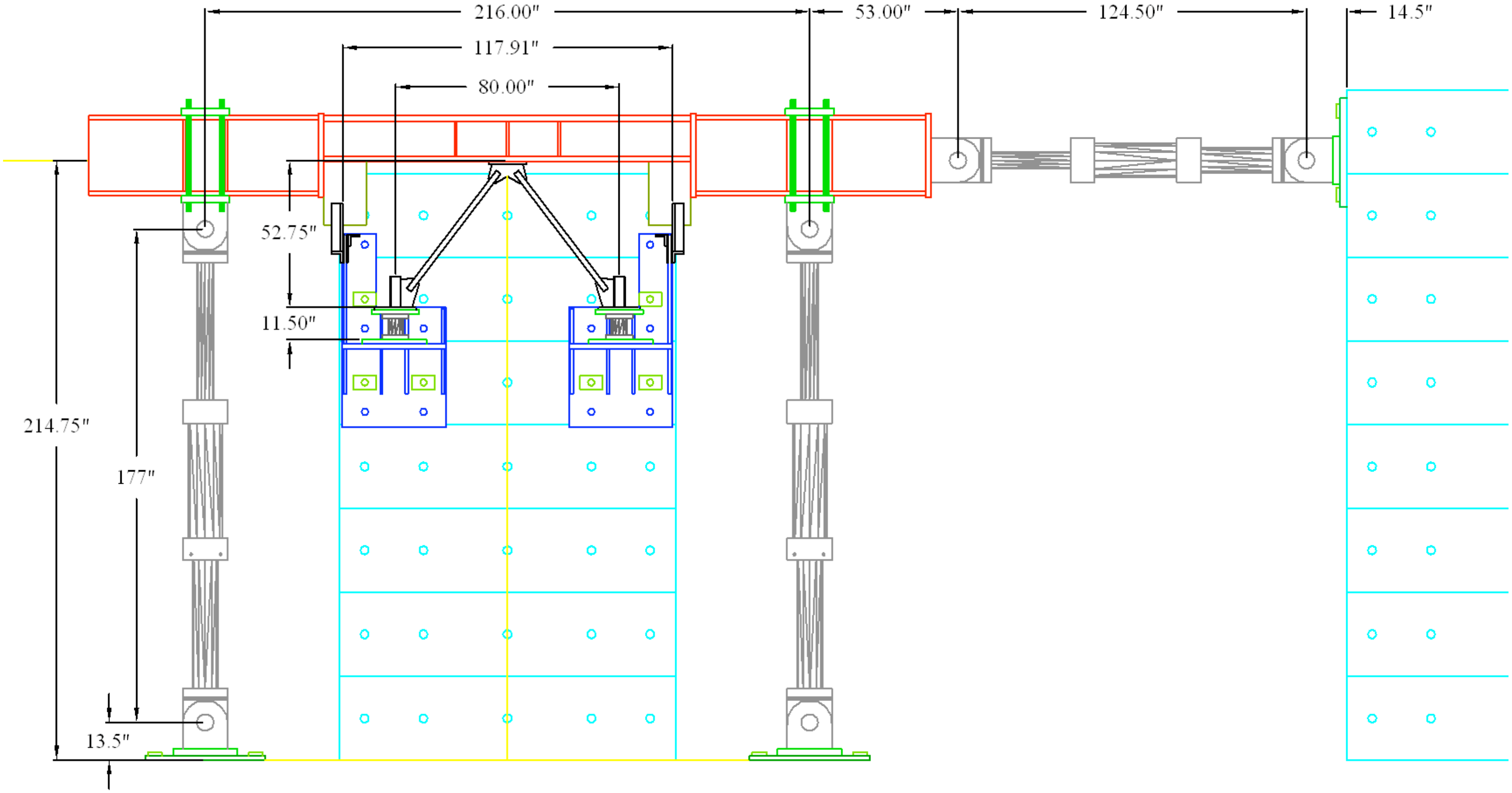

Fig. 2.4 Dimensions of inverted-V braced subassembly test setup.

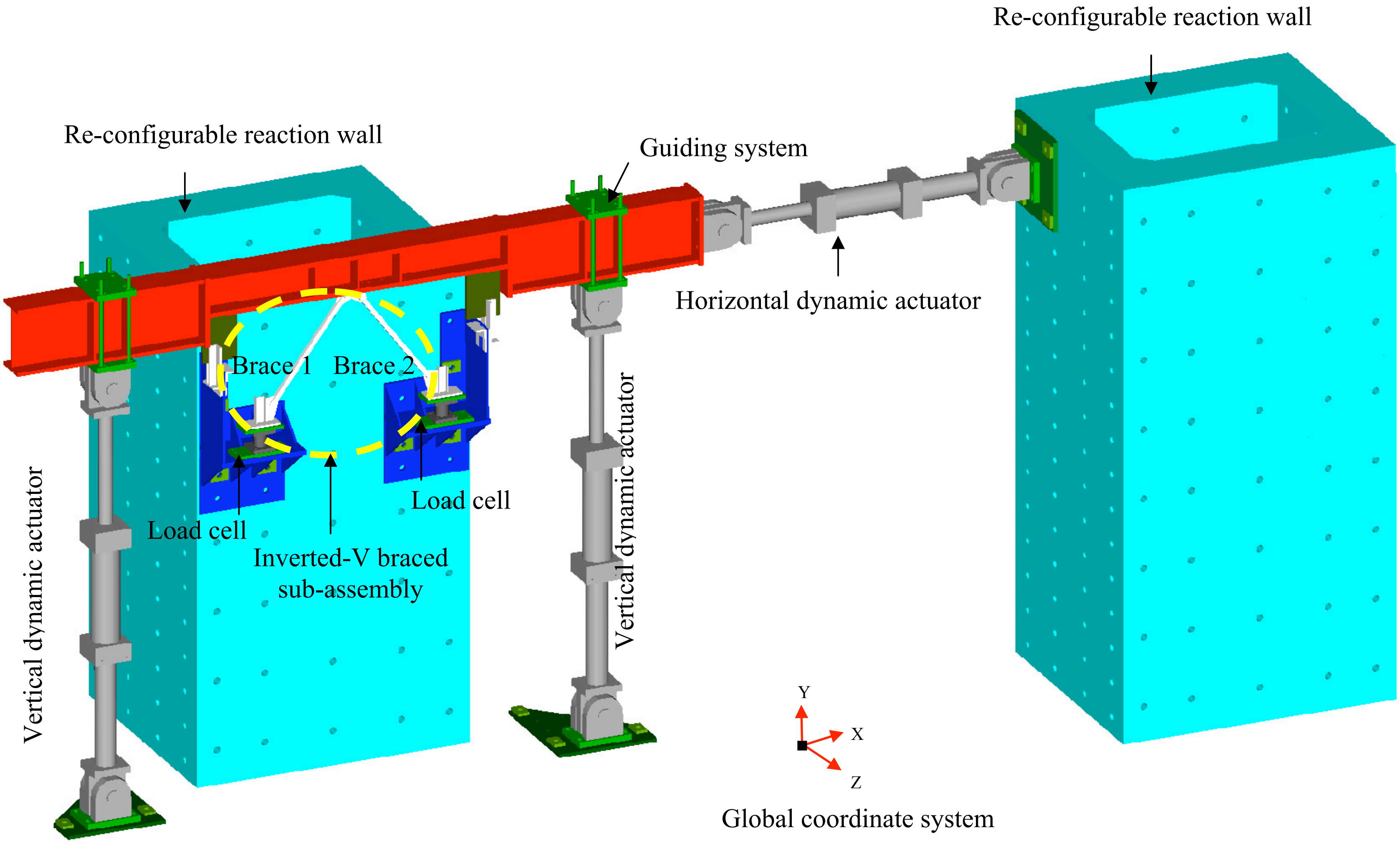

Fig. 2.5 Components of inverted-V braced subassembly test setup.

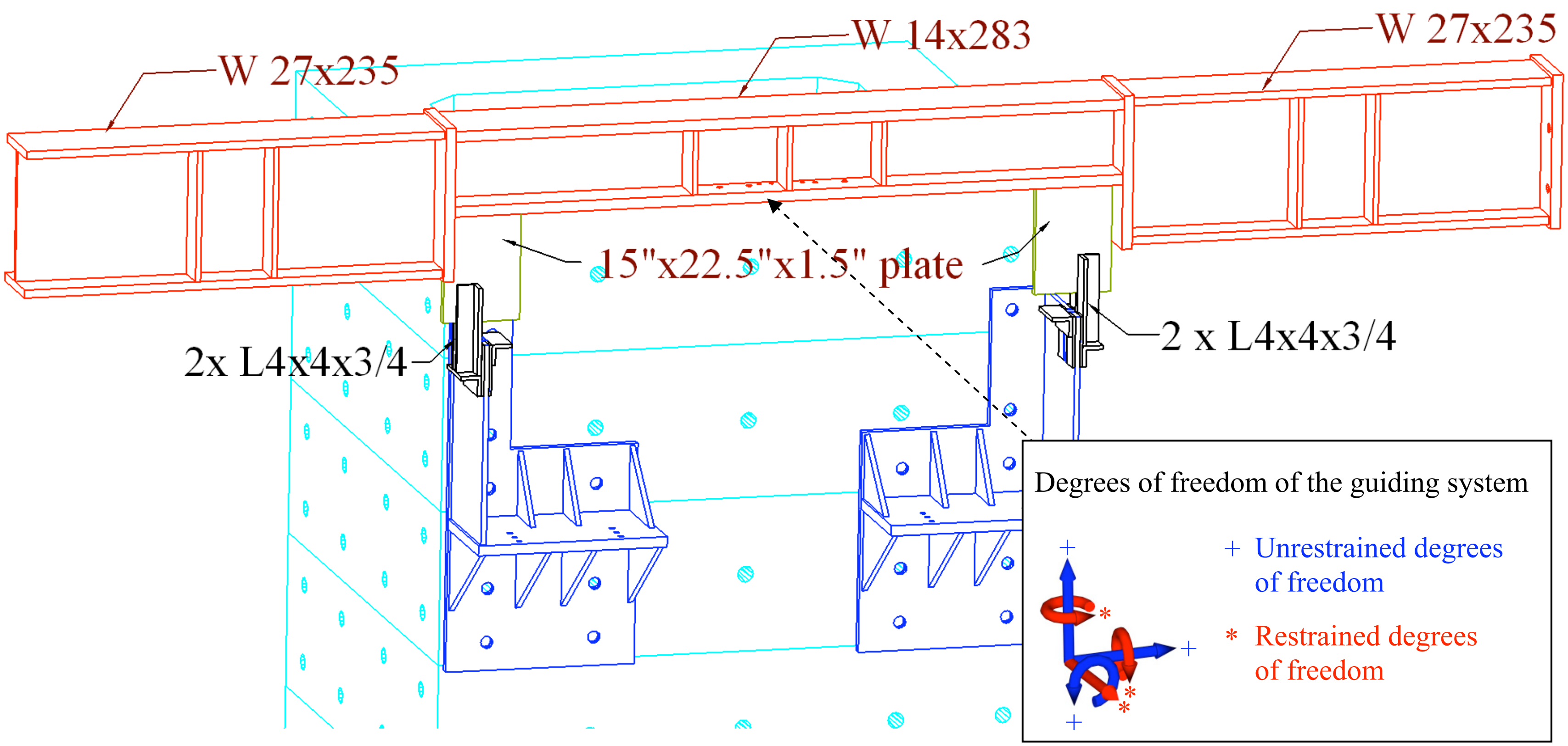

Fig. 2.6 Guiding system of inverted-V braced subassembly test setup.

2.2.2 Instrumentation

The displacements of the guiding system were measured using the instruments shown in Figures 2.7 and 2.8. In addition, the acceleration, and the in-plane and out-of-plane rotation of the guiding system were measured using the accelerometers and tiltmeters shown in Figure 2.9.

The reaction forces at the bottom gusset plates were measured using two VPM load cells (five-degrees-of-freedom load cell, capable of measuring the axial force, the in-plane shear force, the out-of-plane force, the in-plane moment, and the out-of-plane moment). Figure 2.10 shows the VPM load cells and the NovoTech potentiometers used to measure the horizontal displacements at the base of the braces. The deformations of the braces in the global coordinate system were measured using 21 independent displacement transducers. Figure 2.11 shows the locations where the deformations of the braces were recorded. With three independent displacement transducers monitoring each of the selected points, the motions of the selected points in the global coordinate system were calculated using the formulas shown in Appendix C.

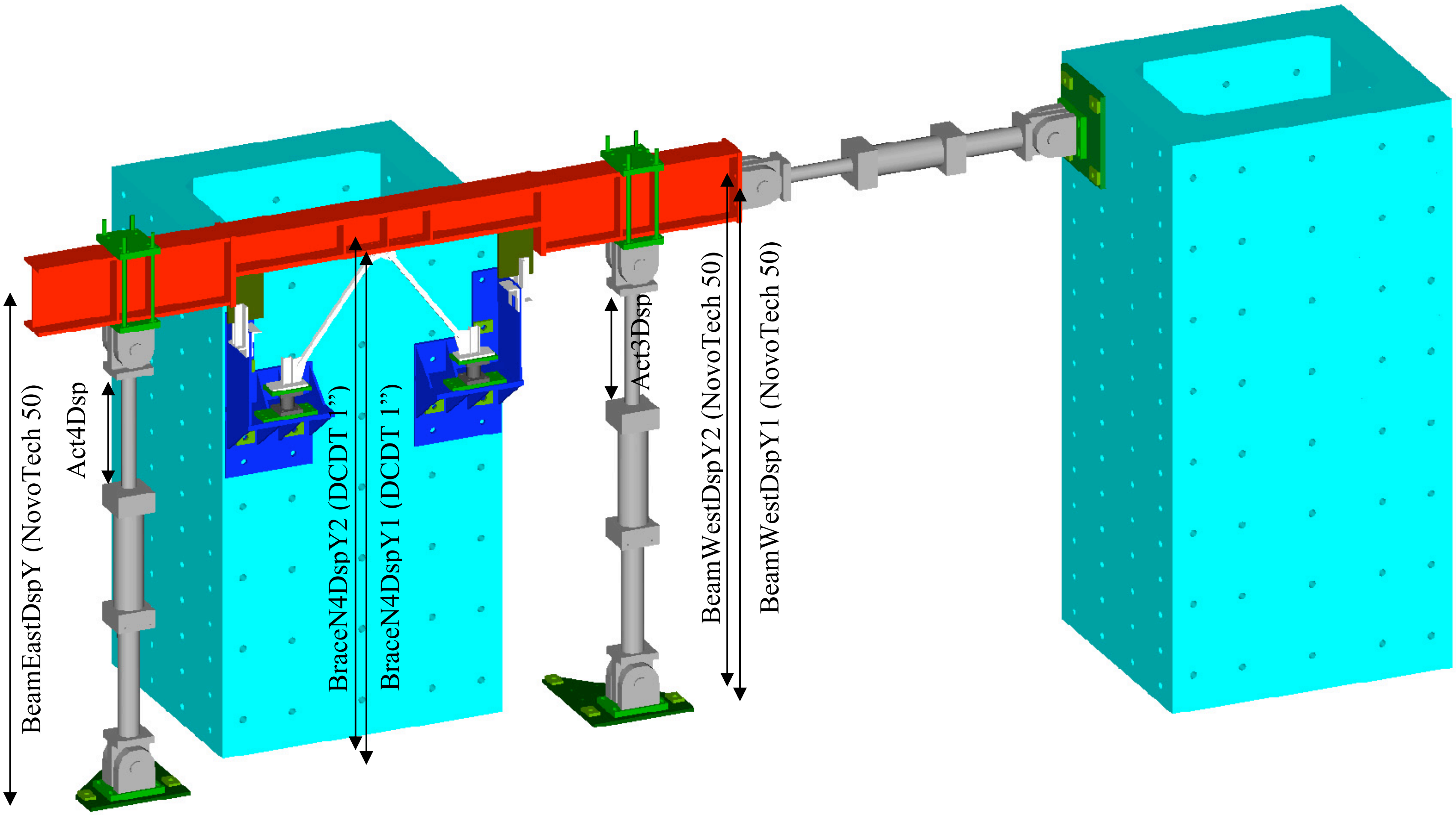

Fig. 2.7 Vertical displacement instrumentation of test setup.

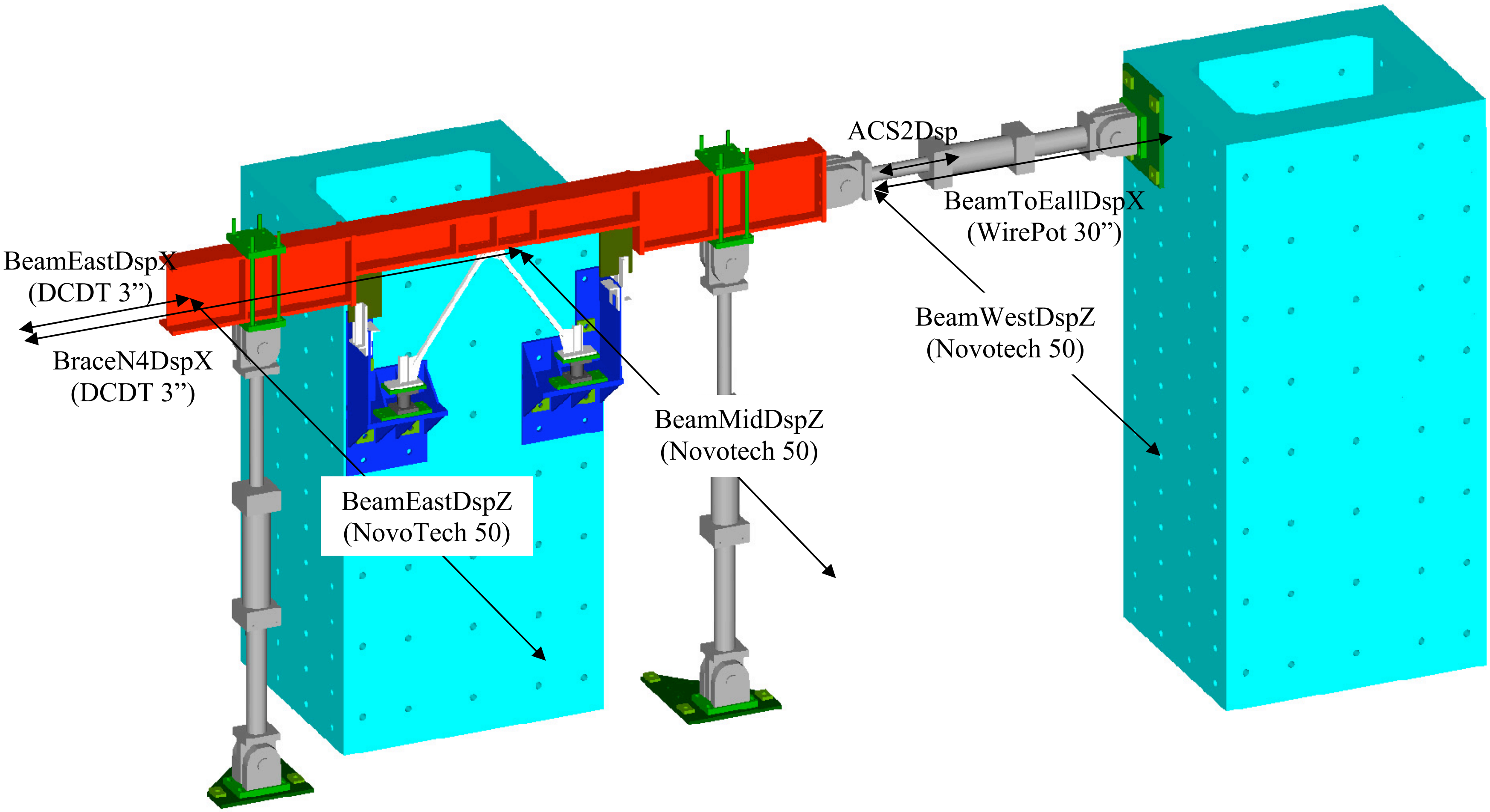

Fig. 2.8 Horizontal and out-of-plane displacement instrumentation of test setup.

Fig. 2.9 Accelerometer and tiltmeter used to measure accelerations and rotations of guiding system.

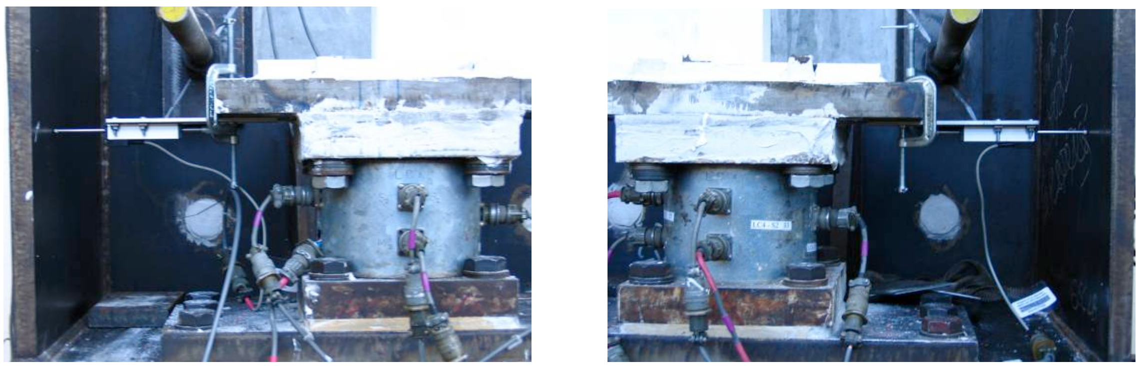

Fig. 2.10 VPM load cells and NovoTech potentiometers located at base of braces.

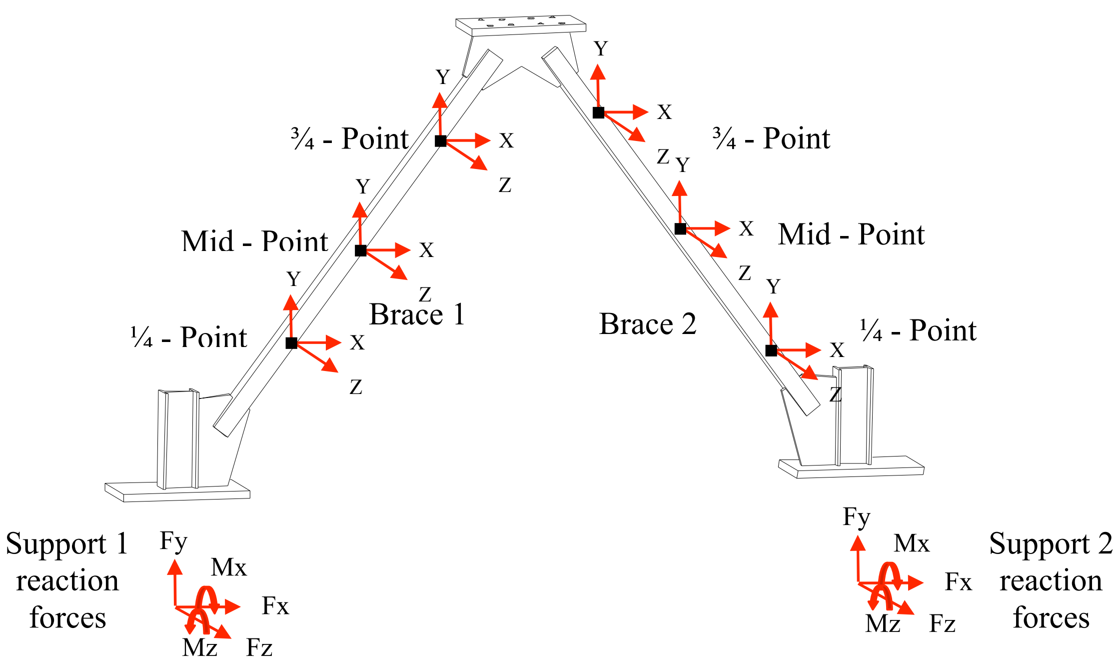

Fig. 2.11 Locations of displacement and force measurement points.

2.2.3 Displacement History

The displacement history used for the quasi-static test was similar to the standard displacement history used for proof-tests of steel moment connections as prescribed in the AISC Seismic Design Provisions (American Inst. of Steel Construction 2002). Because the purpose of the quasi-static test was to calibrate the inverted-V braced finite element model and not to conduct an acceptance test, the displacement history was modified to have more cycles in the linear range and fewer cycles in the nonlinear range. By so doing, the experimental data can provide a good estimate of the elastic stiffness of the inverted-V braced subassembly without inducing low-cycle fatigue. The target elastic displacement, dy, used in the quasi-static test was obtained from a preliminary pushover analysis conducted using a computer model. Based on the target elastic displacement, the displacement history was set to have six cycles of pre-yielding displacements ($dy/2$), four cycles of yielding displacements (dy), four cycles of post yielding displacements ($2dy$), followed by an increase of displacement of dy every two cycles.

Figure 2.12 shows the displacement history, expressed in terms of interstory drift ratio computed using the story height of 52.75 in., applied at the horizontal degree of freedom at the intersection of the braces. The displacement corresponding to the first significant inelastic excursion of the inverted-V braced subassembly was estimated to be 0.2 in., corresponding to an expected first-yield interstory drift ratio of 0.4 percent.

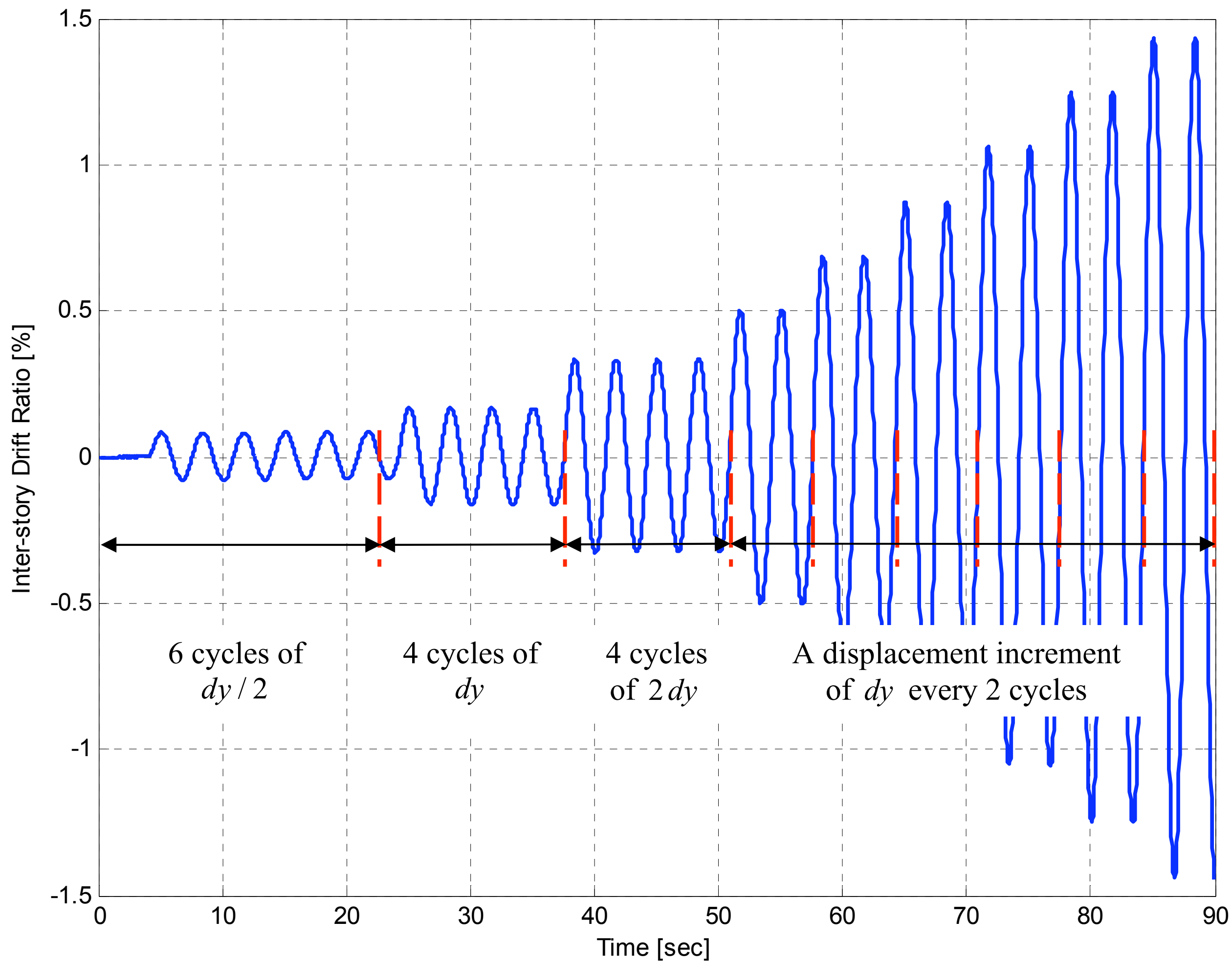

Fig. 2.12 Displacement history used in quasi-static test.

2.3 TEST RESULTS

Under the displacement history shown in Figure 2.12, the braces of the inverted-V braced subassembly experienced significant damage. A photograph of the damaged specimen after the quasi-static test is shown in Figure 2.13.

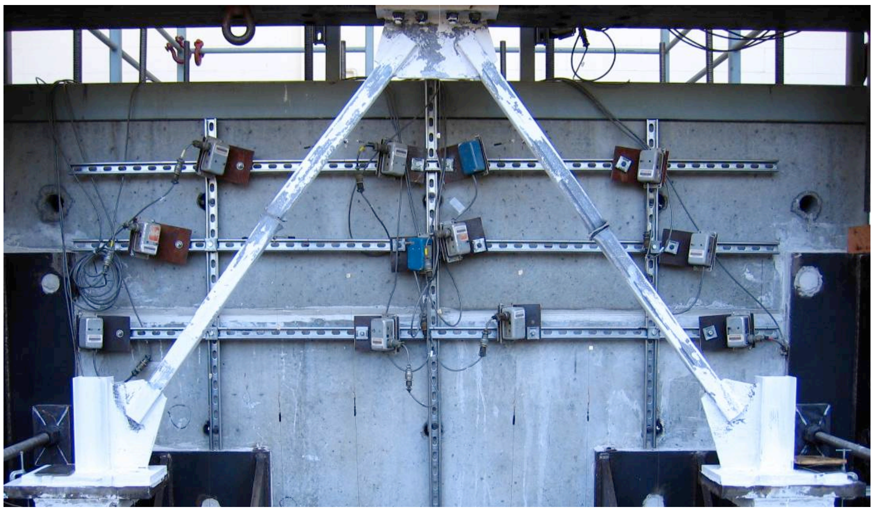

Fig. 2.13 Photograph of damaged inverted-V braced subassembly after quasi-static test.

To compute the force-deformation response of each brace, the braces were assumed to have pin connections at both ends. Hence, the in-plane and out-of-plane moments measured at the ends of the braces were ignored. Displacement at the intersection of the braces in the global coordinate system was measured using the instrumentation shown in Figures 2.7 and 2.8, while the displacements at the bases of the braces were measured using the instruments shown in Figure 2.10. Thus, the axial deformations of the braces were calculated using the relative displacement from the intersection of the braces to the brace bases. Similarly, the axial forces in the braces were calculated by summing the components of the axial, shear, and out-of-plane forces (measured by the VPM load cells) in the direction from the base of the brace to the brace intersection, accounting for the movement of the brace intersection at each time-step. The results are discussed in the sections that follow.

2.3.1 Brace Deformation

The deformations of the braces in the global coordinate system measured at the selected points shown in Figure 2.11 are normalized with respect to the brace length (L_b = 66.2 in.) and plotted in Figure 2.14. From these plots it is apparent that the braces buckled out of plane and out of phase. The maximum out-of-plane displacement reached 5.5 percent of the brace length.

2.3.2 Brace Axial Forces

Figure 2.15 shows the brace axial force history recorded during the quasi-static test. As expected from principles of mechanics, the brace forces were equal and opposite in sign in the elastic response range. Braces started to buckle and lose resistance in compression after the horizontal displacement increased above approximately 0.75 percent interstory drift ratio. Compression resistance reduced to approximately half the peak resistance at approximately 1.5 percent interstory drift ratio.

2.3.3 Unbalanced Vertical and Out-of-Plane Forces

The unbalanced vertical and out-of-plane forces measured at the intersection of the braces are normalized with respect to the expected yield force ($A_g \times F_{ye}$ = 50.23 kips) and plotted in Figure 2.16. Because the braces buckled out of plane and out of phase, the unbalanced vertical and out-of-plane forces caused the intersection of the braces to move down vertically and rotate out of plane at the same time. Based on the plot shown in Figure 2.16, the maximum unbalanced vertical force reached as much as 80 percent of the brace expected yield force, while the maximum unbalanced out-of-plane force reached 2.4 percent of the brace expected yield force.

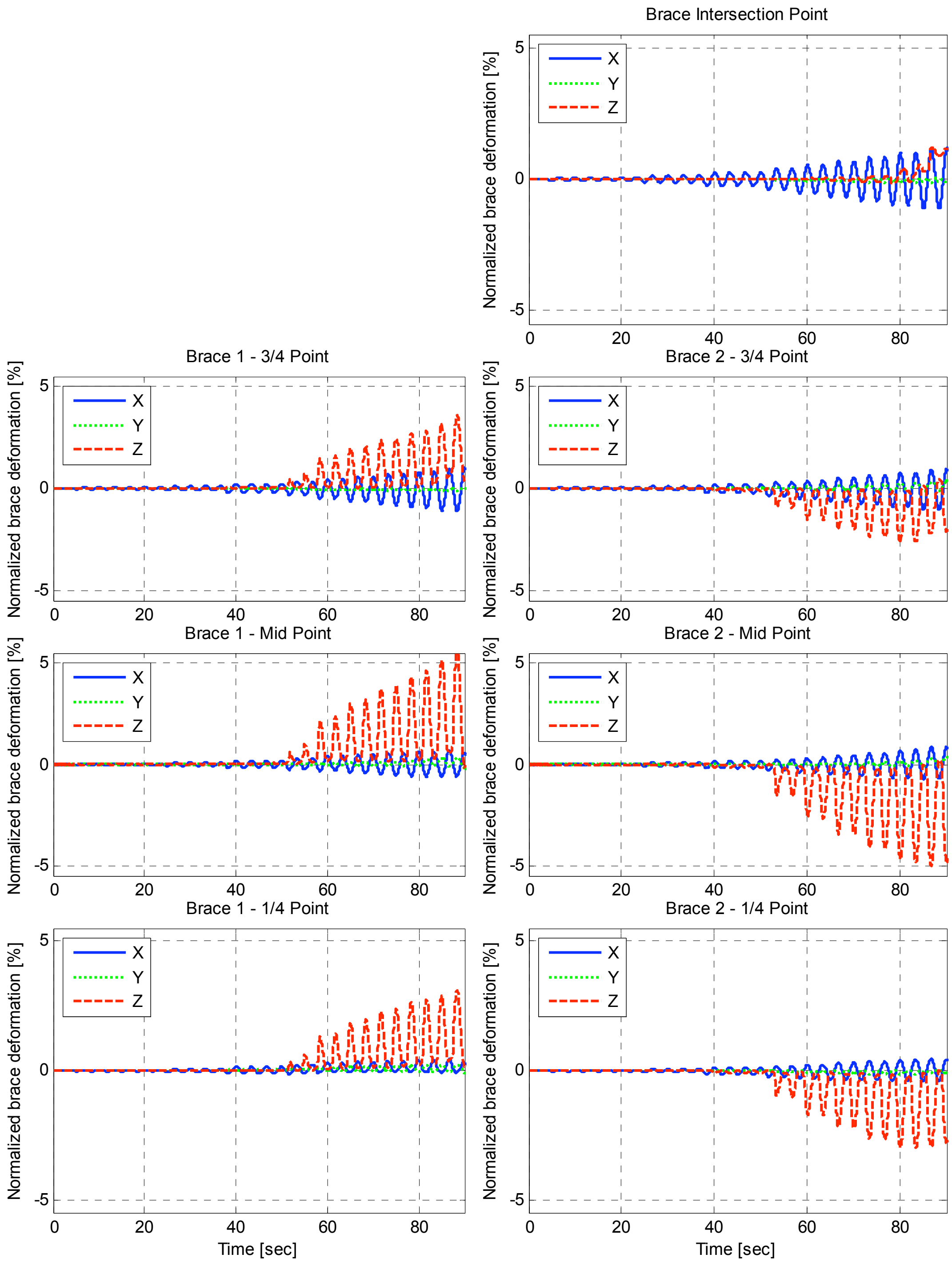

Fig. 2.14 Deformation of braces recorded during quasi-static test.

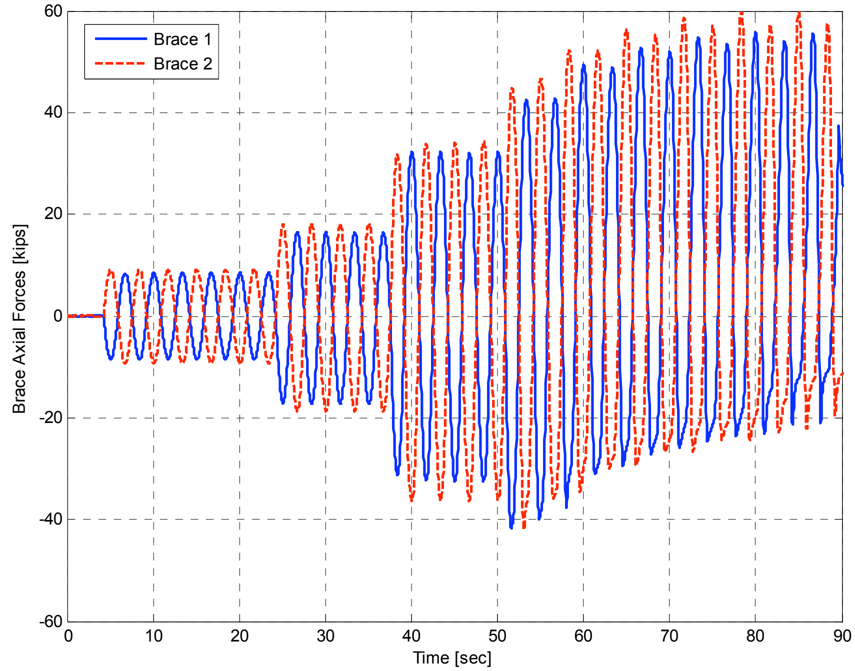

Fig. 2.15 Axial force histories in each of the braces.

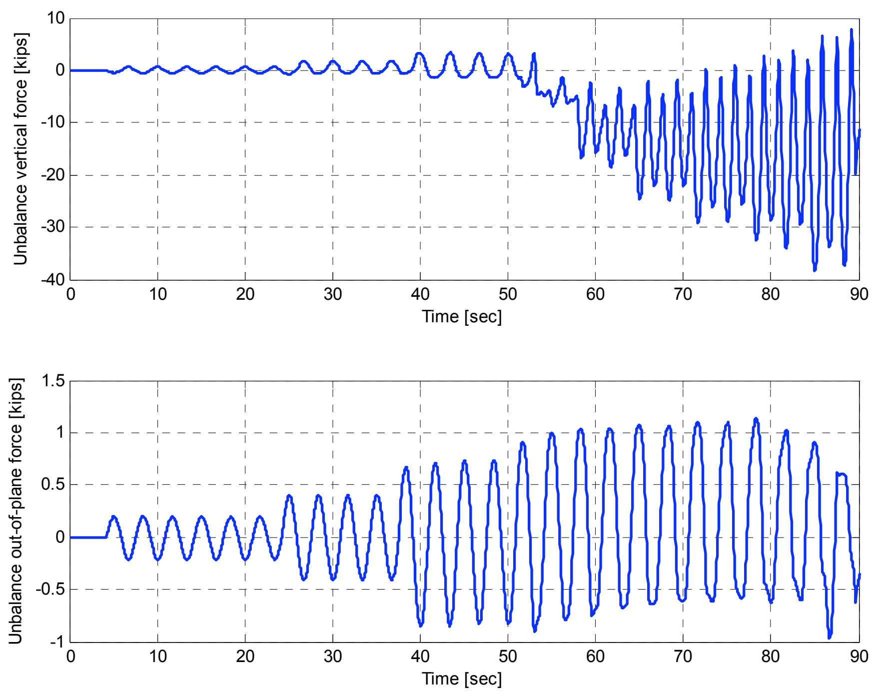

Fig. 2.16 Unbalanced force histories measured at intersection of braces.

2.3.4 Out-of-Plane Rotation

Figure 2.17 shows the measured out-of-plane rotation of the guiding system caused by the unbalanced out-of-plane force at the brace intersection recorded during the quasi-static test. The rotation of the guiding system became permanent when the interstory drift ratio reached 1.25 percent and the braces could not be straightened any more.

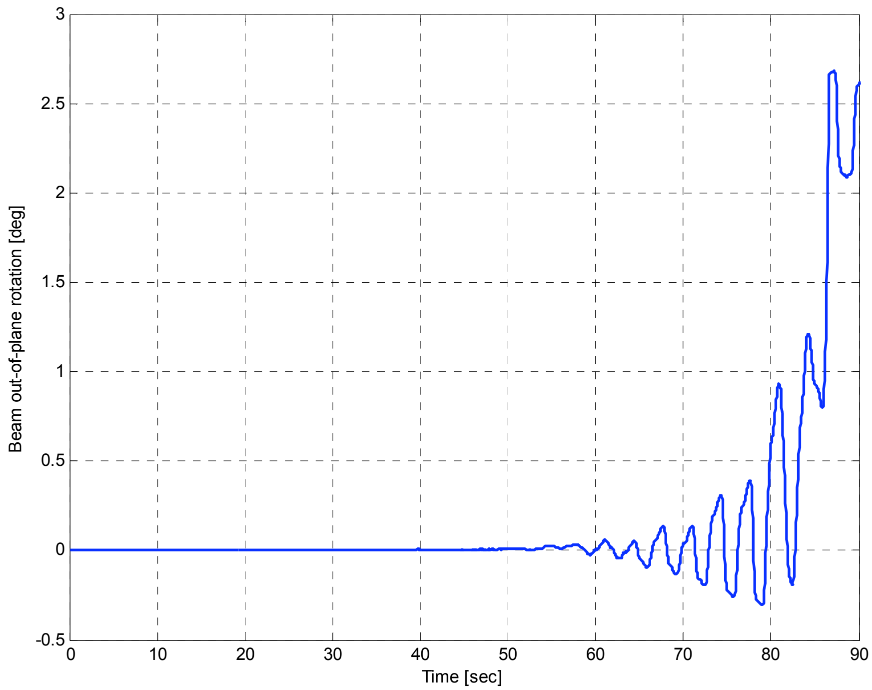

Fig. 2.17 Out-of-plane rotation history of guide beam.

2.3.5 Photographs of Damaged Specimen

Figure 2.18 shows the plastic hinges formed along the braces. Because the braces bent out of plane, the plastic hinges formed at the top and bottom gusset plates and at the mid span of the braces. Figure 2.19 shows that the top and bottom gusset plates bent out of plane, the braces buckled out of phase, and the guiding system rotated out of plane permanently.

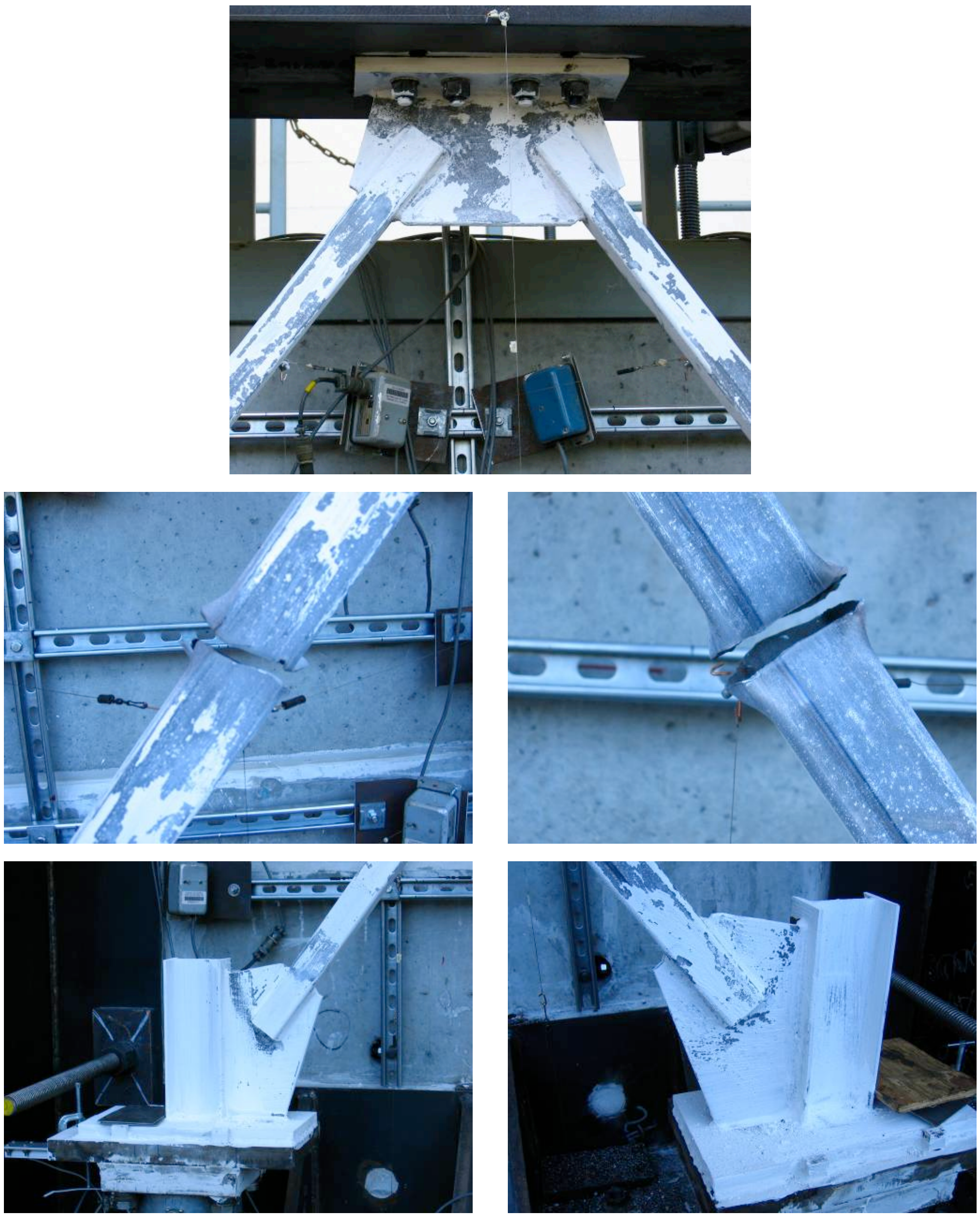

Fig. 2.18 Close-up view of plastic hinges formed along braces.

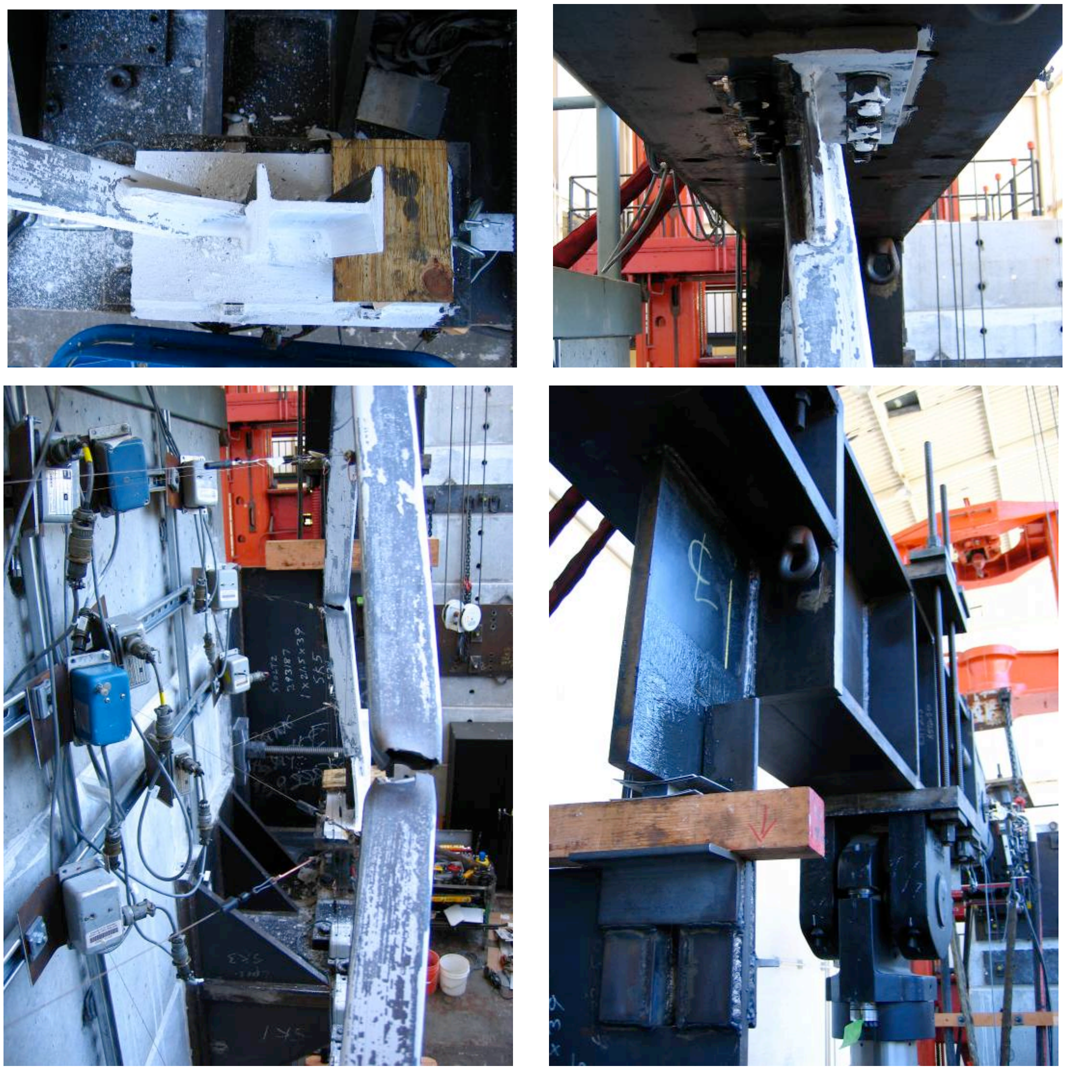

Fig. 2.19 Close-up view of gusset plate bent out of plane, braces buckled out of plane and out of phase, and permanent beam out-of-plane rotation.

2.4 FINITE ELEMENT BRACE MODEL

The hysteretic responses of individual steel braces have been studied extensively in the past 25 years (Black et al. 1980; Gugerli and Goel 1980, 1982; and Lee and Bruneau 2004). Various researchers have modeled brace hysteretic behavior using different approaches (Hall and Challa 1995; Ikeda et al. 1984; Khatib et al. 1988; Uriz 2005; and Zayas et al. 1980). This study adopts the approach pioneered by Uriz (2005), whereby the brace behavior was modeled using a two-dimensional OpenSees model as shown in Figure 2.20.

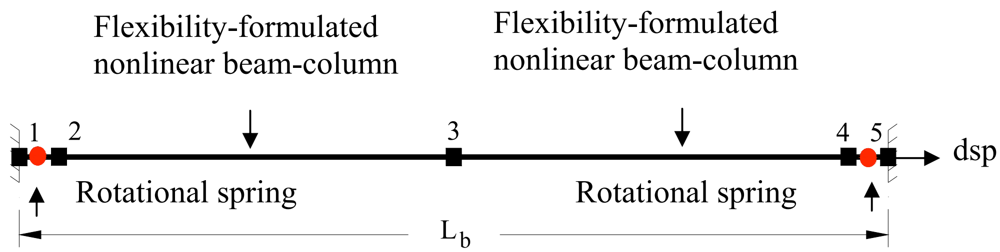

Fig. 2.20 Finite element brace model.

Even though brace buckling behavior is a three-dimensional phenomenon (as shown in Figure 2.14), it was observed from the experimental data that both ends of the brace remained in plane; thus, the axial force-deformation response of the brace can be adequately modeled using a two-dimensional in-plane model.

The finite element model used two flexibility-formulation nonlinear beam-column elements with five fiber cross sections along the length of each element to replicate the brace force-deformation responses. Figure 2.21 shows the fiber discretization and the material properties used to replicate the quasi-static test conducted in Section 2.2. Uniaxial Menegotto-Pinto steel material (Steel02) in OpenSees was used to model the yielding, hardening, and pinching behavior of the material response.

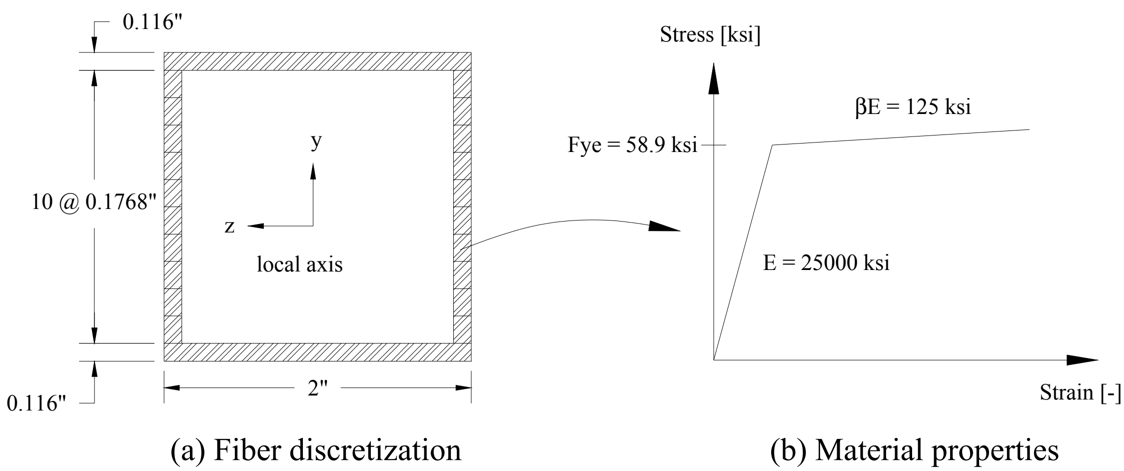

Fig. 2.21 Cross-sectional and material properties of analytical steel brace.

The geometric imperfection of the brace was modeled by shifting the middle node (node 3) of the brace a distance of 0.01 L_b in the direction perpendicular to a line between the end nodes. The corotational transformation was used to model the second-order geometry effects (de Souza 2000). To account for the rotational stiffness at the ends of the braces, three zero-length elements were used to model the gusset plate at each end. Two rigid springs (elastic material with high stiffness) were used to restrain the translational degrees of freedom, while the rotational degree of freedom was modeled using an elastic spring. The rotational stiffness of the zero-length element were modeled using $\frac{EI}{5L_b}$, where E is the modulus of elasticity, I is the moment of inertia about the plane of bending, and L_b is the total length of the brace. The following section shows two validations of the analytical brace model.

2.5 VALIDATION OF FINITE ELEMENT MODEL

The proposed analytical model was verified against two independent quasi-static tests. The first verification test was the quasi-static test, presented in Section 2.2, where the specimen was a steel HSS2x2x1/8 inverted-V braced subassembly. The second verification test was an independent quasi-static test conducted by Uriz (2005), where the tested specimen was a steel HSS6x6x3/8 brace under inelastic displacement history.

2.5.1 Quasi-Static Test of Steel HSS2x2x1/8 Inverted-V Braced Subassembly

Figure 2.22 shows a two-dimensional (in-plane) finite element model of the inverted-V braced subassembly. This model consists of nine nodes, four flexibility-formulation nonlinear beam-column elements, and nine zero-length elements. Node 1 and Node 9 are restrained for all degrees of freedom, while Node 5 is restrained only in the rotational degree of freedom.

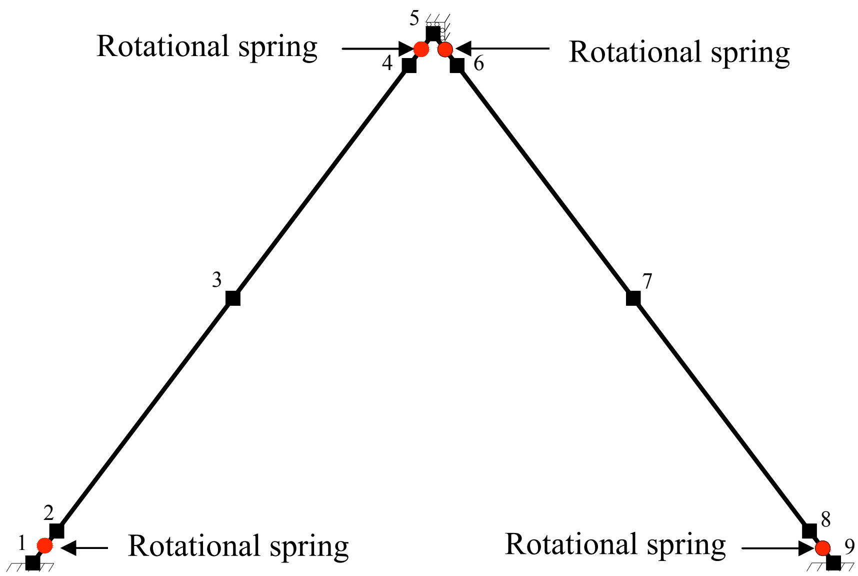

Fig. 2.22 Finite-element model of inverted-V braced subassembly.

Following the procedure presented in the previous section, the cross sections were modeled using fiber sections. The fiber discretization and the material properties are shown in Figure 2.21. The rotational springs were modeled using three zero-length elements as discussed above (with rotational stiffness = $\frac{EI}{5L_b}$), while the geometry imperfection was modeled by offsetting the mid nodes (Node 3 and Node 7) a distance of $0.01\ L_b$ in the direction perpendicular to the line between the end nodes. The displacements at the intersection of the braces recorded during the quasi-static test (Fig. 2.14) were applied at Node 5. Table 2.2 shows the properties of the analytical brace.

The analytically simulated and experimentally measured force-deformation responses of the inverted-V braced subassembly are presented in Figure 2.23. The force-deformation responses of the individual braces are presented in Figure 2.24. In these figures, the axial deformation is normalized with respect to the original brace length (L_b = 66.2 in.) and the axial force is normalized with respect to the expected yield strength ($A_g \times F_{ye}$ = 50.23 kips) of the brace.

Table 2.2 Properties of analytical brace shown in Section 2.5.1.

Properties	Values
Shape	HSS2x2x1/8
Cross sectional area, A_g	0.84 in.2
Moment of inertia about the plane of bending, I	0.486 in.4
Brace length, L_b	66.2 in.
Expected yield stress, $F_{ye} = R_y \times Fy$	59.8 ksi
Modulus of elasticity, E	25000 ksi
Ratio of post yield stiffness to modulus of elasticity, β	0.005

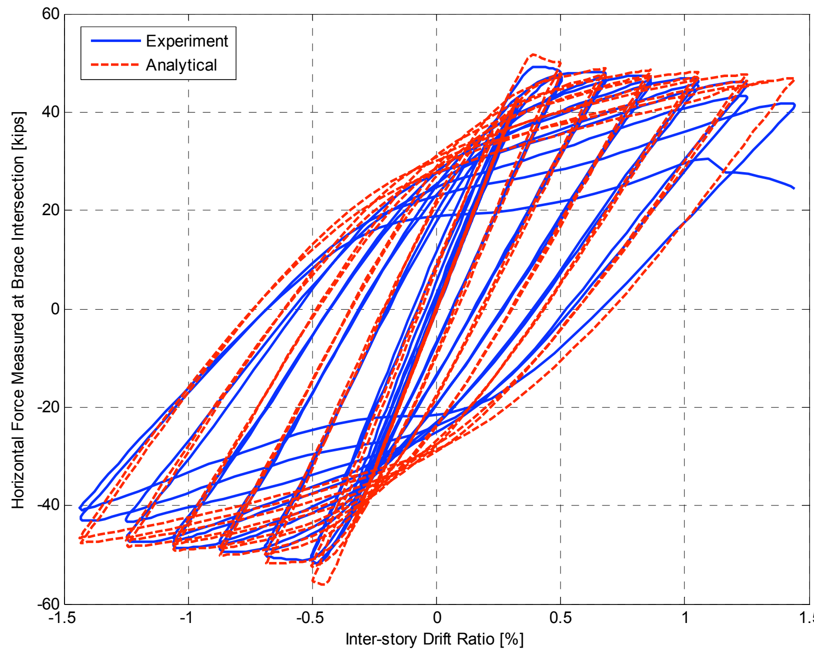

Fig. 2.23 Force-deformation response of inverted-V braced subassembly.

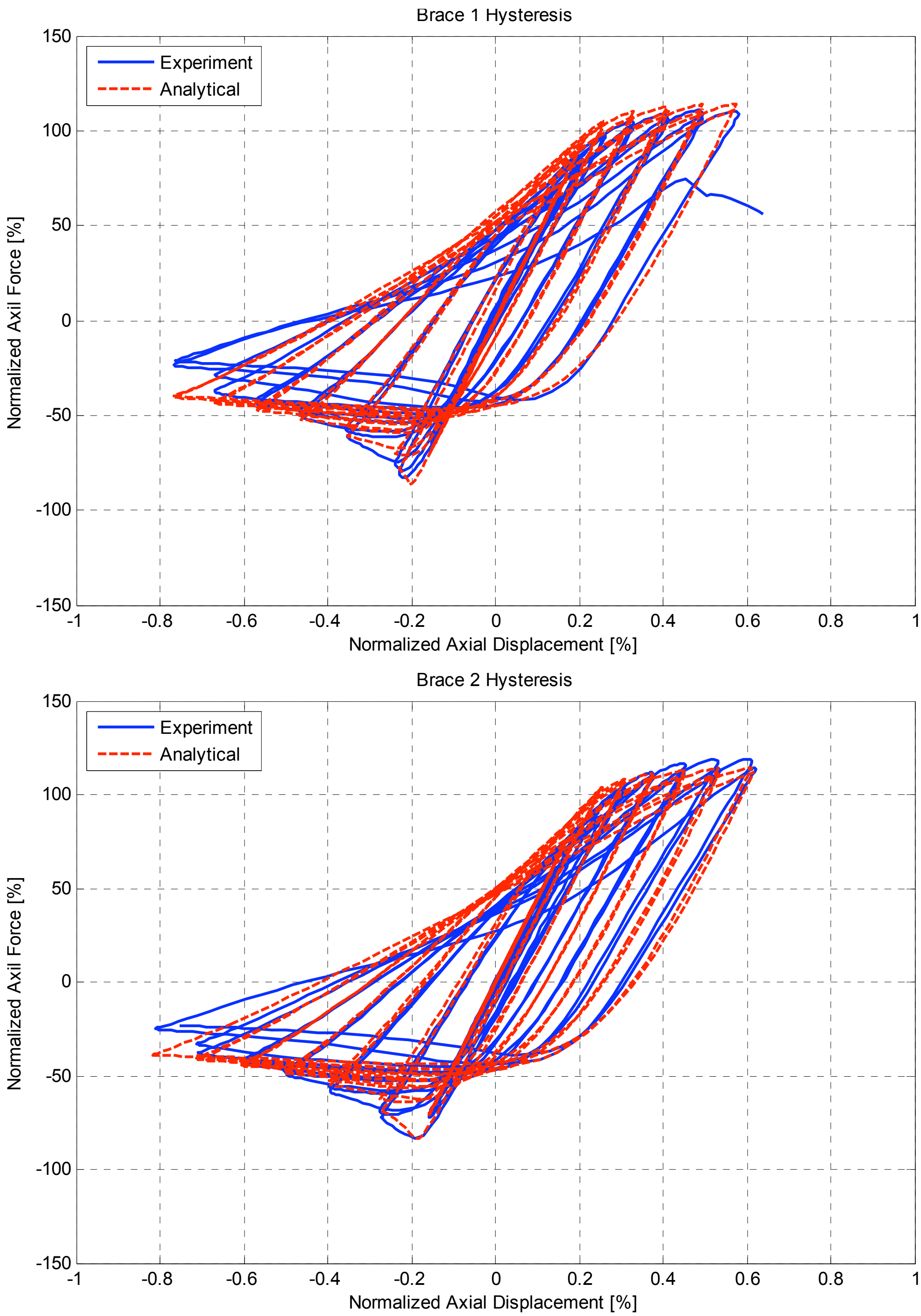

Fig. 2.24 Force-deformation response of HSS2x2x1/8 braces.

2.5.2 Quasi-Static Test of Steel HSS6x6x3/8

The proposed finite element model and rotational springs were further verified against the quasi-static brace test conducted by Uriz (2005). The tested specimen was a steel HSS6x6x3/8 brace under inelastic displacement history. The dimension of the test setup and the displacement history applied at the end of the brace is shown in Figure 2.25 and Figure 2.26, respectively.

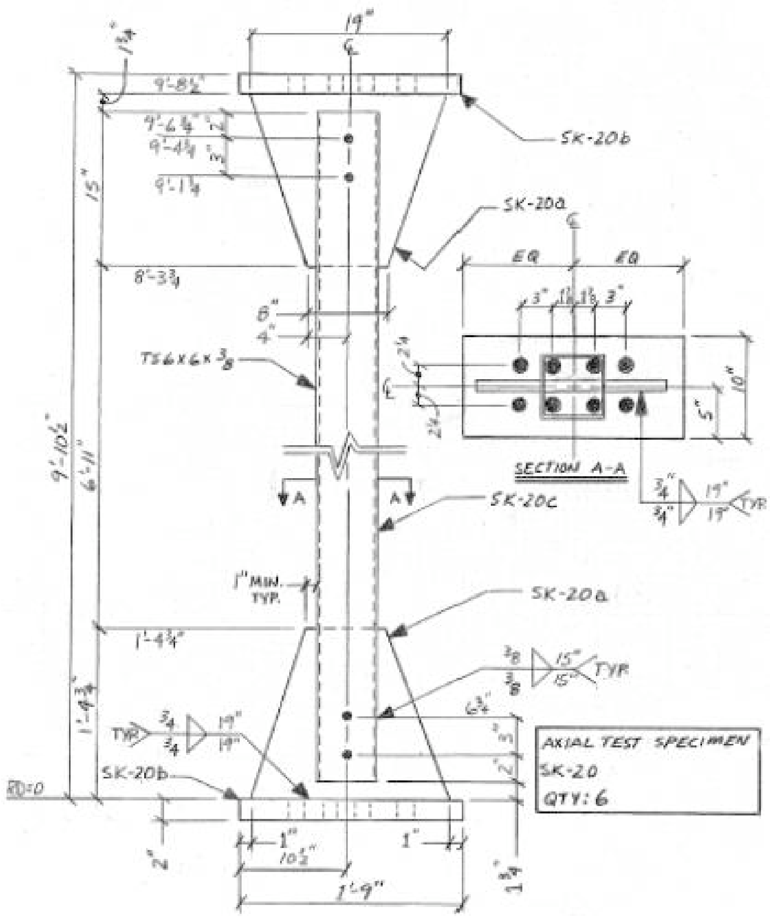

Fig. 2.25 Dimensions of brace component test setup (HSS6x6x3/8) (Uriz 2005).

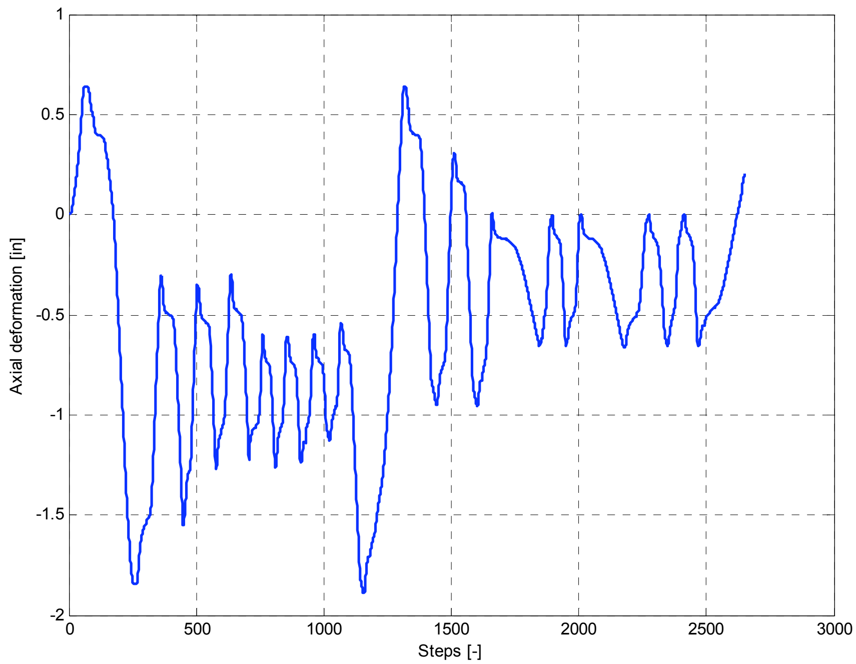

Fig. 2.26 Displacement history used for brace component test (Uriz 2005).

The analytical brace used to replicate this quasi-static test was identical to the finite element model shown in Figure 2.20. Table 2.3 shows the properties of the analytical brace. Figure 2.27 shows the dimension and discretization of the fiber section.

Table 2.3 Properties of analytical brace shown in Section 2.5.2.

Properties	Values
Shape	HSS6x6x3/8
Cross sectional area, A_g	7.58 in.^{2}
Moment of inertia about the plane of bending, I	39.5 in.^{4}
Brace length, L_b	116.5 in.
Expected yield stress, $F_{ye} = R_y \times Fy$	59.8 ksi
Modulus of elasticity, E	25000 ksi
Ratio of post yield stiffness to modulus of elasticity, β	0.005

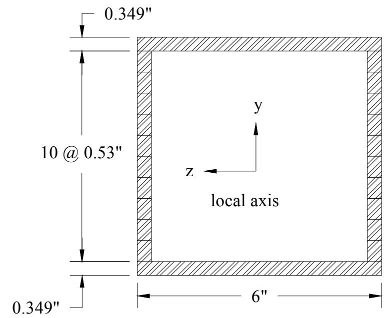

Fig. 2.27 Cross sectional property and fiber discretization of analytical steel brace.

The results of the analytical simulation and experimental measured force-deformation response are shown in Figure 2.28.

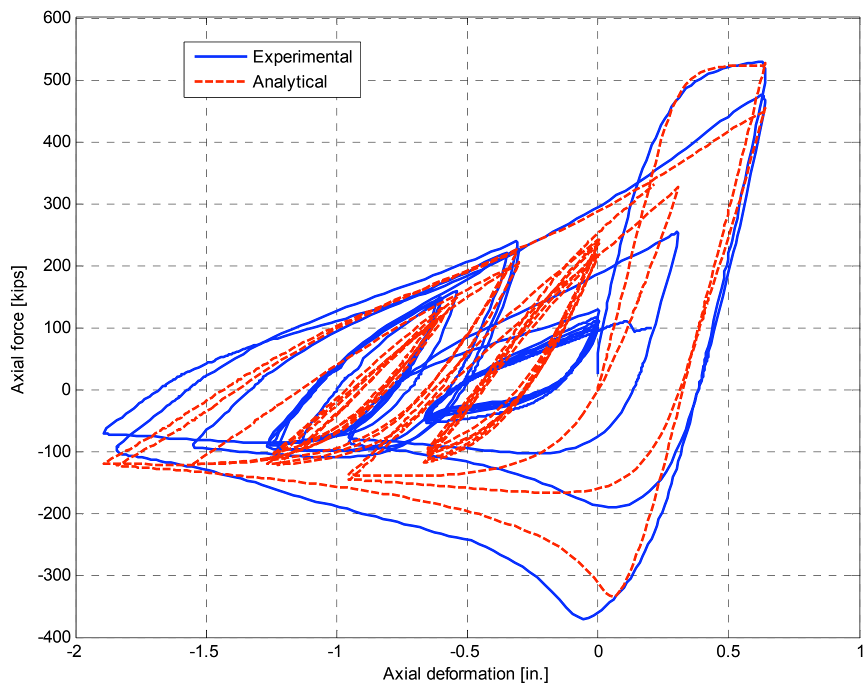

Fig. 2.28 Axial force-deformation behavior of the HSS6x6x3/8 brace.

The results of this model verification indicate that given the appropriate selection of initial imperfection, rotation spring stiffness and steel material properties used in the finite element model, the flexibility-formulation nonlinear beam-column element combined with corotational geometric transformation in OpenSees can be used successfully to model the force-deformation response of steel HSS that buckles out of plane. However, it should be noted that the presented analytical model does not account for dynamic effects (strain rate and mass inertia) or local buckling behavior of the brace. According to Uriz (2005), for compact brace sections, local buckling does not have a significant effect on the global hysteretic behavior of the brace except that it contributes to low-cycle fatigue, which eventually causes the brace to fracture.

2.6 SUMMARY

The quasi-static test presented in this chapter provides an opportunity to study the hysteretic behavior of steel HSS braces under inelastic displacement cycles. The experimental results provide information needed to calibrate the analytical model, as well as an insight to the true three-dimensional buckling behavior of the brace, which is very difficult to predict using analytical simulation alone. An analytical model is proposed to model the hysteretic behavior of steel HSS brace that buckles out of plane. From the results of the study, it is concluded that the proposed analytical brace model can be used to adequately replicate the force-deformation response of steel HSS braces with out-of-plane buckling.

3 Analytical Simulation of Suspended Zipper Braced Frame Response

The purpose of this chapter is to study the system response of the suspended zipper braced frame under static and dynamic loading using the calibrated analytical braces model presented in the previous chapter. The results of this chapter will provide the information needed to verify the system behavior of the suspended zipper braced frame.

3.1 FINITE ELEMENT MODEL

A two-dimensional (in-plane) finite element model (Fig. 3.1) was constructed in OpenSees to study the system response of the 1/3-scale suspended zipper braced frame test model (Fig. 1.1c). The analytical model used the flexibility-formulation nonlinear beam-column elements with fiber sections and zero-length elements to model the beams, braces, zipper columns, and columns of the suspended zipper braced frame. The foundations of the columns and the beam-to-column connections were modeled using the semi-rigid connection model suggested by Astaneh-Asl (2005). Gravity load was ignored in the analytical simulation. The similitude laws governing the scaling of the finite element model are summarized in Table 3.1.

Table 3.1 Similitude laws used for finite element model.

Quantities	Scaling factor $S = \dfrac{\text{Model (1/3 scaled model)}}{\text{Prototype (full scaled model)}}$
Length	$S_L = \dfrac{1}{3}$
Modulus of elasticity	$S_E = 1$ (same material)
Force	$S_F = S_E \times S_L{}^2 = \dfrac{1}{9}$
Acceleration	$S_a = 1$
Inertia mass	$S_M = \dfrac{S_F}{S_a} = \dfrac{1}{9}$
Time	$S_T = \sqrt{\dfrac{S_L}{S_a}} = \dfrac{1}{\sqrt{3}}$

Considering that the full-scale model has a seismic weight of 361.3 kips/floor (Yang 2006), a floor mass of 1242 slugs/floor (weight = 40 kips/floor) was assigned as two lumped masses at the exterior nodes of the 1/3-scale model at each floor. With the element sizes shown in Table 1.1, the modal periods of the 1/3-scale model were calculated and presented in Table 3.2. Rayleigh mass and stiffness proportional damping of 5 percent was assigned to the first and second modes.

Table 3.2 Vibration periods of finite element model.

Mode	Period [sec]
1	0.30
2	0.11
3	0.08

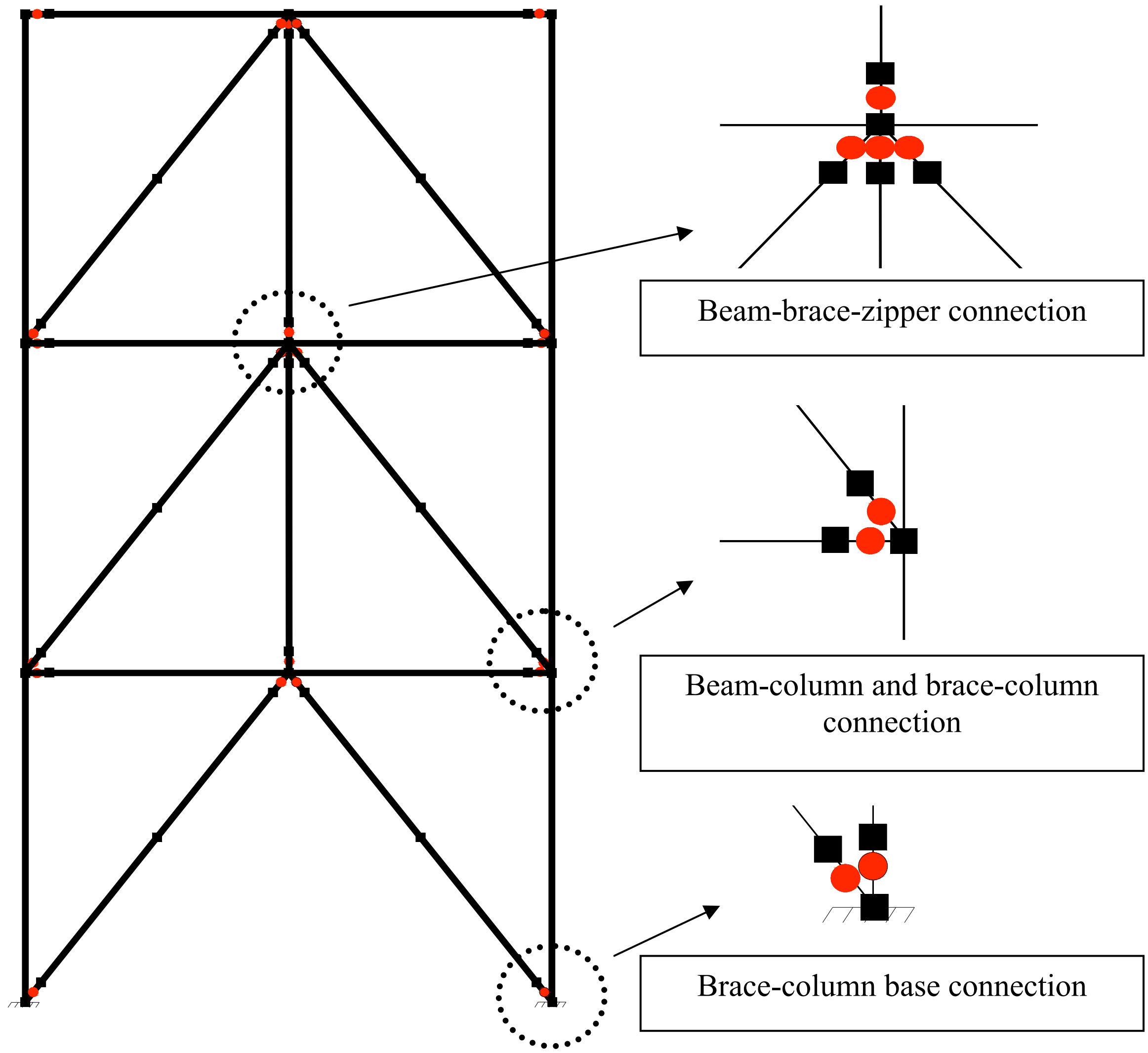

Fig. 3.1 Finite element model of 1/3-scale suspended zipper braced frame.

3.2 NONLINEAR STATIC ANALYSIS

Nonlinear static analysis provides valuable insights into the expected performance of structural systems and components. A static nonlinear analysis (or pushover analysis) was conducted to identify the force-deformation response of the 1/3-scale suspended zipper braced frame. The analysis provides the insight into the force redistribution characteristics of the study frame.

3.2.1 Applied Static Load Pattern

The finite element model was subjected to lateral loads corresponding to lateral floor accelerations varying linearly with distance from the base. The loads were applied as lumped forces at the two exterior nodes at each floor level. The loads were increased monotonically from the left to right until the horizontal displacement at the roof reached 3 percent roof drift ratio. Gravity loads were set equal to zero.

3.2.2 Response of Suspended Zipper Braced Frame Recorded during Nonlinear Static Analysis

The roof drift ratio (roof drift divided by height from base to the roof) vs. the total base shear response recorded during the nonlinear static analysis is presented in Figure 3.2. Axial forces in the braces, zipper columns and columns are presented in Figure 3.3, Figure 3.4 and Figure 3.5, respectively.

In the analysis, the base shear increases linearly until the roof drift ratio reaches 0.39 percent and the base shear reaches 57 kips. After this stage, the first-story brace in compression buckles, which reduces the base-shear resistance to 51 kips. The loss in compression strength in the first-story brace engages the zipper column immediately, causing the unbalanced vertical force to be distributed to the second and third stories. This force redistribution reduces the tension forces in the second- and third-story braces. After the frame reaches the next equilibrium state, the base-shear resistance increases again with increasing roof drift.

As the tension brace in the first story starts to pick up additional tension forces, the unbalanced vertical forces are equilibrated by both the second- and third-story zipper columns. This action increases the compression forces in the second- and third-story braces. As the roof drift ratio reaches 0.48 percent, the second-story brace in compression buckles. This action quickly engages the third-story zipper column to transfer all the unbalanced vertical forces to the third-story braces. At this moment, both braces at the third story start to pick up compression forces to balance the unbalanced vertical forces.

After the forces redistribute, the first- and second-story tension braces pick up additional base shear and transfer all the unbalanced vertical forces to the third-story braces through the zipper columns. The forces are then transferred back to the foundation through axial forces in the columns.

From the element force responses shown in Figure 3.5, the first- and second-story frame columns on the left side of the frame were originally taking tension forces to balance the overturning moment. Once the second-story brace buckles, both columns are loaded with compression forces from the unbalanced vertical forces in the braces. Such force redistribution can be seen when the third-story zipper column starts to pick up additional unbalanced vertical forces after the second-story brace buckles. Since the braces in the third story are designed to remain elastic, the base-shear resistance continues to increase until the tension braces in the first and second stories yield.

This analysis shows that the intended force redistribution in the suspended zipper braced frame is, indeed, occurring. In addition, it is evident that the suspended zipper braced frame structure is quite redundant, providing a number of lateral load paths. Furthermore, the ability to redistribute yielding throughout the height of the structure results in increased system ductility capacity as compared to a conventional zipper braced frame (Yang 2006).

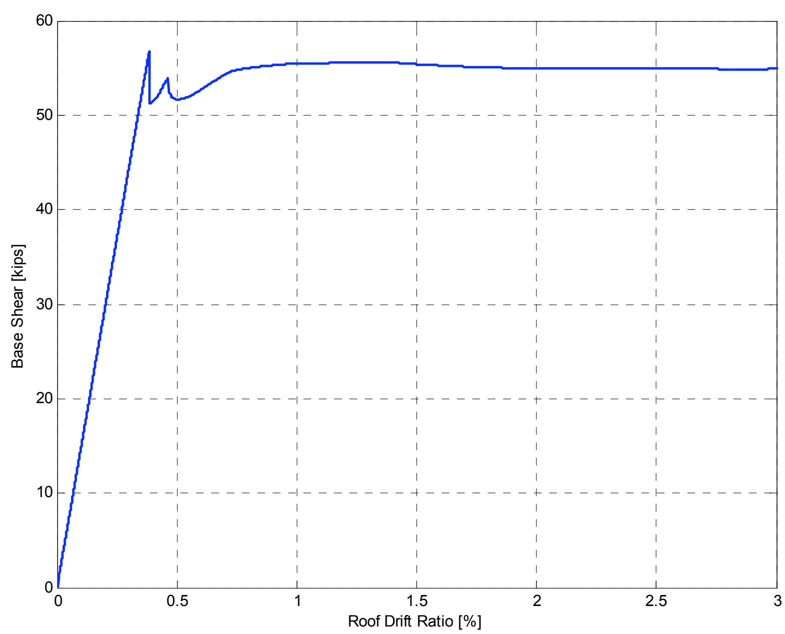

Fig. 3.2 Force-deformation response curve of 1/3-scale suspended zipper braced frame model recorded during nonlinear static analysis.

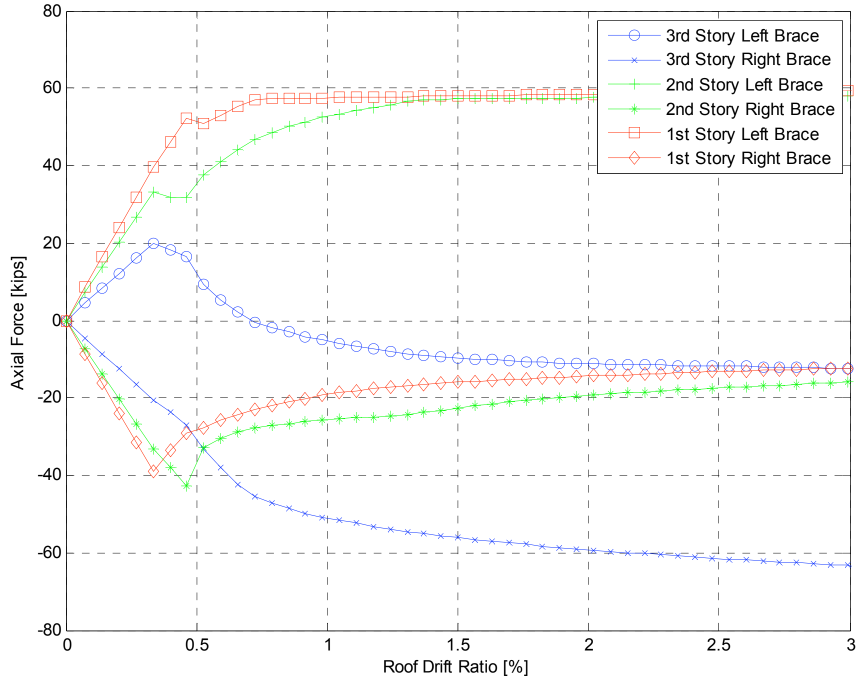

Fig. 3.3 Axial brace forces vs. roof drift ratio (axial tension shown positive).

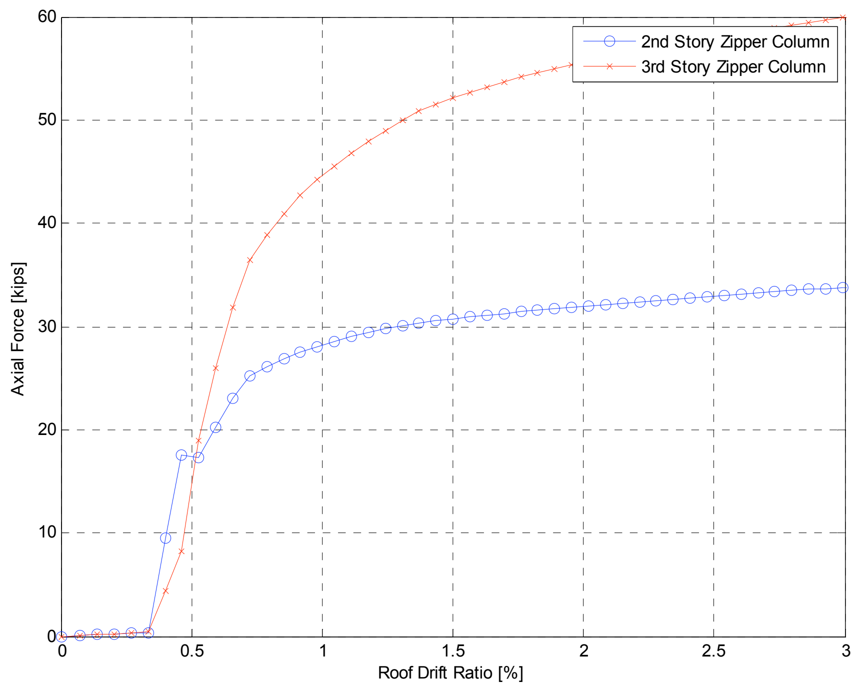

Fig. 3.4 Axial zipper column forces vs. roof drift ratio (axial tension shown positive).

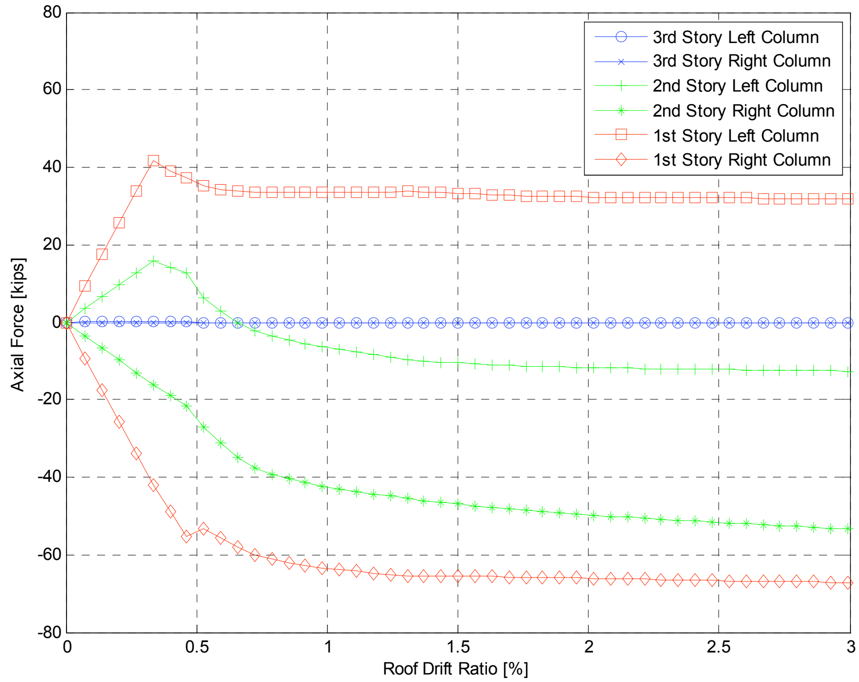

Fig. 3.5 Axial force in columns vs. roof drift ratio (axial tension shown positive).

3.3 NONLINEAR DYNAMIC ANALYSIS

The same finite element model used for the nonlinear static analysis was used to examine the response of the suspended zipper braced frame under a selected earthquake ground motion. The Newmark average-acceleration ($\gamma = \frac{1}{2}, \beta = \frac{1}{4}$) time-step integration method with Newton initial-stiffness interaction was used to solve the differential equation governing the system dynamic response. With 5 percent Rayleigh proportional damping in the first and second modes and the integration time-step of 0.01155 sec (the time interval of the recorded ground motion scaled according to similitude law shown in Table 3.1), the algorithm converged without instability.

3.3.1 Selection of Earthquake Ground Motion

The ground motion used in this study was selected from the suite of ground motions used in the SAC Joint Venture project (Somerville et al. 1997) to study the seismic response of the three-story building located in Los Angeles. Taking into account the requirements for conducting a shaking table test at the University at Buffalo, the LA22 ground motion was selected for the nonlinear dynamic analysis. The LA22 ground motion was recorded at the JMA station during the 1995 Kobe earthquake and was scaled according to the similitude law shown in Table 3.1. The resulting scaled record is shown in Figure 3.6. The record was applied uniformly to the bases of the two columns of the suspended zipper braced frame finite element model.

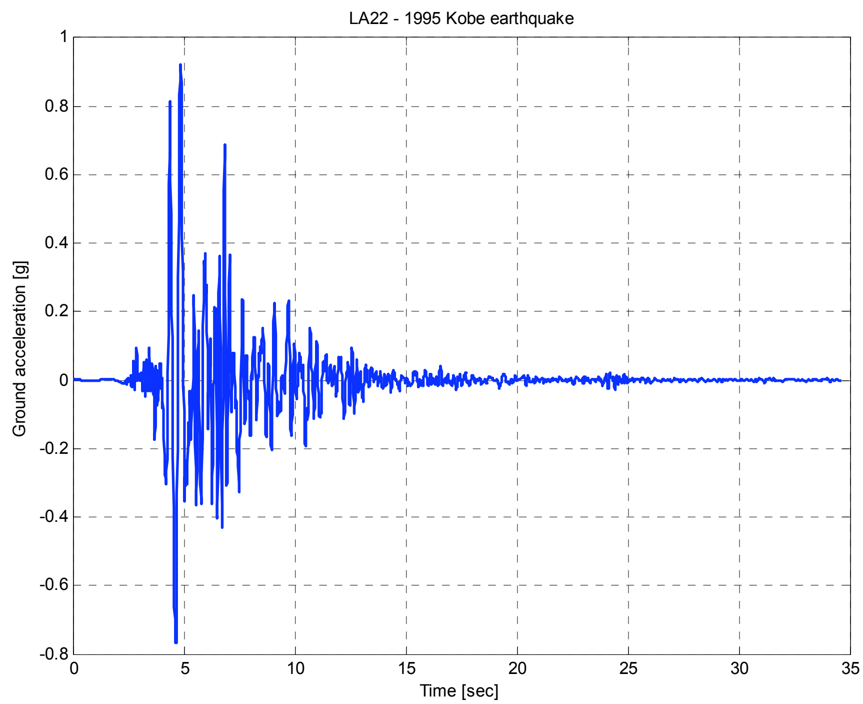

Fig. 3.6 Scaled LA22 record used for nonlinear dynamic analysis.

3.3.2 Response of Suspended Zipper Braced Frame Recorded during Nonlinear Dynamic Analysis

The roof and interstory drift ratio responses to the scaled LA22 ground motion are shown in Figure 3.7 and Figure 3.8, respectively. The maximum roof drift ratio reaches 2.4 percent, while the corresponding maximum interstory drift ratios reach 5.3, 1.6, and 0.35 percent for the first, second, and third stories, respectively. Under such large drift demand, the first- and second-story braces experience significant inelastic response, resulting in a permanent residual interstory drift of 0.8 and 0.25 percent at the first and second stories, respectively.

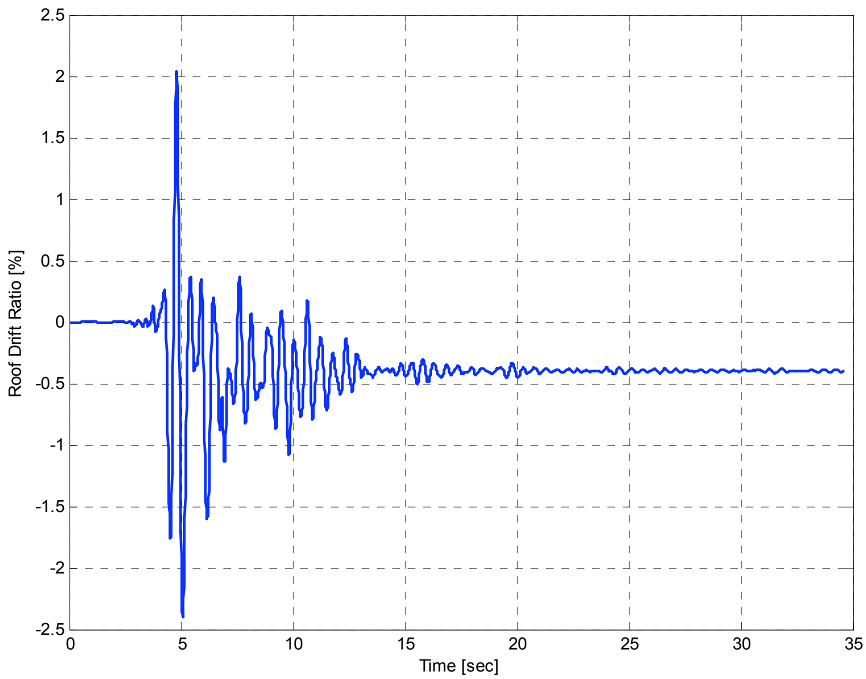

Fig. 3.7 Roof drift ratio response history.

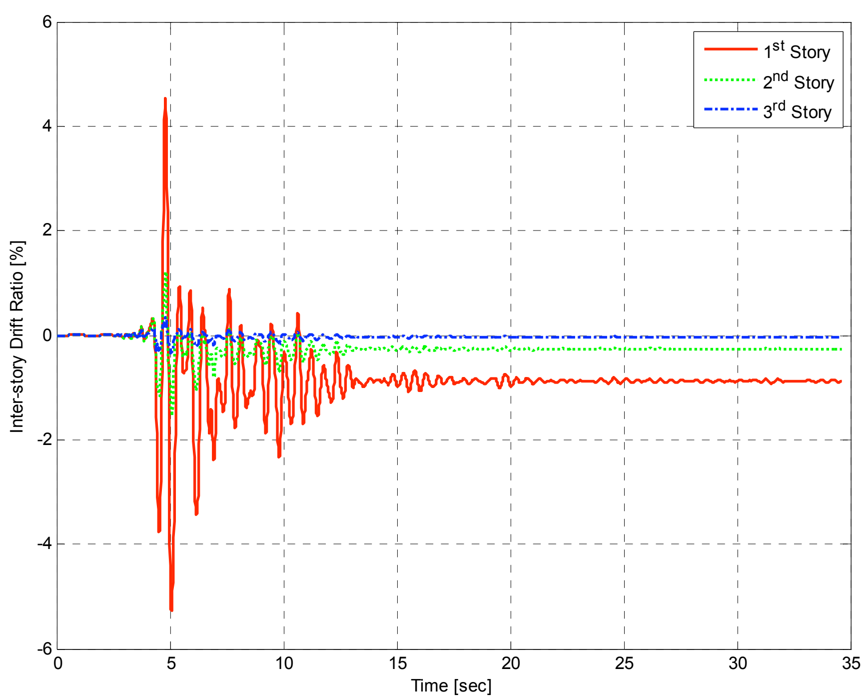

Fig. 3.8 Interstory drift ratio response histories.

Figures 3.9–3.11 show the force-deformation response of the braces, the zipper columns, and the columns recorded during the nonlinear dynamic analysis. The trilinear axial force-deformation response shown in Figure 3.9 indicates that the finite element brace model is capable of modeling the buckling response of the brace under dynamic loading. As calculated by nonlinear static analysis and as intended by the capacity design procedure (Yang 2006), the third-story braces remain elastic and are capable of transferring all of the unbalanced vertical forces to the columns. The zipper columns remain elastic throughout the dynamic analysis, but the first- and second-story columns undergo some inelastic deformation.

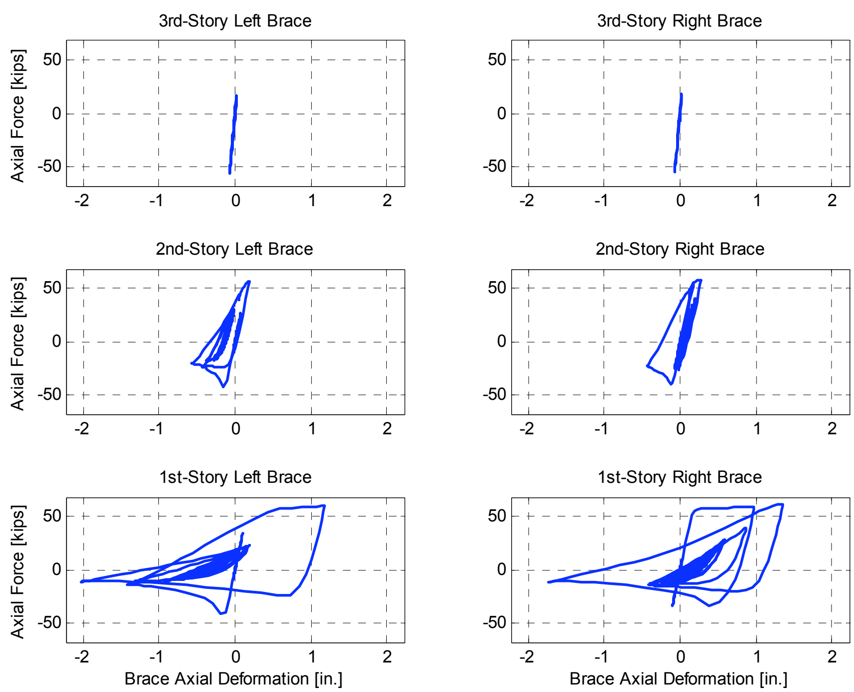

Fig. 3.9 Response of braces recorded during nonlinear dynamic analysis.

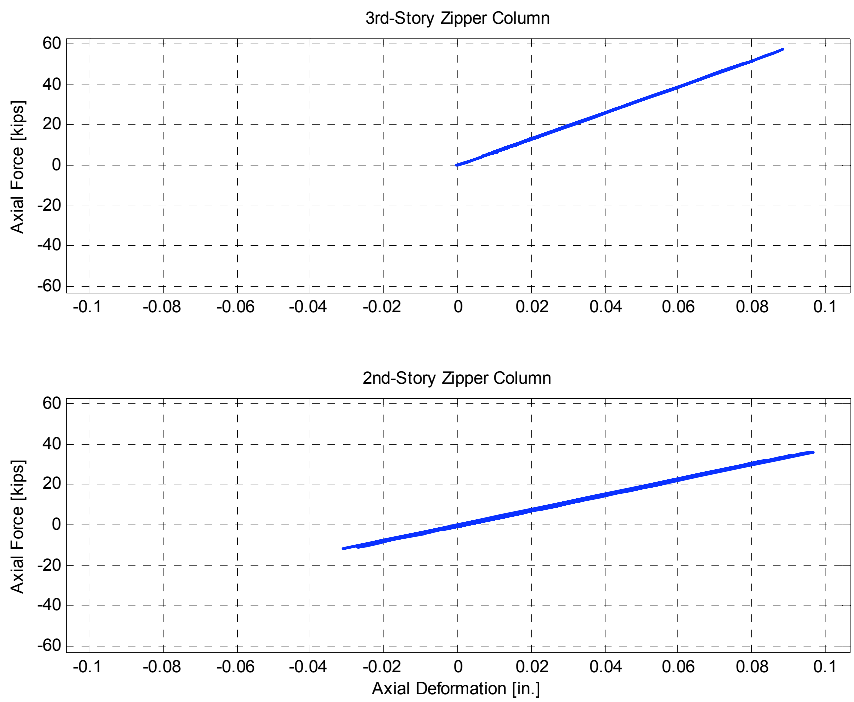

Fig. 3.10 Response of zipper columns recorded during nonlinear dynamic analysis.

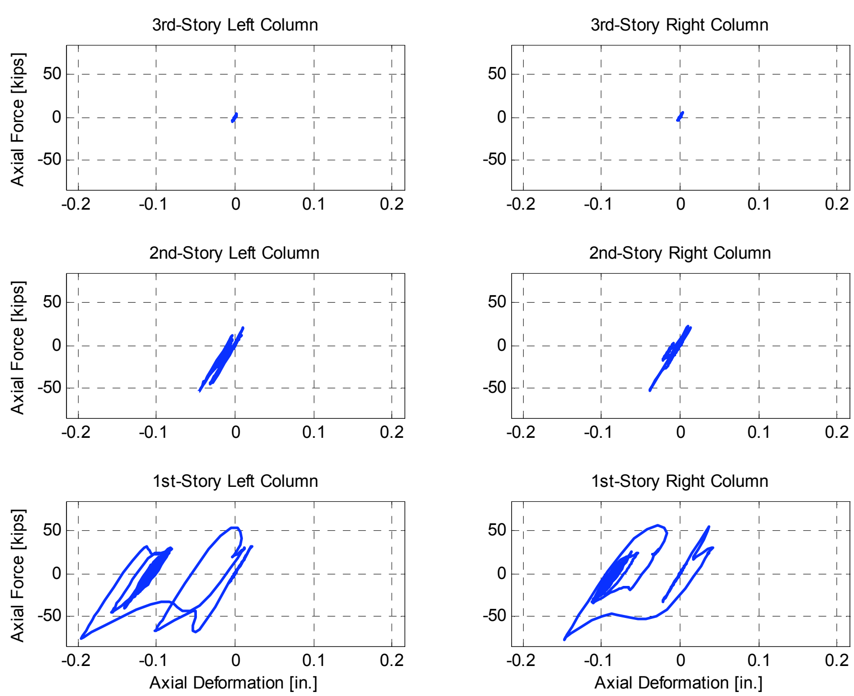

Fig. 3.11 Response of columns recorded during nonlinear dynamic analysis.

Figure 3.12 shows the base shear versus roof drift ratio of the suspended zipper braced frame recorded during the nonlinear dynamic analysis. Also plotted are the nonlinear static analysis results (pushover curves from Fig. 3.2), flipped about the origin. It is evident that the suspended zipper braced frame is capable of responding to the input earthquake motion in a stable manner. In addition, the nonlinear static analysis results provide a reasonably good approximation of the cyclic response backbone curve.

Hysteretic energy dissipated in each story was calculated by integrating the areas under the force-deformation response curves for all the elements at the same story. Figure 3.13 shows the percentage of the hysteretic energy dissipated in each story. Because the third-story braces were designed to remain elastic to prevent formation of the full zipper mechanism, all of the hysteretic energy was dissipated in the first and second stories. The zipper column is very effective in distributing plasticity, and thus, energy dissipation, from the first to the second story. Hence, it is concluded the suspended zipper braced frame has performed as intended under the selected ground motion.

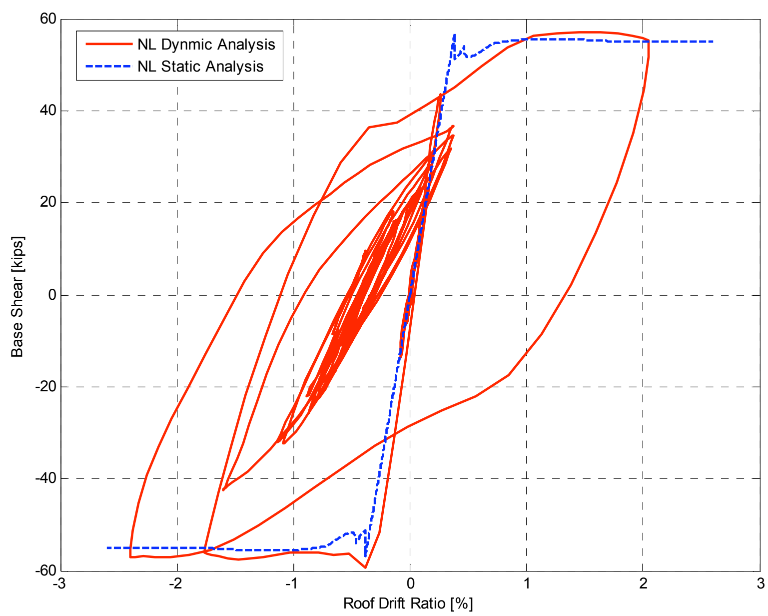

Fig. 3.12 Base shear vs. roof drift ratio frame response.

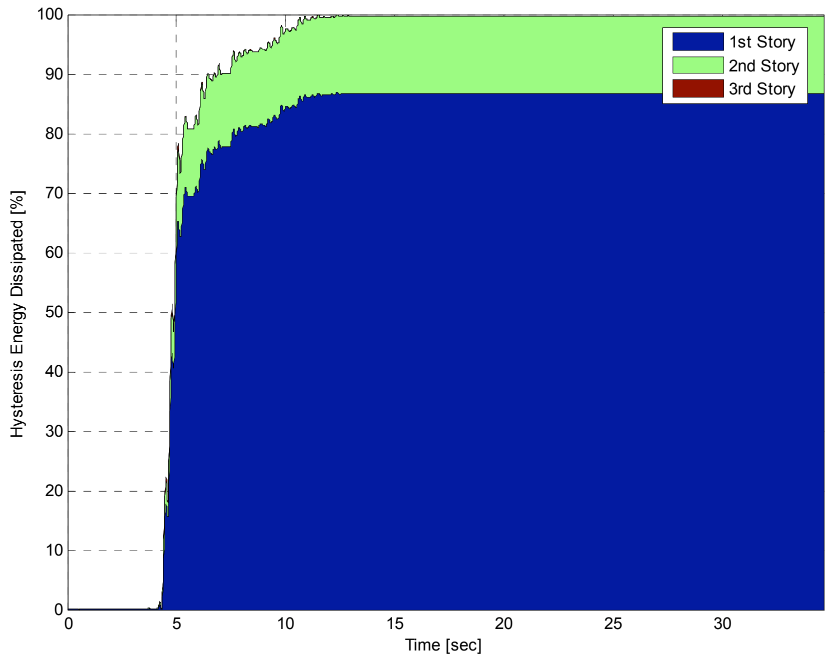

Fig. 3.13 Hysteretic energy-dissipation history at each story.

3.4 SUMMARY

The nonlinear response of a suspended zipper braced frame was analyzed using a finite element model shown in Figure 3.1. The model features the inverted-V braced subassembly model calibrated using the quasi-static test results presented in Chapter 2. The results of the nonlinear static and dynamic analyses indicate that the intended force redistribution is occurring. The input earthquake energy is successfully distributed and dissipated in the suspended zipper braced frame. However, under the selected ground motion, the building experienced large interstory drifts and developed permanent residual drifts at the first and second stories and yielded the first-story columns. Such damage should be considered to evaluate the total repair cost and functionality of the building.

It should be noted that the finite element model used in these analyses is a two-dimensional model. As such, it does not fully account for the out-of-plane buckling of the braces, which will eventually rotate the supporting beam. Thus, to ensure that the intended force redistribution is achieved, the beams must be adequately braced against lateral-torsional buckling. In addition, the analytical model does not account for local buckling and low-cycle fatigue behavior. In particular, if noncompact sections are used, an alternative analytical brace model should be used. Finally, because the results of the nonlinear dynamic analysis are obtained from a single ground motion and single frame configuration, additional analyses under different ground motions are needed to provide a better data set for probability-based evaluation of the seismic performance of the suspended zipper braced frame concept.

4 Hybrid Simulation Evaluation of Suspended Zipper Braced Frame

Investigation of suspended zipper braced frame behavior using a calibrated analytical model provides a good understanding of the behavior of this structural system. However, the accuracy of the simulation depends strongly on the inverted-V braced subassembly model calibrated using the quasi-static test data (Chapter 2). To reduce model uncertainty, the response of the suspended zipper braced frame was further investigated using a hybrid model. The hybrid model combines a physical first-story inverted-V braced subassembly in the laboratory and a finite element model of the remainder of the frame. In doing so, the finite element model of the inverted-V braced subassembly, which is expected to undergo the largest inelastic demand, is replaced by the force-deformation response measured in the laboratory.

There are many advantages of using the hybrid simulation test. First, it provides a cost-effective way to study the system response, where only a portion of the structure is tested in the laboratory, while the rest of the structure is modeled in the computer. Second, with the appropriate boundary conditions, multiple subassemblies can be tested simultaneously to study larger and more complex structural systems. Third, with the event-driven algorithm, structural components can be tested to more extreme states, such as collapse, which might be difficult to conduct and record using a shaking table test. Last, with the use of OpenSees, the experimental elements can be added to the finite element model easily, making the hybrid simulation test very flexible.

The hybrid simulation test presented here, for the first time, combines nonlinear analytical elements in OpenSees and physical element(s) in the laboratory to study the system response of a complex structural system, where the material and geometry nonlinearity are accounted for in both the analytical and experimental elements. To implement the hybrid simulation test, three experimental classes (Schellenberg 2008) have been implemented in OpenSees. The experimental classes are set up to enable communication between the experimental elements, the experimental setup, and the analytical elements. In addition, because the hybrid simulation test for the suspended zipper braced frame uses the displacement control within a continuous testing algorithm (which required a computer with a real-time operating system), a hybrid simulation architecture with four separate computers was established.

4.1 HYBRID SIMULATION MODEL

Figure 4.1 shows the hybrid simulation model used for the system evaluation of the suspended zipper braced frame. The hybrid simulation model is identical to the analytical model shown in Figure 3.1 except that the first-story inverted-V braced subassembly is replaced with a physical inverted-V braced subassembly instantiated in the laboratory.

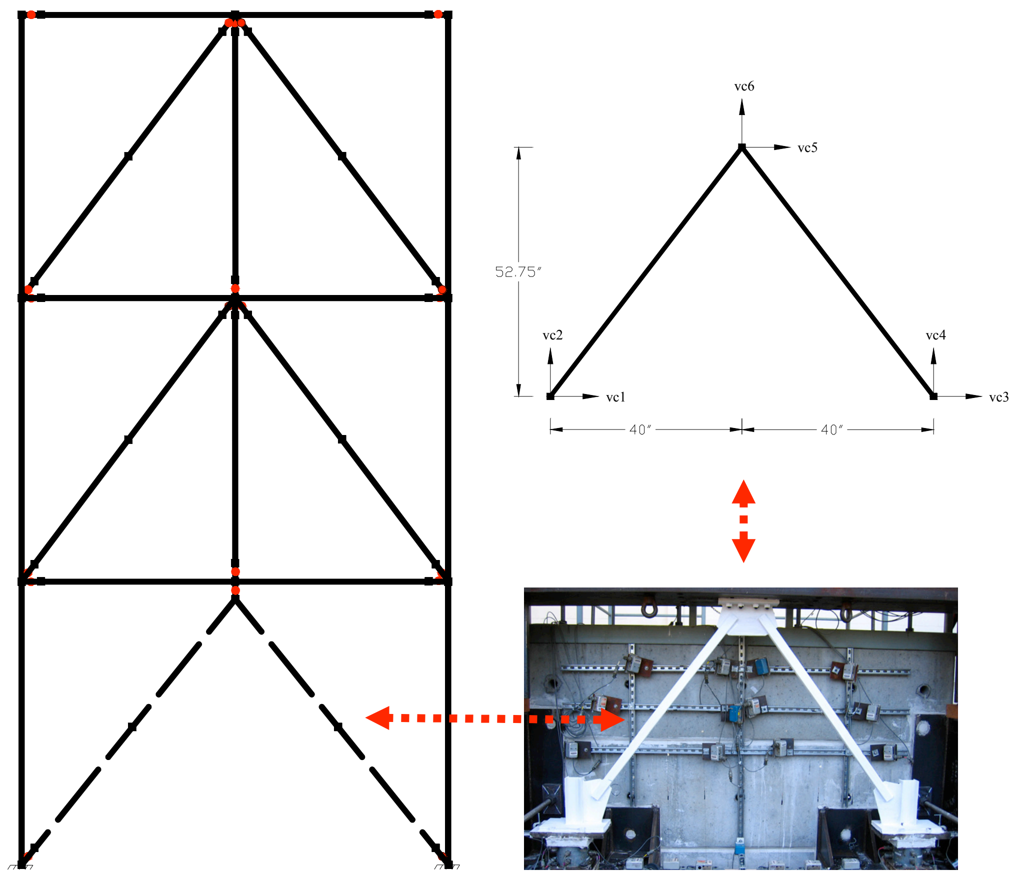

Fig. 4.1 Hybrid simulation model.

Because the shaking table at the University at Buffalo has a weight limitation, therefore requiring a floor mass reduction in the shaking table model, the floor mass assigned to the hybrid simulation model likewise was altered to match that used in the shaking table test. The floor masses were reduced from 1242 slugs/floor (weight = 40 kips/floor) to 621 slugs/floor (weight = 20 kips/floor).

4.2 SIMILITUDE LAWS USED FOR HYBRID SIMULATION TEST

Table 4.1 shows the similitude laws used in the hybrid simulation test. Because gravity effects are largely ignored in both the shaking table test and the analytical simulation, the similitude laws shown in Table 3.1 and Table 4.1 preserve the same system dynamics. Figure 4.2 shows a comparison of the total base shear vs. roof drift ratio for the two finite element models, one scaled according to the similitude laws shown in Table 3.1 and the other according to the similitude laws shown in Table 4.1. Figure 4.3 shows a close-up view of the total base shear vs. roof drift ratio shown in Figure 4.2. Note that mass scaling is different between Table 4.1 and Table 3.1. Hence, the vibration periods for both models are different. Rayleigh mass and stiffness proportional damping of 5 percent assigned to the first and second modes are scaled accordingly using the similitude laws presented.

Table 4.1 Similitude laws used for hybrid simulation model.

Quantities	Scaling factor $S = \dfrac{\text{Hybrid simualtion model}}{\text{Prototype (full scaled model)}}$
Length	$S_L = \dfrac{1}{3}$
Modulus of elasticity	$S_E = 1$ (same material)
Force	$S_F = S_E \times S_L{}^2 = \dfrac{1}{9}$
Acceleration	$S_a = 2$
Inertia mass	$S_M = \dfrac{S_F}{S_a} = \dfrac{1}{18}$
Time	$S_T = \sqrt{\dfrac{S_L}{S_a}} = \dfrac{1}{\sqrt{6}}$

Figure 4.2 shows the LA22 ground motion scaled according to the similitude laws shown in Table 4.1.

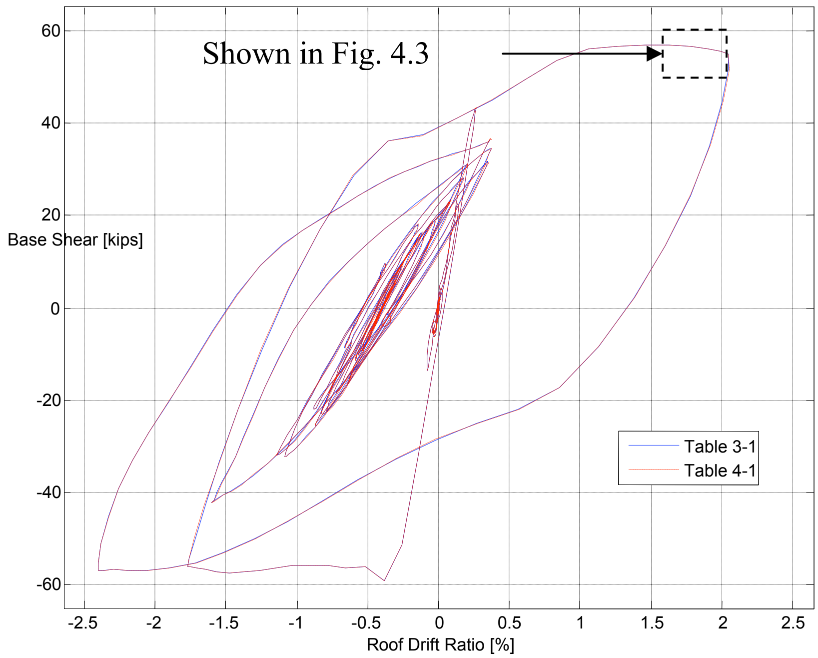

Fig. 4.2 Comparison of system response when finite element model is scaled according to similitude laws shown in Tables 3.1 and 4.1.

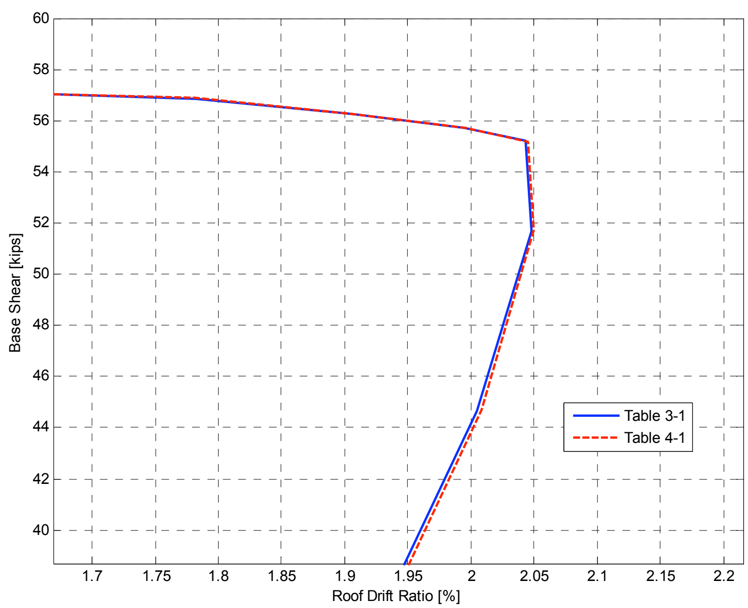

Fig. 4.3 Detail of total base shear vs. roof drift ratio shown in Figure 4.2.

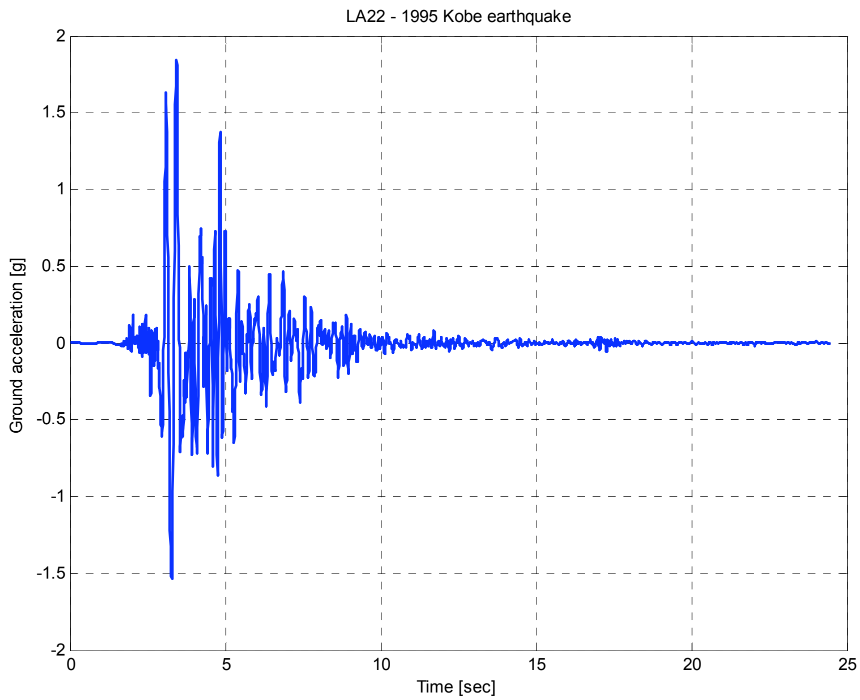

Fig. 4.4 LA22 ground motion scaled according to similitude laws shown in Table 4.1.

4.3 HYBRID SIMULATION ARCHITECTURE

Hybrid simulation using the hybrid model outlined above was conducted using displacement control. In the hybrid simulation procedure used, the integrator (Newmark average-acceleration time-step integration) implemented in OpenSees calculates the structural deformation from the external excitation at the beginning of each time-step. The test setup then executes the displacement and samples the force feedback from the experimental subassembly. Simultaneously, the analytical elements in OpenSees calculate the force feedback at the displacement state. The integrator then combines the force feedback from the experimental and the analytical elements and the external excitation to calculate the structural deformations at the next time-step. The whole process is repeated until the entire response history analysis is complete.

The following hybrid simulation architecture was implemented to conduct the hybrid simulation test. Figure 4.5 shows the communication diagram among different components in the hybrid simulation architecture.

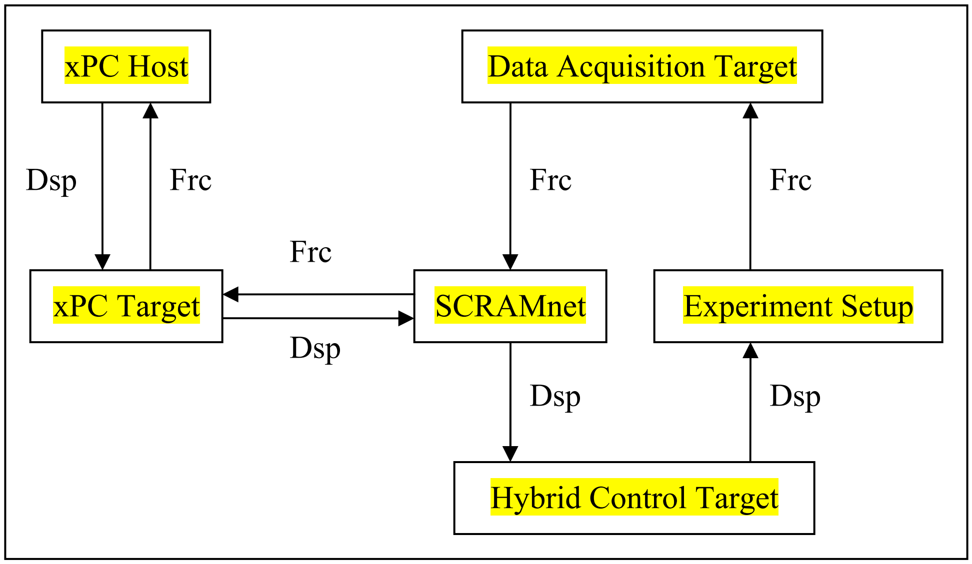

Fig. 4.5 Hybrid simulation architecture communication diagram.

The hybrid simulation architecture consists of four computers (nodes): the xPC Host, the xPC Target, the Hybrid Control Target and the Data Acquisition Target. The remaining components of the setup are the specimen in the Experiment Setup and the communication network between the nodes. A fiber-optic shared-memory network, the SCRAMnet, is used to connect the hybrid simulation nodes. Each computer manages a different part of the hybrid simulation test. The xPC Host is the core of the hybrid simulation test, where the time-step integrator is running in OpenSees. The xPC Host combines the forces computed by the analytical elements in OpenSees, the forces measured from the physical subassemblies, and the external excitation to calculate the displacement responses at one time-step. The SCRAMnet functions as a shared memory among the xPC Target, the Hybrid Control Target, and the Data Acquisition Target. Each computer has access to SCRAMnet shared memory (as implemented, the size of this memory is 2MB), such that any information stored in the SCRAMnet shared memory is mirrored to all connected computers using a fiber-optic network practically in real time. Information shared at the SCRAMnet includes the displacement command sent from the xPC Target, the measured forces feedback from the experimental subassembly, and the time-stamp information to synchronize the hybrid simulation test.

The Hybrid Control Target controls the actuators. It receives the displacement command from the xPC Target at a rate of 1024 Hz (the rate specific to *nees@berkeley*) and controls the actuators to execute the target displacement. A built-in PID controller is used to ensure that the actuator is tracking the target displacement. Since the Hybrid Control Target has a SCRAMnet card on board, it provides access to any information, such as the displacement achieved by the actuator and force feedback measured from the actuators to the other nodes in the hybrid simulation network via the SCRAMnet. However, because the suspended zipper braced frame test uses the Data Acquisition Target to collect such information, the information obtained from the Hybrid Control Target is saved only for data validation purposes.

The Experiment Setup consists of the physical experimental element, the actuators, and the guiding system. The setup receives the target displacement from the Hybrid Control Target and executes the displacement vector at the two degrees of freedom in-plane. At the same time, the Experiment Setup measures the reaction forces from the actuator and the VPM load cells and forwards the data to the Data Acquisition Target. A special set of force and displacement transformations, described below, is used to convert between the actuator and load cell directions and the hybrid model degrees of freedom. Other information, such as the brace deformation, are also recorded and forwarded to the Data Acquisition Target, using a direct connection between the instruments and the data acquisition system rather than the SCRAMnet; this information is not used in the hybrid simulation test. Finally the Data Acquisition Target copies the recorded reaction force measured by the VPM load cells to SCRAMnet. Then, the xPC Target obtains these data from the SCRAMnet and sends it back to the xPC Host. The whole process is repeated until the entire response history analysis has completed.

4.4 HYBRID SIMULATION TEST SETUP

The hybrid simulation test used the same test setup as the quasi-static test shown in Figure 2.3. The two VPM load cells placed at the base of the braces (Fig. 2.10) were used to measure the brace reaction forces. Because the brace is assumed to have pin connections, the moments measured by the VPM load cells at the base of the brace were ignored in the hybrid simulation test. In addition, to account for the cross-talk effect in the VPM load cell (an error in reading the shear forces when large axial forces are applied at the load cell or vice versa), the axial forces in the experimental braces were calculated using the average of the horizontal and vertical force components measured from the VPM load cells. By doing so, the chance for obtaining unstable and inaccurate force measurements from the VPM load cells was reduced.

4.4.1 Transformation of Force and Displacement Degrees of Freedom

To implement the hybrid simulation test using a displacement control algorithm, the displacements at the hybrid model degrees of freedom needed to be transformed to the experimental setup actuator degrees of freedom. At the same time, the force measured by the load cells had to be transformed back to the hybrid model degrees of freedom. Figure 4.6 and Equation (4.1) show the transformation from the forces measured at the base of the braces to the hybrid model degrees of freedom in OpenSees (the cross-talk effect has been accounted for in this transformation). Forces f_1 to f_4 are the shear and axial forces measured by the VPM load cells at the base of the braces. Forces q_1 to q_9 are the element forces at the basic element degrees of freedom. Note that $q_3 = q_6 = q_9 = 0$, as the physical subassembly is assumed to be pinned at both ends.

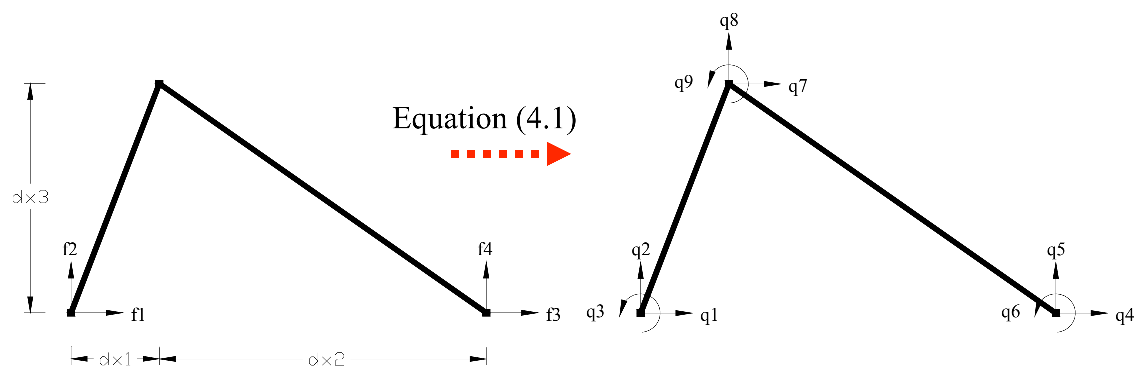

Fig. 4.6 Transformation of forces at measured degrees of freedom to hybrid model degrees of freedom.

$$
\begin{bmatrix} q_1 \\ q_2 \\ q_3 \\ q_4 \\ q_5 \\ q_6 \\ q_7 \\ q_8 \\ q_9 \end{bmatrix} =
\begin{bmatrix}
1/2 & 1/2(dx1/dx3) & 0 & 0 \\
1/2(dx3/dx1) & 1/2 & 0 & 0 \\
0 & 0 & 0 & 0 \\
0 & 0 & 1/2 & 1/2(dx2/dx3) \\
0 & 0 & 1/2(dx3/dx2) & 1/2 \\
0 & 0 & 0 & 0 \\
-1/2 & -1/2(dx1/dx3) & -1/2 & -1/2(dx2/dx3) \\
-1/2(dx3/dx1) & -1/2 & -1/2 & -1/2(dx2/dx3) \\
0 & 0 & 0 & 0
\end{bmatrix}
\begin{bmatrix} f_1 \\ f_2 \\ f_3 \\ f_4 \end{bmatrix} \tag{4.1}
$$

With the reduction of the rotation degrees of freedom at the brace ends, the axial elongation of the braces can be controlled using the two translation degrees of freedom at the intersection of the braces (assuming the brace supports are not moving). Equation (4.2) shows the nonlinear transformation from the six translation degrees of freedom at the braces to the two translation degrees of freedom at the intersection of the braces. Displacements v_1 to v_9 are the displacements at the element degrees of freedom. Displacements v_{c1} to v_{c6} are the reduced displacement degrees of freedom for the experimental element. Displacements U_1 and U_2 are the displacements at the intersection of the braces. Finally, displacements U_{a1} to U_{a3} are the displacements at the actuator degrees of freedom. The lengths $L_1, L_2, L_3, L_{a1}, L_{a2}, L_{a3}, L_{r1}$ and L_{r1} are the dimensions of the test setup shown in Figure 4.7.

$$
\begin{aligned}
U_1 &= \frac{1}{2\,\mathrm{L}\,(-\mathrm{L}_1^{\,2}+\mathrm{L}_2^{\,2}+\overline{\mathrm{L}}_1^{\,2}-\overline{\mathrm{L}}_2^{\,2})} \\
U_2 &= \frac{\sqrt{-\left(L+\overline{L}_1+\overline{L}_2\right)\left(L+\overline{L}_1-\overline{L}_2\right)\left(L-\overline{L}_1+\overline{L}_2\right)\left(L-\overline{L}_1-\overline{L}_2\right)}}{2\,\mathrm{L}}\text{-}\mathrm{L}_3
\end{aligned}
\tag{4.2}
$$

where

$\mathrm{L} = \mathrm{L}_1+\mathrm{L}_2$

$\overline{\mathrm{L}}_1 = \sqrt{\mathrm{L}_1^{\,2}+2\mathrm{L}_1\mathrm{vc}_5-2\mathrm{L}_1\mathrm{vc}_1+\mathrm{vc}_5^{\,2}-2\mathrm{vc}_5\mathrm{vc}_1+\mathrm{vc}_1^{\,2}+\mathrm{L}_3^{\,2}+2\mathrm{L}_3\mathrm{vc}_6-2\mathrm{L}_3\mathrm{vc}_2+\mathrm{vc}_6^{\,2}-2\mathrm{vc}_6\mathrm{vc}_2+\mathrm{vc}_2^{\,2}}$

$\overline{\mathrm{L}}_2 = \sqrt{\mathrm{vc}_5^{\,2}-2\mathrm{vc}_5\mathrm{L}_2-2\mathrm{vc}_5\mathrm{vc}_3+\mathrm{L}_2^{\,2}+2\mathrm{L}_2\mathrm{vc}_3+\mathrm{vc}_3^{\,2}+\mathrm{L}_3^{\,2}+2\mathrm{L}_3\mathrm{vc}_6-2\mathrm{L}_3\mathrm{vc}_4+\mathrm{vc}_6^{\,2}-2\mathrm{vc}_6\mathrm{vc}_4+\mathrm{vc}_4^{\,2}}$

shows the transformation from the two translation degrees of freedom at the intersection of the braces to the actuator degrees of freedom.

$$
\begin{aligned}
U_{a1} &= \sqrt{(U_1-L_{a1})^2+(U_2+L_{a3}-L_{a2})^2}-L_{a1} \\
U_{a2} &= \sqrt{U_1^{\,2}+(U_2+L_{a2})^2}-L_{a2} \\
U_{a3} &= \sqrt{U_1^{\,2}+(U_2+L_{a3})^2}-L_{a3}
\end{aligned}
\tag{4.3}
$$

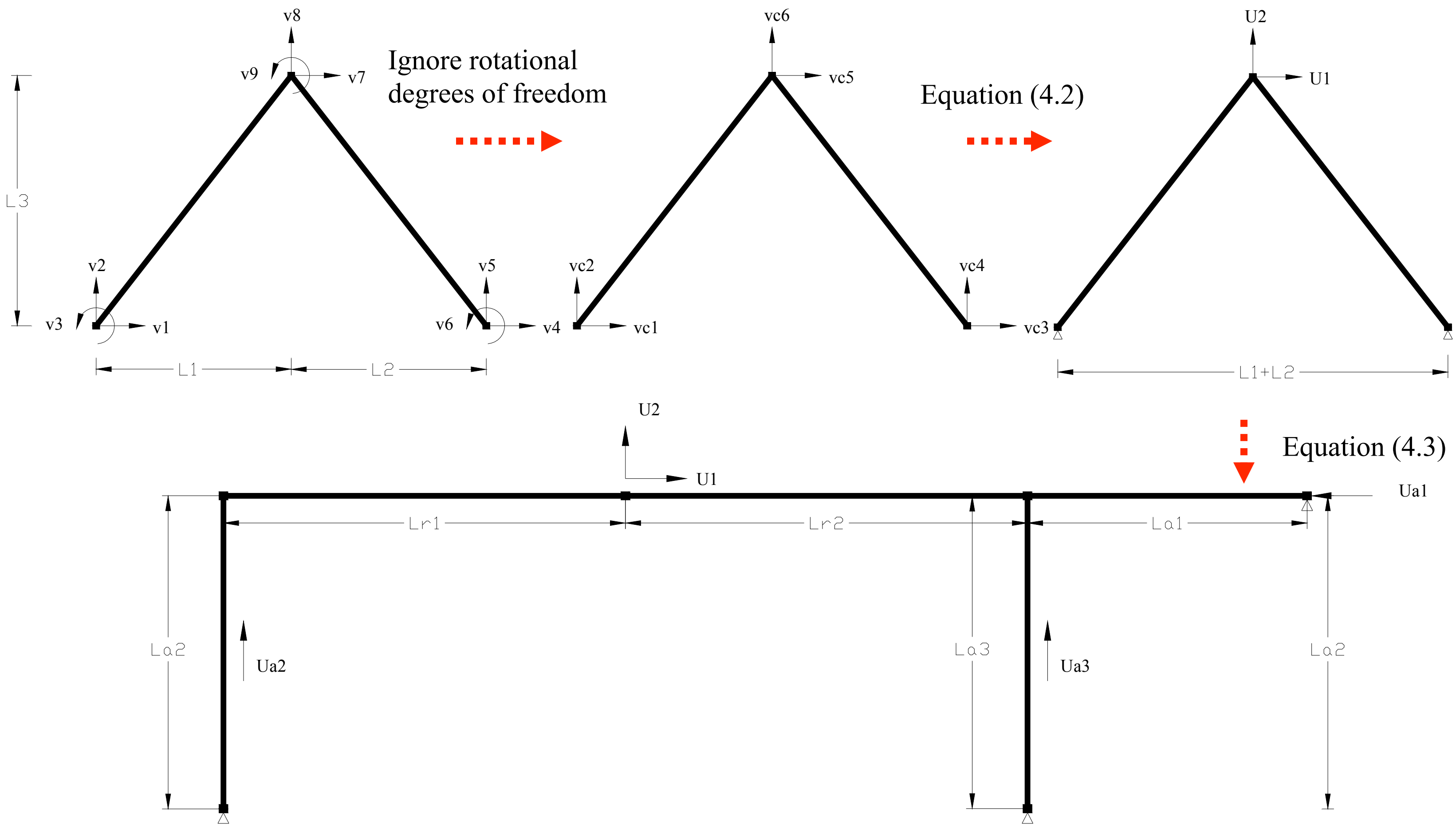

Fig. 4.7 Transformation of displacements from element degrees of freedom to actuator degrees of freedom.

4.4.2 *nees@berkeley* Laboratory

Figure 4.8 shows the setup of the *nees@berkeley* control room. Figure 4.9 shows the data acquisition system (Data Acquisition Target) used to record the experimental data. With the displacement signal generated from the xPC target, the Hybrid Control Target controls the hydraulic pressure in the hydraulic manifold (as shown in Figure 4.10) and the oil flow to control the actuators.

Fig. 4.8 *nees@*berkeley control room.

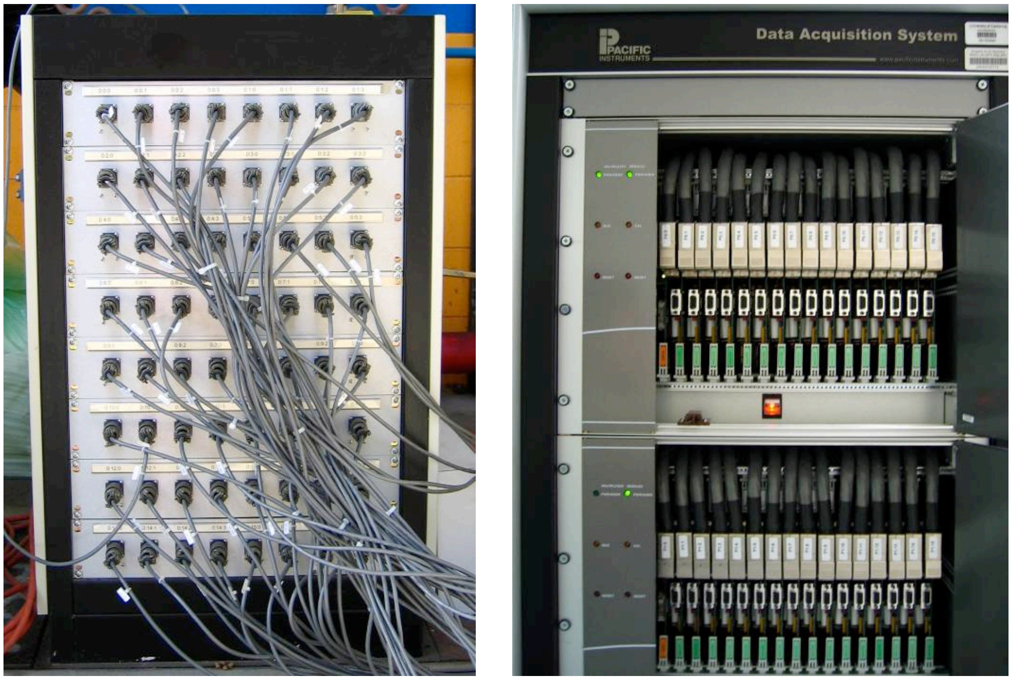

Fig. 4.9 Data acquisition system.

Fig. 4.10 Hydraulic manifold.

4.5 HYBRID SIMULATION ALGORITHM

The classical Newmark average-acceleration time-step integration method (Newmark 1959) with Newton-Raphson initial stiffness iteration was used to solve the differential equation for the hybrid simulation. The discrete differential equation governing the system dynamics at time t_n is shown in Equation (4.4).

$$\mathbf{M}\ddot{\mathbf{u}}_{\mathrm{n}} + \mathbf{C}\dot{\mathbf{u}}_{\mathrm{n}} + \mathbf{Pr}\left(\mathbf{u}_{\mathrm{n}}, \dot{\mathbf{u}}_{\mathrm{n}}\right) = -\mathbf{M}\boldsymbol{\iota}\ddot{\mathbf{u}}_{\mathrm{g,n}} \tag{4.4}$$

where $\mathbf{M}$ is the mass matrix of the structure; $\mathbf{C}$ is the damping matrix of the structure; and $\mathbf{u}_{\mathrm{n}}, \dot{\mathbf{u}}_{\mathrm{n}}, \ddot{\mathbf{u}}_{\mathrm{n}}$ are the displacement, velocity, and acceleration vectors at the element degrees of freedom at time t_n. $\mathbf{Pr}\left(\mathbf{u}_n, \dot{\mathbf{u}}_n\right)$ is the resisting force vector at the element degrees of freedom at time t_n. Note that the resisting force can be nonlinear functions of $\mathbf{u}_n$ and $\dot{\mathbf{u}}_n$. Vector $\boldsymbol{\iota}$ is the influence vector that relates the degree of freedom at the ground excitation to the element degrees of freedom. $\ddot{\mathbf{u}}_{g,n}$ is the ground acceleration vector at time t_n. The Newmark time-step integration method assumes that

$$\dot{\mathbf{u}}_{n+1} = \dot{\mathbf{u}}_n + \mathrm{h}\left((1-\gamma)\ddot{\mathbf{u}}_n + \gamma\ddot{\mathbf{u}}_{n+1}\right) \tag{4.5}$$

$$\mathbf{u}_{n+1} = \mathbf{u}_n + h\,\dot{\mathbf{u}}_n + h^2\left(\left(\frac{1}{2}-\beta\right)\ddot{\mathbf{u}}_n + \beta\ddot{\mathbf{u}}_{n+1}\right) \tag{4.6}$$

where $h = t_{n+1} - t_n$ and γ and β are constant coefficients. When $\gamma = \frac{1}{2}, \beta = \frac{1}{4}$ the method is commonly known as the average-acceleration method. Similarly, when $\gamma = \frac{1}{2}, \beta = \frac{1}{6}$ the method is commonly known as the linear-acceleration method. Substituting Equation (4.5) and Equation (4.6) into Equation (4.4), the differential equation governing the system dynamics at time t_{n+1} is

$$\begin{aligned}\mathbf{F}(\mathbf{u}) = \mathbf{M}&\left(\frac{1}{\beta h^2}(\mathbf{u}-\mathbf{u}_n)-\frac{1}{\beta h}\dot{\mathbf{u}}_n-\left(\frac{1}{2\beta}-1\right)\ddot{\mathbf{u}}_n\right)\\ &+\mathbf{C}\left(\frac{\gamma}{\beta h}(\mathbf{u}-\mathbf{u}_n)-\left(\frac{\gamma}{\beta}-1\right)\dot{\mathbf{u}}_n-h\left(\frac{\gamma}{2\beta}-1\right)\ddot{\mathbf{u}}_n\right)\\ &+\mathbf{Pr}\left(\mathbf{u},\mathbf{u}_n,\dot{\mathbf{u}}_n,\ddot{\mathbf{u}}_n\right)-\mathbf{P}_{n+1}=\mathbf{0}\end{aligned} \tag{4.7}$$

where $\mathbf{u}$ is the displacement vector at the element degrees of freedom at time t_{n+1} and $\mathbf{P}_{n+1} = -\mathbf{M}\boldsymbol{\iota}\,\ddot{\mathbf{u}}_{g,n+1}$ is the applied force at the element degrees of freedom at the time t_{n+1}. Note that $\mathbf{Pr}(\mathbf{u}_{n+1},\dot{\mathbf{u}}_{n+1})$ can be expressed in terms of $\mathbf{Pr}(\mathbf{u},\mathbf{u}_n,\dot{\mathbf{u}}_n,\ddot{\mathbf{u}}_n)$ using Equation (4.5) and Equation (4.6).

The nonlinear equation shown in Equation (4.7) can be solved using the Newton-Raphson initial stiffness iteration. It should be noted that the initial stiffness is used instead of the tangent stiffness associated with the conventional Newton iteration because the term $\mathbf{Pr}'(\mathbf{u},\mathbf{u}_n,\dot{\mathbf{u}}_n,\ddot{\mathbf{u}}_n)$ in $\mathbf{F}'(\mathbf{u})$ cannot be readily evaluated for the experimental subassemblies of the hybrid model. Equation (4.8) shows the Newmark time-step integration method with Newton-Raphson initial stiffness iteration used in the hybrid simulation test.

$$\begin{aligned}\mathbf{u}^{k+1} = \mathbf{u}^k - \frac{\mathbf{F}(\mathbf{u}^k)}{\mathbf{F}'(\mathbf{u}^k)} &\Rightarrow \mathbf{F}'(\mathbf{u}^k)\Delta\mathbf{u}^k = -\mathbf{F}(\mathbf{u}^k)\\ \mathbf{F}'(\mathbf{u}^k) &= \frac{1}{\beta h^2}\mathbf{M}+\frac{\gamma}{\beta h}\mathbf{C}+\mathbf{K}_i\\ \mathbf{F}(\mathbf{u}^k) = \mathbf{M}&\left(\frac{1}{\beta h^2}(\mathbf{u}^k-\mathbf{u}_n)-\frac{1}{\beta h}\dot{\mathbf{u}}_n-\left(\frac{1}{2\beta}-1\right)\ddot{\mathbf{u}}_n\right)\\ &+\mathbf{C}\left(\frac{\gamma}{\beta h}(\mathbf{u}^k-\mathbf{u}_n)-\left(\frac{\gamma}{\beta}-1\right)\dot{\mathbf{u}}_n-h\left(\frac{\gamma}{2\beta}-1\right)\ddot{\mathbf{u}}_n\right)\\ &+\mathrm{Pr}\left(\mathbf{u}^k,\mathbf{u}_n,\dot{\mathbf{u}}_n,\ddot{\mathbf{u}}_n\right)-\mathbf{P}_{n+1}\end{aligned} \tag{4.8}$$

where $\mathbf{u}^k$ is the displacement vector at time t_{n+1} at the k$^{\text{th}}$ iteration, $\Delta\mathbf{u}^k = \mathbf{u}^{k+1}-\mathbf{u}^k$, and $\mathbf{K}_i$ is the initial stiffness matrix of the structure. This initial stiffness of the experimental subassembly is obtained from the results of the quasi-static test described in Chapter 2.

4.5.1 Predictor and Corrector Algorithm

To implement the hybrid simulation architecture shown in Section 4.3, the xPC Target was set up to receive a displacement command vector from the xPC Host at a random time interval and to send a displacement command vector to the Hybrid Control Target (through SCRAMnet) at a fixed time interval governed by the actuator controller update frequency of 1024 Hz. (The time interval to go from one time-step integration to the next is random because it depends on the structural model nonlinearity, communication delays, and processor speed.) At the same time, the xPC Target was set up to record the force feedback from the Experiment Setup and to send the data to the xPC Host whenever a displacement signal was received.

To do the tasks outlined above, the xPC Target node needed a real-time operating system to enable constant-rate displacement command output, a SCRAMnet card to communicate to the network, and a predictor and corrector algorithm to reconcile the random-interval input and the constant-interval output requirements. The predictor and corrector program was written using the Simulink toolbox in MATLAB at the xPC Host and compiled to the xPC Target using the Ethernet connection. Once the program was compiled to xPC Target, the predictor and corrector program were designed to receive the displacement commend signals from the xPC Host at a random time interval and predict the appropriate displacement signal at 1024 Hz and send it through SCRAMnet to the Hybrid Control Target.

There are many ways to devise the predictor and corrector algorithm. One approach (Mosqueda 2003; Nakashima and Masaoka 1999) is to use polynomial interpolation to predict the displacement, while another (Schellenberg 2008) is to use the velocity and acceleration to construct explicit displacement predictors and correctors. Once the xPC Target receives the displacement signal at the next time-step, the corrector program starts to correct the command displacement to the calculated displacement. If it takes too long for the displacement signals to arrive from the xPC Host (due to communication or convergence problems in the analytical portion of the hybrid model) the predictor and corrector program will automatically slow down and, if necessary, hold the displacement (while sending the same displacement signal at the 1024 Hz rate to the Hybrid Control Target) until the next displacement signal arrives.

The hybrid model used to conduct hybrid simulation of the suspended zipper braced frame is quite complex. It accounts for nonlinear buckling behavior in both the analytical and the experimental subassemblies using a second-order displacement formulation and nonlinear material behavior. Furthermore, the solution algorithm deployed in OpenSees to move the analytical subassemblies of the hybrid model from one displacement state to the next uses substep iterations. This means that many of the displacement signals sent from xPC Host to xPC Target are the solutions of substep iteration. This makes it very difficult to predict the target displacement using higher-order polynomials. It is even more challenging to implement the predictor method suggested by Schellenberg (2008), which uses velocity and acceleration to predict the displacement between the signals generated from the xPC Host. Moreover, as was observed in the laboratory, both higher-order displacement-based polynomial predictors and the velocity and acceleration predictors suggested in Schellenberg (2008) may predict the target displacement in the wrong direction, causing jerking motion of the actuators and eventually leading to instability of the actuation system.

To implement the testing architecture, the predictor and corrector program were modified to predict the displacement signal using a zero-order polynomial and to correct the displacement signal with a first-order polynomial. Thus, the predictor program sends the same displacement signal to the Hybrid Control Target (at 1024 Hz) until the target displacement arrives, and ramps the displacement to the new target displacement once the target displacement has arrived. In so doing, the predictor will not predict displacement using subspace iteration data, hence, avoiding instability. The hybrid simulation results indicate that with appropriately short simulation time-steps, this predictor and corrector method can provide a smooth transition between displacement signals and minimize any slow down or hold phases during the test.

4.6 RESPONSE OF INVERTED-V BRACED SUBASSEMBLY

A hybrid simulation test of the suspended zipper braced frame was conducted using the hybrid model, the test setup and the algorithms described above. The amplitude of ground motion was further reduced by half, with peak ground acceleration of 0.92g, to match the shaking table input motion. The damaged physical subassembly of the hybrid model after the hybrid simulation test is shown in Figure 4.11.

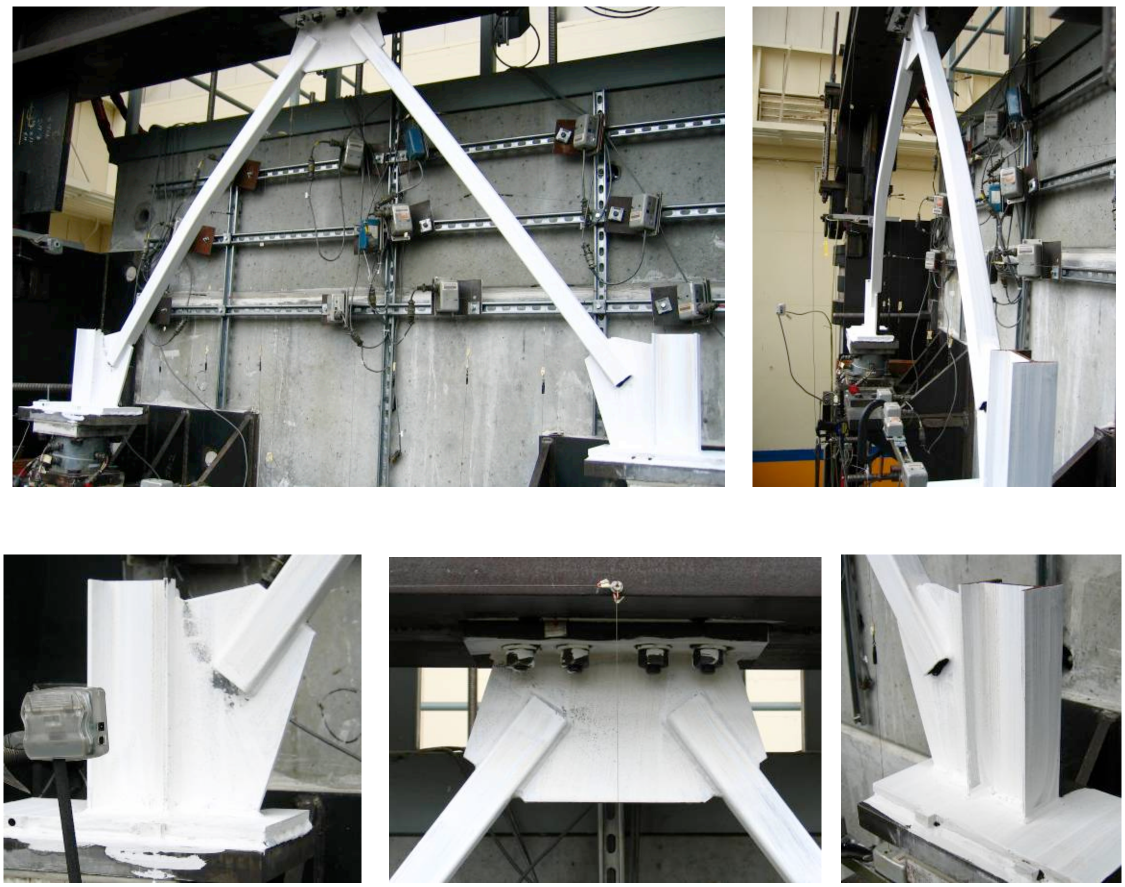

Fig. 4.11 Damaged inverted-V braced subassembly after hybrid simulation test.

4.6.1 Interstory and Permanent-Residual Story Drift Ratios

The displacement histories at the brace intersection, normalized with respect to the story height (52.75 in.), are plotted in Figure 4.12. The displacements Dsp X, Dsp Y, and Dsp Z are the displacements measured at the intersection of the brace in the horizontal, vertical, and out-of-plane directions, respectively. Based on the results shown in Figure 4.12, the maximum horizontal displacement reached 1.4 percent of the story height, while the maximum vertical displacement and out-of-plane displacement reached 0.33 and 0.2 percent of the story height, respectively. The braces experienced some inelastic response, resulting in permanent interstory drift of 0.25 percent in the horizontal direction and minor residual deformation in the vertical direction.

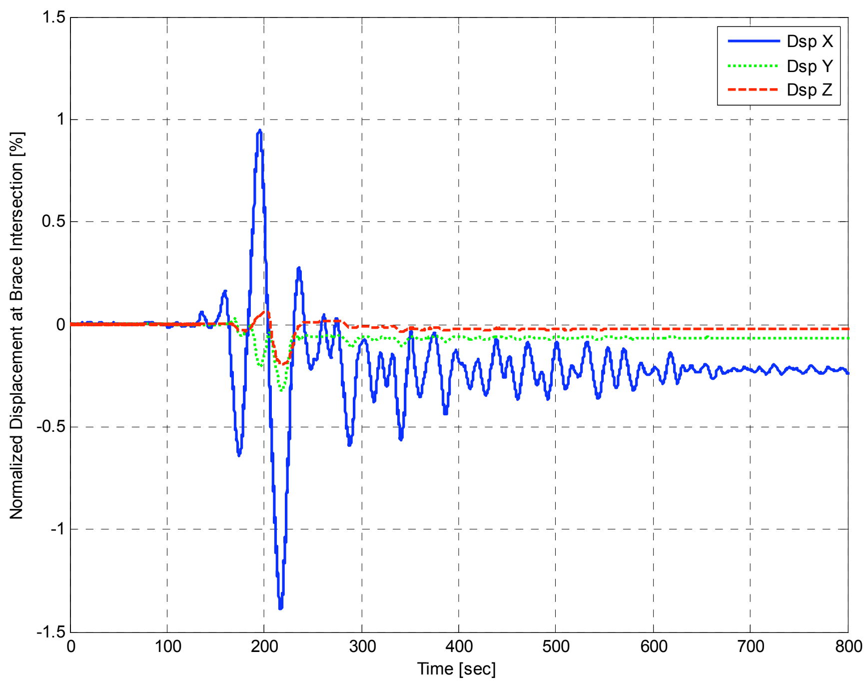

Fig. 4.12 Normalized displacement histories at brace intersection.

4.6.2 Unbalanced Vertical and Out-of-Plane Forces

The unbalanced vertical and out-of-plane forces measured at the intersection of the braces was normalized with respect to the expected yield force ($A_g \times F_{ye}$ = 50.23 kips) and is plotted in Figure 4.13. The supporting beam experienced a large unbalanced vertical force, the maximum value reaching as much as 70 percent of the brace expected yield force. While, the maximum unbalanced out-of-plane force reached 2.3 percent of the brace expected yield force. The unbalanced vertical and out-of-plane forces eventually contributed to the vertical displacement at the intersection of the braces and the rotation of the beam. The peak unbalanced vertical and out-of-plane forces are very similar to those recorded during the quasi-static test presented in Chapter 2 (Fig. 2.16).

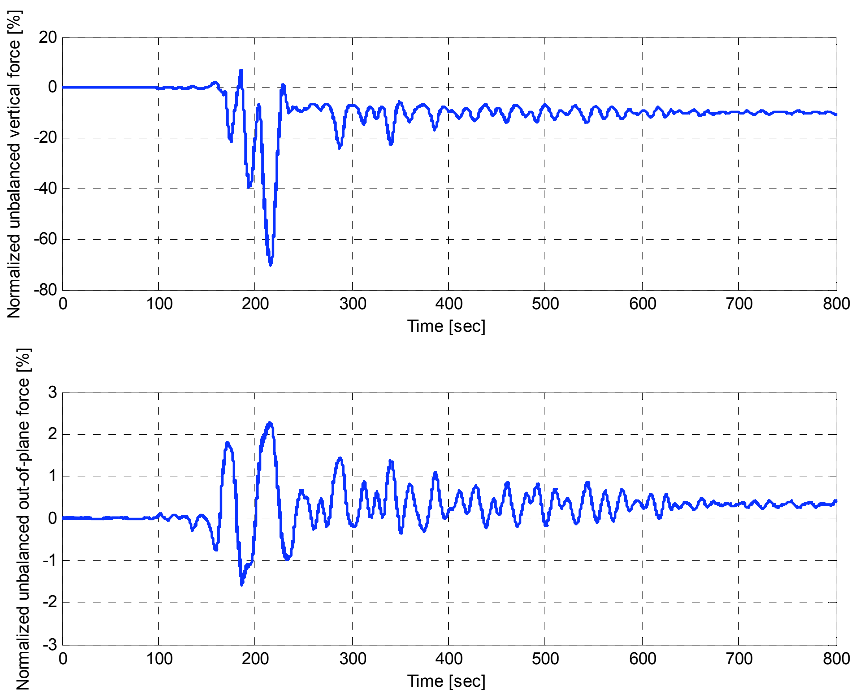

Fig. 4.13 Unbalanced forces measured at intersection of braces.

4.6.3 Out-of-Plane Rotation

Because the cross-beam guiding system was not snugly fitted, the cross beam rotated out of plane when the unbalanced out-of-plane force became sufficiently large. Figure 4.14 shows the amount of out-of-plane rotation of the beam. As the magnitude of the out-of-plane force reduced toward the end of the test, the rotation of the beam reduced and the cross beam returned to the upright position.

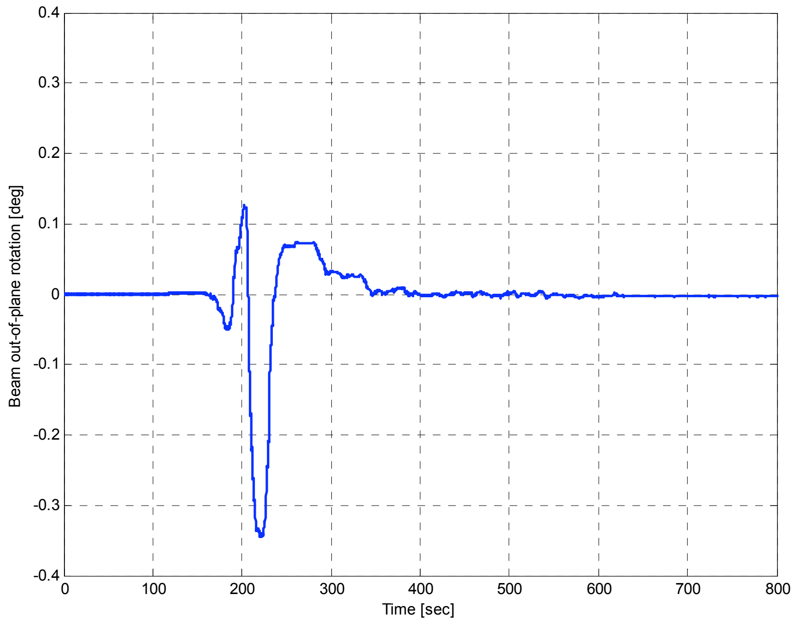

Fig. 4.14 Out-of-plane beam rotation.

4.6.4 Normalized Brace Deformation

Brace deformation in the global coordinate system at the selected points shown in Figure 2.11 was normalized with respect to the brace length (L_b = 66.2 in.) and is plotted in Figure 4.15. These results indicate that the braces buckle out of plane and out of phase. The maximum out-of-plane displacement reaches as much as 5 percent of the brace length. In addition, visible out-of-plane residual displacement was observed in the inverted-V braced subassembly.

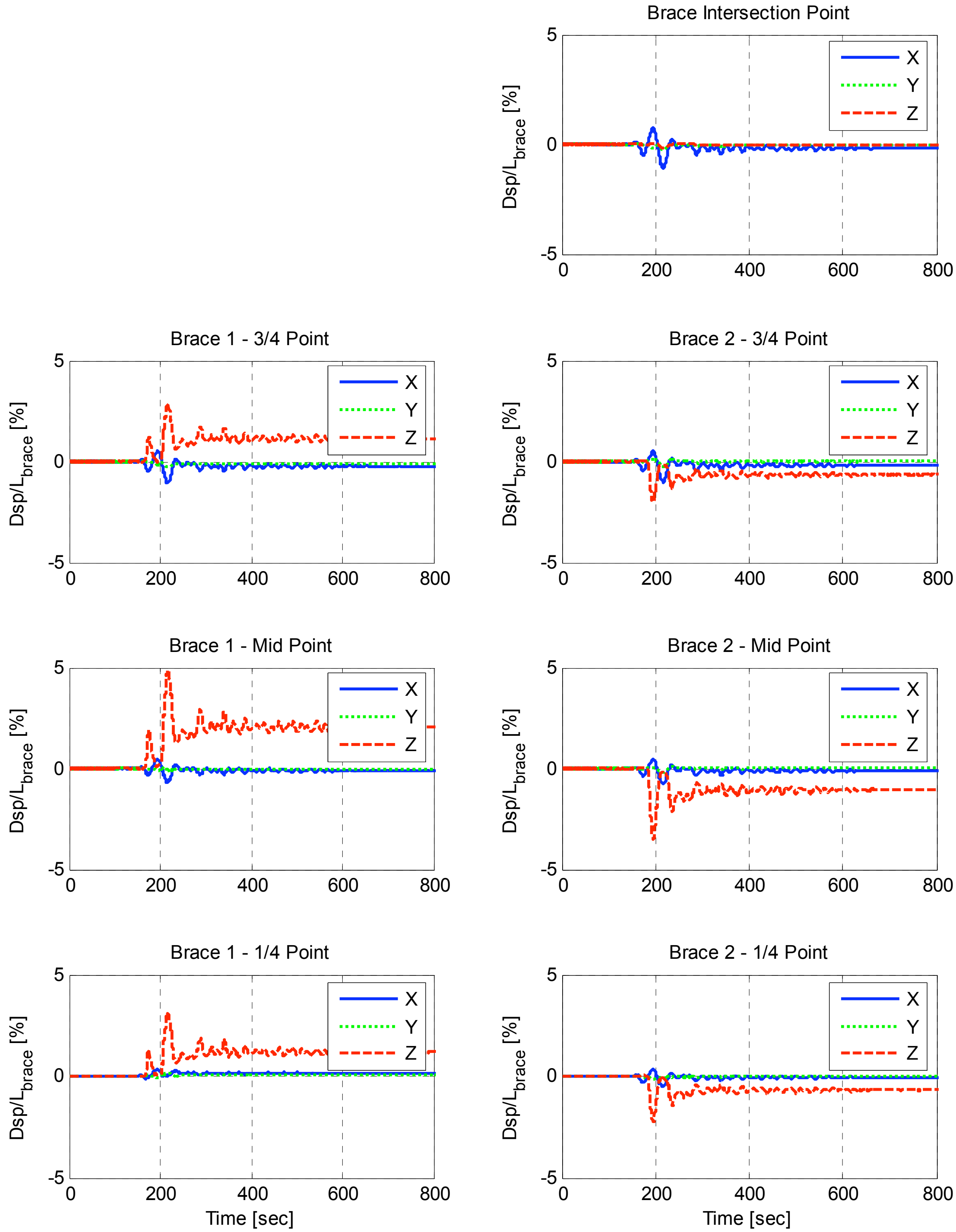

Fig. 4.15 Deformation of braces recorded during hybrid simulation test.

4.6.5 Summary

The inverted-V braced subassembly behaved similarly in the hybrid simulation test and the quasi-static test. The braces buckled out of plane and out of phase and formed plastic hinges at the gusset plates and mid span of the braces. In both cases, the maximum out-of-plane displacement reached 5 percent of the brace length. As part of the suspended zipper braced frame mechanism, the brace buckling behavior created large unbalanced vertical and out-of-plane forces at the intersection of the braces. The maximum unbalanced vertical force reached 70 percent of the brace expected yield force ($A_g \times F_{ye}$ = 50.23 kips) in the hybrid simulation test, compared with 80 percent during the quasi-static test. Last, both inverted-V braced subassemblies suffered some inelastic response that resulted in significant residual out-of-plane displacement.

4.7 SYSTEM BEHAVIOR OF SUSPENDED ZIPPER BRACED FRAME

The previous section discusses the behavior of the inverted-V braced subassembly observed during the hybrid simulation test. This section focuses on the system response of the suspended zipper braced frame recorded during the hybrid simulation test.

4.7.1 Interstory and Roof Drift Ratio

The response of the roof displacement was normalized with respect to the total building height (H = 154.25 in.) and is plotted in Figure 4.16. The maximum roof drift ratio reached 0.75 percent. Under this inelastic roof drift demand, the structure yields and develops a small residual roof drift of 0.1 percent of building height.

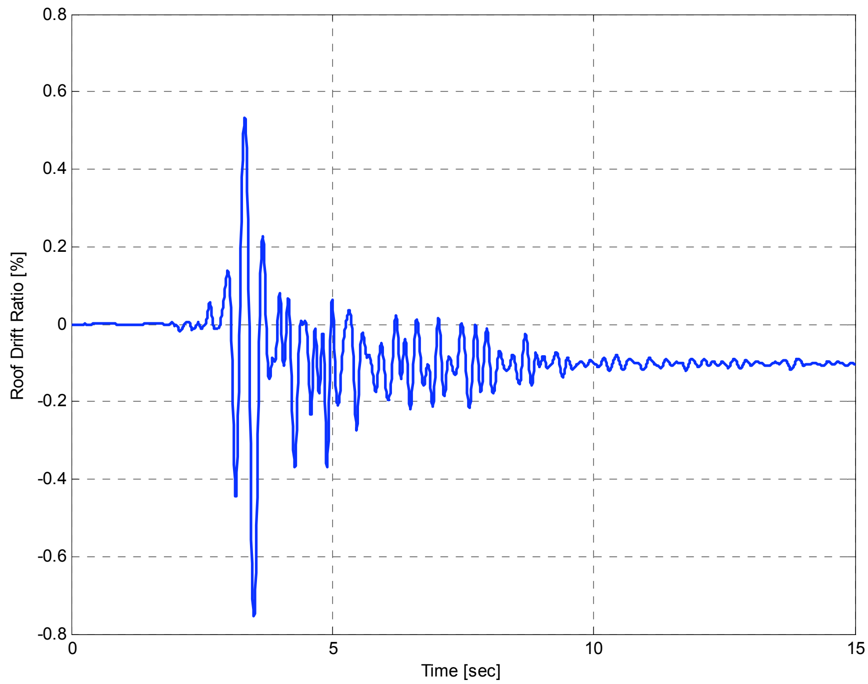

Fig. 4.16 Roof drift ratio history.

Figure 4.17 shows the interstory drift ratios recorded during the hybrid simulation test at the first, second, and third stories of the suspended zipper braced frame. As shown, the individual stories drifted substantially in phase, indicating the frame drift response was dominated by its apparent first vibration mode. The maximum interstory drift ratios reached 1.5 percent, 0.55 percent and 0.25 percent for the first, second, and third stories, respectively. This shows that the structure has concentrated interstory drift at the first story. Under these inelastic displacement demands, the structure yielded and developed a residual interstory drift of 0.25 percent in the first story and a minor residual drift in the second story.

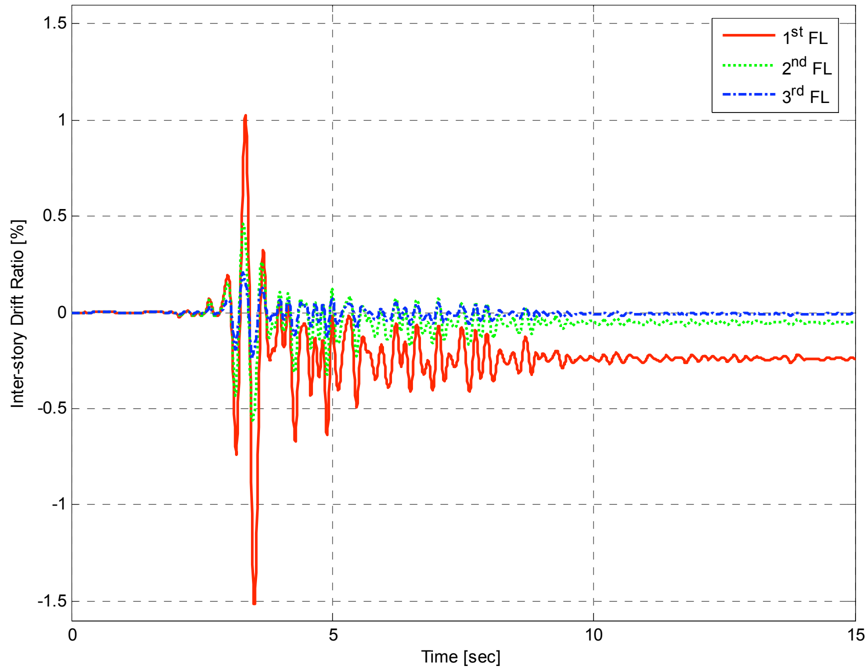

Fig. 4.17 Interstory drift ratio histories.

4.7.2 Element Response

The responses of the braces, zipper columns, and frame columns are shown in Figures 4.18–4.20. Similar to the nonlinear dynamic analysis results shown in Figure 3.9, the first-story braces experienced some inelastic response and developed a force-deformation response that approximates a trilinear force-deformation response envelope, as shown in Figure 4.18. As predicted by nonlinear dynamic analysis, the third-story braces and the zipper columns remained elastic and were capable of transferring all of the unbalanced vertical forces to the columns. The columns remained elastic throughout the test except for some inelastic deformations observed at the base of the first-story columns.

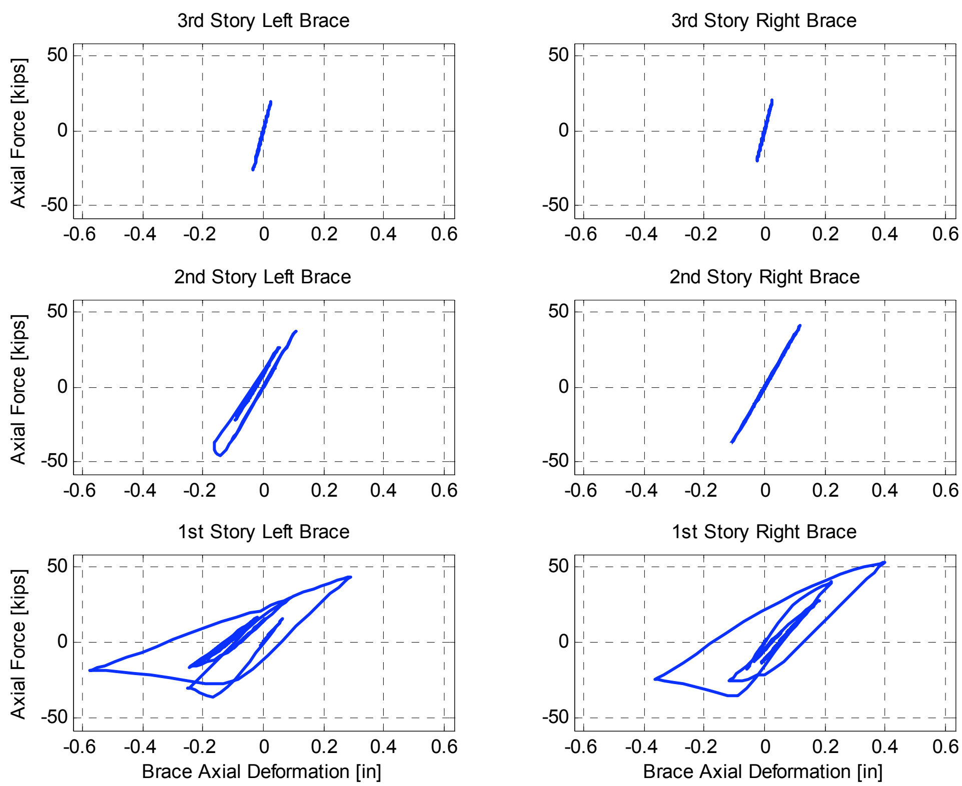

Fig. 4.18 Response of braces recorded during hybrid simulation test.

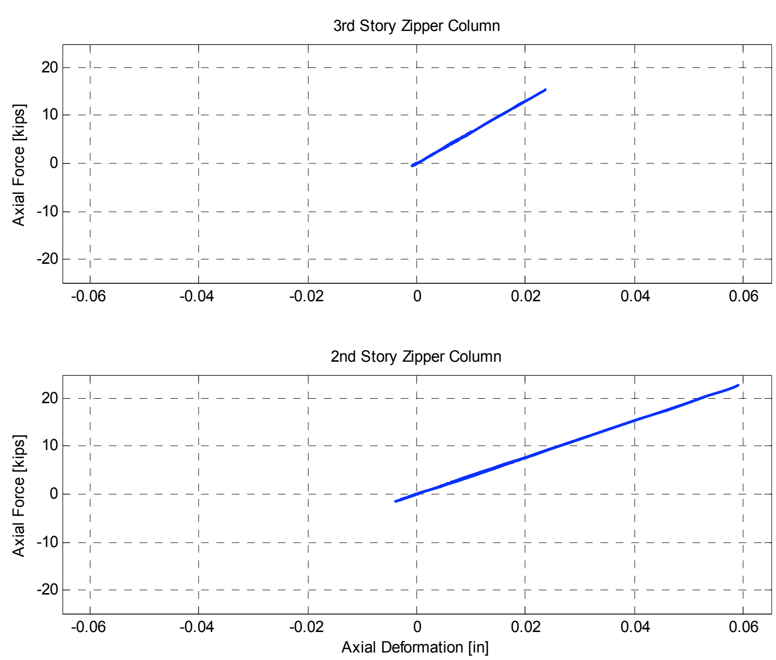

Fig. 4.19 Response of zipper columns recorded during hybrid simulation test.

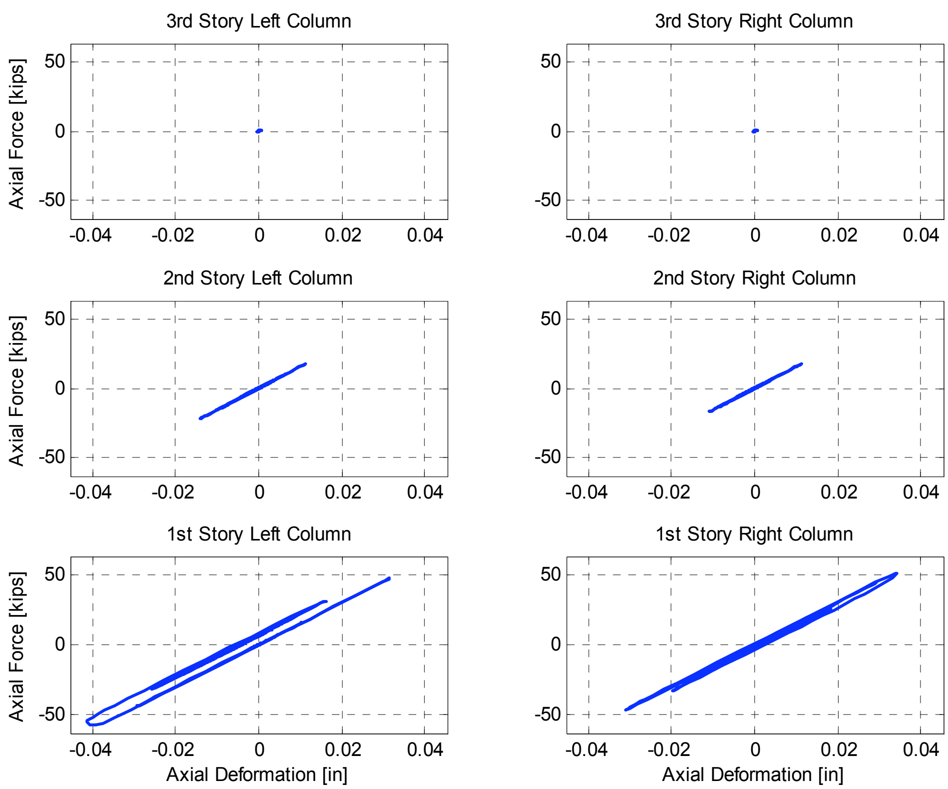

Fig. 4.20 Response of columns recorded during hybrid simulation test.

4.7.3 System Force-Deformation Response and Energy Dissipation

Figure 4.21 shows the relation between total base shear and roof drift ratio for the suspended zipper braced frame recorded during the hybrid simulation test. The plot indicates that the suspended zipper braced frame absorbed and dissipated the input earthquake energy in a stable manner. Figure 4.22 shows the percentage of the hysteretic energy dissipated in each story. The third story is designed to remain elastic to prevent formation of the full zipper mechanism. Thus, all the hysteretic energy is dissipated in the first and second stories. Thus, the zipper column was effective in distributing energy dissipation from the first to the second story. Hence, it is evident that the intended distribution of inelasticity is, indeed, occurring in the suspended zipper braced frame.

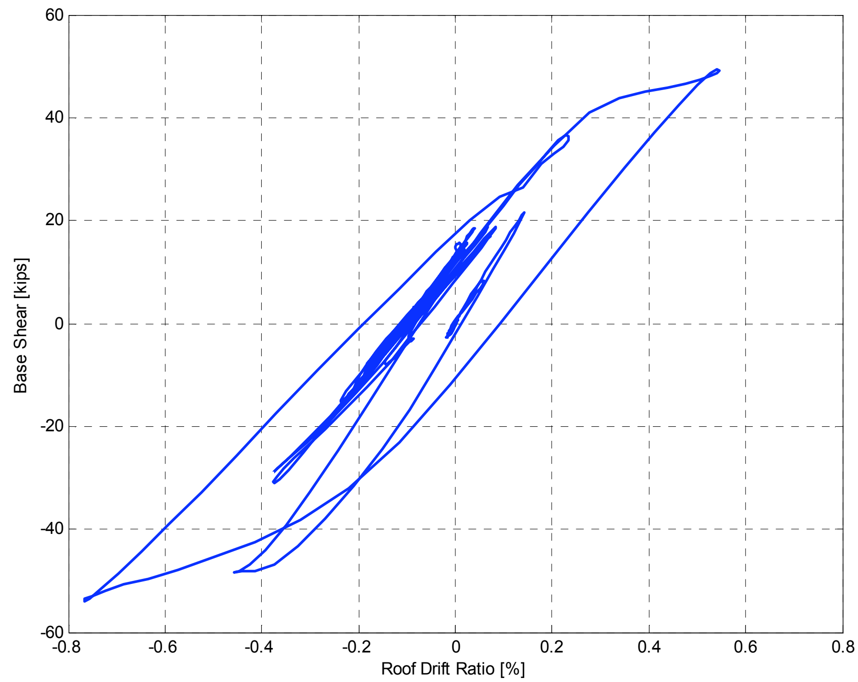

Fig. 4.21 Relation between base shear and roof drift ratio.

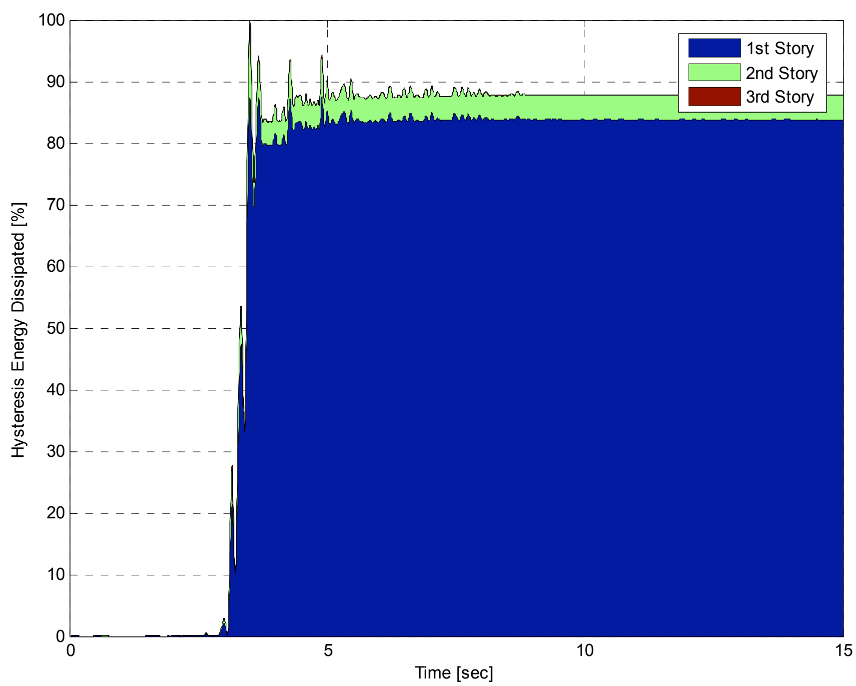

Fig. 4.22 Hysteretic energy-dissipation history at each story.

4.8 VERIFICATION OF HYBRID SIMULATION RESULTS USING ANALYTICAL SIMULATION

To verify the hybrid simulation test, the analytical model shown in Figure 3.1 was modified to match the mass, loading history, boundary condition, and damping ratio of the hybrid model used in the hybrid simulation test. Selected results are compared in Figures 4.23–4.29.

4.8.1 Roof and Interstory Drift Ratios

Comparisons of the roof drift and interstory drift ratios in the hybrid simulation and the analytical simulation are shown in Figures 4.23–4.26. These results indicate that the analytical simulation matches the hybrid simulation test very well.

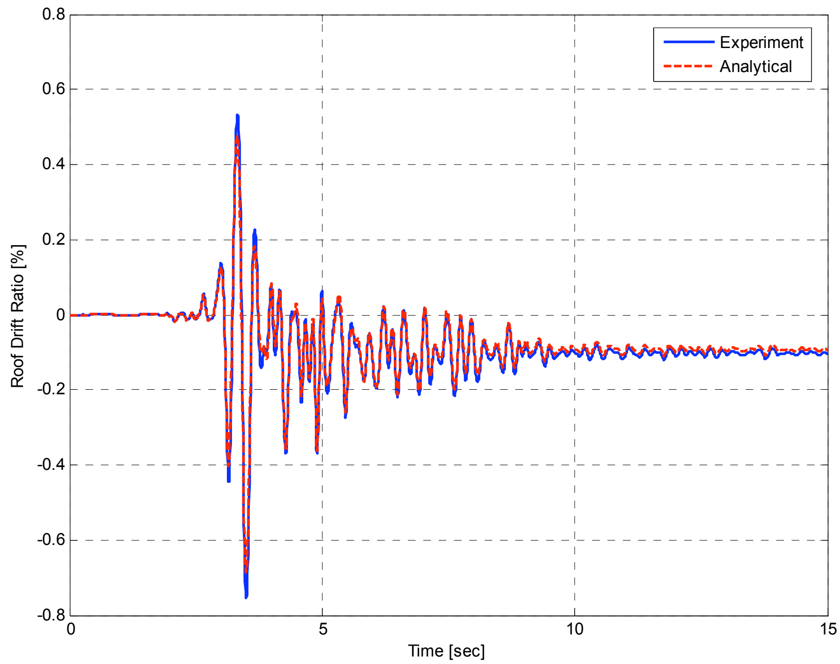

Fig. 4.23 Roof drift ratios in hybrid and analytical simulations.

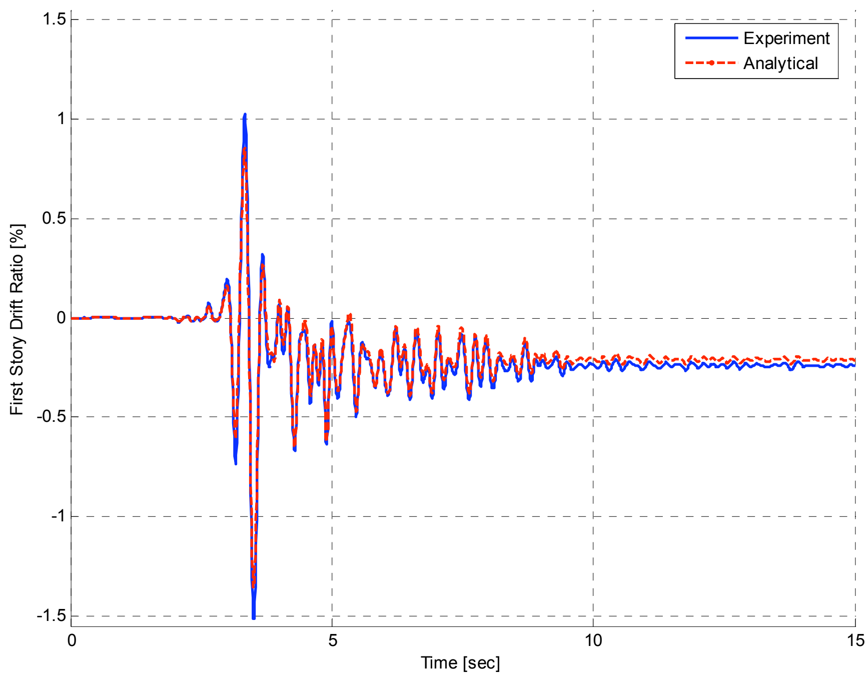

Fig. 4.24 First-story drift ratios in hybrid and analytical simulations.

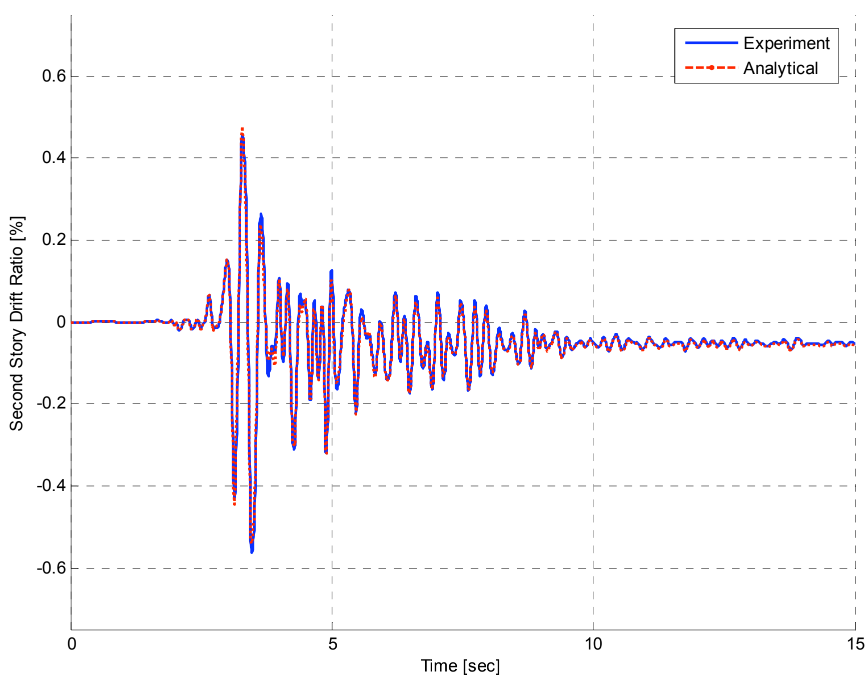

Fig. 4.25 Second-story drift ratios in hybrid and analytical simulations.

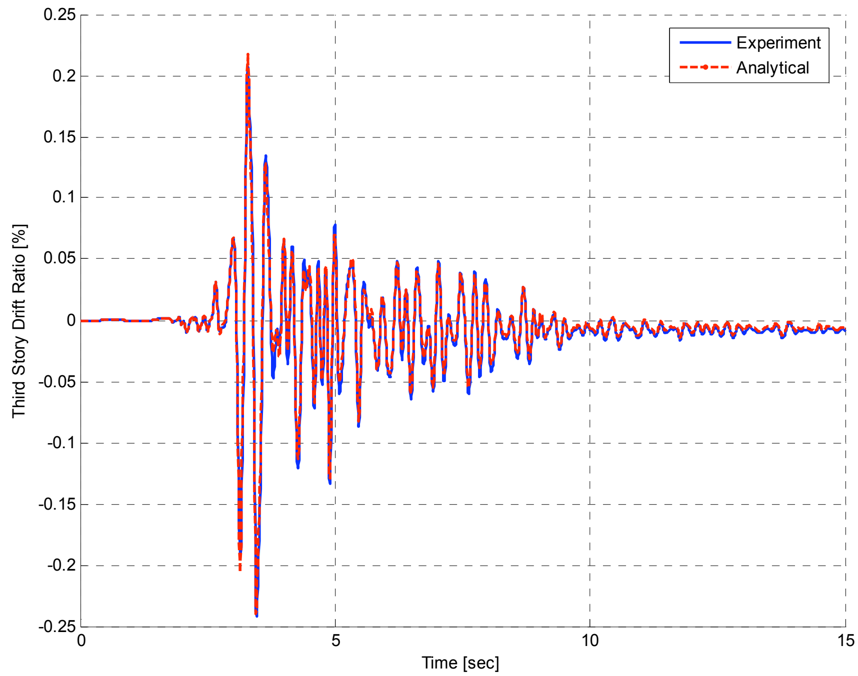

Fig. 4.26 Third-story drift ratio in hybrid and analytical simulations.

4.8.2 Element Response

Figure 4.27 compares the axial force-deformation hysteretic response of the braces recorded during the hybrid simulation test and the analytical simulation. The results indicate that the second- and third-story braces experienced almost identical response in the hybrid simulation test and the analytical simulation. The axial force-deformation hysteretic response of the first-story braces show that the physical subassembly had slightly lower compression and tension capacities than its analytical counterpart. This difference in the axial forces in the first-story braces results in the slight difference in the axial forces in the zipper columns and the frame columns, as shown in Figures 4.28–4.29. The second- and third-story columns remain elastic, while the first-story column undergoes some inelastic displacement cycles. Therefore, similar behavior is observed in hybrid and analytical simulation.

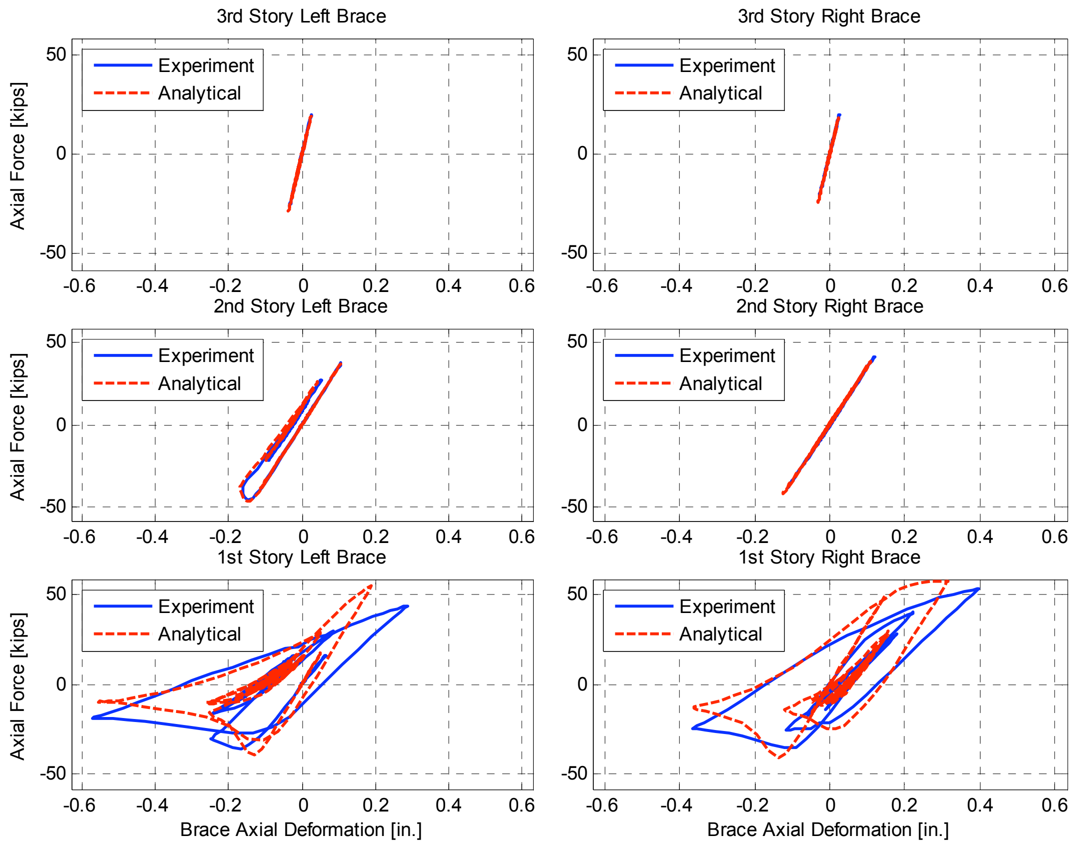

Fig. 4.27 Brace hysteretic response comparison.

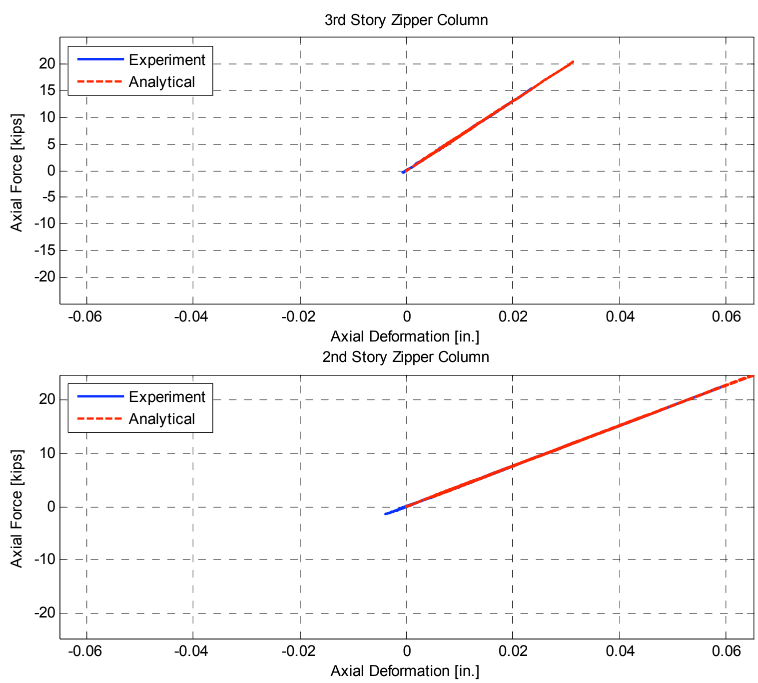

Fig. 4.28 Zipper column hysteretic response comparison.

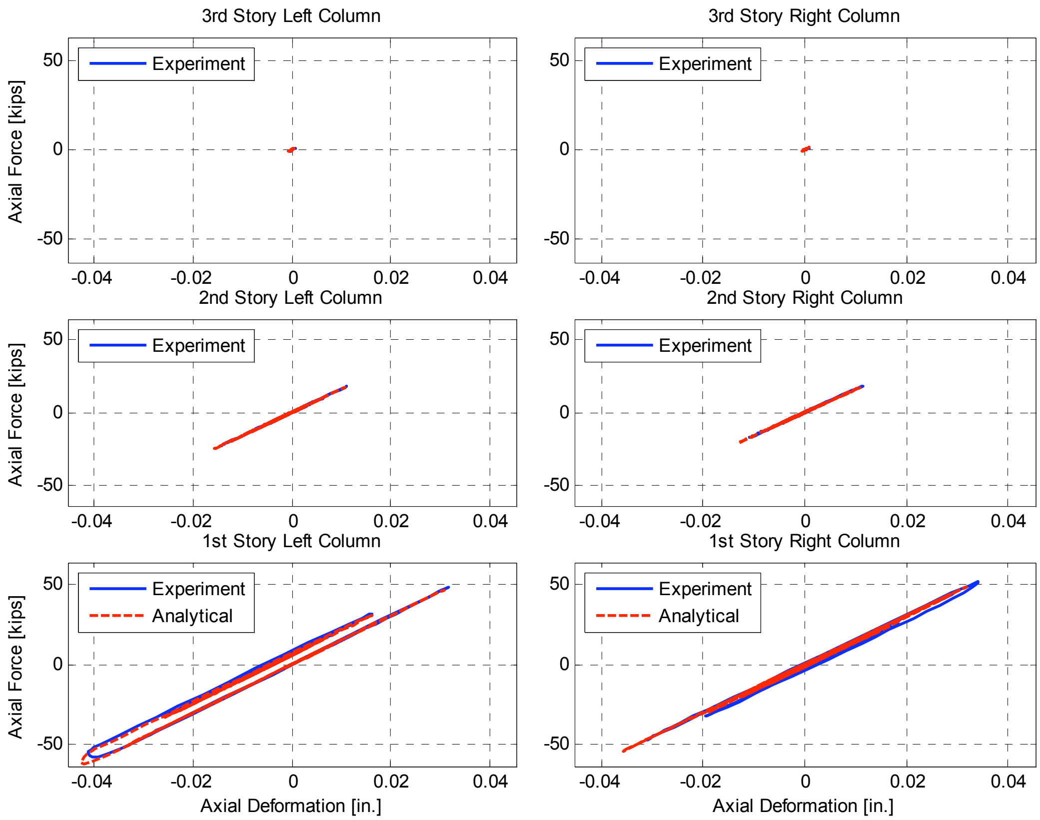

Fig. 4.29 Frame column hysteretic response comparison.

4.9 CONCLUSION

To conduct the hybrid simulation test using OpenSees, new experimental classes (Schellenberg 2008), hybrid simulation architecture, and a continuous testing algorithm have been implemented. An excellent agreement was obtained between the analytical simulation and hybrid simulation: thus (1) the finite element model of the inverted-V braced subassembly calibrated in Chapter 2 worked well; (2) the nonlinear buckling behavior of the brace can be modeled effectively and accurately using the OpenSees framework; and (3) the hybrid simulation test method can be used to investigate the system response of complex structural systems such as the suspended zipper braced frame.

5 Performance-Based Methodology for Evaluating Structural Framing Systems

Earthquake engineering has evolved from using a set of prescriptive provisions, indirectly aimed at providing life safety, to performance-based approaches with direct consideration of a range of performance objectives. Performance-based approaches have several advantages, including a more comprehensive consideration of the various performance metrics that might be of interest to stakeholders, more direct methods for computing performance, and increasing the involvement of stakeholders in decisions on design acceptability. Whereas engineers are familiar with performance measures such as drift, acceleration, strain, and perhaps damage state, many decision makers prefer performance metrics that relate more directly to business decisions, such as downtime or repair costs. An engineering challenge has been to consistently consider seismic hazard, structural response, and resulting damage and consequences, such that a fully probabilistic statement of expected performance can be made.

A rigorous, yet practical approach to performance-based earthquake engineering (PBEE) is pursued here. The approach considers the seismic hazard, structural response, resulting damage, and repair costs associated with restoring the building to its original condition using a fully consistent, probabilistic analysis of the associated parts of the problem. The approach could be generalized to consider other performance measures such as casualties and downtime, though these have not been pursued at this time. The procedure is organized to be consistent with conventional building design, construction, and analysis practices so that it can be readily incorporated as a design approach.

5.1 PERFORMANCE-BASED EARTHQUAKE ENGINEERING FRAMEWORK

To account for uncertainties in earthquake engineering problems, some prior understanding of basic probability is needed. Appendix A summarizes the basic probability theory that is used in deriving the performance-based earthquake engineering (PBEE) framework. Additional references can be found in probability and statistics textbooks, such as (Soong 1981). Equation

(5.1) shows the notation of the conditional complementary cumulative distribution function (CCDF) of a random variable X given the value of another random variable $Y = y$. Equation (5.2) shows the total probability theorem for the occurrence of event A given the conditional probability of the occurrence of n mutually exclusive and collective exhaustive discrete random variables E_i.

$$G(x \mid y) = P(X > x \mid Y = y) \tag{5.1}$$

$$P(A) = \sum_{i=1}^{n} P(A \mid E_i) P(E_i) \tag{5.2}$$

Equation (5.2) is modified to Equation (5.3) to account for E being a continuous random variable. Similar to Equation (5.2), Equation (5.3) shows the total probability of event $A > a$ given that event E has occurred.

$$P(A > a) = \int_E P(A > a \mid E = de)\, dP(de) = \int_E G(a \mid e)\, dG(e) \tag{5.3}$$

where de represents a small range of the continuous random variable E and the integration bound is set over the entire range of E.

5.1.1 Derivation of Performance-Based Earthquake Engineering Framework

Moehle and Deierlein (2004) describe the application of Equation (5.3) as adopted in research of the Pacific Earthquake Engineering Research Center (PEER). As implemented, Equation (5.3) is decomposed into four analysis steps:

1. **Seismic hazard analysis:**
   Probabilistic seismic hazard analysis is used to describe the seismic hazard for the structure. The outcome of the probabilistic seismic hazard analysis is a seismic hazard curve, $\lambda(IM)$, that quantifies the annual rate of exceeding a given value of seismic intensity measure (IM). (For example, the rate at which peak ground acceleration will exceed 0.2 g for a particular location in a given year.) In addition, seismic hazard analysis is used to characterize the ground motions that can be used in the response analysis.

2. **Response analysis:**

   The response of structural and nonstructural components of the structure to seismic excitation is obtained using a model of the structure. This model may be analytical, physical, or hybrid. The ground motions used in this analysis are chosen to represent the seismic hazard range of interest for the site, and may induce inelastic response of the structure: thus, nonlinear dynamic analysis is commonly used in this PBEE step. The outcomes of response analysis are statistical functions that relate engineering demand parameters (such as drift or stress) to the hazard experienced by the structure.

3. **Damage analysis:**

   Based on test data, post-earthquake reconnaissance reports, or analysis of behavior, structural and nonstructural component damage can be characterized in terms of fragility curves. The fragility curves are cumulative distribution functions (CDFs) representing the probability that a damage state has been reached or exceeded given a quantitative measure of the engineering demand parameter (EDP).

4. **Loss analysis:**

   A translation of damage analysis results, from damage quantities to decision variables, that can be used by building owners and stakeholders to make a risk management decision is done during loss analysis. The outputs of the loss analysis can be, for example, the probability of exceeding a certain threshold repair cost for a set period of time, the expected monetary loss for repair of the structure using continuous hazard scenarios, and the total monetary loss for the structure with a particular probability of exceedance, among others.

Random variables are used to quantify performance and to preserve the statistical uncertainties inherent to the problem. The seismic hazard analysis uses a probabilistic analysis of the seismic environment, ground shaking attenuation relations, and site conditions to derive a model for the seismic shaking intensity at a site. The output of the seismic hazard analysis is a statistical function that represents the annual rate of exceedance of certain intensity measures (IM), that is, $\nu(IM > im)$. Response analysis uses the engineering demand parameter (EDP) as the random variable and produces the conditional probability function, $G(edp\,|\,im)$, to represent the statistical relationship between EDP and IM.

Damage analysis uses damage measure (DM) as the random variable and the results of the analysis is a conditional probability function, $G(dm|edp)$, that relates DM and EDP. Last, the loss analysis uses decision variable (DV) as the random variable and produces a conditional probability function, $G(dv|dm)$, that relates DV and DM.

Figure 5.1 illustrates the underlying performance-based earthquake engineering framework.

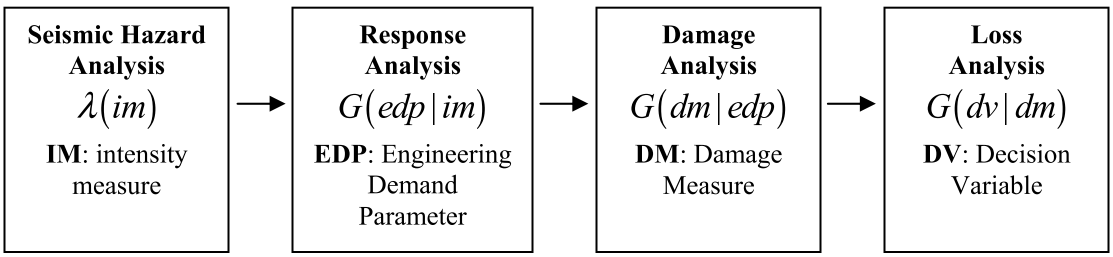

Fig. 5.1 Performance-based earthquake engineering framework.

Note: The decomposition of the PBEE process outlined above is made possible using the statistical independence assumptions listed below:

1. $G(dm|edp,im) = G(dm|edp) \Leftarrow$ (Conditional probability of DM given EDP and IM is equivalent of conditional probability of DM given EDP).
2. $G(dv|dm,edp) = G(dv|dm) \Leftarrow$(Conditional probability of DV given DM and EDP is equivalent to conditional probability of DV given DM).
3. $G(dv|dm,im) = G(dv|dm) \Leftarrow$(Conditional probability of DV given DM and IM is equivalent to conditional probability of DV given DM).

Using the total probability theorem, the probability of exceedance for each intermediate random variable is presented in Equations (5.4)–(5.6).

1. **Response analysis**

$$
\begin{aligned}
P\left(EDP > edp\right) &= \int_{im} G\left(edp \mid im\right) dG\left(im\right) \\
\Rightarrow dP\left(EDP > edp\right) &= \int_{im} dG\left(edp \mid im\right) dG\left(im\right)
\end{aligned}
\tag{5.4}
$$

2. **Damage analysis**

$$
\begin{aligned}
P\left(DM > dm\right) &= \int_{edp} G\left(dm \mid edp\right) dG\left(edp\right) \\
\Rightarrow dP\left(DM > dm\right) &= \int_{edp} dG\left(dm \mid edp\right) dG\left(edp\right)
\end{aligned}
\tag{5.5}
$$

3. **Loss analysis**

$$
P\left(DV > dv\right) = \int_{dm} G\left(dv \mid dm\right) dG\left(dm\right) \tag{5.6}
$$

By conditioning Equation (5.6) on im

$$
\begin{aligned}
P\left(DV > dv \mid im\right) &= \int_{dm} G\left(dv \mid dm, im\right) dG\left(dm \mid im\right) \\
&= \int_{dm} G\left(dv \mid dm\right) dG\left(dm \mid im\right) \\
\Rightarrow G\left(dv \mid im\right) &= \int_{dm} G\left(dv \mid dm\right) dG\left(dm \mid im\right)
\end{aligned}
\tag{5.7}
$$

By conditioning Equation (5.5) on im

$$
\begin{aligned}
dP\left(DM > dm \mid im\right) &= \int_{edp} dG\left(dm \mid edp, im\right) dG\left(edp \mid im\right) \\
\Rightarrow dG\left(dm \mid im\right) &= \int_{edp} dG\left(dm \mid edp\right) dG\left(edp \mid im\right)
\end{aligned}
\tag{5.8}
$$

Substituting Equation (5.8) to Equation (5.7).

$$
G\left(dv \mid im\right) = \int_{dm} \int_{edp} G\left(dv \mid dm\right) dG\left(dm \mid edp\right) dG\left(edp \mid im\right) \tag{5.9}
$$

Equation (5.9) represents the conditional probability of a decision variable having a value *dv* given a value of intensity measure $IM = im$. Similar derivation can be made for $G(dm|im)$ and is shown in Equation (5.10).

$$G(dm \mid im) = \int_{edp} G(dm \mid edp)\, dG(edp \mid im) \tag{5.10}$$

5.1.2 Annual Rate of Exceeding Threshold Value

$G(dv|im)$, $G(dm|im)$, and $G(edp|im)$ are the conditional probabilities of the performance measures DV, DM, and EDP given an intensity measure $IM = im$. To translate the conditional probability to a quantity that can be readily used by building owners/stakeholders to make a risk management decision, these conditional probabilities are multiplied by the absolute value of the derivative of the annual rate of exceedance of a given value of the ground motion intensity measure, $\left|\frac{d\lambda(im)}{d\,im}\right|$. Because the seismic hazard curve, $\lambda(im)$, is defined as the annual rate that the earthquake ground motion intensity measure IM exceeds a value im, a derivative is used to compute the annual frequency (rate of occurrence) of the intensity measure $IM = im$. An absolute value is used to insure that this rate is a positive number regardless of the shape of the hazard curve itself.

The product of the annual rate of occurrence and the conditional probability of the performance measure given an intensity measure gives the annual rate of the performance measure exceeding a threshold value. In other words, $\left|\frac{d\lambda(im)}{d\,im}\right|$ represents the annual frequency of a random variable IM equaling im and $G(dv|im)$ represents the probability that the random variable DV takes values larger than dv for shaking intensity equaling im. Thus, their product gives the number of occurrences of $DV > dv$ annually, as shown in Equation (5.11).

$$\frac{\lambda(DV > dv)}{d\,im} = G(dv \mid im)\left|\frac{d\lambda(im)}{d\,im}\right| \tag{5.11}$$

Integrating Equation (5.11) for all intensity measures, Equation (5.12) gives the annual rate that DV exceeds a threshold value dv for all intensity measures considered.

$$\lambda\left(DV > dv\right) = \int_{im} G\left(dv \mid im\right) \frac{\left|d\lambda\left(im\right)\right|}{\cancel{\left|d\,im\right|}} \cancel{d\,im} = \int_{im} G\left(dv \mid im\right)\left|d\lambda\left(im\right)\right| \tag{5.12}$$

The final form of the performance-based earthquake engineering framing equation, Equation (5.13) is obtained by substituting Equation (5.9) into Equation (5.12).

$$\lambda\left(DV > dv\right) = \int_{im}\int_{dm}\int_{edp} G\left(dv \mid dm\right) dG\left(dm \mid edp\right) dG\left(edp \mid im\right)\left|d\lambda\left(im\right)\right| \tag{5.13}$$

Note that Equation (5.13) uses the same conditional probability for successive earthquake events. This implies that the structure is nondeteriorating or is restored to its original condition immediately after any damage to the structure occurs in an earthquake event (Der Kiureghian 2005a).

5.2 AN IMPLEMENTATION OF PERFORMANCE-BASED EARTHQUAKE ENGINEERING FRAMEWORK

The PBEE framework described previously can be used as the basis for developing rigorous PBEE procedures. The challenge is to implement the methodology in a manner that is practicable for practitioners to use in a typical design office setting. Two issues must be addressed to achieve this goal: (1) the performance measures (DV, DM, and EDP) and their conditioned cumulative distribution functions, $G(x \mid y)$, must be easily quantified and formulated in a straightforward way using data readily available to practicing engineers and (2) the intense computations required to integrate the PEER PBEE framework (Eq. 5.13) must be encapsulated into procedures and routines that are transparent and easy to implement. An implementation that fulfills these two goals is presented in the following steps:

1. **Define structural and nonstructural components to be considered in performance assessment**

The outcome of this step is a series of repair quantity tables for the structure. These tables correlate the structural and/or nonstructural component damage states and repair actions needed to restore them. They are formulated using a procedure described below.

Depending on the structural system and intended function of the structure, relevant structural and nonstructural components of the building are selected and separated into different performance groups (PG). Each performance group consists of one or more building components whose performance is similarly affected by a particular engineering demand parameter (EDP). For example, one performance group might consist of all similar nonstructural components whose performance is sensitive to floor acceleration or to interstory drift between the second and third floors. The selection of components in each performance group is based on an engineering judgment of the importance of the contribution of these components to the overall performance of the structure.

A sufficient number of damage states (DS) are defined for each performance group to completely describe the range of damage to the components in the performance group. The damage states are defined in relation to the repair actions needed to correct them. For each damage state, a damage model (fragility relation) is used to define the probability that the component will be equal or less than the damage state given an EDP value. Figure 5.2 shows an example of fragility curves defined for a performance group.

The example fragility curves shown in Figure 5.2 indicate that the performance group has four damage states. For example, these might be no damage (DS1), slight damage (DS2), severe but repairable damage (DS3), and total replacement (DS4). Depending on the demand expressed using the EDP value, the probabilities of the performance group being in each damage state can be identified from the fragility curves. For example, if the EDP equals 1.5 g, the probability of the components in the PG being in DS1 is close to zero, DS2 is approximately 0.5, DS3 is approximately 0.42, and DS4 is approximately 0.08.

After the performance groups are identified, building data, such as as-built documents or in-use surveys, are used to quantify the components of each performance group in the building. For example, square footage of partition walls and number of pocket doors may be computed.

Because each damage state is defined according to the repair action, the total repair quantities for each item in the PG at different damage states can be defined according to the functionality of the structure. Table 5.1 shows an example of the repair quantities for each item in the sample performance group shown in Figure 5.2 at different damage states. Additional damage states and repair items can be added for different performance groups.

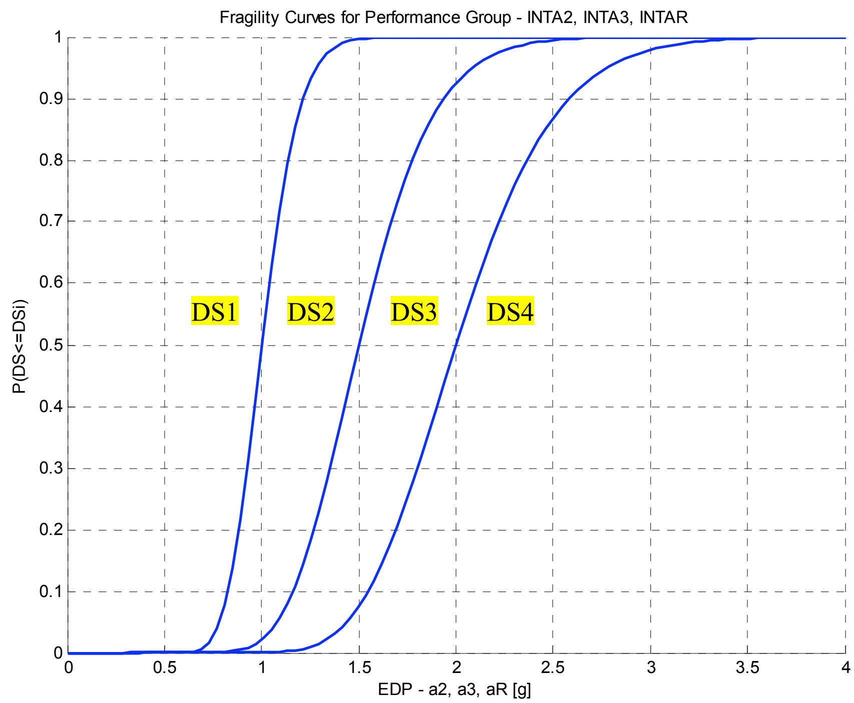

Fig. 5.2 Example of four fragility curves for one component of a performance group.

Table 5.1 Sample repair quantity table for performance group shown in Figure 5.2.

Repair quantity type	Units	DS1	DS2	DS3	DS4
General clean-up					
Water damage	sf	0	0	10,000	20,000
STRUCTURAL					
Demolition/Access					
Finish protection	sf	0	4,000	10,000	20,000
NONSTRUCTURAL INTERIOR					
Interior Demolition					
Remove furniture	sf	0	4,000	10,000	20,000
Ceiling system removal	sf	0	0	0	20,000
MEP removal	sf	0	0	500	2,000
Interior Construction					
Replace ceiling tiles	sf	0	2,500	8,000	8,000
Replace ceiling system	sf	0	0	0	20,000
MEP replacement	sf	0	0	500	2,000

2. **Conduct seismic hazard analysis and ground motion selection**

A conventional seismic hazard analysis is conducted, taking into account the site and the layout of the building. One outcome of the seismic hazard analysis is a hazard curve that quantifies ground motion intensity measures considered in the PBEE analysis of the building. The hazard curve and engineering judgment are used to identify the discrete hazard levels for which the building will be further examined. Another outcome of the seismic hazard analysis is suites of ground motions representing the seismicity of the site at different seismic hazard levels. For example, a suite of ground motions representing the seismic hazard with a 10% probability of exceedance in 50 years at the site may be provided. A typical suite comprises several ground motions with their intensity scaled to the level implied by the seismic hazard function. The motions may be further subclasses by type, such as near-field or far-field ground motions.

3. **Evaluate response of building**

   With the selected ground motions, a series of dynamic analyses, including nonlinear response if necessary, can be used to determine the earthquake response of the building. Depending on the EDP associated with each performance group (defined in step 1), the peak $EDPs$ obtained from the dynamic analyses are summarized in an EDP matrix, $\mathbf{X}$, as shown in Table 5.2. The columns of the $\mathbf{X}$ represent the different $EDPs$ of interest (for example interstory drift or floor acceleration) and the rows of the $\mathbf{X}$ represent the peak $EDPs$ collected from the dynamic analysis of a single ground motion. One EDP matrix will be defined for each intensity measure considered.

Table 5.2 Sample *EDP* matrix, $\mathbf{X}$.

Filename	*EDP* 1	*EDP* 2	$\cdots$	*EDP* N
GM 1	0.66	1.07	$\cdots$	0.75
GM 2	0.68	0.95	$\cdots$	0.27
$\vdots$	$\vdots$	$\vdots$	$\vdots$	$\vdots$
GM M	0.76	1.10	$\cdots$	0.52

4. **Generate additional correlated *EDP* vectors**

   Computing additional EDP vector realizations using additional dynamic analysis is hampered by the paucity of recorded strong ground motions and the computational cost. Therefore, to preclude running additional nonlinear dynamic analyses, a joint lognormal distribution is fitted to the EDP matrix. Correlated EDP vectors can then be generated using a computationally inexpensive procedure presented in Section 5.3.

5. **Compute total repair cost**

   With the generated correlated EDP vectors, the total repair quantities for all repair items in the building after each scenario earthquake can be calculated. For a given EDP vector, the cost simulation loops through each performance group defined in Step 1. Depending on the values of the EDP associated with the performance group, a random number generator with a uniform distribution is used to select the damage state for the damaged model defined in Step 1. Once the damage states are identified, the repair quantities for each item in the performance group are located from the repair quantity table, such as the one shown in Table 5.1. This process is repeated for all performance groups and the total repair quantities for each item are summed from the quantities obtained from each performance group.

Once the total repair quantities are identified, the total repair cost for the building is computed by multiplying the total repair quantity by the unit repair cost. Figure 5.3 shows an example of the unit repair cost function. The price uncertainty is represented by using a random number generator, based on the tabulated "beta" factors for the cost functions, to adjust base unit costs up or down before multiplying by the total quantities associated with each repair measure. This is the repair cost for one realization of $EDPs$. The process is repeated a sufficiently large number of times to obtain a distribution of total repair costs given the hazard level. In the methodology adopted here, the performance groups are assumed to be statistically independent.

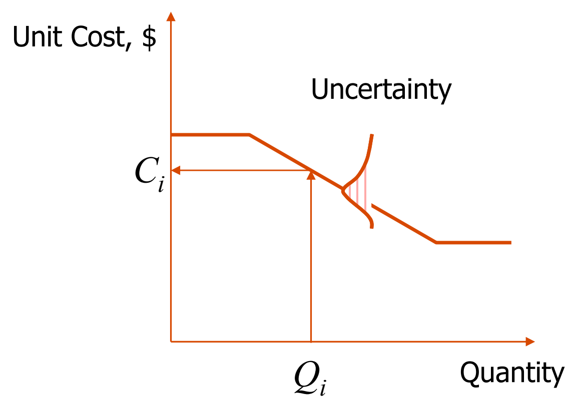

Fig. 5.3 Example of cost function.

6. **Different representations of total repair cost**

Steps 1 through 5 present a logical and consistent methodology that can be used to obtain a distribution of the total repair cost of the building for one intensity measure. Figure 5.4 shows an example of such distribution curves for different intensity measures considered. Curves such as these can be readily used as a basis for making risk management decisions. For example, the curve demonstrates the amount of seismic risk increase (in terms of the total repair cost) as a function of the return period of earthquake ground shaking. Similar curves can be generated to compare the performance of different structural framing systems or different retrofitting strategies on the same building.

The repair cost information can be further refined by computing the annual rate of total repair cost exceeding a threshold value. Such annual rate information is obtained by first computing the complement of the cumulative distribution function shown in Figure 5.4, then multiplying it by the slope of the hazard curve at the corresponding ground motion intensity measure level, and finally integrating the resulting curves across the intensity measure interval considered in the seismic hazard analysis. Repeating this process for all repair cost values produces a loss curve that represents the annual rate of the total repair cost (TC) exceeding a threshold value. Figure 5.5 shows a sample loss curve obtained from the sample building performance assessment shown in Figure 5.4. Note that the procedure presented here is identical to the process presented in Equation (5.12) where the conditional probability, $G(TC \mid im)$ (complement of the CDF generated using the procedure presented in Steps 1 through Step 5), is multiplied by the derivative of the seismic hazard curve and integrated through all intensity measures.

Last, following the derivation presented in Der Kiureghian (2005a) valid for a nonnegative random variable X, the expected cumulative value of X is

$$E\left[\sum X\right] = \int_0^\infty x\left|d\lambda(x)\right| = \int_0^\infty \lambda(x)\,dx \tag{5.14}$$

where the last expression is obtained from integration by parts. Thus, the area under the loss curve represents the mean cumulative annual total repair cost for all earthquake events in one year. Information such as this can be used by building owners/stakeholders to make rational decisions regarding building insurance.

The procedures in Steps 3 through 5 have been implemented in a computer program and thus automated. Input to the program requires the user to define the performance groups, the repair quantity table, the repair cost functions, the EDP matrices obtained by running a limited number of response history analyses, and the total number of repair cost simulations required to compute the loss function. Given these input quantities, the program generates loss functions in a variety of different formats, including those described above.

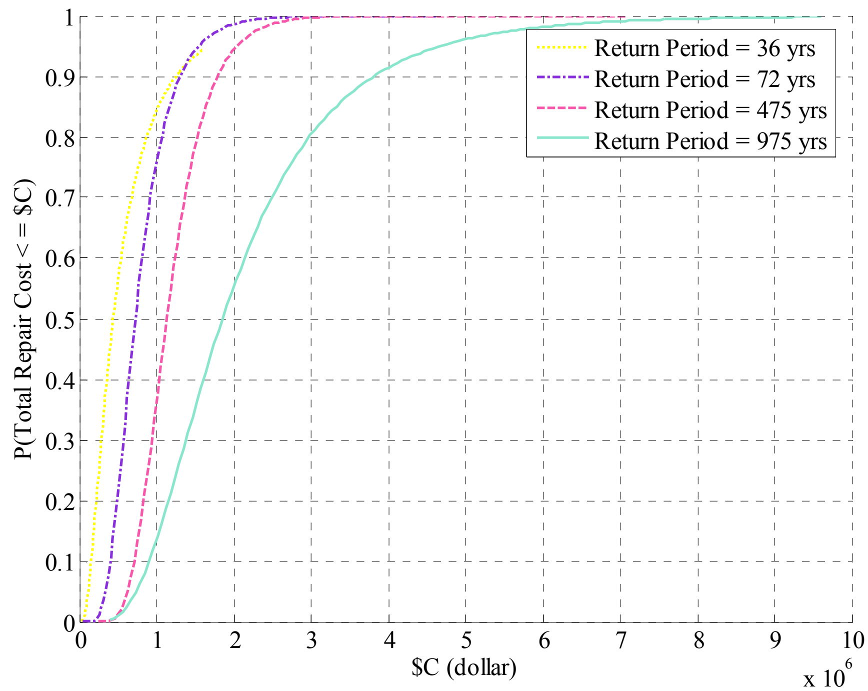

Fig. 5.4 Sample cumulative probability distribution function for cost not exceeding a threshold value generated according to methodology presented above.

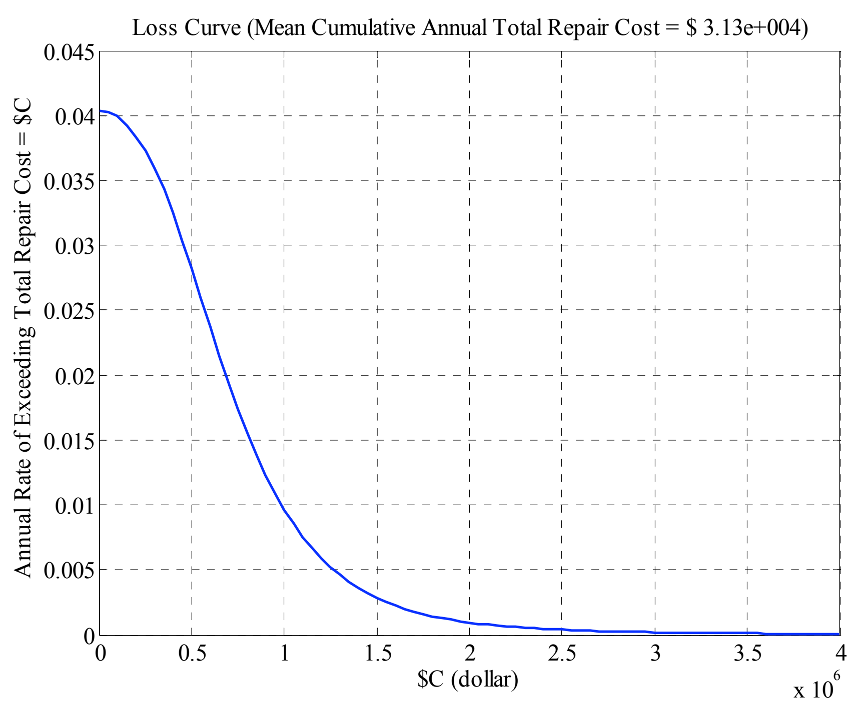

Fig. 5.5 Sample loss curve.

5.3 GENERATING CORRELATED *EDP* VECTORS

5.3.1 Functions of Random Variables

Following the derivation shown in Appendix A, the mean vector and covariance matrix of dependent random variables, $\mathbf{Z}$, can be calculated from the mean vector and covariance matrix of the independent random variables, $\mathbf{U}$, if the transformation from $\mathbf{U}$ to $\mathbf{Z}$ is linear or affine (note an affine function is just a linear function plus a translation). Equation (5.15) shows an example of an affine function from $\mathbf{U}$ to $\mathbf{Z}$.

$$\mathbf{Z} = \mathbf{AU} + \mathbf{B} \tag{5.15}$$

where $\mathbf{Z} = [Z_1\, Z_2 \cdots Z_n]^t$ is a vector of n random variables and the superscript t represents matrix transpose. Each entry of $\mathbf{Z}$ represents a random variable (e.g., first-story drifts, second-story drifts, … etc). $\mathbf{A}$ is an n x m constant coefficient matrix representing the linear transformation from $\mathbf{U}$ to $\mathbf{Z}$. $\mathbf{U} = [U_1\, U_2 \cdots U_m]^t$ is a vector of m random variables. $\mathbf{B}$ is an n x 1 constant coefficient vector representing the translation from $\mathbf{U}$ to $\mathbf{Z}$.

Because the transformation from $\mathbf{U}$ to $\mathbf{Z}$ is affine, the mean vector and covariance matrix of $\mathbf{Z}$ are related to the mean vector and covariance matrix of $\mathbf{U}$ by Equations (5.16) and (5.17).

$$\mathbf{M_Z} = \mathbf{AM_U} + \mathbf{B} \tag{5.16}$$

$$\mathbf{\Sigma_{ZZ}} = \mathbf{A\Sigma_{UU}A}^t \tag{5.17}$$

where $\mathbf{M_Z}$ and $\mathbf{M_U}$, and $\mathbf{\Sigma_{ZZ}}$ and $\mathbf{\Sigma_{UU}}$ are the mean vector and covariance matrix for $\mathbf{Z}$ and $\mathbf{U}$, respectively.

If $\mathbf{U}$ is selected to be a vector of uncorrelated standard normal random variables with zero mean and unit standard deviation, the mean vector and covariance matrix of $\mathbf{U}$ can be simplified to

$$\mathbf{M_U} = \mathbf{0} \text{ and } \mathbf{\Sigma_{UU}} = \mathbf{I} \tag{5.18}$$

where $\mathbf{0}$ is a vector of m x 1 zeros (because the mean of the random variables, $U_{i=1,2,\cdots,m}$, is selected to be 0), $\mathbf{I}$ is an m x m identity matrix (this shows U_i and U_j is uncorrelated, for $i \neq j$).

Substituting Equation (5.18) into Equations (5.16) and (5.17), the mean vector and covariance matrix of $\mathbf{Z}$ can be reduced to

$$\mathbf{M_Z} = \mathbf{A0} + \mathbf{B} = \mathbf{B} \text{ and } \mathbf{\Sigma_{ZZ}} = \mathbf{AIA}^{t} = \mathbf{AA}^{t} \tag{5.19}$$

If $\mathbf{Z}$ is a joint normal distribution, where the statistics of the distribution can be completely defined by the mean vector and covariance matrix, and $\mathbf{U}$ is a vector of uncorrelated standard normal random variables with zero mean and unit standard deviation, the statistics of $\mathbf{Z}$ can be assigned using different combinations of $\mathbf{A}$ and $\mathbf{B}$. In other words, with different combinations of the matrix $\mathbf{A}$ and vector $\mathbf{B}$, the *EDP* vector, $\mathbf{Z}$, can be generated to fit into any joint normal distribution.

To generate an *EDP* vector, $\mathbf{Z}$, with the same statistical distribution as a normally distributed random variable, $\mathbf{Y}$, the matrix $\mathbf{A}$ and vector $\mathbf{B}$ are selected to match the mean vector and covariance matrix of $\mathbf{Y}$. Equation (5.20) and Equation (5.21) show the selection of matrix $\mathbf{A}$ and vector $\mathbf{B}$ such that the *EDP* vectors, $\mathbf{Z}$, will have the same statistical distribution as a normally distributed random variable, $\mathbf{Y}$.

$$\mathbf{M_Z} = \mathbf{M_Y} \Rightarrow \mathbf{B} = \mathbf{M_Y} \tag{5.20}$$

$$\mathbf{\Sigma_{ZZ}} = \mathbf{\Sigma_{YY}} \Rightarrow \mathbf{AA}^{t} = \mathbf{\Sigma_{YY}} \Rightarrow \mathbf{A} = \left(\text{chol}(\mathbf{\Sigma_{YY}})\right)^{t} \tag{5.21}$$

where chol is the Choleski factorization of any square and positive definite matrix.

Because the entry of the covariance matrix is not bounded, the computations might cause numerically instability. The Choleski factorization of $\mathbf{\Sigma_{YY}}$ is calculated using Equation (5.22).

$$\begin{gathered} \mathbf{\Sigma_{YY}} = \mathbf{D_Y R_{YY} D_Y} \\ \mathbf{AA}^{t} = \mathbf{D_Y R_{YY} D_Y} \Rightarrow \mathbf{A} = \left(\text{chol}\left(\mathbf{D_Y R_{YY} D_Y}\right)\right)^{t} = \mathbf{D_Y}\left(\text{chol}\left(\mathbf{R_{YY}}\right)\right)^{t} \end{gathered} \tag{5.22}$$

where $\mathbf{D_Y}$ is a diagonal matrix with standard deviations of random variables $\mathbf{Y}$ along its diagonal and $\mathbf{R_{YY}}$ is the correlation coefficient matrix of random variables $\mathbf{Y}$.

Because the correlation coefficient matrix has bounded elements and ones along the diagonal, it is numerically more stable to calculate the Choleski factorization using Equation (5.22).

5.3.2 Generate Correlated *EDP* Vectors

To generate correlated *EDP* vectors, the peak *EDP* quantities recorded from sets of dynamic analysis are tabulated into matrix, $\mathbf{X}$, as shown in Table 5.2. Each column of $\mathbf{X}$ represents an *EDP* of interest, while each row of $\mathbf{X}$ represents different *EDP* recorded from a single ground motion. Because the entry of $\mathbf{X}$ represents the peak response quantity, a joint lognormal distribution is assumed for $\mathbf{X}$.

The *EDP* matrix, $\mathbf{X}$, is then transformed to a normal distribution, $\mathbf{Y}$, by taking the natural log of $\mathbf{X}$. The mean vector, $\mathbf{M_Y}$, diagonal standard deviation matrix, $\mathbf{D_Y}$, and the correlation coefficient matrix, $\mathbf{R_{YY}}$, are then sampled from $\mathbf{Y}$. Equations (5.23)–(5.26) show the formulas used for the statistical sample. Detailed formulas for the statistic samples are summarized in Appendix A.

$$\mathbf{M_Y} = \left(mean(\mathbf{Y})\right)^t \tag{5.23}$$

$$\mathbf{D_Y} = diag(std(\mathbf{Y})) \tag{5.24}$$

$$\mathbf{R_{YY}} = corrcoef(\mathbf{Y}) \tag{5.25}$$

$$\mathbf{L_Y} = \left(chol(\mathbf{R_{YY}})\right)^t \tag{5.26}$$

Following the derivation shown in previous section, additional correlated *EDP* vectors, $\mathbf{Z}$, can be generated to fit the probability distribution of $\mathbf{Y}$ if a vector of uncorrelated standard normal random variables, $\mathbf{U}$, with zero mean and unit standard deviation is used. Equation (5.27) shows the transformation from $\mathbf{U}$ to $\mathbf{Z}$.

$$\mathbf{Z} = \mathbf{AU} + \mathbf{B} \tag{5.27}$$

where $\mathbf{A}$ is a constant coefficient matrix representing the linear transformation from $\mathbf{U}$ to $\mathbf{Z}$, and $\mathbf{B}$ is a constant coefficient vector representing the translation from $\mathbf{U}$ to $\mathbf{Z}$.

If $\mathbf{B} = \mathbf{M_Y}$ and $\mathbf{A} = \mathbf{D_Y} \mathbf{L_Y}$, $\mathbf{Z}$ will have the same probability distribution as $\mathbf{Y}$. Equation (5.28) shows the formula used to generate additional correlated *EDP* vectors.

$$\mathbf{Z} = \mathbf{D_Y} \mathbf{L_Y} \mathbf{U} + \mathbf{M_Y} \ \mathbf{Z} = \mathbf{A}\mathbf{U} + \mathbf{B} \tag{5.28}$$

Finally, the generated *EDP* vectors are transformed to the lognormal distribution, $\mathbf{W}$, by taking the exponential of $\mathbf{Z}$. Figure 5.6 shows the process of generating correlated *EDP* vectors.

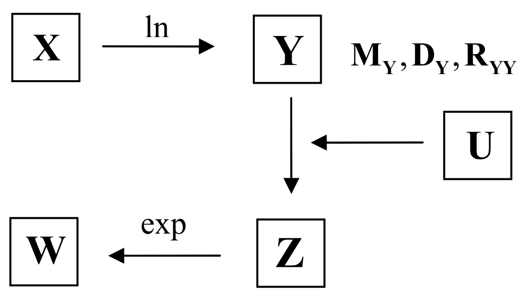

Fig. 5.6 Process of generating correlated *EDP* vectors.

5.4 SUMMARY AND CONCLUSIONS

This chapter introduces a fully probabilistic performance-based earthquake engineering evaluation framework as well as a practical implementation of that framework using a novel solution strategy.

Recognizing that a major obstacle in implementing the performance-based earthquake engineering is the need to conduct numerous dynamic analyses to obtain realizations of response of the structure to likely earthquake ground motions, a method for generating such response realizations using a limited number of dynamic analyses and correlated *EDP* matrix approach is proposed. This method requires that a relatively smaller number of dynamic analyses are done to generate a database for deriving the correlation among the principal engineering demand parameters needed to evaluate the performance of the building. Once such a database is populated, a statistical procedure is used to generate additional vectors of engineering demand parameters with the property that they have the same correlation as the *EDPs* computed directly by dynamic analysis of the building.

This computationally inexpensive generation procedure enables a Monte-Carlo type implementation of the PBEE framework. The procedure for conducting the performance-based evaluation is outlined. It starts with a systematic data collection to describe the seismic environment and the vulnerability of the structure. The seismic environment is described in a seismic hazard analysis. The vulnerability of the structure is described using the fragility of the structural and nonstructural components and the associated engineering demand parameters, as well as the quantities of the vulnerable structural and nonstructural components and the repair methods and associated unit repair costs. The seismic response of the structure is examined by conducting a limited number of nonlinear dynamic analyses on a finite element model of the structure to generate a database for finding the statistical correlation structure among the engineering demand parameters that describe the response of the structure to a ground motion. Once the correlation is defined, a Monte-Carlo technique is used to generate numerous realizations of the seismic response of the building and damage to structural and nonstructural components in order to compute the statistics of the total repair cost. Such data are used to express the performance of the structure in terms of total repair cost.

This procedure has been implemented in a computer program to facilitate the computations. An example of using the procedure to evaluate the seismic performance of two structural systems for the same building is presented in the next chapter. This example illustrates how the PBEE framework can be used to rationalize the selection of a structural system for a new building.

6 Performance-Based Evaluation of Suspended Zipper Braced Frame and Inverted-V Braced Frame

Dynamic response of the suspended zipper braced frame under a selected ground motion was analyzed in Chapter 3 and verified using the hybrid simulation test presented in Chapter 4. The results of these simulations indicate that the zipper column is effective in distributing the unbalanced vertical force and that the system is quite redundant. To further demonstrate the robustness of suspended zipper braced frame system, the theoretical performance of a building using that system was examined for suites of ground motions representing multiple hazard levels. In this study, system performance was assessed using the performance-based earthquake engineering (PBEE) methodology presented in Chapter 5. For comparison purposes, an inverted-V braced frame was evaluated using the same PBEE methodology. This comparison shows the advantages of the suspended zipper braced frame.

6.1 DESCRIPTION OF BUILDING MODEL

To improve the short coming of having concentrated story damage in the conventional concentrically braced steel frames, the suspended zipper and the inverted-V braced frames were designed to have ductile response using the design procedure presented in Yang (2006) and AISC 2002 Seismic Provisions for Structural Buildings Section 13 (American Inst. of Steel Construction 2002). Both of these procedures used compact sections and capacity design methodology to resist the unbalanced vertical force created by brace buckling. The inverted-V braced frame used deep beam sections to resist the unbalanced vertical load, while the suspended zipper braced frame uses the top-story braces and the zipper columns truss system to resist the unbalanced vertical load. Note that current building codes permit other forms of steel braced frames wherein the unbalanced vertical load is not fully resisted by adjacent framing members, and such braced frames may not perform equivalent to the frames studied here.

An idealized building model was designed using these concentrically braced frames. As idealized, the building is located in downtown Berkeley, California, and designed according to the International Building Code (IBC 2000) (ICC 2000). Detailed design calculations for the building are presented in Appendix B.

6.1.1 Building Dimensions and Member Sizes

Figure 6.1 shows a global view and the coordinate system of the idealized building. The building is a regular three-story office building with equal floor heights of 14 feet. Figure 6.2 shows the plan view and the orientation of the column axes. The lateral-load-resisting systems (LLRS) are located at the perimeter of the building. With two axes of symmetry and the rigid diaphragm assumption, each of the braced frame bays of the LLRS is designed for one sixth of the lateral load.

Member sizes of the gravity load carrying system are shown in Tables 6.1–6.4.

Table 6.1 Size of gravity columns.

Element size	Locations (Same member size for all stories)
W10x39	2-A, 2-F, 4-A, 4-F, 7-A, 7-F, 9-A, 9-F
W10x49	3-A, 3-B, 3-C, 3-D, 3-E, 3-F, 4-C, 4-D, 5-C, 5-D, 6-C, 6-D, 7-C, 7-D, 8-A, 8-B, 8-C, 8-D, 8-E, 8-F

Table 6.2 Size of gravity beams at roof level.

Element size	Locations
W12x19	All beams at the roof floor level in the global X direction, except the beams on the perimeter of the building.
W14x22	All beams along line A and F at the roof floor level.
W18x35	All beams along line 3 and 8 at the roof floor level. All beams in between line B and E in the direction along line 4, 5, 6 and 7 at the roof floor level.
W18x40	All perimeter beams in the global Y direction at the roof floor level, except the beams of the LLRS.

Table 6.3 Size of gravity beams at third-floor level.

Element size	Locations
W16x31	All beams at the third-floor level in the global X direction, except the beams on the perimeter of the building.
W18x40	All beams along line A and F at the third-floor level.
W18x35	All beams along line 3 and 8 at the third-floor level. All beams in between line B and E in the direction along line 4, 5, 6 and 7 at the third-floor level.
W24x62	All perimeter beams in the global Y direction at the third-floor level, except the beams of the LLRS.

Table 6.4 Size of gravity beams at second-floor level.

Element size	Locations
W14x22	All beams at the second-floor level in the global X direction, except the beams on the perimeter of the building.
W18x35	All beams along line A and F at the second-floor level.
W18x40	All beams along line 3 and 8 at the second-floor level. All beams in between line B and E in the direction along line 4, 5, 6 and 7 at the second-floor level.
W24x62	All perimeter beams in the global Y direction at the second-floor level, except the beams of the LLRS.

Figures 6.3a–b show the member sizes of the inverted-V braced frame and the suspended zipper braced frame, respectively. Table 6.5 shows the self-weight comparison of the two lateral-load-resisting systems. Based on this comparison, the suspended zipper braced frame is 25% lighter than the inverted-V braced frame.

Table 6.5 Self weight comparison of lateral-load-resisting systems.

	Inverted-V braced frame	Suspended zipper braced frame
Weight (kips)	40.11	29.75
Weight (%)	100%	74.2%

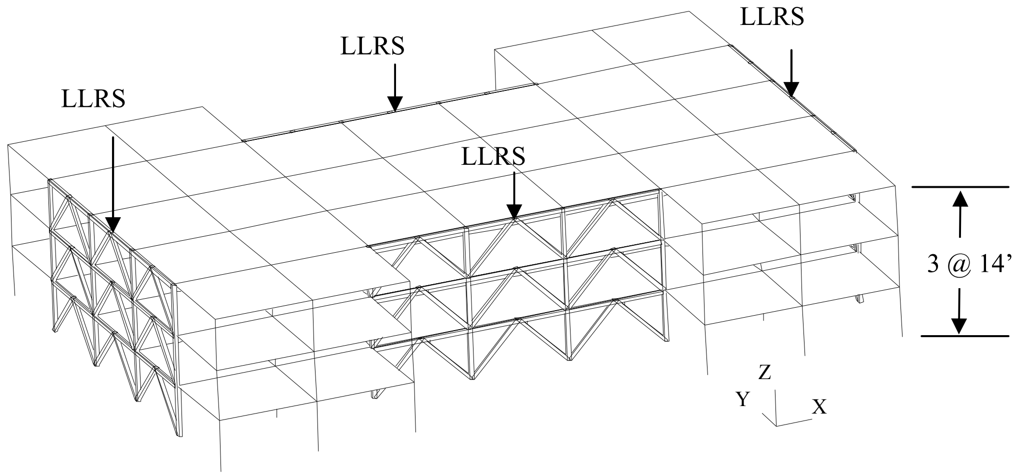

Fig. 6.1 Global view of idealized building.

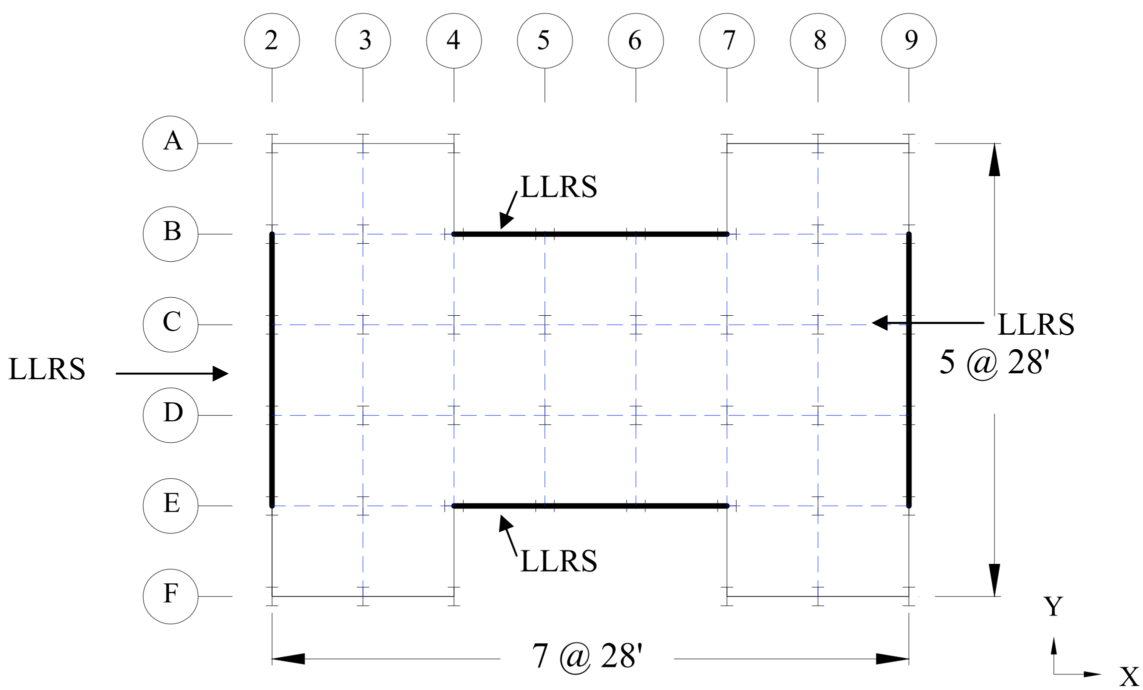

Fig. 6.2 Plan view of idealized building.

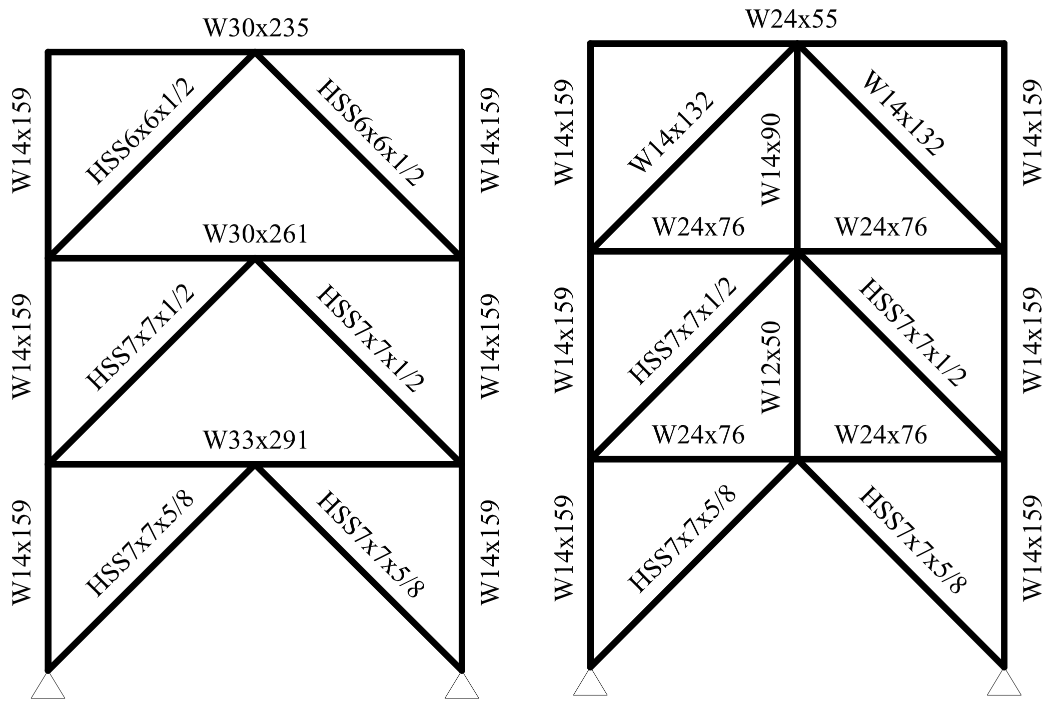

(a) Inverted-V braced frame (b) Suspended zipper braced frame

Fig. 6.3 Member sizes in lateral-load-resisting systems.

6.1.2 Gravity Load and Seismic Weight

Items considered in the calculation of the dead load (DL), the live load (LL), and the seismic weight of the building model at the roof, third-, and second-floor levels are shown in Table 6.6 to Table 6.8, respectively. The dead load consists of an area load uniformly distributed on the floor area and a perimeter load to represent the facade. The live load is uniformly distributed on the floor area. Live load reduction is not implemented. The total seismic weight of the building model is calculated to be 8586 kips.

Table 6.6 Gravity load and seismic weight of idealized building at roof level.

Roof			
DL - area load	Description	Gravity weight	Seismic weight
Roofing & Insulation		6.5 psf	6.5 psf
Concrete on deck	Lightweight, 6-1/4 total	41 psf	41 psf
Deck	18 ga. W3 deck, 10'-8" span	2.7 psf	2.7 psf
Beams		5 psf	5 psf
Columns, braces		5 psf	5 psf
Ceiling / Lights		3.5 psf	3.5 psf
Sprinklers		3.5 psf	3.5 psf
Mechanical/Electrical		2.5 psf	2.5 psf
Partitions		-	6 psf
Roof Screen		-	6 psf
Misc	Equipment	26.5 psf	26.5 psf
DL - perimeter load			
Typ. punched window panel	7' in elevation	50 psf	50 psf
Typ. ext metal stud wall/thin wall panel	7' in elevation	30 psf	30 psf
Lr - area load			
Live load	Reducible	20 psf	-
Total seismic weight (kips)	Not including the LL		2,899 kips

* Source: provided by Anindya Dutta of Simpson Gumpertz and Heger Inc.

Table 6.7 Gravity load and seismic weight of idealized building at third-floor level.

Third-floor data center			
DL - area load	Description	Gravity weight	Seismic weight
Access Floor		2.5 psf	2.5 psf
Floor Finish		2.5 psf	2.5 psf
Concrete on deck	Lightweight, 6-1/4 total	41 psf	41 psf
Deck	18 ga. W3 deck, 10'-8" span	2.7 psf	2.7 psf
Beams		5 psf	5 psf
Columns, braces		5 psf	5 psf
Ceiling / Lights		2 psf	2 psf
Sprinklers		2 psf	2 psf
Mechanical/Electrical		1 psf	1 psf
Partitions		20 psf	10 psf
DL - perimeter load			
Typ. punched window panel	14’ in elevation	50 psf	50 psf
Typ. ext metal stud wall/thin wall panel	14’ in elevation	30 psf	30 psf
LL - area load			
Live load	Reducible	100 psf	25 psf
Total seismic weight (kips)	Including 25% LL		3,122 kips

* Source: provided by Anindya Dutta of Simpson Gumpertz and Heger Inc.

Table 6.8 Gravity load and seismic weight of idealized building at second-floor level.

Second-floor office			
DL - area load	Description	Gravity weight	Seismic weight
Floor Finish		2.5 psf	2.5 psf
Concrete on deck	Lightweight, 6-1/4 total	41 psf	41 psf
Deck	18 ga. W3 deck, 10'-8" span	2.7 psf	2.7 psf
Beams		5 psf	5 psf
Columns, braces		5 psf	5 psf
Ceiling / Lights		2.5 psf	2.5 psf
Sprinklers		0.5 psf	0.5 psf
Mechanical/Electrical		1 psf	1 psf
Misc		4 psf	4 psf
Partitions		20 psf	10 psf
DL - perimeter load			
Typ. punched window panel	14’ in elevation	50 psf	50 psf
Typ. ext metal stud wall/thin wall panel	14’ in elevation	30 psf	30 psf
LL - area load			
Live load	Reducible	80 psf	-
Total seismic weight (kips)	Not including the LL		2,565 kips

* Source: provided by Anindya Dutta of Simpson Gumpertz and Heger Inc.

6.1.3 Selection of Performance Groups

Following the performance-based earthquake engineering assessment methodology prescribed in Chapter 5, major structural and nonstructural components of the building were identified and separated into different performance groups. Each performance group consists of one or more building components whose performance is similarly affected by a particular engineering demand parameter. For example, one performance group might comprise all similar nonstructural components whose performance is sensitive to the second-story interstory drift.

For this idealized building, major components of the building were divided into 16 performance groups (as shown in Table 6.9). The structural components were assigned to PGs whose performance is associated with interstory drift ratio in the story where the components are located. The nonstructural components and contents of the building were subdivided into displacement-sensitive and acceleration-sensitive groups. The displacement-sensitive groups use interstory drift to define the performance of the group, while the acceleration-sensitive groups use absolute acceleration at different floor levels to define the performance.

Multiple damage states were defined for each performance group. The damage states were defined in relation to the repair actions. For each component damage state, a damage model (fragility relation) defines the probability of component damage being equal to or greater than the threshold damage given the value of the engineering demand parameter associated with the component. Figures 6.5–6.10 show the fragility curves used to identify the damage state of each performance group. The numerical values of the fragility relations was not the subject of research conducted in this study. Instead, the fragility models were provided by participants in the ATC 58 project (Yang et al. 2006), and the objective of this study was to demonstrate their implementation.

Using the data about the idealized model, repair quantities for each item in each PG were identified based on the repair actions. The repair quantities associated with each damage state are shown in Tables 6.10–6.15. In accordance with the PBEE methodology outlined in Chapter 5, the total repair quantities for the structure are obtained by summing up the repair quantities in each performance group, given their damage state. Because the unit cost for each repair item generally reduces as the total repair quantity increases due to the amortization of the fixed setup costs, a trilinear function shown in Figure 6.4 was used to compute the unit repair cost of each item. The quantities Min qty, Max qty, Max cost, and Min cost shown in Figure 6.4 stand for the minimum quantities, maximum quantities, maximum cost, and minimum cost parameters of the cost function. The values of these cost function parameters for each repair method are summarized in Table 6.16. Depending on the complexity of the cost model, different cost functions can be used. In addition, uncertainty of the unit repair cost can be accounted for in the cost model by treating the repair cost as a normally distributed random variable with a mean given by the cost function and a constant standard deviation.

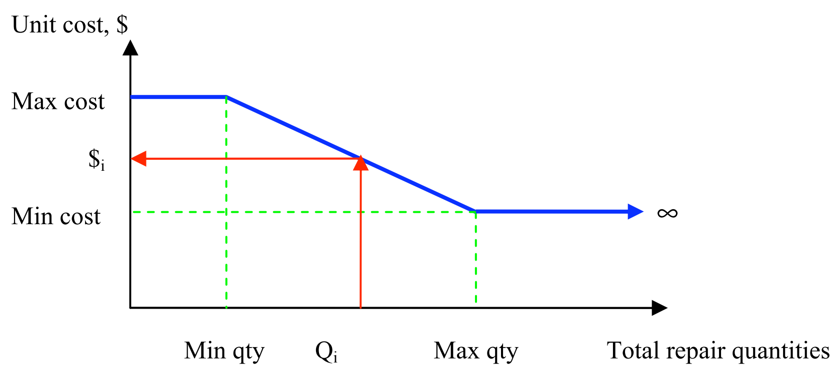

Fig. 6.4 Repair cost function model.

Table 6.9 Summary of performance group data.

PG #	PG Name	Location	EDP	Components
1	SH12	between levels 1 and 2	du_1	Structural: lateral-load-resisting system
2	SH23	between levels 2 and 3	du_2	
3	SH3R	between levels 3 and R	du_3	
4	EXTD12	between levels 1 and 2	du_1	Exterior enclosure: panels, glass, etc.
5	EXTD23	between levels 2 and 3	du_2	
6	EXTD3R	between levels 3 and R	du_3	
7	INTD12	between levels 1 and 2	du_1	Interior nonstructural drift sensitive: partitions, doors, glazing, etc
8	INTD23	between levels 2 and 3	du_2	
9	INTD3R	between levels 3 and R	du_3	
10	INTA2	below level 2	a_2	Interior nonstructural acceleration sensitive: ceilings, lights, sprinkler heads, etc
11	INTA3	below level 3	a_3	
12	INTAR	below level R	a_R	
13	CONT1	at level 1	a_g	Contents: General office on first and second floor, computer center on third
14	CONT2	at level 2	a_2	
15	CONT3	at level 3	a_3	
16	EQUIPR	at level R	a_R	Equipment on roof

Where du_i = interstory drift ratio at the i^{th} story and a_i = total acceleration at the i^{th} floor.

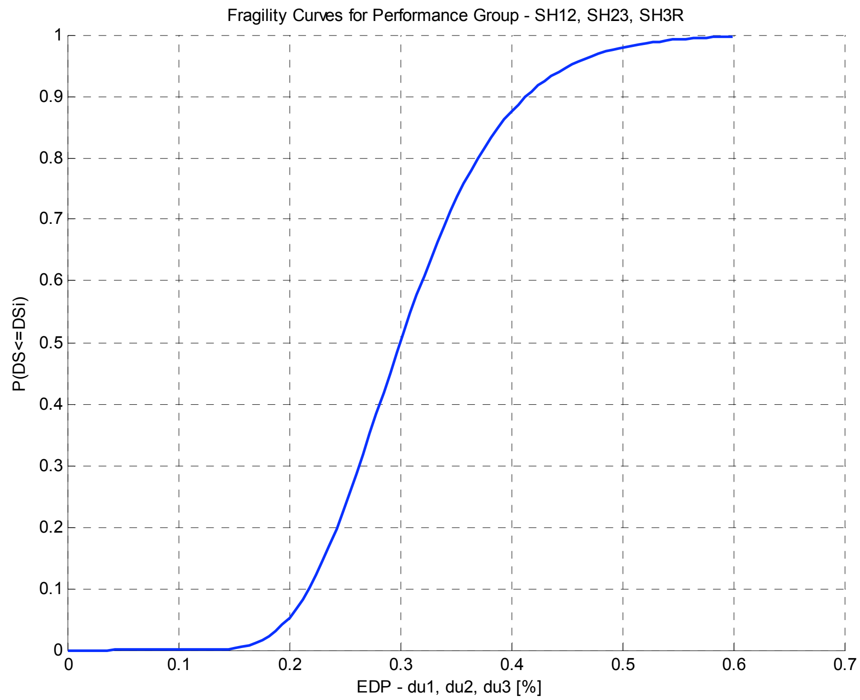

Fig. 6.5 Fragility curves for PG SH12, SH23, and SH3R.

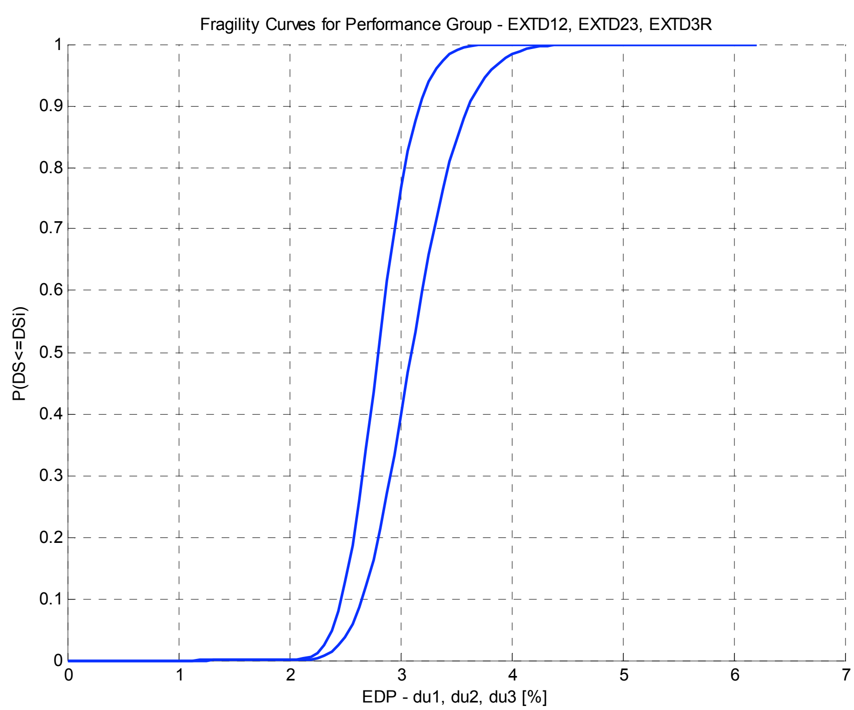

Fig. 6.6 Fragility curves for PG EXTD12, EXTD23, and EXTD3R.

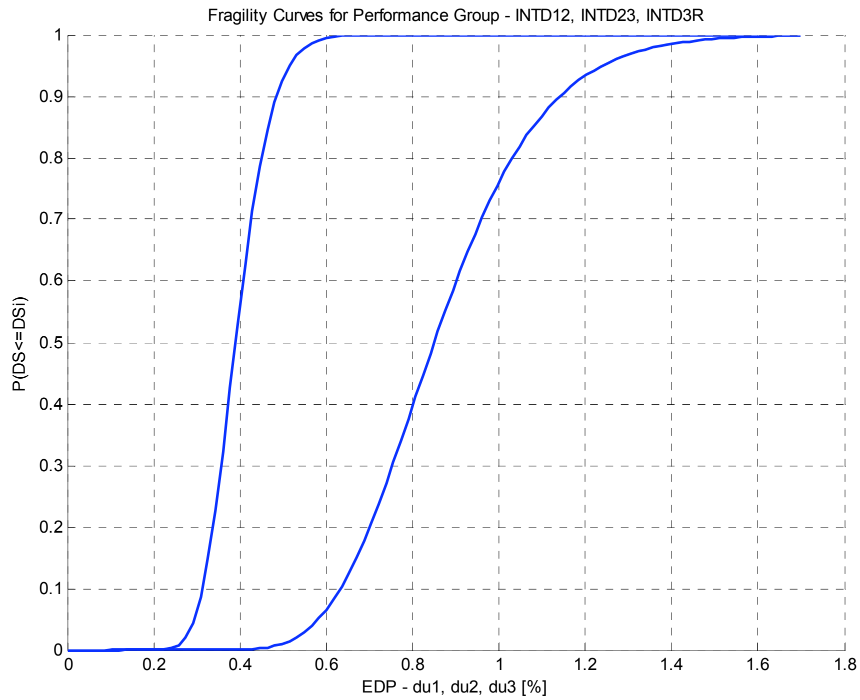

Fig. 6.7 Fragility curves for PG INTD12, INTD23, and INTD3R.

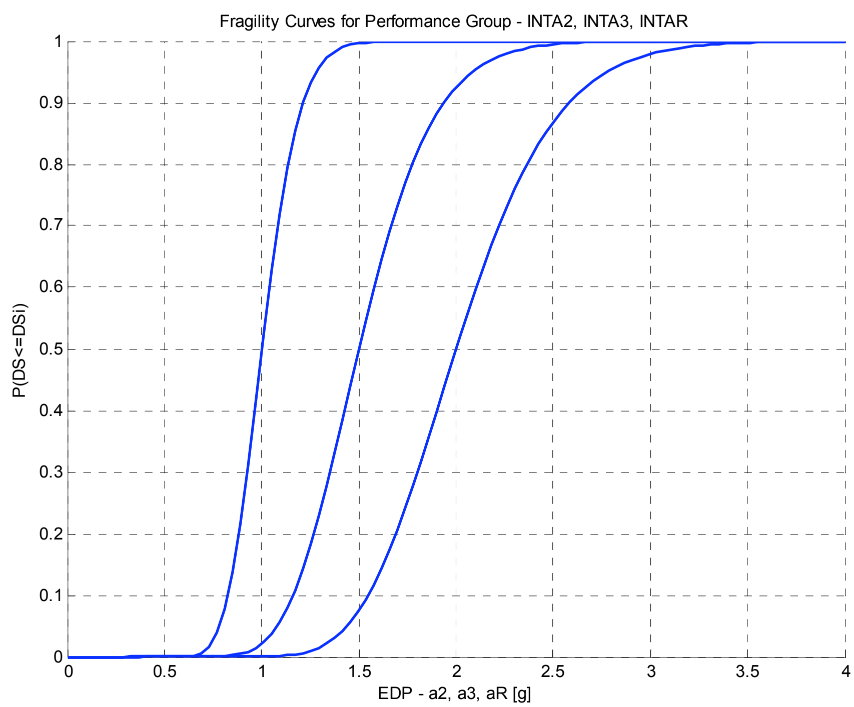

Fig. 6.8 Fragility curves for PG INTA2, INTA3, and INTAR.

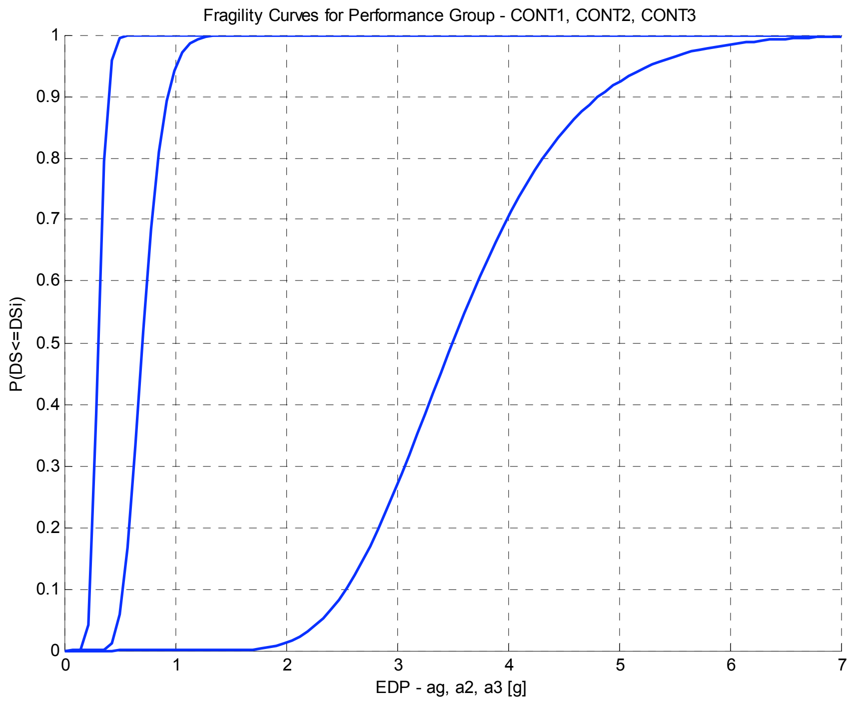

Fig. 6.9 Fragility curves for PG CONT1, CONT2, and CONT3.

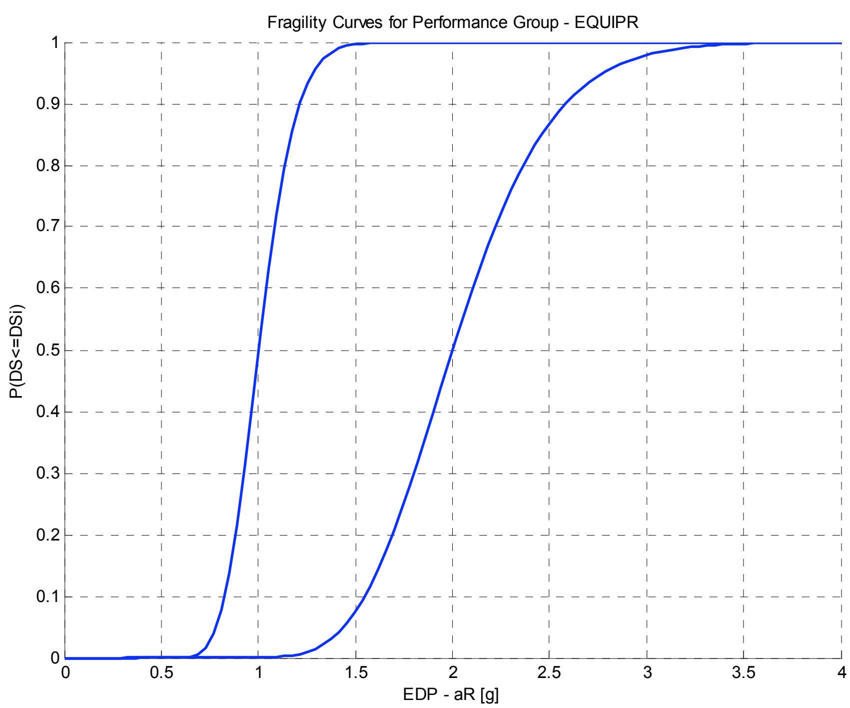

Fig. 6.10 Fragility curves for PG EQUIPR.

Table 6.10 Repair quantities for PG SH12, SH23, and SH3R.

Structural performance groups							
		SH12		SH23		SH3R	
Repair items	Units	DS1	DS2	DS1	DS2	DS1	DS2
Demolition/Access							
Finish protection	sf	0	6,000	0	6,000	0	6,000
Ceiling system removal	sf	0	5,000	0	5,000	0	5,000
Drywall assembly removal	sf	0	6,000	0	6,000	0	6,000
Miscellaneous MEP	loc	0	6	0	6	0	6
Remove exterior skin (salvage)	sf	0	5,600	0	4,000	0	3,000
Repair							
Welding protection	sf	0	1,500	0	1,500	0	1,500
Shore beams below & remove	loc	0	12	0	12	0	12
Cut floor slab at damaged connection	sf	0	1,600	0	1,600	0	1,600
Carbon arc out weld	lf	0	50	0	50	0	50
Remove portion of damaged beam/column	sf	0	100	0	100	0	100
Replace weld - from above	lf	0	40	0	40	0	40
Remove/replace connection	lb	0	3,000	0	3,000	0	2,000
Replace slab	sf	0	1,600	0	1,600	0	1,600
Put-back							
Miscellaneous MEP and clean-up	loc	0	6	0	6	0	6
Wall framing (studs, drywall, tape and paint)	sf	0	6,000	0	6,000	0	6,000
Replace exterior skin (from salvage)	sf	0	5,600	0	5,600	0	5,600
Ceiling system	sf	0	5,000	0	5,000	0	5,000

Table 6.11 Repair quantities for PG EXTD12, EXTD23, and EXTD3R.

Exterior nonstructural performance groups										
		EXTD12			EXTD23			EXTD3R		
Repair items	Units	DS1	DS2	DS3	DS1	DS2	DS3	DS1	DS2	DS3
Non Structural Exterior Envelope Demolition										
Erect scaffolding	sf	0	6,000	6,000	0	6,000	6,000	0	6,000	6,000
Remove damaged windows	sf	0	3,400	3,400	0	3,400	3,400	0	3,400	3,400
Remove damage precast panels (demo)	sf	0	0	8,400	0	0	8,400	0	0	8,400
Miscellaneous access	sf	0	8,400	8,400	0	8,400	8,400	0	8,400	8,400
Non Structural Exterior Envelope Put-back										
Install new windows	sf	0	3,400	3,400	0	3,400	3,400	0	3,400	3,400
Provide new precast concrete panels	sf	0	0	8,400	0	0	8,400	0	0	8,400
Patch and paint exterior panels	sf	0	5,000	5,000	0	5,000	5,000	0	5,000	5,000
Miscellaneous put-back	ea	0	8,400	8,400	0	8,400	8,400	0	8,400	8,400
Site clean-up	sf	0	6,000	6,000	0	6,000	6,000	0	6,000	6,000

Table 6.12 Repair quantities for PG INTD12, INTD23, and INTD3R.

Interior nonstructural performance groups (drift sensitive)										
		INTD12			INTD23			INTD3R		
	Units	DS1	DS2	DS3	DS1	DS2	DS3	DS1	DS2	DS3
STRUCTURAL										
Demolition/Access										
Finish protection	sf	0	5,000	10,000	0	5,000	10,000	0	5,000	10,000
NONSTRUCTURAL INTERIOR										
Interior Demolition										
Remove furniture	sf	0	5,000	10,000	0	5,000	10,000	0	5,000	10,000
Carpet and rubber base removal	sf	0	0	10,000	0	0	10,000	0	0	10,000
Drywall construction removal	sf	0	0	10,000	0	0	10,000	0	0	10,000
Door and frame removal	ea	0	8	8	0	8	8	0	8	8
Interior glazing removal	sf	0	100	100	0	100	100	0	100	100
Ceiling system removal	sf	0	0	5,000	0	0	5,000	0	0	5,000
MEP removal	sf	0	0	1,000	0	0	1,000	0	0	1,000
Remove casework	lf	0	0	200	0	0	200	0	0	200

Table 6.12—*Continued.*

Interior nonstructural performance groups (drift sensitive)										
		INTD12			INTD23			INTD3R		
	Units	DS1	DS2	DS3	DS1	DS2	DS3	DS1	DS2	DS3
Interior Construction										
Drywall construction/paint	sf	0	0	10,000	0	0	10,000	0	0	10,000
Doors and frames	ea	0	8	25	0	8	25	0	8	25
Interior glazing	sf	0	100	400	0	100	400	0	100	400
Carpet and rubber base	sf	0	0	10,000	0	0	10,000	0	0	10,000
Patch and paint interior partitions	sf	0	5,000	5,000	0	5,000	5,000	0	5,000	5,000
Replace ceiling system	sf	0	0	5,000	0	0	5,000	0	0	5,000
MEP replacement	sf	0	0	1,000	0	0	1,000	0	0	1,000
Replace casework	lf	0	0	200	0	0	200	0	0	200

Table 6.13 Repair quantities for PG INTA2, INTA3, and INTAR.

Interior nonstructural performance groups (acceleration sensitive)													
		INTA2				INTA3				INTAR			
	Units	DS1	DS2	DS3	DS4	DS1	DS2	DS3	DS4	DS1	DS2	DS3	DS4
General clean-up													
Water damage	sf	0	0	10,000	20,000	0	0	10,000	20,000	0	0	10,000	20,000
STRUCTURAL													
Demolition/Access													
Finish protection	sf	0	4,000	10,000	20,000	0	4,000	10,000	20,000	0	4,000	10,000	20,000
NONSTRUCTURAL INTERIOR													
Interior Demolition													
Remove furniture	sf	0	4,000	10,000	20,000	0	4,000	10,000	20,000	0	4,000	10,000	20,000
Ceiling system removal	sf	0	0	0	20,000	0	0	0	20,000	0	0	0	20,000
MEP removal	sf	0	0	500	2,000	0	0	500	2,000	0	0	500	2,000
Interior Construction													
Replace ceiling tiles	sf	0	2,500	8,000	8,000	0	2,500	8,000	8,000	0	2,500	8,000	8,000
Replace ceiling system	sf	0	0	0	20,000	0	0	0	20,000	0	0	0	20,000
MEP replacement	sf	0	0	500	2,000	0	0	500	2,000	0	0	500	2,000

Table 6.14 Repair quantities for PG CONT1, CONT2, and CONT3.

Contents performance groups performance groups (acceleration sensitive)													
		CONT1				CONT2				CONT3			
	Units	DS1	DS2	DS3	DS4	DS1	DS2	DS3	DS4	DS1	DS2	DS3	DS4
General clean-up													
Office papers & books	sf	0	0	10,000	10,000	0	0	10,000	10,000	0	0	10,000	10,000
Office equipment	sf	0	5,000	10,000	10,000	0	5,000	10,000	10,000	0	5,000	10,000	10,000
Loose furniture / file drawers	sf	0	10,000	20,000	20,000	0	10,000	20,000	20,000	0	10,000	20,000	20,000
Contents													
Conventional office	sf	0	0	0	20,000	0	0	0	20,000	0	0	0	10,000
Computer center	sf	0	0	0	0	0	0	0	0	0	0	0	10,000

Table 6.15 Repair quantities for PG EQUIPR.

Contents performance groups performance groups (acceleration sensitive)				
		EQUIPR		
	Units	DS1	DS2	DS3
General clean-up				
Loose furniture / file drawers	sf	0	0	50,000
Roof-top MEP				
Repair in place	sf	0	1	1
Remove and replace	sf	0	0	1

Table 6.16 Unit cost of repair items.

	Units	Min qty	Max cost	Max qty	Min cost
General clean-up					
Office papers & books	sf	1,000	$ 0.1	10,000	$ 0.06
Office equipment	sf	1,000	$ 0.06	10,000	$ 0.04
Loose furniture / file drawers	sf	1,000	$ 0.05	10,000	$ 0.03
Water damage	sf	1,000	$ 0.15	20,000	$ 0.1
Contents					
Computer center	sf	10,000	$ 100	50,000	$ 75
Conventional office	sf	10,000	$ 25	50,000	$ 21
Roof-top MEP					
Repair in place	ls	-	$ 10,000	-	$ 10,000
Remove and replace	ls	-	$ 200,000	-	$ 200,000
STRUCTURAL					
Demolition/Access					
Finish protection	sf	1,000	$ 0.3	40,000	$ 0.15
Ceiling system removal	sf	1,000	$ 2	10,000	$ 1.25
Drywall assembly removal	sf	1,000	$ 2.5	20,000	$ 1.5
Miscellaneous MEP	loc	6	$ 200	24	$ 150
Remove exterior skin (salvage)	sf	3,000	$ 30	10,000	$ 25
Repair					
Welding protection	sf	1,000	$ 1.5	10,000	$ 1
Shore beams below & remove	loc	6	$ 2,100	24	$ 1,600
Cut floor slab at damaged connection	sf	10	$ 200	100	$ 150
Carbon arc out weld	lf	100	$ 15	1,000	$ 10
Remove portion of damaged beam/column	sf	100	$ 80	2,000	$ 50
Replace weld - from above	lf	100	$ 50	1,000	$ 40
Remove/replace connection	lb	2,000	$ 6	20,000	$ 5
Replace slab	sf	100	$ 20	1,000	$ 16
Put-back					
Miscellaneous MEP and clean-up	loc	6	$ 300	24	$ 200
Wall framing (studs, drywall, tape and paint)	sf	100	$ 12	1,000	$ 8
Replace exterior skin (from salvage)	sf	1,000	$ 35	10,000	$ 30
Ceiling system	sf	100	$ 8	60,000	$ 5

Table 6.16—*Continued.*

	Units	Min qty	Max cost	Max qty	Min cost
NONSTRUCTURAL INTERIOR					
Interior Demolition					
Remove furniture	sf	100	$ 2	1,000	$ 1.25
Carpet and rubber base removal	sf	1,000	$ 1.5	20,000	$ 1
Drywall construction removal	sf	200	$ 2.5	20,000	$ 1.5
Door and frame removal	ea	12	$ 40	48	$ 25
Interior glazing removal	sf	500	$ 2.5	5,000	$ 2
Ceiling system removal	sf	1,000	$ 2	20,000	$ 1.25
MEP removal	sf	100	$ 40	10,000	$ 15
Remove casework	lf	100	$ 20	1,000	$ 15
Interior Construction					
Drywall construction/paint	sf	500	$ 12	25,000	$ 8
Doors and frames	ea	12	$ 600	48	$ 400
Interior glazing	sf	100	$ 45	15,000	$ 30
Carpet and rubber base	sf	500	$ 6	30,000	$ 4
Patch and paint interior partitions	sf	1,000	$ 2.5	10,000	$ 2
Replace ceiling tiles	sf	1,000	$ 2	20,000	$ 1.5
Replace ceiling system	sf	1,000	$ 3	20,000	$ 2.5
MEP replacement	sf	100	$ 80	1,000	$ 60
Replace casework	lf	100	$ 70	1,000	$ 50
NONSTRUCTURAL EXTERIOR					
Non Structural Exterior Envelope Demolition					
Erect scaffolding	sf	1,000	$ 2.5	10,000	$ 2
Remove damaged windows	sf	100	$ 20	1,000	$ 15
Remove damage precast panels (demo)	sf	3,000	$ 12	10,000	$ 8
Miscellaneous access	sf	100	$ 20	1,000	$ 15
Non Structural Exterior Envelope Put-back					
Install new windows	sf	100	$ 80	1,000	$ 70
Provide new precast concrete panels	sf	1,000	$ 80	10,000	$ 65
Patch and paint exterior panels	sf	500	$ 4.5	5,000	$ 3.5
Miscellaneous put-back	ea	100	$ 10	1,000	$ 7
Site clean-up	sf	1,000	$ 1.5	10,000	$ 0.75

6.2 DESCRIPTION OF ANALYTICAL MODEL

An analytical model was constructed using OpenSees to study the dynamic response of the idealized building. With two axis of symmetry and a rigid diaphragm assumption, the responses of the idealized building in the global X and Y directions were calculated using two-dimensional in-plane OpenSees models. Coupling of the building response in the global X and Y directions was ignored and only the response in the global X direction is presented. Because the idealized building is symmetric about the global X axis, only half of the idealized building was modeled analytically and shown in Figure 6.11.

A multi-point constraint was used to slave the horizontal degrees of freedom at each floor level to simulate a rigid diaphragm. The column bases and the connections between the beams and the columns of the gravity load carrying system were modeled using the semi-rigid connections proposed by Astaneh-Asl (2005), where the rotational stiffness of the connections were modeled using half of the elastic flexural stiffness of the element $\left(\frac{EI}{2L}\right)$ and the moment capacity of the connection was limited to one fifth of the nominal plastic moment $\left(\frac{M_p}{5}\right)$. Shear deformation of the connections were restrained using a rigid material. The braces in the lateral-load-resisting systems were modeled using the analytical model presented in Chapter 2 (Fig. 2.20). The remaining beams and columns of the analytical model were modeled using the flexibility-formulation nonlinear fiber-cross-section beam-column elements in OpenSees.

Gravity loads and masses were lumped at the nodes according to the tributary area. The P-Δ effect was accounted for in the nonlinear dynamic analysis using the corotational transformation in OpenSees. Based on the modal analyses, the first-mode period of idealized building was calculated to be 0.448 sec and 0.424 sec for the inverted-V braced frame (IVBF) and the suspended zipper braced frame (SZBF), respectively. Stiffness proportional damping of 2 percent was assigned to the first mode.

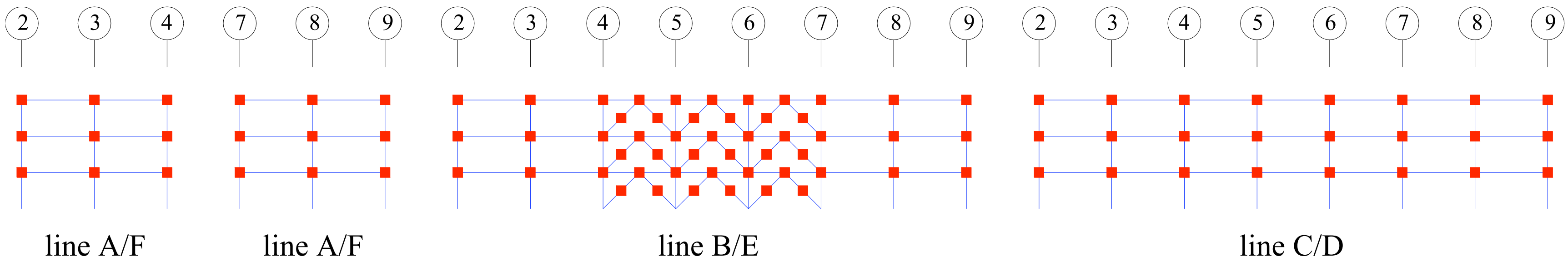

(a) Inverted-V braced frame (IVBF).

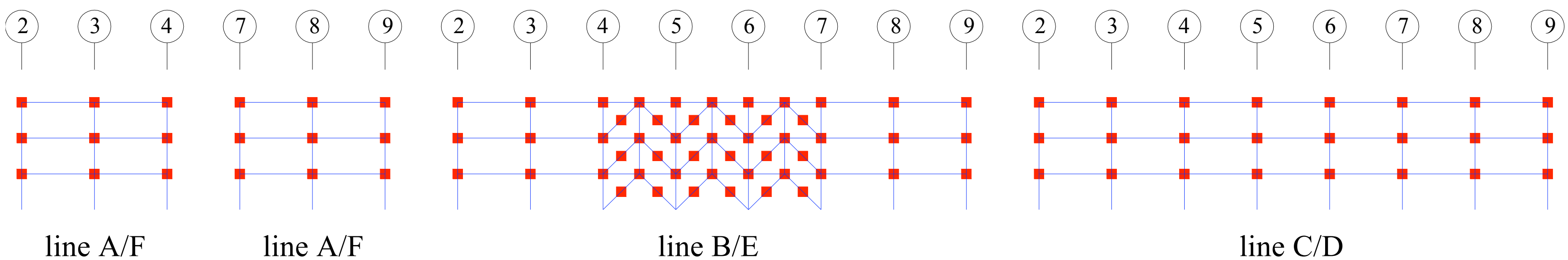

(b) Suspended zipper braced frame (SZBF).

Fig. 6.11 Analytical models used to compute dynamic response of idealized building.

6.3 SELECTION OF GROUND MOTIONS

To study the dynamic response of the idealized building, suites of ground motions representing the hazard at the building site were selected from the U.C. Berkeley Seismic Guidelines (UCB 2003). This document presents uniform hazard spectra derived based on probabilistic seismic hazard analysis in which the seismic source uncertainties and directivity effect were accounted for. Based on the seismic hazard de-aggregation, the Hayward fault dominates the seismic hazard at the site. The Hayward fault is a strike-slip fault with a potential of generating magnitude 7 earthquakes.

Three hazard levels (50%, 10%, and 5% probability of exceedance in 50 years) were selected to represent the seismic hazard at the site. Ten pairs (fault-normal and fault-parallel) of ground motions were selected to represent the ground motions for each of the hazard levels. Tables 6.17–6.18 summarize the selected ground motions.

In this investigation, the ground motions were scaled to match the target uniform hazard spectrum (UCB 2003) at the first-mode period of the structure. Alternative approaches to scale ground motions can be used, but this aspect of the problem is not studied here. Figures 6.12–6.17 show the scaling factors, peak scaled ground accelerations, and response spectra for the scaled ground motions.

Table 6.17 Ground motions representing 50% probability of exceedance in 50 years hazard level.

Earthquake	Mw	Station	Distance	Soil Type	Record
Coyote Lake, 1979/6/8	5.7	Coyote Lake, Dam Abutment	4.0 km	C	CL_clyd
		Gilroy # 6	1.2 km	C	CL_gil6
Parkfield, 1996/6/27	6.0	Temblor	4.4 km	C	PF_temb
		Cholome Array # 5	3.7 km	D	PF_cs05
		Cholome Array # 8	8.0 km	D	PF_cs08
Livermore, 1980/1/27	5.5	Fagundes Ranch	4.1 km	D	LV_fgnr
		Morgan Territory Park	8.1 km	C	LV_mgnp
Morgan Hill, 1984/4/24	6.2	Coyote Lake, Dam Abutment	0.1 km	C	MH_clyd
		Anderson Dam, Downstream	4.5 km	C	MH_andd
		Hall Valley	2.5 km	C	MH_hall

Table 6.18 Ground motions representing 10% and 5% probability of exceedance in 50 years hazard levels.

Earthquake	Mw	Station	Distance	Soil Type	Record
Loma Prieta, 1989/10/17	7.0	Los Gatos Present Center	3.5 km	C	LP_lgpc
		Saratoga Aloha Ave	8.3 km	C	LP_srtg
		Corralitos	3.4 km	C	LP_cor
		Gavilan College	9.5 km	C	LP_gav
		Gilroy Historic Building		C	LP_gilb
		Lexington Dam Abutment	6.3 km	C	LP_lex1
Kobe, Japan 1995/1/17	6.9	Kobe JM A	4.4 km	C	KB_kobj
Tottori, Japan 2000/10/6	6.6	Kofu	10 km	C	TO_kofu
		Hino	1 km	C	TO_hino
Erzincan, Turkey 1992/3/13	6.7	Erzincan	1.8 km	C	EZ_erzi

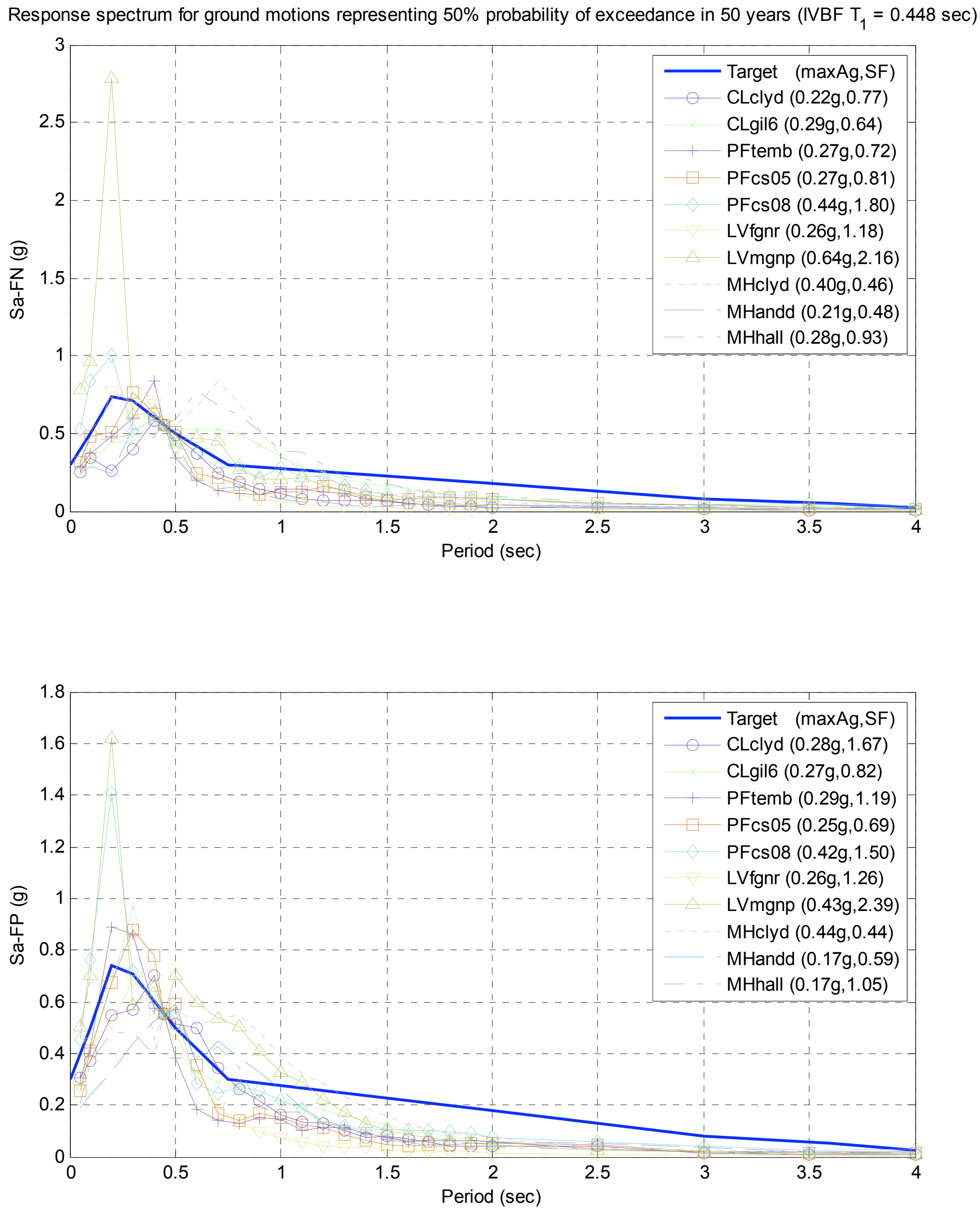

Fig. 6.12 Response spectra of scaled ground motions used for inverted-V braced frame at 50% probability of exceedance in 50 years hazard level.

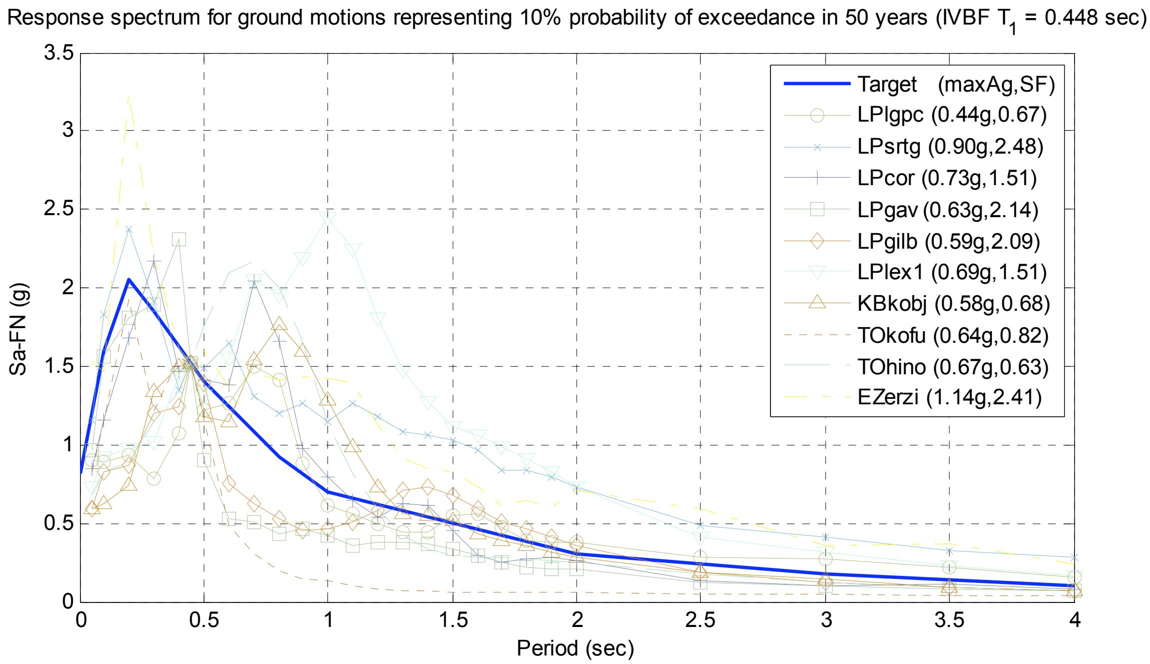

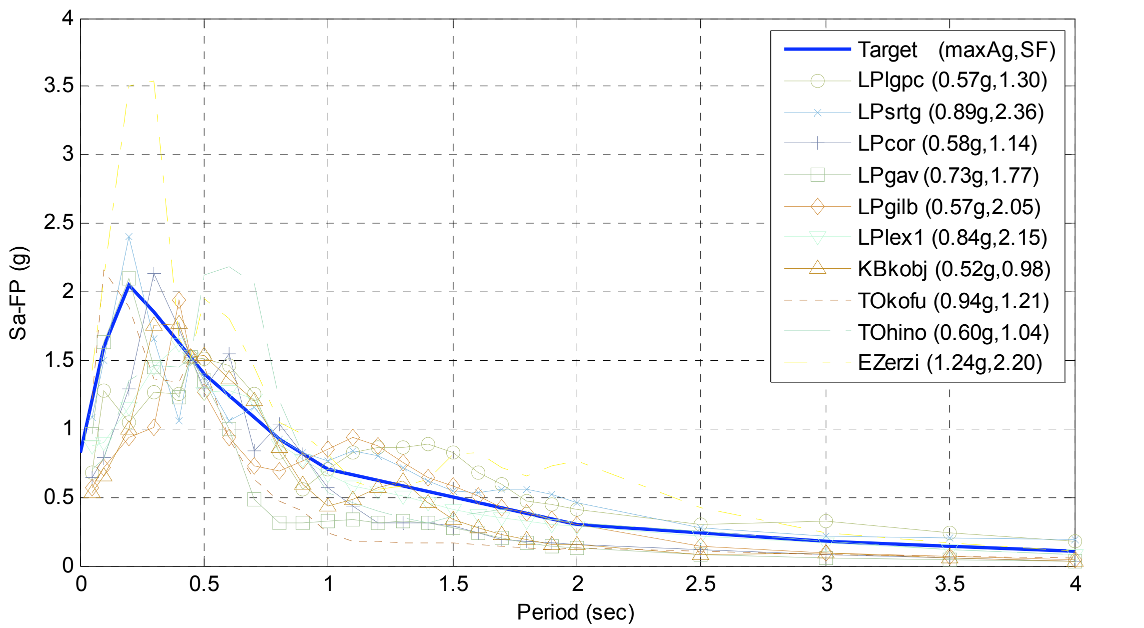

Fig. 6.13 Response spectra of scaled ground motions used for inverted-V braced frame at 10% probability of exceedance in 50 years hazard level.

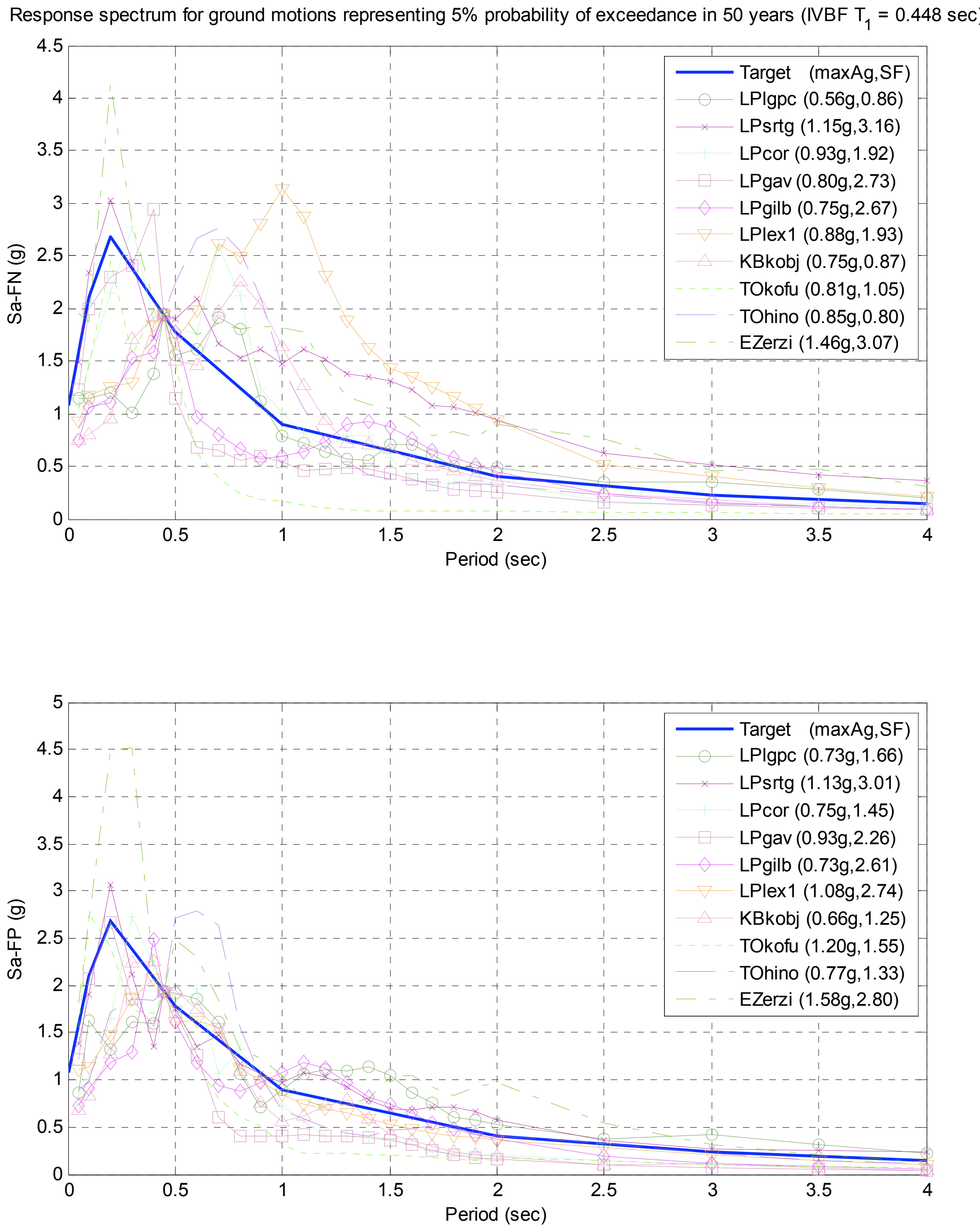

Fig. 6.14 Response spectra of scaled ground motions used for inverted-V braced frame at 5% probability of exceedance in 50 years hazard level.

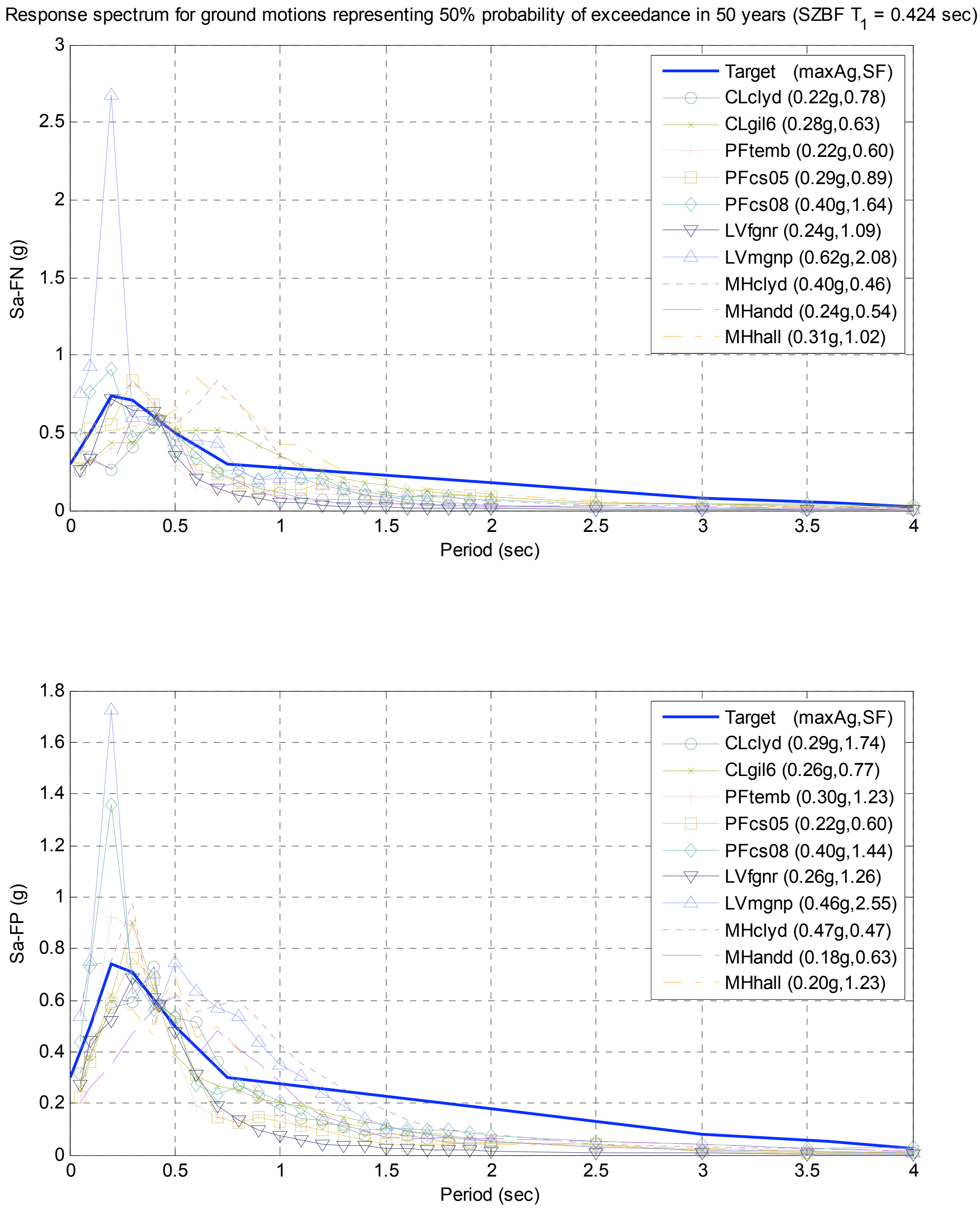

Fig. 6.15 Response spectra of scaled ground motions used for suspended zipper braced frame at 50% probability of exceedance in 50 years hazard level.

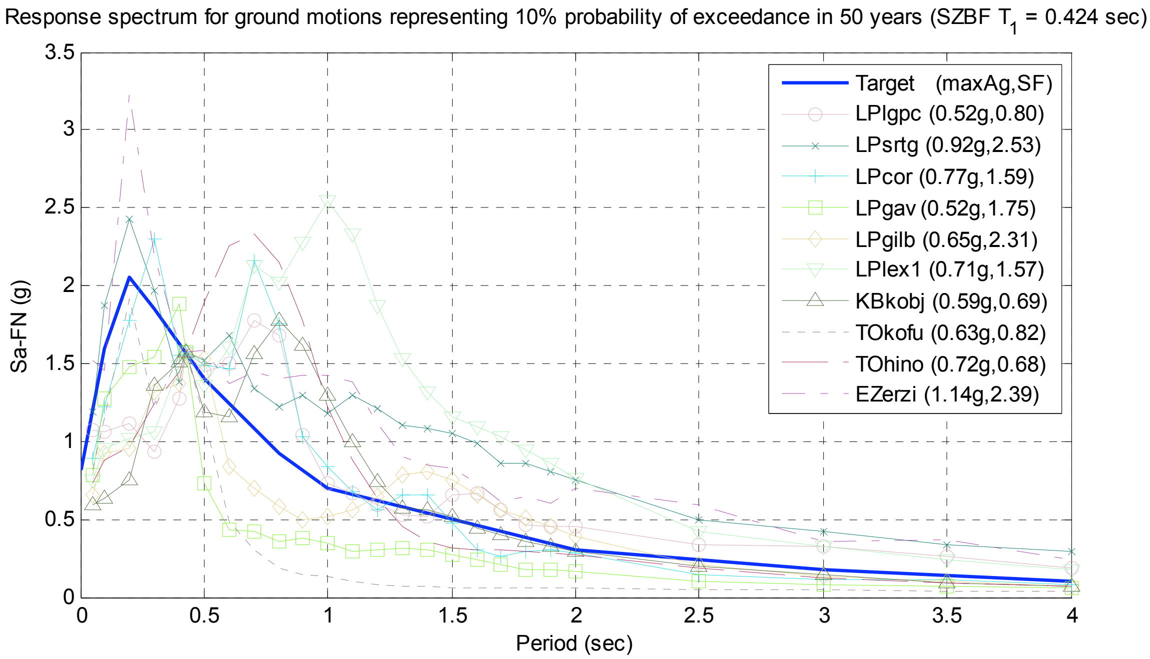

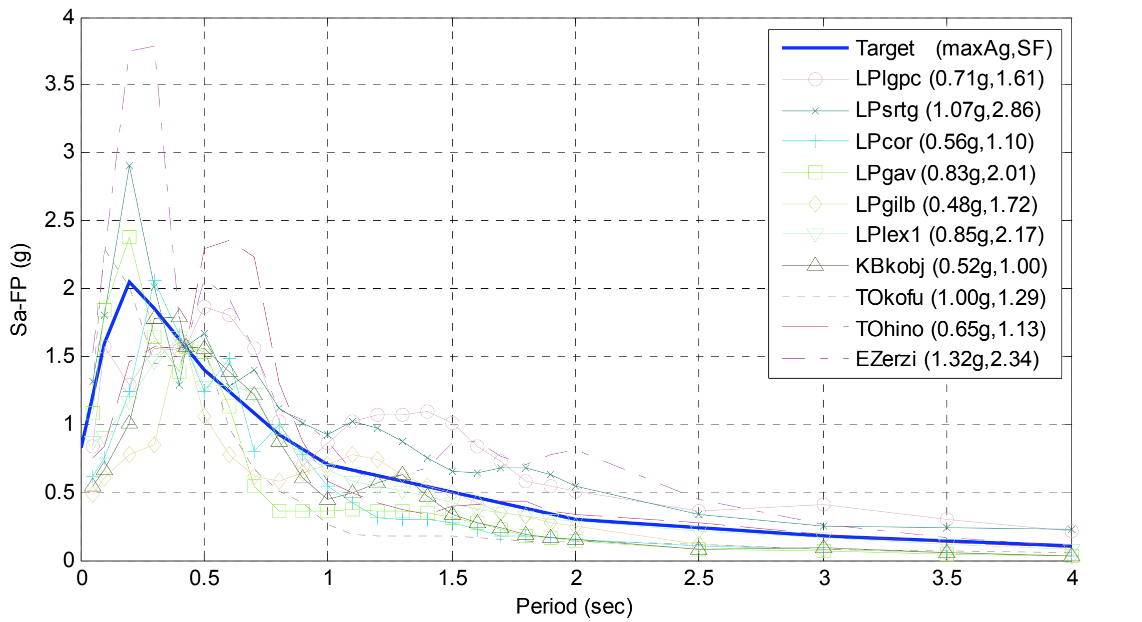

Fig. 6.16 Response spectra of scaled ground motions used for suspended zipper braced frame at 10% probability of exceedance in 50 years hazard level.

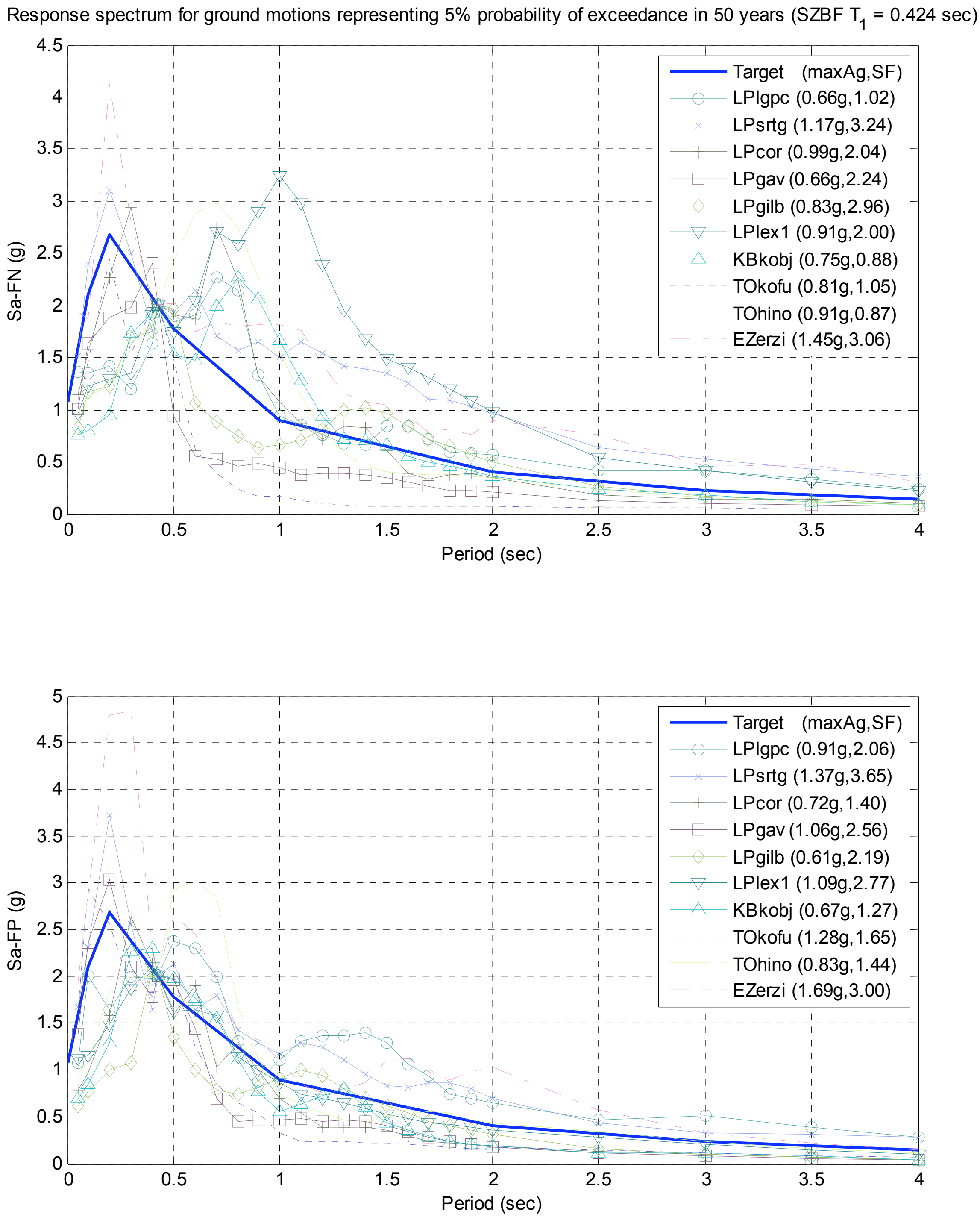

Fig. 6.17 Response spectra of scaled ground motions used for suspended zipper braced frame at 5% probability of exceedance in 50 years hazard level.

6.4 RESPONSE QUANTIFICATION

Nonlinear dynamic analyses were conducted to determine the system response of the idealized building to each of the selected scaled ground motions. Figures 6.18–6.21 show selected building responses histories of the inverted-V braced frame and the suspended zipper braced frame at 50% and 5% probability of exceedance in 50 years hazard levels.

At the 50% probability of exceedance in 50 years hazard level (for example, Figs. 6.18 and 6.19), displacement profiles for both frames are predominated by an apparent first mode. In this regard, the interstory drift ratios were fairly uniform among the stories (except that the third story in the suspended zipper braced frame) and the floor accelerations increased approximately as the story number increased.

At the 5% probability of exceedance in 50 years hazard level (for example, Figs. 6.20 and 6.21), both frames show significant residual first- and second-story interstory drift ratios, indicating that the first- and second-story braces in both frames were buckled. The brace buckling behavior reduced the floor stiffness significantly, which changed the predominant displaced shape from being linearly proportional to story height to having larger deformation in the lower stories. Such changes in the response resulted in a reduction in amplification of the floor accelerations in the higher stories.

The peak engineering demand parameters recorded from the nonlinear dynamic analyses are summarized in Tables 6.19–6.24. The symbols du_i and a_i used in Tables 6.19–6.24 represent the interstory drift ratio and the floor acceleration at the ith floor, respectively. The data of the peak engineering demand parameters were fitted with lognormal distribution and plotted as cumulative distribution function (CDF) in Figures 6.22–6.28.

Based on the lognormal distributions presented, both frames show very similar responses, with some exceptions. The suspended zipper braced frame has slightly higher first-story interstory drift ratio at the higher intensity level (Fig. 6.22), but negligible third-story interstory drift ratio for all hazard levels considered (Fig. 6.24). Such behavior is expected because the third-story braces in the suspended zipper braced frame were designed to be very stiff and to remain linear-elastic under the action of the unbalanced vertical load.

In terms of peak floor acceleration, the suspended zipper braced frame has higher peak ground acceleration than the inverted-V braced frame (Fig. 6.25). This is because of the scaling procedure presented in Section 6.3 whereby the ground motions were scaled at the first-mode period. Because the suspended zipper braced frame has slightly lower first-mode period, the scaling factors for the suspended zipper braced frame were slightly higher. Such an increase in peak ground acceleration also increased the second- and third-story peak floor accelerations for the suspended zipper braced frame (Figs. 6.26 and 6.27). However, because the suspended zipper braced frame has negligible third-story interstory drift, the roof and third-floor accelerations were very similar. On the other hand, the inverted-V braced frame picks up some additional floor acceleration from the vibration of the third story. In this regard, the suspended zipper braced frame has lower roof acceleration than the inverted-V braced frame for all hazard levels considered (Fig. 6.28).

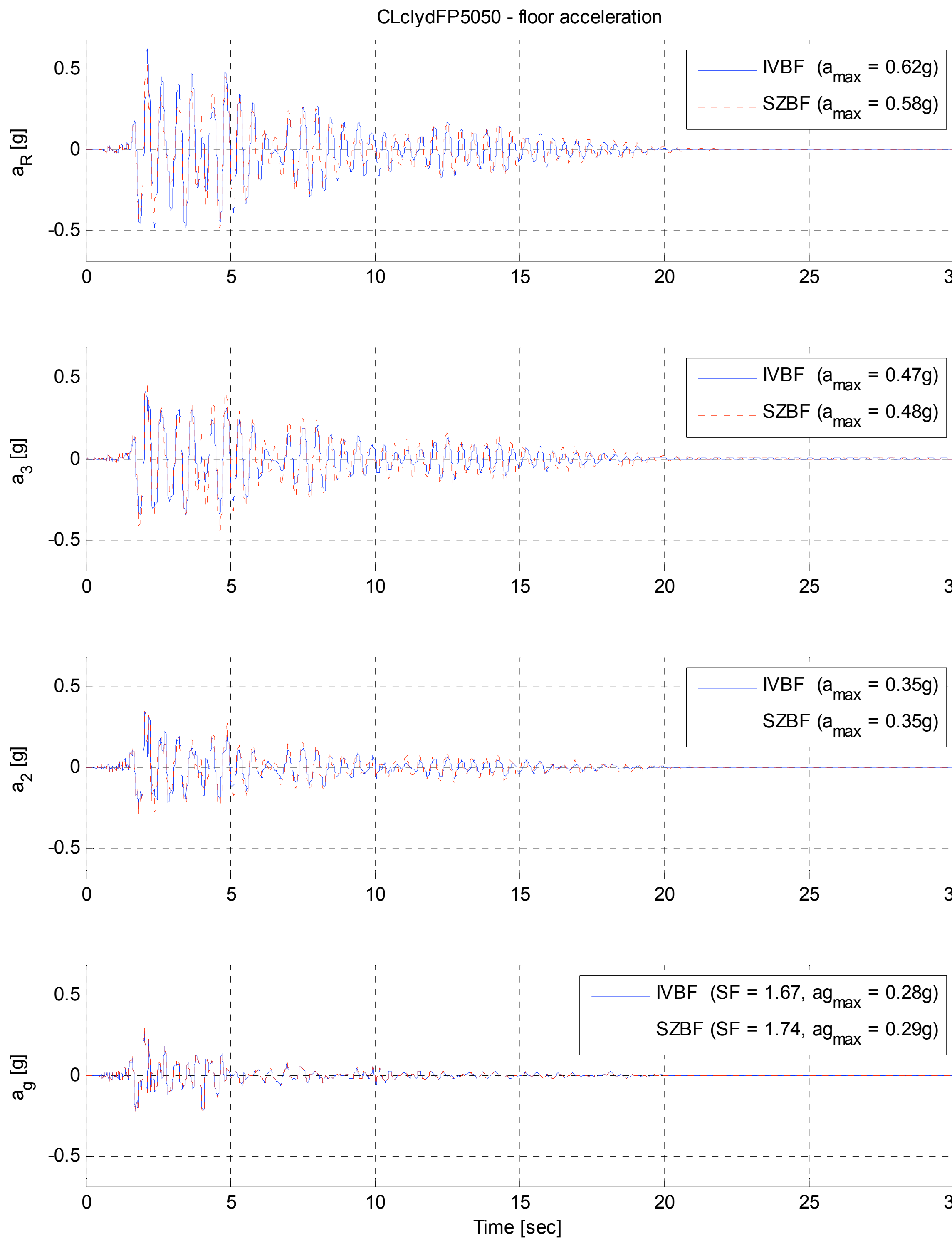

Fig. 6.18 Floor acceleration histories recorded during nonlinear dynamic analysis when buildings are subjected to CL_clyd fault parallel motion scaled to match 50% probability of exceedance in 50 years hazard level.

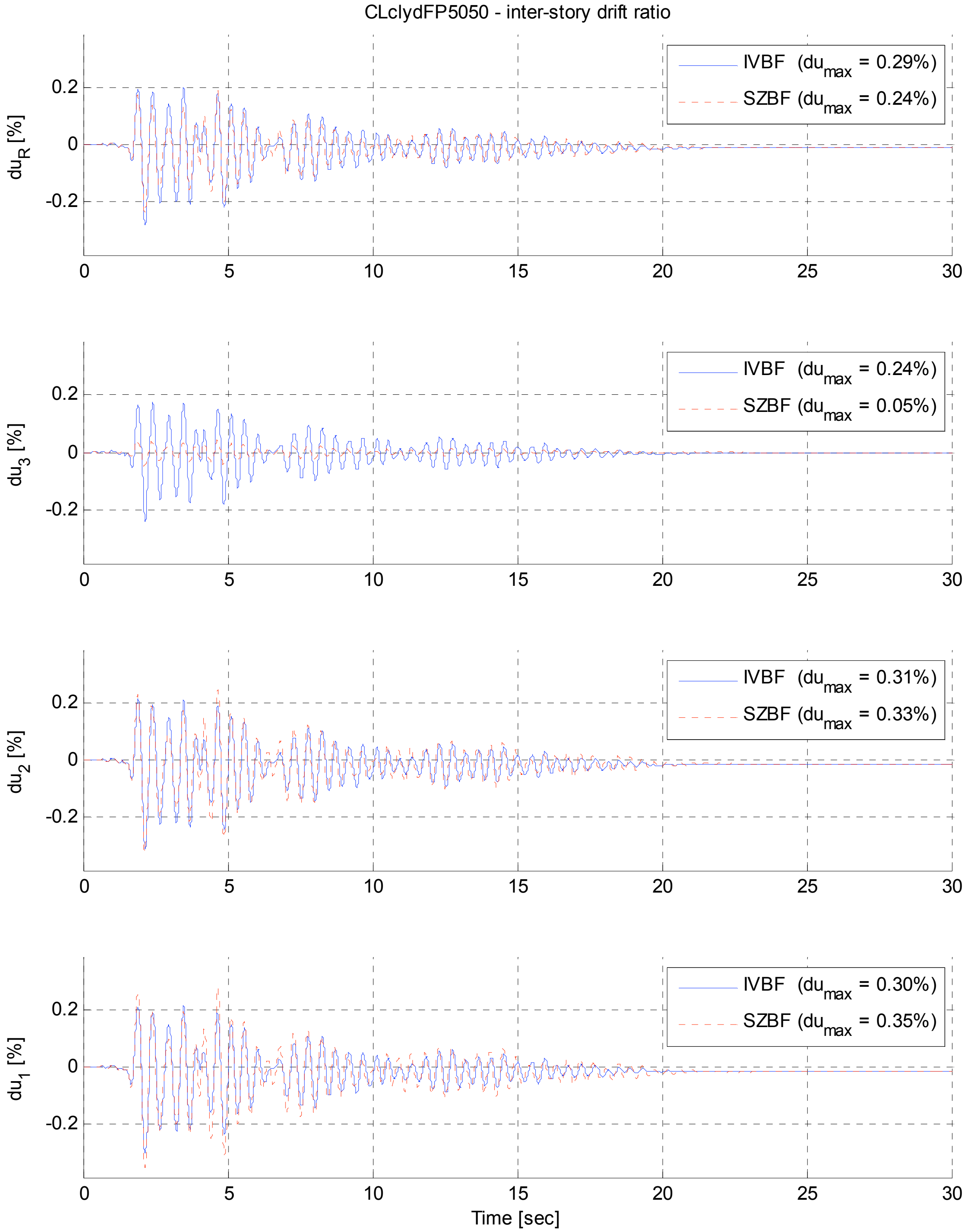

Fig. 6.19 Interstory drift ratio histories recorded during nonlinear dynamic analysis when buildings are subjected to CL_clyd fault parallel motion scaled to match 50% probability of exceedance in 50 years hazard level.

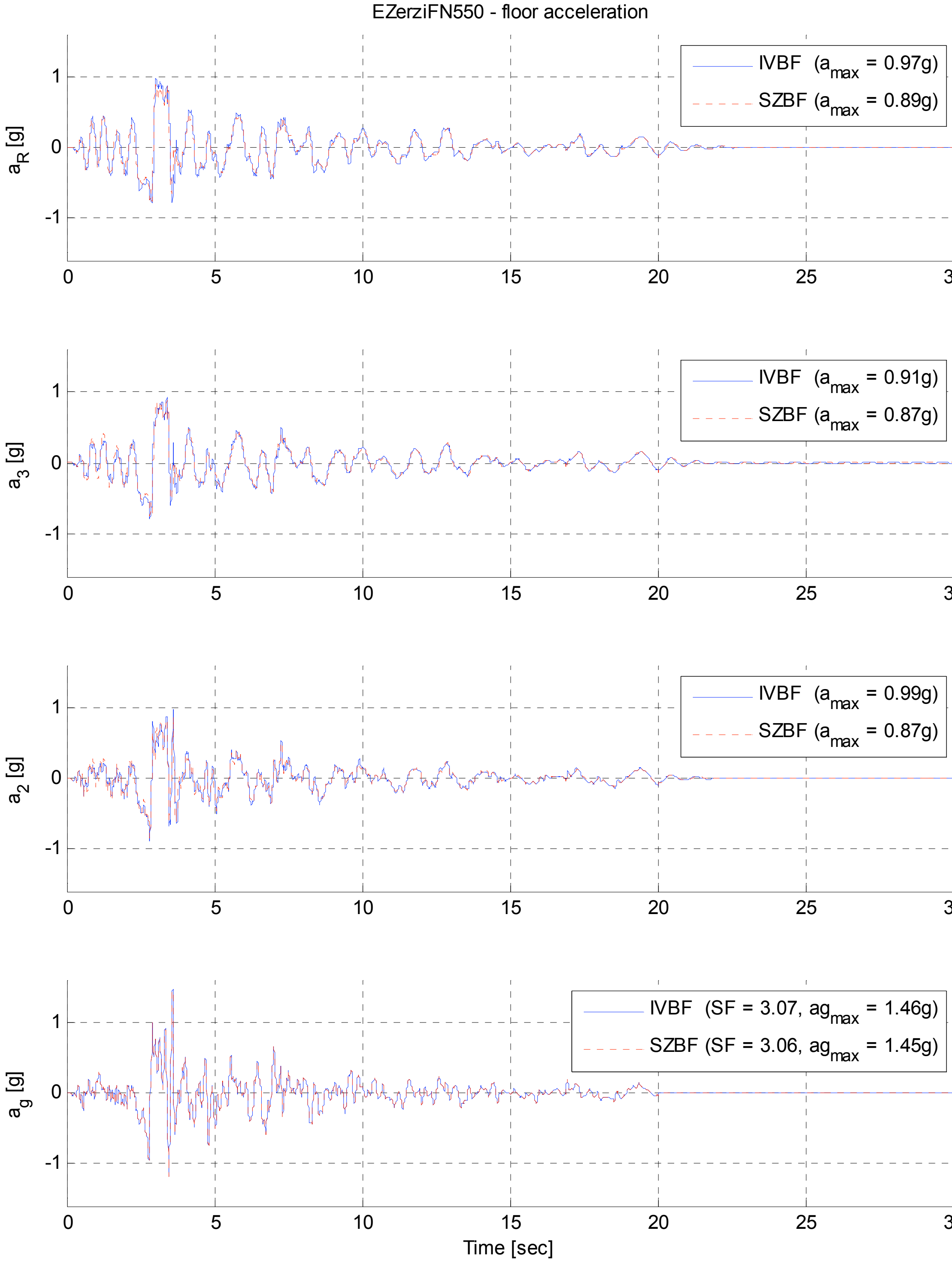

Fig. 6.20 Floor acceleration histories recorded during nonlinear dynamic analysis when buildings are subjected to EZ_erzi fault normal scaled to match 5% probability of exceedance in 50 years hazard level.

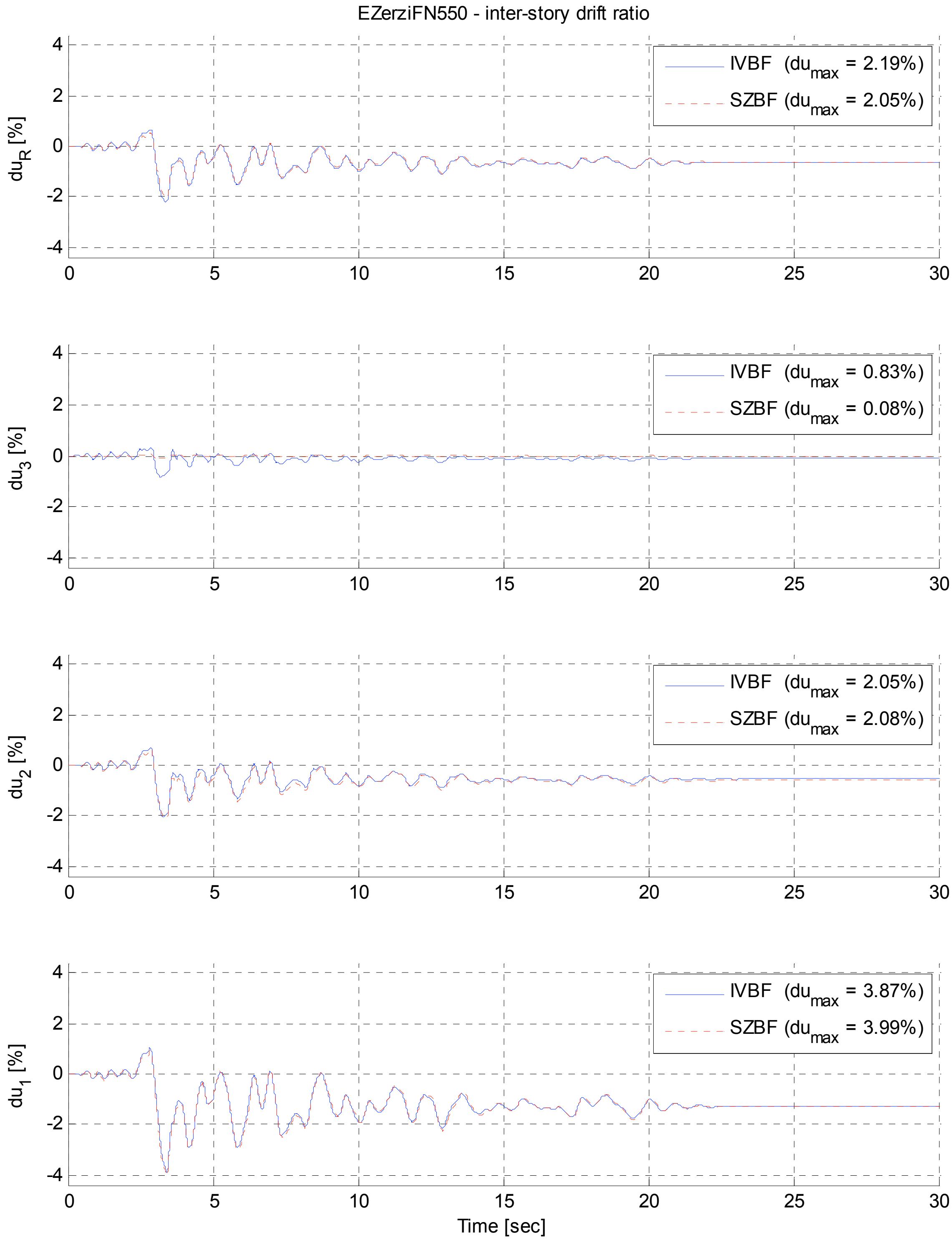

Fig. 6.21 Interstory drift histories recorded during nonlinear dynamic analysis when buildings are subjected to EZ_erzi fault normal scaled to match 5% probability of exceedance in 50 years hazard level.

Table 6.19 Peak response quantity table for inverted-V braced frame at 50% probability of exceedance in 50 years hazard level.

Filename	du_1 (%)	du_2 (%)	du_3 (%)	a_g (g)	a_2 (g)	a_3 (g)	a_R (g)
CLclydFN	0.29	0.29	0.23	0.22	0.25	0.40	0.59
CLclydFP	0.30	0.31	0.24	0.28	0.35	0.47	0.62
CLgil6FN	0.35	0.29	0.20	0.29	0.33	0.43	0.58
CLgil6FP	0.27	0.29	0.22	0.27	0.28	0.41	0.58
PFtembFN	0.26	0.29	0.23	0.27	0.24	0.45	0.65
PFtembFP	0.26	0.30	0.26	0.29	0.33	0.44	0.66
PFcs05FN	0.27	0.27	0.21	0.27	0.29	0.43	0.57
PFcs05FP	0.28	0.31	0.25	0.25	0.30	0.42	0.63
PFcs08FN	0.29	0.28	0.21	0.44	0.54	0.39	0.56
PFcs08FP	0.28	0.29	0.28	0.42	0.52	0.60	0.71
LVfgnrFN	0.25	0.27	0.23	0.26	0.29	0.41	0.59
LVfgnrFP	0.30	0.30	0.21	0.26	0.34	0.51	0.58
LVmgnpFN	0.25	0.33	0.39	0.64	0.78	0.66	0.81
LVmgnpFP	0.42	0.32	0.22	0.43	0.51	0.48	0.58
MHclydFN	0.31	0.32	0.26	0.40	0.36	0.42	0.64
MHclydFP	0.41	0.30	0.20	0.44	0.43	0.48	0.55
MHanddFN	0.30	0.29	0.22	0.21	0.27	0.38	0.58
MHanddFP	0.31	0.31	0.24	0.17	0.24	0.40	0.61
MHhallFN	0.39	0.33	0.22	0.28	0.31	0.41	0.59
MHhallFP	0.33	0.31	0.22	0.17	0.25	0.41	0.58

Table 6.20 Peak response quantity table for inverted-V braced frame at 10% probability of exceedance in 50 years hazard level.

Filename	du_1 (%)	du_2 (%)	du_3 (%)	a_g (g)	a_2 (g)	a_3 (g)	a_R (g)
LPlgpcFN	0.85	0.62	0.26	0.44	0.55	0.65	0.68
LPlgpcFP	1.09	0.87	0.45	0.57	0.57	0.74	0.73
LPsrtgFN	2.20	1.34	0.64	0.90	0.78	0.87	0.84
LPsrtgFP	0.79	0.54	0.38	0.89	0.75	0.70	0.79
LPcorFN	1.61	1.16	0.59	0.73	0.70	0.81	0.92
LPcorFP	1.17	0.98	0.53	0.58	0.55	0.70	0.81
LPgavFN	0.45	0.55	0.40	0.63	0.58	0.68	0.85
LPgavFP	0.86	0.77	0.41	0.73	0.54	0.67	0.84
LPgilbFN	0.81	0.74	0.45	0.59	0.54	0.60	0.84
LPgilbFP	0.79	0.59	0.31	0.57	0.50	0.59	0.69
LPlex1FN	3.62	2.04	0.82	0.69	1.08	0.95	0.98
LPlex1FP	1.11	0.97	0.60	0.84	0.91	0.99	0.94
KBkobjFN	1.98	1.31	0.65	0.58	0.75	0.90	0.90
KBkobjFP	1.04	0.87	0.46	0.52	0.53	0.71	0.88
TOkofuFN	0.48	0.50	0.34	0.64	0.67	0.66	0.84
TOkofuFP	0.72	0.68	0.38	0.94	1.27	0.83	0.93
TOhinoFN	1.99	1.38	0.69	0.67	0.58	0.82	0.86
TOhinoFP	1.33	1.07	0.54	0.60	0.62	0.74	0.86
EZerziFN	2.04	1.21	0.62	1.14	0.70	0.74	0.89
EZerziFP	1.17	1.02	0.65	1.24	0.98	0.90	0.92

Table 6.21 Peak response quantity table for inverted-V braced frame at 5% probability of exceedance in 50 years hazard level.

Filename	du_1 (%)	du_2 (%)	du_3 (%)	a_g (g)	a_2 (g)	a_3 (g)	a_R (g)
LPlgpcFN	1.37	0.95	0.41	0.56	0.66	0.79	0.78
LPlgpcFP	1.42	1.08	0.56	0.73	0.67	0.77	0.78
LPsrtgFN	3.40	2.15	0.88	1.15	1.03	0.94	0.96
LPsrtgFP	1.30	0.93	0.43	1.13	0.88	0.81	0.88
LPcorFN	2.23	1.56	0.83	0.93	0.82	0.91	1.02
LPcorFP	1.57	1.23	0.68	0.74	0.67	0.81	0.89
LPgavFN	0.56	0.67	0.50	0.80	0.65	0.79	0.95
LPgavFP	1.01	0.93	0.53	0.93	0.62	0.72	0.94
LPgilbFN	1.07	0.94	0.58	0.75	0.66	0.69	0.89
LPgilbFP	1.33	0.99	0.50	0.73	0.61	0.74	0.77
LPlex1FN	5.85	3.44	1.21	0.88	1.17	1.20	1.18
LPlex1FP	1.60	1.25	0.75	1.08	1.05	1.15	1.10
KBkobjFN	3.06	2.07	0.92	0.74	1.00	1.10	0.98
KBkobjFP	1.49	1.11	0.60	0.66	0.59	0.80	0.96
TOkofuFN	0.56	0.58	0.40	0.81	0.80	0.75	0.92
TOkofuFP	0.80	0.80	0.47	1.20	1.51	0.92	1.00
TOhinoFN	2.68	1.79	0.85	0.85	0.67	0.89	0.90
TOhinoFP	1.64	1.24	0.64	0.77	0.76	0.82	0.93
EZerziFN	3.87	2.05	0.83	1.46	0.99	0.91	0.97
EZerziFP	1.53	1.20	0.78	1.58	1.17	0.97	1.01

Table 6.22 Peak response quantity table for suspended zipper braced frame at 50% probability of exceedance in 50 years hazard level.

Filename	du_1 (%)	du_2 (%)	du_3 (%)	a_g (g)	a_2 (g)	a_3 (g)	a_R (g)
CLclydFN	0.34	0.30	0.05	0.22	0.27	0.46	0.53
CLclydFP	0.35	0.33	0.05	0.29	0.35	0.48	0.58
CLgil6FN	0.40	0.31	0.04	0.28	0.38	0.49	0.51
CLgil6FP	0.31	0.28	0.04	0.26	0.25	0.46	0.50
PFtembFN	0.31	0.29	0.05	0.22	0.26	0.50	0.58
PFtembFP	0.34	0.32	0.05	0.30	0.33	0.51	0.61
PFcs05FN	0.32	0.28	0.04	0.29	0.35	0.49	0.49
PFcs05FP	0.32	0.30	0.05	0.22	0.29	0.47	0.54
PFcs08FN	0.32	0.28	0.05	0.40	0.36	0.46	0.52
PFcs08FP	0.32	0.30	0.05	0.40	0.50	0.50	0.52
LVfgnrFN	0.30	0.28	0.05	0.24	0.28	0.45	0.51
LVfgnrFP	0.37	0.31	0.05	0.26	0.36	0.49	0.54
LVmgnpFN	0.31	0.36	0.06	0.62	0.48	0.54	0.71
LVmgnpFP	0.42	0.31	0.04	0.46	0.48	0.46	0.50
MHclydFN	0.38	0.33	0.05	0.40	0.40	0.47	0.57
MHclydFP	0.47	0.34	0.04	0.47	0.51	0.52	0.53
MHanddFN	0.36	0.30	0.05	0.24	0.32	0.47	0.53
MHanddFP	0.37	0.32	0.05	0.18	0.28	0.48	0.55
MHhallFN	0.50	0.37	0.05	0.31	0.36	0.51	0.53
MHhallFP	0.39	0.30	0.05	0.20	0.35	0.47	0.51

Table 6.23 Peak response quantity table for suspended zipper braced frame at 10% probability of exceedance in 50 years hazard level.

Filename	du_1 (%)	du_2 (%)	du_3 (%)	a_g (g)	a_2 (g)	a_3 (g)	a_R (g)
LPlgpcFN	1.18	0.77	0.06	0.52	0.68	0.72	0.73
LPlgpcFP	1.67	1.07	0.07	0.71	0.69	0.79	0.81
LPsrtgFN	2.48	1.43	0.07	0.92	0.91	0.82	0.83
LPsrtgFP	1.22	0.79	0.07	1.07	0.87	0.76	0.77
LPcorFN	1.94	1.27	0.08	0.77	0.74	0.86	0.83
LPcorFP	1.25	0.86	0.07	0.56	0.59	0.75	0.73
LPgavFN	0.51	0.47	0.06	0.51	0.62	0.64	0.74
LPgavFP	1.09	0.81	0.07	0.83	0.70	0.79	0.76
LPgilbFN	1.07	0.79	0.07	0.65	0.57	0.74	0.84
LPgilbFP	0.71	0.57	0.06	0.48	0.42	0.62	0.65
LPlex1FN	4.04	2.26	0.08	0.71	0.94	0.97	0.98
LPlex1FP	1.39	0.95	0.08	0.85	0.83	0.92	1.07
KBkobjFN	2.10	1.29	0.08	0.59	0.78	0.86	0.89
KBkobjFP	1.21	0.82	0.07	0.52	0.59	0.75	0.79
TOkofuFN	0.60	0.47	0.06	0.63	0.67	0.71	0.75
TOkofuFP	0.91	0.67	0.06	1.00	1.24	0.84	0.79
TOhinoFN	2.33	1.44	0.08	0.72	0.79	0.77	0.80
TOhinoFP	1.60	1.11	0.07	0.65	0.67	0.72	0.79
EZerziFN	2.16	1.11	0.07	1.14	0.68	0.77	0.81
EZerziFP	1.45	1.17	0.08	1.32	0.99	0.93	0.95

Table 6.24 Peak response quantity table for suspended zipper braced frame at 5% probability of exceedance in 50 years hazard level.

Filename	du_1 (%)	du_2 (%)	du_3 (%)	a_g (g)	a_2 (g)	a_3 (g)	a_R (g)
LPlgpcFN	1.84	1.21	0.08	0.66	0.84	0.87	0.90
LPlgpcFP	1.87	1.24	0.08	0.91	0.85	0.82	0.83
LPsrtgFN	3.78	2.36	0.09	1.17	1.03	0.92	0.90
LPsrtgFP	2.21	1.32	0.08	1.37	1.13	0.88	0.88
LPcorFN	2.59	1.76	0.09	0.99	0.80	0.92	0.90
LPcorFP	1.77	1.17	0.08	0.72	0.66	0.86	0.84
LPgavFN	0.61	0.57	0.07	0.66	0.75	0.71	0.89
LPgavFP	1.33	1.00	0.08	1.06	0.82	0.89	0.82
LPgilbFN	1.49	1.01	0.08	0.83	0.65	0.81	0.93
LPgilbFP	0.88	0.61	0.06	0.61	0.49	0.61	0.64
LPlex1FN	6.35	3.97	0.10	0.91	1.28	1.14	1.14
LPlex1FP	1.93	1.26	0.08	1.09	1.00	1.03	1.17
KBkobjFN	3.32	2.19	0.09	0.75	1.10	0.96	1.02
KBkobjFP	1.78	1.10	0.08	0.67	0.69	0.84	0.87
TOkofuFN	0.72	0.57	0.06	0.81	0.79	0.81	0.84
TOkofuFP	1.05	0.79	0.07	1.28	1.52	0.94	0.91
TOhinoFN	3.07	1.91	0.09	0.91	0.87	0.82	0.87
TOhinoFP	1.98	1.35	0.08	0.83	0.79	0.83	0.85
EZerziFN	3.99	2.08	0.08	1.45	0.87	0.87	0.89
EZerziFP	1.93	1.55	0.09	1.69	1.17	1.02	1.06

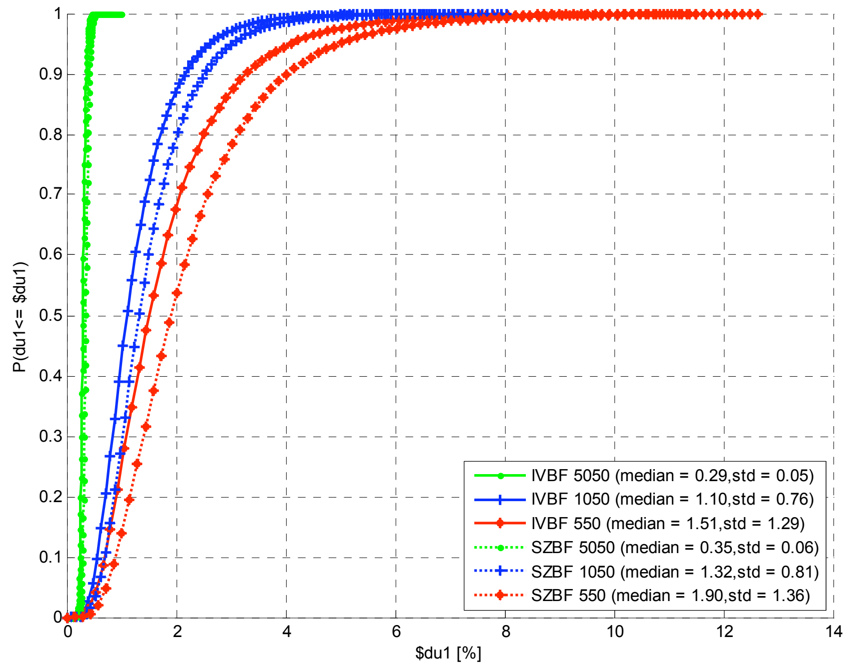

Fig. 6.22 CDF of peak first-story interstory drift ratios.

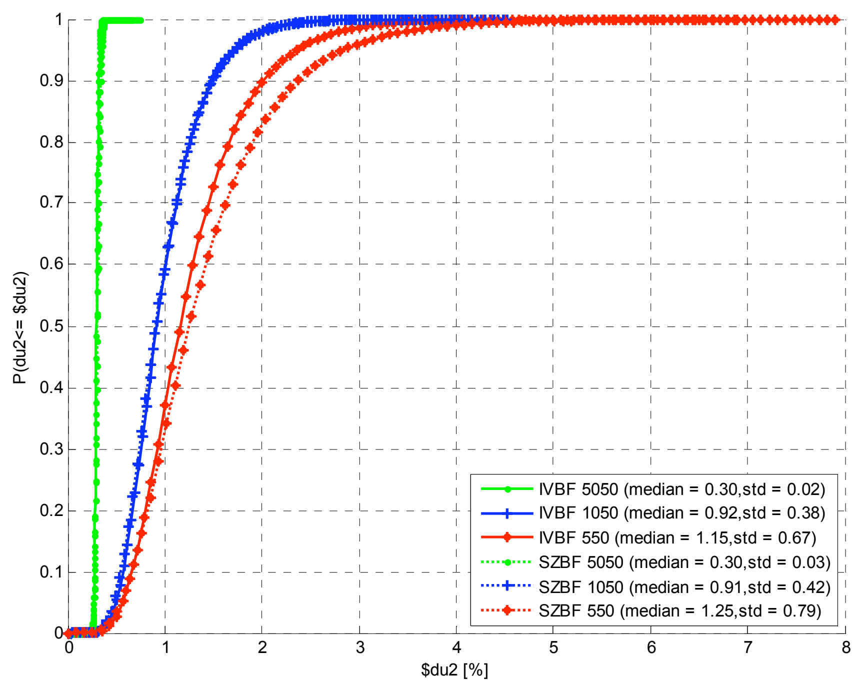

Fig. 6.23 CDF of peak second-story interstory drift ratios.

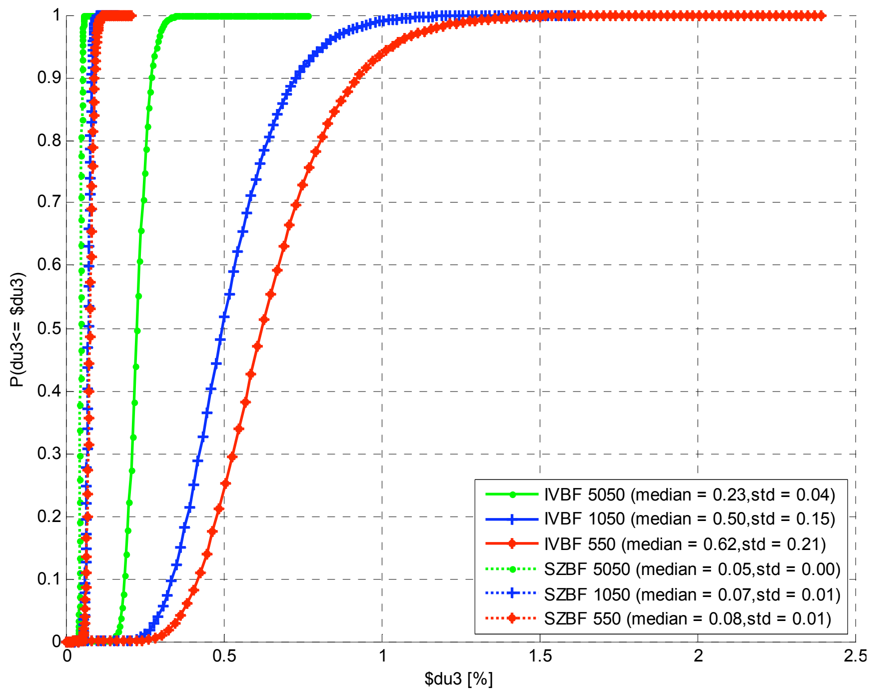

Fig. 6.24 CDF of peak third-story interstory drift ratios.

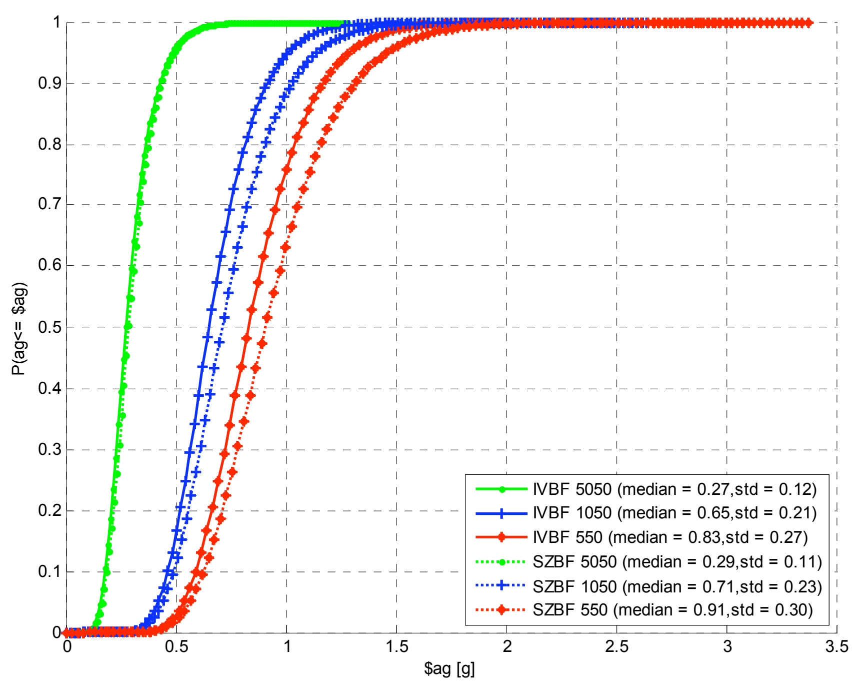

Fig. 6.25 CDF of peak ground accelerations.

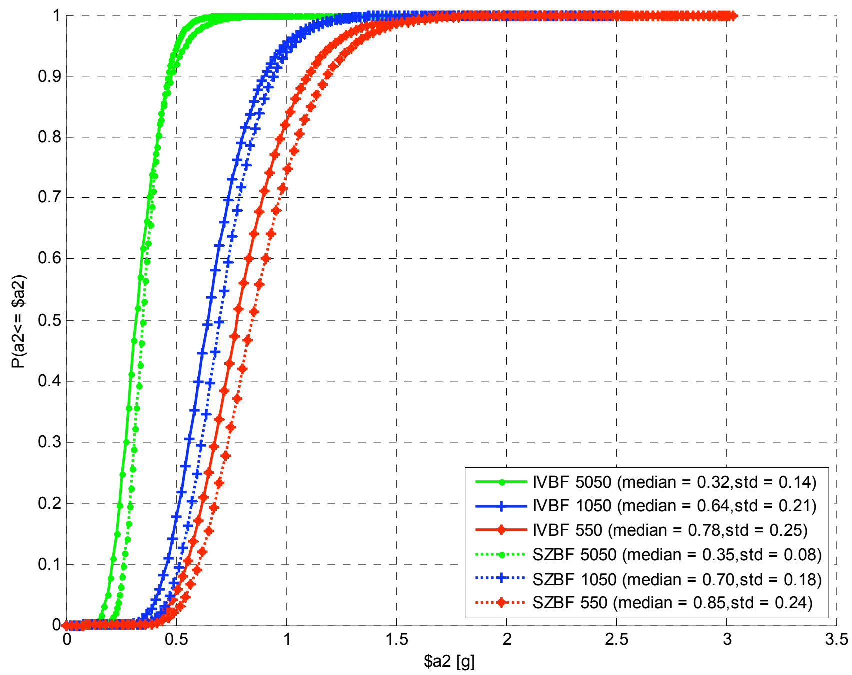

Fig. 6.26 CDF of peak second-floor accelerations.

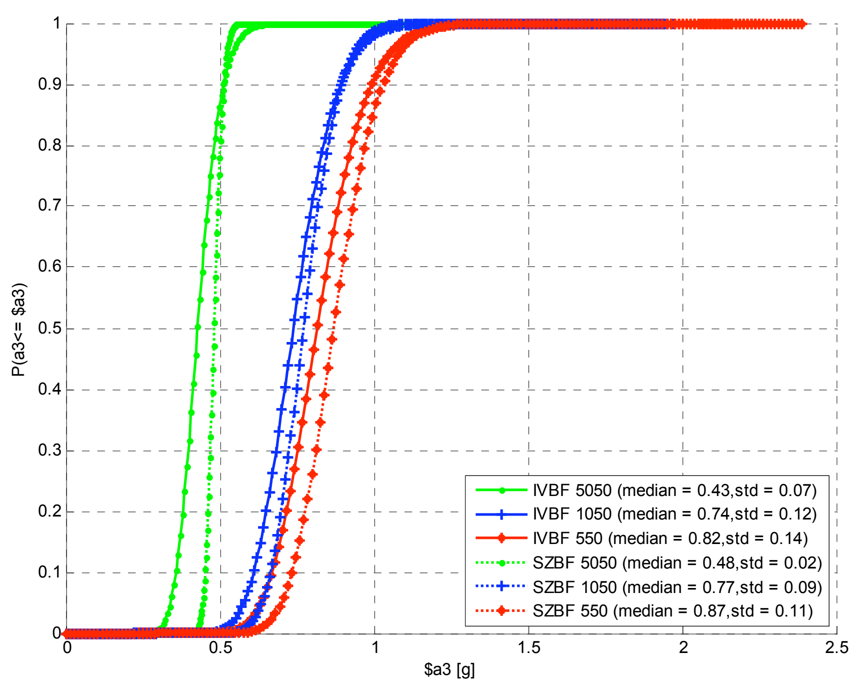

Fig. 6.27 CDF of peak third-floor accelerations.

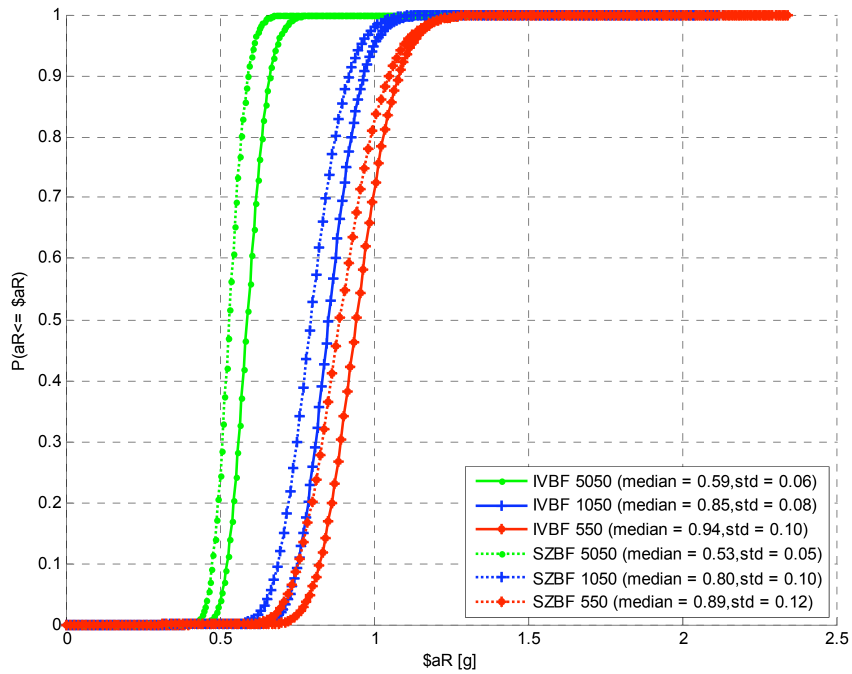

Fig. 6.28 CDF of peak roof accelerations.

To compare the system response among the different hazard levels, the median peak interstory drift ratios and floor accelerations are plotted in Figure 6.29 and Figure 6.30, respectively. At 50% probability of exceedance in 50 years hazard level, both frames show an increase in floor acceleration as the story number increases. As the shaking intensity increases to 5% probability of exceedance in 50 years hazard level, the median peak floor acceleration were reduced at the higher stories. This is because the story stiffness was reduced when the lower-story braces buckled. Such brace buckling mechanism prevented the floor acceleration from being amplified significantly in the higher stories. In this regard, the median peak floor accelerations for both frames were under 1.0 g for all hazard levels considered. Based on the median peak interstory drift ratio presented in Figure 6.29, both frames show some distribution of nonlinear response to the higher stories, but the advantage of more uniform distribution of nonlinear response is not demonstrated in this idealized building.

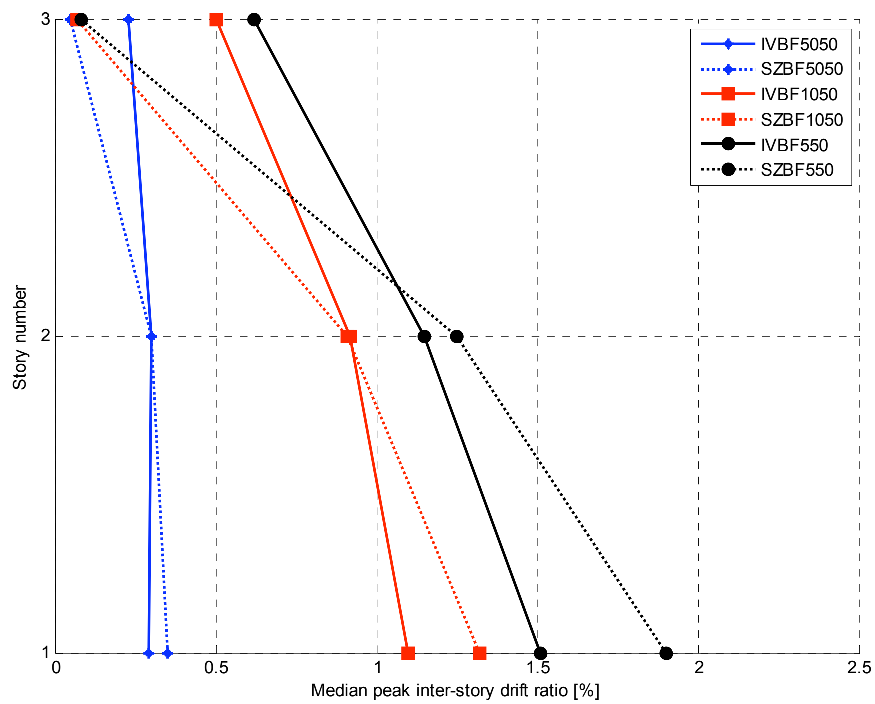

Fig. 6.29 Median peak interstory drift ratios.

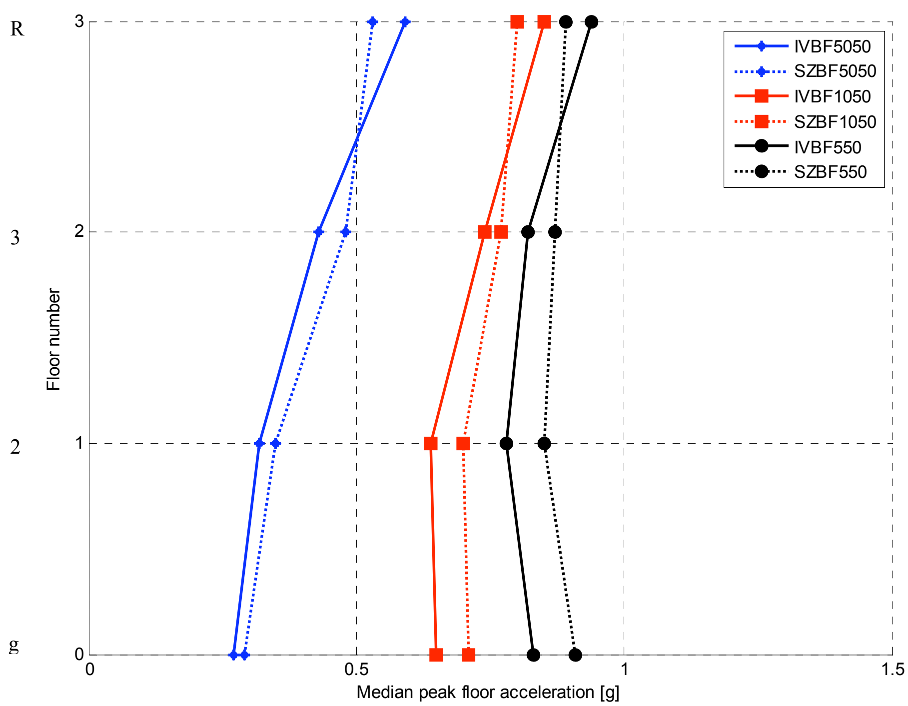

Fig. 6.30 Median peak floor accelerations.

6.5 COST SIMULATION

The repair cost simulation was conducted using the methodology described in Chapter 5 and the quantity and cost data presented in Section 6.1. The discrete cumulative distribution function of the total repair costs for the suspended zipper braced frame and the inverted-V braced frame for the three hazard levels considered are shown in Figure 6.31.

The results of the 50% probability of exceedance in 50 years hazard level indicate both frames have comparable median total repair costs. However, the inverted-V braced frame has a higher dispersion and, also, a higher maximum total repair cost.

The results of the 10% and 5% probability of exceedance in 50 years hazard levels indicate that the suspended zipper braced frame has lower total repair cost than the inverted-V braced frame. In particular, the median total repair cost for the suspended zipper braced frame is \$2.1 million dollars for both hazard levels, while the median total repair costs for the inverted-V braced frame are \$2.5 million dollars and \$2.75 million dollars, for the 10% and 5% probability of exceedance in 50 years hazard levels, respectively.

If a constant dollar repair cost amount is used as the decision variable, the probability of total repair cost being less than a certain threshold repair cost can be identified from distributions shown in Figure 6.31. For example, if a building owner is interested in the probability of total repair cost less than or equal to \$2 million dollars, the computed results indicate this nonexceedance probability at the 10% probability of exceedance in 50 years hazard level is 0.44 for the suspended zipper braced frame and only 0.09 for the inverted-V braced frame. Similarly, at the 5% probability of exceedance in 50 years hazard level, the probability of not exceeding the \$2 million dollars repair cost is 0.22 for the suspended zipper braced frame and only 0.04 for the inverted-V braced frame. This comparison clearly shows that the inverted-V braced frame is more vulnerable than the suspended zipper braced frame under the same seismic hazard scenarios.

A de-aggregation of the total repair cost contributions from each of the performance group is shown in Figures 6.32–Figure 6.37. For 50% probability of exceedance in 50 year hazard level (Fig. 6.32 and Fig. 6.33 for the inverted-V braced frame and the suspended zipper braced frames, respectively), the results indicate that most of the repair cost is concentrated in the structural component performance groups SH12, SH23, and SH3R. This is because the idealized model is a regular office building, where most of the acceleration-sensitive performance groups have significant tolerance for the acceleration demand and the associated repair items are relatively inexpensive (see Fig. 6.9 and Table 6.14). For example, if the peak floor acceleration reached 1.0 g, the items (in PG CONT1, CONT2, and CONT3) that are most likely to be damaged are office paper, books, office equipment and loose furniture. The peak floor acceleration has to reach 3.5 g to pick up the more expansive contents such as conventional office and computer center. On the other hand, because the braced frame has low tolerance to interstory drift (see Fig. 6.5), as soon as the interstory drift exceeds 0.3%, the lateral-load-resisting system performance groups (SH12, SH23, and SH3R) are considered damaged and need to be replaced.

Because the suspended zipper braced frame had negligible third-story interstory drift ratio, performance group SH3R does not contribute significantly to the total repair cost of the suspended zipper braced frame. Such behavior is also observed in the discrete CDF of the total repair cost (Fig. 6.31). The principal contributions to the total repair cost of the suspended zipper braced frame are originated from the repair cost of performance groups SH12 and SH23. There are three major repair cost states for the suspended zipper braced frame, representing the repair cost associated with "none," "one," or "two" of these structural component performance groups (SH12 and SH23) being damaged. On the other hand, the principal contributions to the total repair cost of the inverted-V braced frame come from the repair cost for "none," "one," "two," or "three" structural component performance groups (SH12, SH23, and SH3R) being damaged. Because the total repair cost contributed from performance group SH3R is less than 5 percent for the inverted-V braced frame at the 50% probability of exceedance in 50 years hazard level, the total repair cost distribution at this hazard level is very similar for these two frames.

The de-aggregation of total repair cost contributions at 10% probability of exceedance in 50 years hazard level are shown in Figure 6.34 and Figure 6.35 for the inverted-V braced frame and the suspended zipper braced frame, respectively. The results indicate that the total repair cost is concentrated in the structural component performance groups and the interior nonstructural interstory drift sensitive performance groups INTD12, INTD23, and INTD3R. Such behavior is expected because the peak floor acceleration is not very large compared with accelerations required to trigger significant repair actions in acceleration-sensitive performance groups.

The inverted-V braced and the suspended zipper braced frames have similar repair cost contributions from structural component and nonstructural drift-sensitive performance groups.

The only exception is that performance groups SH3R and INTD3R of the suspended zipper braced frame do not contribute to the total repair cost because the interstory drift demand at the third story of this frame is relatively small. Hence, the total repair cost for the suspended zipper braced frame is less than for the inverted-V braced frame.

The de-aggregation of total repair cost contribution at 5% probability of exceedance in 50 years hazard level are shown in Figure 6.36 and Figure 6.37 for the inverted-V braced frame and suspended zipper braced frame, respectively. Similar to the 10% probability of exceedance in 50 years hazard level, most of the repair cost is contributed by the structural component performance groups and the interior nonstructural drift-sensitive performance groups. Because the structural component performance groups have only two damage states (damage or no damage), no additional damage state can occur and no additional repair cost can be accumulated from the structural component performance groups when the hazard level increases from 10% probability of exceedance in 50 years to 5% probability of exceedance in 50 years. This is why the median total repair cost for the suspended zipper braced frame is very similar for these two hazard levels. On the other hand, the exterior enclosure performance groups EXTD12, EXTD23, and EXTD3R have multiple damage states: thus, additional damage can be detected in these performance groups as the hazard level is increased from 10% probability of exceedance in 50 years to 5% probability of exceedance in 50 years. Such behavior is also observed in the discrete CDF shown in Figure 6.31.

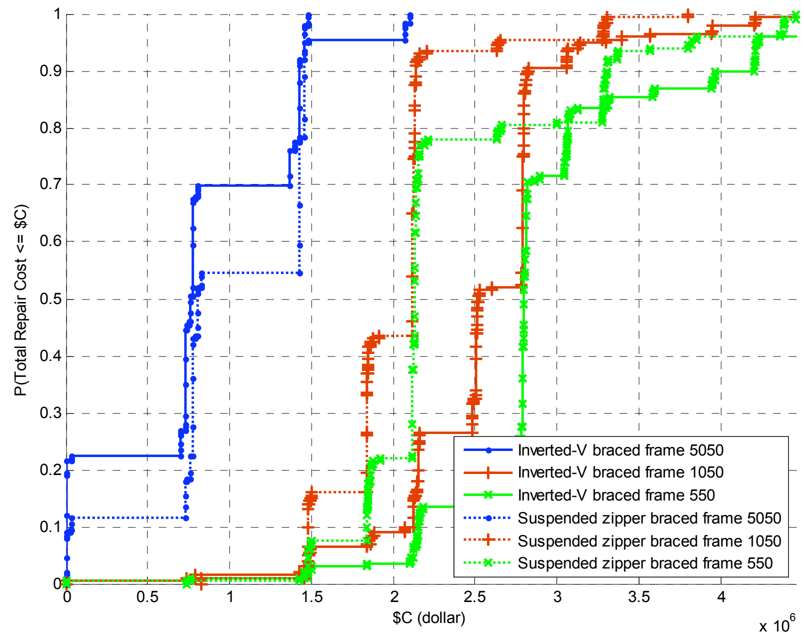

Fig. 6.31 Discrete CDF of repair cost distribution.

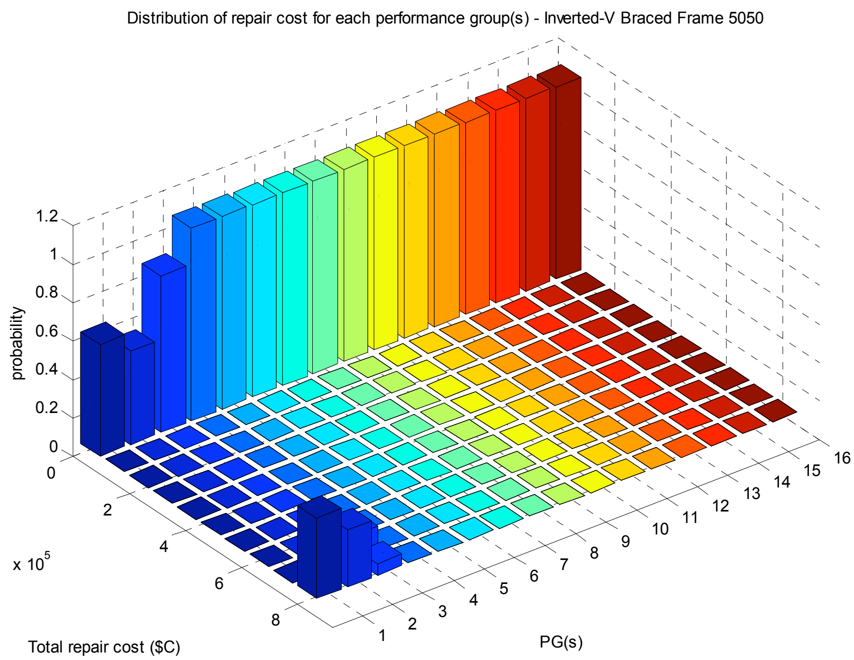

Fig. 6.32 De-aggregation of total repair cost for inverted-V braced frame at 50% probability of exceedance in 50 years hazard level.

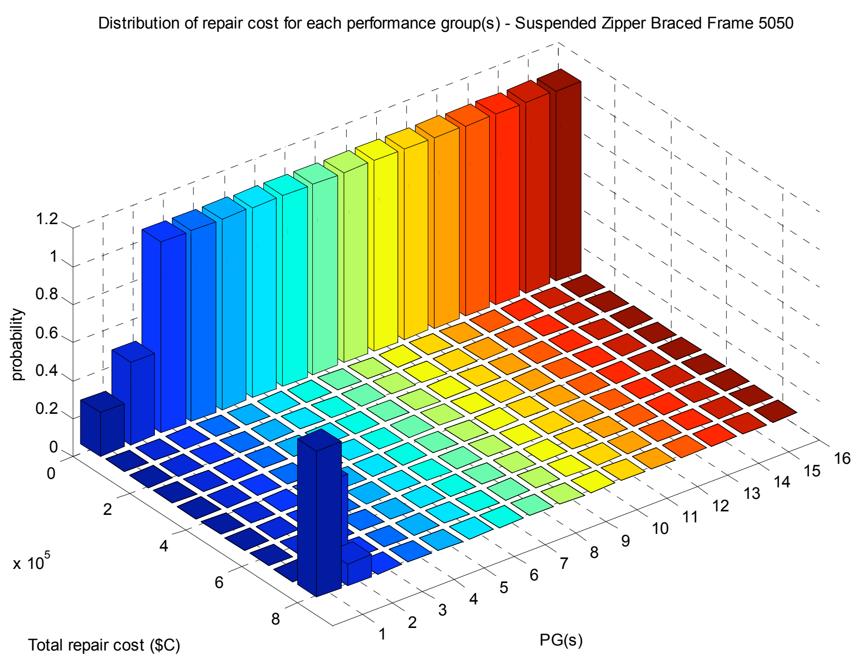

Fig. 6.33 De-aggregation of the total repair cost for the suspend zipper braced frame at the 50% probability of exceedance in 50 years hazard level.

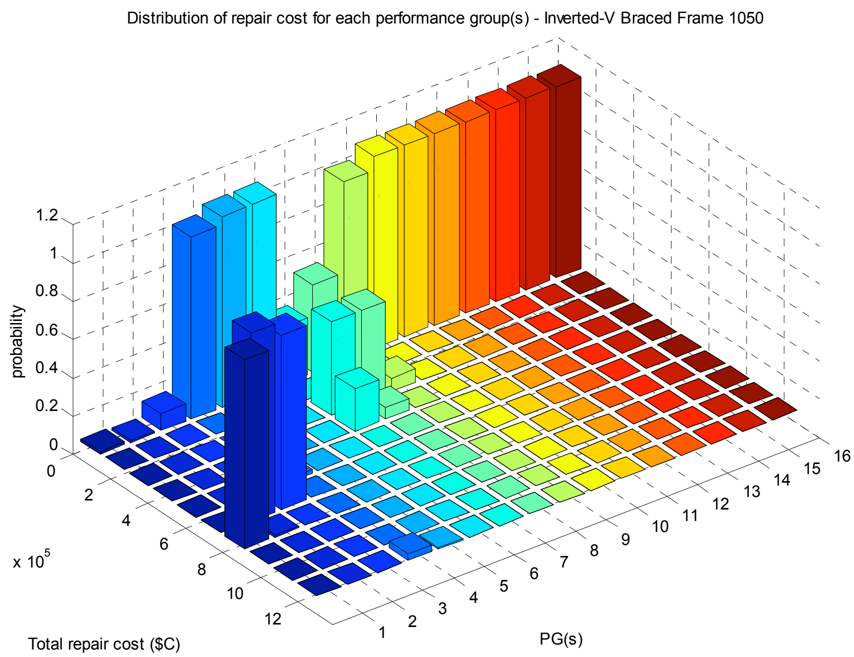

Fig. 6.34 De-aggregation of total repair cost for inverted-V braced frame at 10% probability of exceedance in 50 years hazard level.

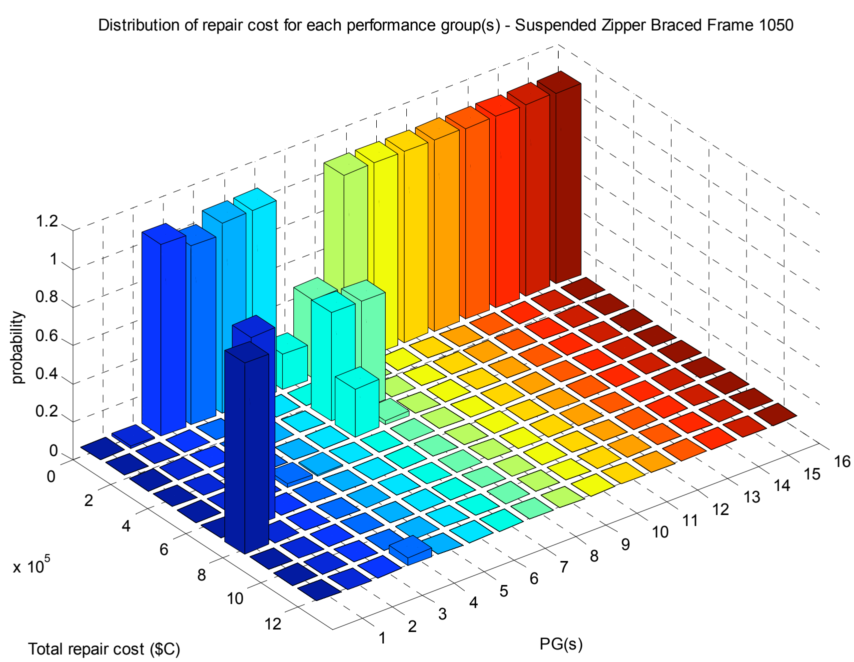

Fig. 6.35 De-aggregation of total repair cost for the suspended zipper braced frame at 10% probability of exceedance in 50 years hazard level.

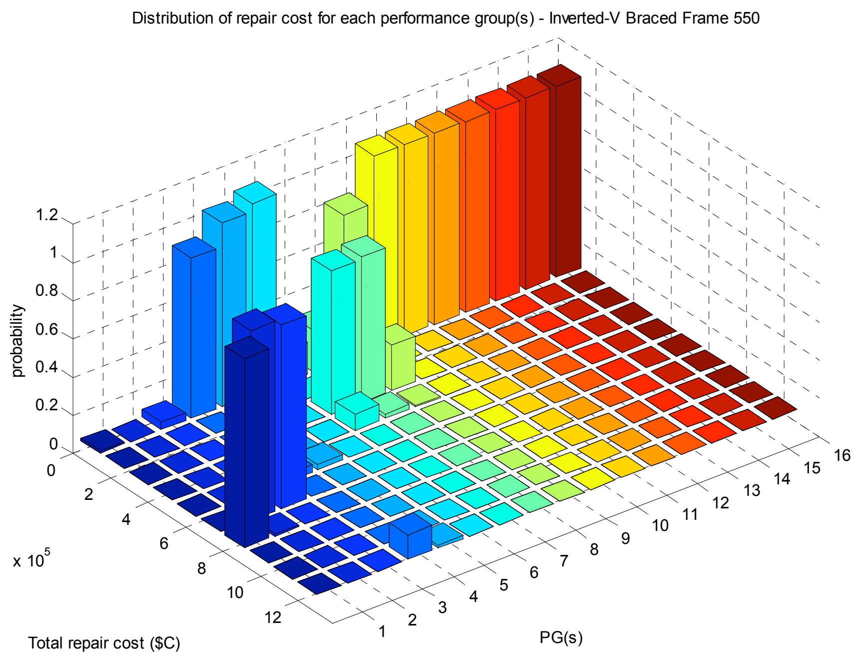

Fig. 6.36 De-aggregation of total repair cost for inverted-V braced frame at 5% probability of exceedance in 50 years hazard level.

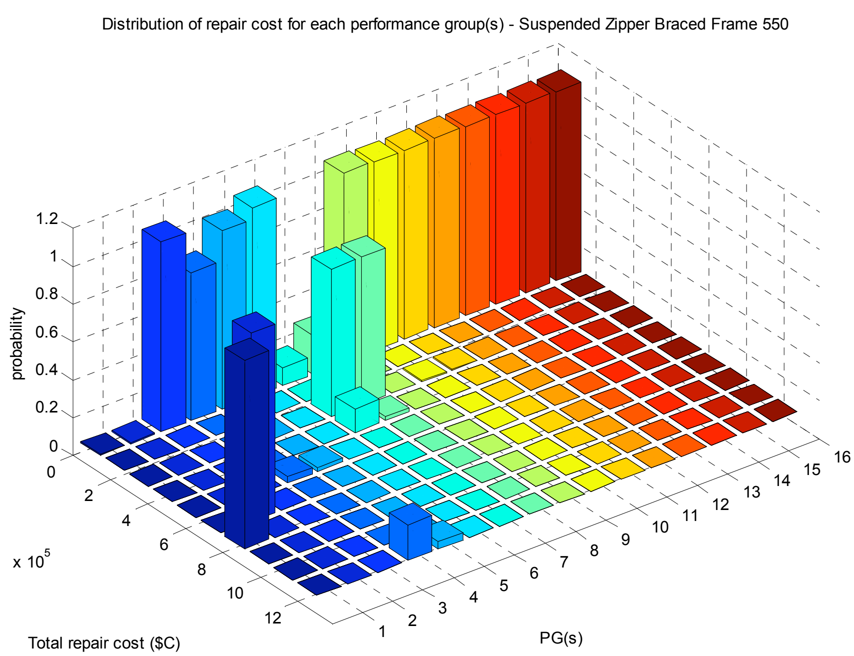

Fig. 6.37 De-aggregation of the total repair cost for the suspended zipper braced frame at 5% probability of exceedance in 50 years hazard level.

6.6 SUMMARY AND CONCLUSIONS

The behavior of the inverted-V braced frame has been studied extensively by research in the last decade. The inverted-V braced frame is very effective in providing lateral stiffness to limit interstory drifts. However, under large lateral loading, the braces are designed to buckle, thereby creating an unbalanced vertical force at the intersection of the braces and the floor beam. To directly deal with such problem, alternative braced framing systems have been proposed. One system is the inverted-V braced frame in which the floor beams are designed to have sufficient strength to resist the unbalanced force. This system can require relatively large floor beams, reducing system economy. Another option is the suspended zipper braced frame. The suspended zipper braced frame is designed to have a zipper column attached to the brace intersections with the goal to transfer the unbalanced vertical force to the upper stories of the structure when the lower-story braces buckle. To transfer the unbalanced force collected at the top of the frame to the foundation, the top-story braces are designed to remain elastic under the maximum considered earthquake loading. In doing so, the member sizes of the top-story braces are typically larger. Nevertheless, because the top-story braces and the zipper columns provide a continuous support at the mid span of the beams, the beam member sizes are smaller, saving material and reducing cost. Based on the self-weight comparison for the idealized model studied here, the suspended zipper braced frame weighs 25% less than the inverted-V braced frame.

The performance-based earthquake engineering methodology implementation presented in Chapter 5 was used to compare the system performance of a prototype suspended zipper braced frame and an equivalent inverted-V braced frame with beams designed to resist the unbalanced brace force. An idealized model, located in downtown Berkeley, California, was designed and modeled using the OpenSees software and the brace model presented in Chapter 2. Suites of ground motions representing multiple hazard levels at the site were selected from the U.C. Berkeley Seismic Guidelines (UCB 2003) and used to conduct nonlinear dynamic analyses. The results of the nonlinear dynamic analyses indicate that the suspended zipper braced frame has higher peak demand, as measured by the interstory drift and floor acceleration, at the lower stories, but lower peak demand at the top story.

Based on such peak demand distribution, the suspended zipper braced frame is expected to have higher total repair cost than the inverted-V braced frame. However, because the total repair costs are contributed mostly by the drift-sensitive performance groups (the idealized model is a regular office building with few acceleration-sensitive equipment items) and both frames reach the highest-damage state in their structural component performance groups, no additional cost is contributed by the somewhat higher demand observed in the lower stories of the suspended zipper braced frame. On the other hand, because the third-story interstory drift ratio for the suspended zipper braced frame is always very small, performance groups at this story do not contribute to the total repair cost. Therefore, the total repair cost for the suspended zipper braced frame tends to be less than that of the inverted-V braced frame. Such information can be observed from the de-aggregation of the total repair cost computed using the performance-based earthquake engineering methodology presented in Chapter 5. The probabilistic performance evaluation accounts for the ground motion, demand model, damage assessment, and repair cost uncertainties to give the stakeholders a quantitative probabilistic description of the total repair cost for both systems under scenario earthquakes. This approach provides the information needed to demonstrate the performance advantage of using the suspended zipper braced frame.

7 Summary and Conclusions

7.1 INTRODUCTION

There are three objectives of the study reported herein. The first objective is to develop and implement nonlinear modeling techniques capable of representing the nonlinear dynamic response of buildings using the suspended zipper braced frame. The second objective is to demonstrate the use of hybrid simulation testing of complex structural framing systems using a novel framework developed under OpenSees (Schellenberg 2008). The third objective is to demonstrate the use of a newly implemented performance-based assessment methodology to evaluate the system performance of complex building systems, with a specific application to a building designed using the suspended zipper braced frame.

To accomplish these objectives, a quasi-static test was conducted and presented in Chapter 2 to study the force-deformation hysteresis behavior of an inverted-V braced subassembly. The results of the quasi-static test were used to calibrate an analytical brace element capable of simulating general hysteresis behavior of steel braces that buckle out of plane. With the calibrated analytical buckling element, the response of the suspended zipper braced frame was investigated using an analytical model in Chapter 3 and verified using the hybrid simulation test presented in Chapter 4. The results of the analytical simulation and hybrid simulation test demonstrate that the system has many redundancies and that the intended force redistribution in the system can occur under design earthquake loading. To further demonstrate the performance of the suspended zipper braced frame, a new methodology was developed in Chapter 5 to consistently account for the earthquake uncertainties and to produce performance metrics suitable for risk management decision making. Chapter 6 uses the methodology presented in Chapter 5 to compare the system performance of the suspended zipper braced frame with the inverted-V braced frame. The results of the performance evaluation provide information to demonstrate the relative merits of using the suspended zipper braced frame in a specific application.

7.2 RESPONSE OF SUSPENDED ZIPPER BRACED FRAME

The system response of the suspended zipper braced frame under monotonic static loading and dynamic loading was analyzed using OpenSees. The results demonstrate that the zipper columns enable redistribution of force unbalance caused by brace buckling. Although the intended force redistribution in the system is occurring, the results also indicate that the structure, under selected ground motions, experiences relatively large interstory drifts and develops permanent residual drift at the first and second stories. Furthermore, the large unbalanced vertical force, which is transferred to the third-story braces, acts as a compression force on the columns, resulting in accelerated formation of plastic hinges at the base of the first-story columns. Thus, column base connections needed to be designed to ensure the resulting reactions can be transferred to the foundation. It should be noted that even though the two-dimensional analytical model (Fig. 2.22) reproduces the force-deformation hysteresis behavior of the braces very well, it does not fully account for the out-of-plane buckling of the braces, which can cause the beam to rotate out of plane. Thus, the beam must be adequately braced to ensure that the intended force redistribution occurs.

7.3 PERFORMANCE OF HYBRID SIMULATION TEST

The hybrid simulation test of the suspended zipper braced frame uses the displacement control continuous testing algorithm, where the nonlinear differential equation governing the system dynamics is solved using the Newmark time-step integration with Newton-Raphson initial stiffness iteration. To implement the hybrid simulation test, three OpenSees experimental element classes (Schellenberg 2008) and new hybrid simulation architecture have been implemented. The predictor-corrector algorithm used in this test implementation has been modified to predict the target displacement with a zero-order polynomial and to correct to the target displacement with a first-order polynomial within each step, thus avoiding instabilities caused by subspace iterations performed by the integrator. The experimental results indicate that this predictor-corrector algorithm works well.

The behavior of the inverted-V braced subassembly in the hybrid simulation test was very similar to the behavior observed in the quasi-static test presented in Chapter 2. The braces formed plastic hinges at the gusset plates and buckled out of plane and out of phase. In both cases, the maximum out-of-plane displacement at the center of the brace reached 5 percent of the brace length. Brace buckling created large unbalanced vertical and out-of-plane forces at the intersection of the braces. These forces were equilibrated by the zipper columns and transferred to the upper stories of the suspended zipper braced frame, as intended by design. Last, both braces in the inverted-V braced subassemblies suffered some inelastic damage and developed significant residual displacement at the center of the braces.

An analytical model was constructed to verify the results obtained from the hybrid simulation test. The excellent agreement between the analytical simulation and hybrid simulation indicates that the analytical brace model calibrated from the quasi-static test can be used effectively in predicting the system behavior. In addition, the test technique allows tracing the response at each time-step and, thus, provides a clear representation of the force redistribution in the system. Hence, the hybrid simulation test method is an efficient way to investigate the complex force redistribution in the suspended zipper braced frame structure.

7.4 PERFORMANCE EVALUATION OF SUSPENDED ZIPPER BRACED FRAME

A rigorous and consistent performance assessment methodology has been pursued and presented. The performance methodology accounts for the seismic hazard, model, damage, and cost uncertainties to compute a quantitative description of the total repair cost of the structural system under scenario earthquakes.

To evaluate the performance of the suspended zipper braced frame using this methodology, an idealized building located at downtown Berkeley, California, was designed and modeled. Both a suspended zipper braced framing system and an inverted-V braced framing system (with beams designed to resist the unbalanced vertical force associated with brace buckling) were designed and analyzed. Key structural and nonstructural components of the building were identified and separated into performance groups. Sets of fragility functions were used to define the damage state of each performance group (Yang et al. 2006). With ground motions selected from the U.C. Berkeley seismic guidelines (UCB 2003), a series of nonlinear dynamic analysis were analyzed using the validated analytical model presented in Chapters 3 and 4. Peak engineering demand parameters were identified and used in the performance evaluation of the suspended zipper braced frame.

The results of the performance evaluation for the specific building system investigated indicate that the suspended zipper braced frame requires 25% less material than the inverted-V braced frame. Because repair costs in this building were dominated by drift-sensitive structural components, and because the suspended zipper braced frame had a capacity-protected upper story (where the zipper forces were resolved), the suspended zipper braced frame had a lower repair cost than the inverted-V braced frame.

The performance assessment methodology provides consistent steps for repair cost modeling and can be extended to other structural types and performance measures.

7.5 FUTURE WORK

The focus of this study is on developing and demonstrating modeling techniques for seismic analysis of a suspended zipper braced frame, on developing and implementing a hybrid simulation testing method, and on use of a performance-based assessment methodology to evaluate the system performance of complex building systems. While the study has been successful in its objectives to study these issues, several research questions remain unanswered.

1. The analytical brace model presented in Chapter 2 is the basis of the analytical simulations presented in this study. This model is intended for steel HSS braces that buckle out of plane. However, it has been verified using results from only two experimental tests. A more rigorous systematic parameter study should be conducted analytically and experimentally to verify the response of the proposed analytical brace model. Furthermore, modeling of in-plane buckling of steel HSS braces and modeling of braces made using other typical steel sections should be done to form a complete brace model portfolio. Finally, realistic models of brace boundary conditions, including gusset plate deformation and lateral-torsional deformation of beams and columns of the frame should be conceptualized, implemented, and validated. Such complete analytical models of braced frames would be useful for further analytical and hybrid simulations of complex structural systems under earthquake loads and comparative studies of the seismic behavior of different framing systems.
2. The hybrid simulation test presented in Chapter 4 should be extended to utilize several experimental substructures in the same hybrid simulation model. This is simply an extension of the well-known substructuring testing technique. However, the testing space

in a single laboratory is usually limited. While geographically distributed hybrid simulation involving several laboratories has been tried before (Kwon et al. 2005; Mosqueda 2003; Mosqueda et al. 2004), additional work is needed to improve the reliability and shorten the duration of such tests. One application of such multi-substructure hybrid simulation is an evaluation of the response of the structure using a model that includes an inverted-V braced subassembly, gravity columns, and a nonstructural element such as a partition wall. The results of this simulation would provide an experimental validation point for the analytical performance assessment methodology.

3. The performance assessment methodology presented in Chapter 5 provides a consistent manner for engineers to evaluate the repair cost of a building after select scenario earthquakes. Additional research should be done to improve the methodology and to provide better hazard and fragility data used for performance evaluation. Methodology improvements should focus on accurate assessment and representation of correlations among damage states, repair methods, and repair quantities for the structure, and on extensions to account for other performance metrics such as downtime and casualties. A sensitivity study evaluating the effects of ground motion selection and scaling, selection and correlation among demand and damage measures, and choice of fragility models on the results of performance evaluation is also needed. Considering the advances in sensor technology, and the likely ubiquity of sensors and plethora of sensor-acquired data, a fundamental investigation on how to utilize such data within a probability-based performance evaluation framework should be done. Finally, and most importantly, more research is needed to improve the fragility relations for structural and nonstructural components and systems commonly found in buildings today. Such data, if it existed, would be universally applicable in a wide range of seismic performance studies regardless of the performance evaluation methodology used. Coupled with the performance methodology developed in this study, improved fragility relations could be used to, for example, to compare the performance of different structural systems of the range of building structures designed and built today.

REFERENCES

American Institute of Steel Construction. 2002. “Seismic Provisions for Structural Steel Buildings.” *AISC*, Chicago, IL, S6.2.

Astaneh-Asl. A. 2005. “Design of Shear Tab Connections for Gravity and Seismic Loads.” *SteelTips*, Structural Steel Educational Council.

Black, G.R., Wenger, B.A., and Popov, E. P. 1980. “Inelastic buckling of steel struts under cyclic load reversal.” *UCB/EERC-80/40*, Earthquake Engineering Research Center, University of California, Berkeley, California.

Bruneau, M., Uang, C.M. and Whittaker, A. 1998 “Ductile Design of Steel Structures.”, *McGraw-Hill*, New York, New York.

Der Kiureghian, A. 2005a. “Non-ergodicity and PEER’s framework formula”, *Journal of Earthquake Engineering and Structural Dynamics.* Volume 34, Issue 13 , Pages 1643 – 1652.

Der Kiureghian, A. 2005b. “CE 193 - Engineering Risk Analysis Lecture Notes”, *Department of Civil and Environmental Engineering,* University of California, Berkeley.

de Souza, R.M. 2000. “Force-based Finite Element for Large Displacement Inelastic Analysis of Frames.” *Doctoral dissertation*, Graduate Division of the University of California at Berkeley, University of California, Berkeley, California.

Gugerli, H. and Goel, S.C. 1980. “Large scale test for the hysteresis of inclined bracing members” *7th World Conference on Earthquake Engineering,* Istanbul, Turkey.

Gugerli, H. and Goel, S.C. 1982. “Inelastic cyclic behavior of steel bracing member.” *UMEE 82R1*, College of Engineering, University of Michigan, Ann Arbor, MI.

Hall, J. and Challa, M.V.R. 1995. “Beam-column modeling.” *Journal of Engineering Mechanics*, ASCE, 121(12), 1284-1291.

Ikeda, K., Mahin, S.A. and Dermitzakis, S.N. 1984. “Phenomenological modeling of steel braces under cyclic loading.” *UCB/EERC-84/09*, Earthquake Engineering Research Center, University of California, Berkeley, California.

International Code Council. 2000. “International Building Code”, *International Code Council*, Fall Church, VA.

Khatib, I., Mahin, S. and Pister, K. 1988. “Seismic Behavior of concentrically braced steel frames.” *UCB/EERC-88/01*, Earthquake Engineering Research Center, University of California, Berkeley, California.

Kwon, O. S., Nakata, N., Elnashai, A. S., and Spencer, B. 2005. “A Framework for Multi-Site Distributed Simulation and Application to Complex Structural Systems.” *Journal of Earthquake Engineering,* 9(5), 741-753.

Lee, K. and Bruneau, M. 2004. “Seismic vulnerability evaluation of axially loaded steel build-up lacing members.” *MCEER 04-0007*, Multidisciplinary Center for Earthquake Engineering Research, University of Buffalo, Buffalo, NY.

Leon, T. R. and Yang, C.S. 2003. “Special Inverted-V-Braced Frames with Suspended Zipper Structs.” *International Workshop on Steel and Concrete Composite Construction*, IWSCCC, National Center for Research on Earthquake Engineering, Taipei, Taiwan.

Leon, T. R. and Yang, C.S. 2005. “Results of Early Collaboration Research on Behavior of Braced Steel Frames with Innovative Bracing Schemes (Zipper Frames).” *The First International Conferences on Advances in Experimental Structural Engineering*, Nagoya, Japan.

Magonette, G.E. and Negro, P. 1998. “Verification of pseudo dynamic testing method.” *European Earthquake Engineering*, PUB 40-50.

Mahin, S.A., Shing, P.B., Thewalt, C.R. and Hanson, R.D. 1989. “Pseudo dynamic test method – current status and future direction.” *Journal of Structural Engineering*, ASCE, 115(8): 2113-2128.

Moehle, Jack and Deierlein Gregory. 2004 “A Framework Methodology for Performance-Based Earthquake Engineering,” *13th World Conference on Earthquake Engineering,* Vancouver, British Columbia.

Molina, F.G., Verzeletti, G., Magonette, G., Buchet, P.H. and Geradin, M. 1998. “Bi-directional pseudodynamic test of a full-size three story building.” *Earthquake Engineering and Structural Dynamics*, Wiley, 28(12):1541-1566.

Mosqueda, G., Stojadinovic B. and Mahin S. A. 2004. “Geographically Distributed Continuous Hybrid Simulation”, *13th World Conference on Earthquake Engineering*, Paper 959, Vancouver, Canada, August 2004.

Mosqueda, G. 2003. “Continuous hybrid simulation with geographically distributed substructure.” *Doctoral dissertation*, Graduate Division of the University of California at Berkeley, University of California, Berkeley, California.

Nakashima, M., Kaminosono, T., Ishida, I. and Ando, K. 1990. “Integration techniques for substructure pseudo dynamic test.” Proceeding, *Fourth U.S. National Conference on Earthquake Engineering*, EERI.

Nakashima, M. and Masaoka, N. 1999. “Real-time on-line test for MSDOF systems.” *Earthquake Engineering and Structural Dynamics*, Wiley, 28(4):393-420.

Nakata, N., Spencer, B., Johoson, E. A., Elnashai, A. S., Kuchma, D. A. 2003. *Finite Element Modeling in MOST Simulation Code*. Department of Civil and Environmental Engineering, University of Illinois at Urbana-Champaign.

Newmark, N.M. 1959. “A method of computation for structural dynamics.” *Journal of Engineering Mechanics*, ASCE, VOL: 67:949.

Open System for Earthquake Engineering Simulation (OpenSees) Framework, *Pacific Earthquake Engineering Research Center*, University of California, Berkeley, http://opensees.berkeley.edu/.

Reinhorn, A. and Schater, M. 2005. “Preliminary report – UB shaking table test Specimen #2”, *internal report*, University at Buffalo, Buffalo, New York.

Schellenberg, A. 2008. “Advanced implementation of hybrid simulation.” *Doctoral dissertation*, Graduate Division of the University of California, Berkeley, University of California, Berkeley, California.

Shing, P.B., Bursi, O.S. and Vannan, M.T. 1996. “Application of pseudo dynamic test method to structural research.” *Earthquake Spectra*, EERI, 12(1): 29-54.

Shing, P.B. and Mahin, S.A, 1984. “Pseudo dynamic test method for seismic performance evaluation: theory and implementation.” *UCB/EERC-84/01*, Earthquake Engineering Research Center, University of California, Berkeley, California.

Somerville, P., Smith, N., Punyamurthula, S. and Sun, J. 1997. “Development of ground motion time history for phase 2 of the FEMA SAC steel project.” *SAX/BD-97/04*, SAC Joint Venture, Sacramento, CA, USA.

Soong, T.T. 1981. “Probabilistic Modeling and Analysis in Science and Engineering”, *John Wiley & Sons*, New York.

Takanashi, K. 1975. "Non-linear earthquake response analysis of structure by a computer-actuator on-line system." *Architecture institute of Japan*, 229: 77-83.

Takanashi, K. and Nakashima, M. 1987. "Japanese activities on on-line testing." *Journal of Engineering Mechanics*, ASCE, 113(7): 1014-1032.

Thewalt, C.R. and Mahin, S.A. 1987. "Hybrid solutions techniques for generalized pseudo dynamic testing." *UCB/EERC-87/09*, Earthquake Engineering Research Center, University of California, Berkeley, California.

Thewalt, C.R. and Roman, M. 1994. "Performance parameters for pseudodynamic tests." *Journal of Structural Engineering Mechanics*, ASCE, 120(9), 2768-2781.

Tsai, K.C., Weng, Y. T., Lin, S.L. and Goel, S. 2004. "pseudo dynamic test of a full scale cftbrb frame: part 1 – performance based design" *13World Conference on Earthquake Engineering,* August 1st ~ 6th 2004, Vancouver, British Columbia, Canada.

UCB. 2003. "U.C. Berkeley seismic guideline", *University of California, Berkeley*, Berkeley, California, USA.

Uriz, P. 2005. "Towards Earthquake Resistant Design of Concentrically Braced Steel Structures." *Doctoral dissertation*, Graduate Division of the University of California at Berkeley, University of California, Berkeley, California.

USGS 2002. "USGS National seismic hazard maps", *U.S. Geological Survey (USGS)*, Reston, Virginia, http://earthquake.usgs.gov/research/hazmaps/.

Yang, C.S. 2006. "Special inverted-V-Braced Frames with Suspended Zipper Struts." *Doctoral dissertation*, Georgia Institute of Technology, Georgia.

Yang, T.Y., Moehle, J., Stojadinovic, B., and Der Kiureghian, A. 2006. "An application of PEER performance-based earthquake engineering methodology." *8th National Conference of Earthquake Engineering*, April 18-22 2006, San Francisco, CA.

Zayas, V.A., Popov, E.P. and Mahin, S.A. 1980. "Cyclic inelastic buckling of tubular steel braces." *UCB/EERC-80/16*, Earthquake Engineering Research Center, University of California, Berkeley, California.

Appendix A: Basic Probability Theorem

A.1 INTRODUCTION

To account for uncertainties in earthquake engineering related problems, some prior understanding of basic probability theory is needed. This appendix provides the probability theory that is used in deriving the PBEE methodology. Additional references can be located from any probability and statistics textbooks. One recommended text is the CE193 lecture notes provided by Professor Armen Der Kiureghian from the University of California, Berkeley, Department of Civil and Environmental Engineering (Der Kiureghian 2005b). Some of the text presented in this appendix is adopted directly from this text.

A.2 BASIC PROBABILITY THEORY

Table A.1 shows a summary of the notations used in this appendix.

Table A.1 Summary of notations.

Notation	Definition
S	Sample space. A collection of all possible events.
$\varnothing$	Empty set. A set contains no events.
E_i	Event i.
$\overline{E}_i$	Complement of event i.
E_i â E_j	Union of event i and event j.
E_iE_j or $E_i \cap E_j$	Intersect of event i and event j.
$P(E_i)$	Probability of event i.
$P(E_i \mid E_j)$	Conditional probability. Probability of event i given event j.

Axioms of probability

Equations (A.1)–(A.3) show the axioms of probability that are used to define the rest of the probability rules.

$$0 \le P(E_i) \le 1 \tag{A.1}$$

$$P(S) = 1 \tag{A.2}$$

$$\begin{gathered}\text{Event } E_i \text{ and } E_j \text{ are said to be mutually exclusive,}\\ \text{if } P(E_i \cup E_j) = P\left(E_i\right) + P\left(E_j\right) \Rightarrow P\left(E_i E_j\right) = 0 \text{ for } i \ne j\end{gathered} \tag{A.3}$$

Collective exclusive

Event E_1 to E_n are said to be collective exclusive if

$$E_1 \cup E_2 \cup \cdots \cup E_n = S \tag{A.4}$$

Elementary rules of probability

Equations (A.5)–(A.11) show some elementary rules of probability. Detailed proof can be located from the list of references.

$$P(E_i \cup E_j) = P\left(E_i\right) + P\left(E_j\right) - P\left(E_i E_j\right) \tag{A.5}$$

$$\begin{aligned}P(E_i \cup E_j \cup E_k) = P\left(E_i\right) + P\left(E_j\right) + P\left(E_k\right) - P\left(E_i E_j\right)\\ - P\left(E_j E_k\right) - P\left(E_i E_k\right) - P\left(E_i E_j E_k\right)\end{aligned} \tag{A.6}$$

Conditional probability

$$P(E_i \mid E_j) = \frac{P\left(E_i E_j\right)}{P\left(E_j\right)}, \textbf{ if } P\left(E_j\right) \ne 0 \tag{A.7}$$

$$P\left(E_1 E_2 \cdots E_n\right) = P(E_1 \mid E_2 \cdots E_n) P(E_2 \mid E_3 \cdots E_n) \cdots P(E_n) \tag{A.8}$$

Statistical independence

Event E_i and E_j are said to be statistically independent if

$$P(E_i \mid E_j) = P\left(E_i\right) \Leftrightarrow P(E_j \mid E_i) = P\left(E_j\right) \tag{A.9}$$

Bayes's rule

$$P(E_i \mid E_j) = P(E_j \mid E_i)\frac{P(E_i)}{P(E_j)} \tag{A.10}$$

Theorem of total probability

$$P(A) = \sum_{i=1}^{n} P(A \mid B_i)P(B_i), \tag{A.11}$$

provided B_i is mutually exclusive and collective exclusive.

A.3 SINGLE RANDOM VARIABLE

As the number of events in a sample space increases, it is mathematically more challenging to express the probability of each event happening using symbols. Hence, the concept of a single random variable is introduced (concept of multiple random variables will be introduced in Section A.4). A single random variable is defined as a mapping from events in a sample space to numerical values. Each value represents possible outcomes of the sample space. Since the events are mapped into real numbers, formal mathematical equations can be used to deal with the random phenomena. The following example illustrates the concept of a random variable.

Example 1: The damage states (DS) of a component in a building after an earthquake can be identified as No Damage (ND), Slight Damage (SD), Moderate Damage (MD), and Heavy Damage (HD). A random variable, X, can be used to represent the damage states of the component, then the possible damage state of the component after an earthquake can be expressed as

$$
\begin{aligned}
ND &\Rightarrow X = 0 \\
SD &\Rightarrow X = 1 \\
MD &\Rightarrow X = 2 \\
HD &\Rightarrow X = 3
\end{aligned}
$$

At the same time, another random variable, Y, can be used to represent the state of the component With Damage (WD) or No Damage (ND). This means that

$$
\begin{aligned}
ND &\Rightarrow Y = 0 \\
SD, MD, HD &\Rightarrow Y = 1
\end{aligned}
$$

This example illustrates the concept of two separate random variables and their corresponding mapping. Note the mapping of random variable Y is not one-to-one.

Probability distribution

Once a random variable is defined, the probability of occurrence of each outcome of a random variable can be completely characterized by its probability distribution. The following section defines some of the probability distributions that can be used to characterize a random variable.

If a random variable, X, has discrete outcomes (say $x_1, x_2, \cdots, x_n$), the likelihood of each outcome of the random variable to occur is related to the probability of each event to occur in the original sample space. Hence, a *probability mass function* (PMF), $p_X(x)$, is defined as

$$p_X(x) = P(X = x_i) \tag{A.12}$$

Since $p_X(x) = 0$ for any $x \neq x_i$ for $i = 1 \cdots n$, PMF must satisfy the following rules

$$0 \leq p_X(x) \leq 1 \tag{A.13}$$

$$\sum_{i=1}^{n} p_X(x_i) = 1 \tag{A.14}$$

If a random variable, X, does not have discrete outcomes, the definition of PMF is not useful to define the probability distribution (since $p_X(x) = 0$ for all x). Hence, a *probability* *density function* (PDF), $f_X(x)$, is defined for a continuous random variable. Equation (A.15) shows the definition of PDF,

$$\int_{x}^{x+dx} f_X(x)\,dx = P(x < X \le x + dx) \tag{A.15}$$

Similar to PMF, PDF has to satisfy the following rules:

$$0 \le f_X(x) \tag{A.16}$$

$$\int_{-\infty}^{\infty} f_X(x)\,dx = 1 \tag{A.17}$$

\

Alternatively, the probability distribution of a random variable can be characterized using the *cumulative distribution function* (CDF), $F_X(x)$, where the $F_X(x)$ is defined as

$$\begin{aligned} F_X(x) = P(X \le x) &= \sum_{x_i \le x} p_X(x_i) \quad \text{(discrete random variable)} \\ &= \int_{-\infty}^{x} f_X(x)\,dx \quad \text{(continuous random variable)} \end{aligned} \tag{A.18}$$

To ensure that the axioms of probability is satisfied, the CDF must satisfy the following rules:

$$F_X(-\infty) = 0 \text{ and } F_X(\infty) = 1 \tag{A.19}$$

Partial descriptors of a single random variable

While a probability distribution contains the complete description of a random variable, it is often useful to capture the characteristics of the random variable using partial descriptors. Equation (A.20) shows the definition of the nth moment of a random variable and Table A.2 summarizes some commonly used partial descriptors and their relationships to the nth moment of a random variable.

Definition: The n^{th} *moment* of random variable, X, is defined as

$$E\{X^n\} = \sum_i x_i^n p_X(x_i) \quad \text{(discrete random variable)}$$

$F_X(-\infty) = 0$ **and**

$$= \int_{-\infty}^{\infty} x^n f_X(x)\,dx \quad \text{(continuous random variable)} \qquad \text{(A.20)}$$

$$F_X(\infty) = 1$$

Table A.2 Commonly used partial descriptors for single random variable, X .

Notation	Descriptions	Equations
Mean $_X$	Average value of X . Also known as the first moment of random variable X .	$_X = E\{X\} = \sum_i x_i p_X(x_i)$ (discrete) $= \int_{-\infty}^{\infty} x f_X(x)\,dx$ (continuous)
Median $x_{0.5}$	Value of random variable X , when 50% of the probability lies below and above it.	$F_X(x_{0.5}) = 0.5$
Mode $\tilde{x}$	Value of random variable X , where the outcome has the highest probability.	$p_X(\tilde{x}) = \max(p_X(x))$ (discrete) $f_X(\tilde{x}) = \max(f_X(x))$ (continuous)
Mean Square $E[X^2]$	Second moment of random variable X .	$E\{X^2\} = \sum_i x_i^2 p_X(x_i)$ (discrete) $= \int_{-\infty}^{\infty} x^2 f_X(x)\,dx$ (continuous)
Variance $Var[X]$	Measure the dispersion of the distribution about its mean. Large value of $Var[X]$ denote large dispersion about the mean.	$Var[X] = \sum_i (x_i - {}_X)^2 p_X(x_i)$ (discrete) $= \int_{-\infty}^{\infty} (x - {}_X)^2 f_X(x)\,dx$ (continuous) Note, $Var[X] = E[X^2] - (E[X])^2$

Table A.2—*Continued.*

Notation	Descriptions	Equations
Standard deviation σ_X	Square root of the variance. Measure the dispersion of the distribution about its mean. Large value of σ_X denote large dispersion about the mean.	$\sigma_X = \sqrt{\mathrm{var}[X]}$
Coefficient of variance δ_X	Normalized measure of dispersion about its mean.	$\delta_X = \frac{\sigma_X}{\left\| \ _X \right\|}$, Note this only make sense if $\ _X$ is not close to 0.
Third central moment $\ _{X,3}$	Third central moment of random variable X. Measure the skewness of the distribution about its mean.	$\ _{X,3} = \sum_i (x_i - \ _X)^3 p_X(x_i)$ (discrete) $= \int_{-\infty}^{\infty} (x - \ _X)^3 f_X(x)dx$ (continuous) $\ _{X,3} > 0 \Rightarrow$ Skew to the right about its mean $= 0 \Rightarrow$ Symmetric about its mean $< 0 \Rightarrow$ Skew to the left about its mean
Coefficient of skewness γ_X	Dimensionless quantity to characterize skewness of the distribution.	$\gamma_X = \frac{\ _{X,3}}{\sigma_X^{\ 3}}$ $\gamma_X > 0 \Rightarrow$ Skew to the right about its mean $= 0 \Rightarrow$ Symmetric about its mean $< 0 \Rightarrow$ Skew to the left about its mean
Coefficient of excess	Measure the flatness of the distribution around its peak.	$\frac{E\left[(X - \ _X)^4\right]}{\sigma_X^{\ 4}} - 3 > 0 \Rightarrow$ sharp peak $< 0 \Rightarrow$ flattened peak

A.4 MULTIPLE RANDOM VARIABLES

While section A.3 illustrates the concept of a single random variable, most earthquake-engineering-related problems require concurrent consideration of multiple random variables. This section will summarize the probability distributions and the corresponding partial descriptor for multiple random variables.

A.4.1 Probability Distribution of Multiple Random Variables

Consider two discrete random variables X and Y, the joint PMF of the random variables is defined as

$$p_{XY}(x,y) = P(X = x_i \cap Y = y_i) \tag{A.21}$$

To satisfy the axioms of probability, the joint PMF of the random variables must satisfy the following rules,

$$0 \le p_{XY}(x,y) \le 1 \tag{A.22}$$

$$\sum_i p_{XY}(x_i, y) = p_Y(y) \textbf{ and } \sum_j p_{XY}(x, y_j) = p_X(x) \tag{A.23}$$

$$\sum_i \sum_j p_{XY}(x_i, y_j) = 1 \tag{A.24}$$

If the random variables are continuous, the joint PDF of the random variables is defined as

$$\int_y^{y+dy} \int_x^{x+dx} f_{XY}(x,y)\,dx\,dy = P(x < X \le x + dx \cap y < Y \le y + dy) \tag{A.25}$$

Again, to satisfy the axioms of probability, the joint PDF of the random variables must satisfy the following rules,

$$0 \le f_{XY}(x,y) \tag{A.26}$$

$$\int_{-\infty}^{\infty} f_{XY}(x,y)\,dx = f_Y(y) \text{ and } \int_{-\infty}^{\infty} f_{XY}(x,y)\,dy = f_X(x) \tag{A.27}$$

$$\int_{-\infty}^{\infty}\int_{-\infty}^{\infty} f_{XY}(x,y)\,dx\,dy = 1 \tag{A.28}$$

The CDF for the joint random variable is defined as

$$\begin{aligned} F_{XY}(x,y) &= \sum_{y_j \le y}\sum_{x_i \le x} p_{XY}(x_i, y_j) \quad \text{(discrete random variables)} \\ &= \int_{-\infty}^{y}\int_{-\infty}^{x} f_{XY}(x,y)\,dxdy \quad \text{(continuous random variables)} \end{aligned} \tag{A.29}$$

Similarly, the joint CDF of the random variables must satisfy the following rules

$$\begin{gathered} F_{XY}(-\infty, y) = 0, F_{XY}(x, -\infty) = 0, \\ F_{XY}(x, \infty) = F_X(x), F_{XY}(\infty, y) = F_Y(y) \\ F_{XY}(\infty, \infty) = 1 \end{gathered} \tag{A.30}$$

A.4.2 Moments of Multiple Random Variables

Like the moments of single random variables, the joint moment of multiple random variables provides partial description of the random variables. Table A.3 shows some of the commonly used partial descriptors for two joint random variables X and Y.

Table A.3 Commonly used partial descriptors for two joint random variables, X and Y.

Notation	Descriptions	Equations
Mean of product $E[XY]$	Mean of the product of random variables X and Y.	$E[XY]$ $=\sum_j \sum_i x_i y_j p_{XY}(x_i, y_j)$ (discrete) $=\int_{-\infty}^{\infty}\int_{-\infty}^{\infty} x\, y\, f_{XY}(x,y)\, dx\, dy$ (continuous)
Covariance $Cov[X,Y]$	Joint central moment. $=E\left[(X-\ {}_X)(Y-\ {}_Y)\right]$ Where ${}_X$ and ${}_Y$ are the mean of random variable X and Y respectively.	$Cov[X,Y]$ $=\sum_j \sum_i (x_i-\ {}_X)(y_j-\ {}_Y)\, p_{XY}(x_i, y_j)$ (discrete) $=\int_{-\infty}^{\infty}\int_{-\infty}^{\infty} (x-\ {}_X)(y-\ {}_Y)\, f_{XY}(x,y)\, dx\, dy$ (continuous) Note, $Cov[X,Y]=E[XY]-E[X]E[Y]$
Correlation coefficient ρ_{XY}	Dimensionless measure related to covariance. Both covariance and correlation coefficient measure the linear dependence between two random variables.	$\rho_{XY}=\dfrac{Cov[X,Y]}{\sigma_X \sigma_Y}$, $-1 \le \rho_{XY} \le 1$ $\rho_{XY}=\pm 1$ $\Rightarrow$ linear relation between X and Y $\rho_{XY}=0$ $\Rightarrow$ Complete lack of linear dependence

Table A.3 shows some of the partial descriptors that are commonly used to characterize two joint random variables. If there are more than two random variables, it is more convenient to use matrix notation to present a set of n random variables.

Let $\mathbf{X}=[X_1\, X_2 \cdots X_n]^t$ be a vector of n random variables. The superscript t represents matrix transpose. It is useful to introduce the mean matrix, $\mathbf{M}_X$, and the covariance matrix, Σ_{XX}

,

$$\mathbf{M}_X = \begin{bmatrix} _1 \\ _2 \\ \vdots \\ _n \end{bmatrix} \qquad \Sigma_{XX} = \begin{bmatrix} \sigma_1^{\ 2} & & & sym \\ Cov[X_2, X_1] & \sigma_2^{\ 2} & & \\ \vdots & \vdots & \ddots & \\ Cov[X_n, X_1] & Cov[X_n, X_2] & \cdots & \sigma_n^{\ 2} \end{bmatrix} \tag{A.31}$$

where $_i$ and $\sigma_i^{\ 2}$ are the mean and variance of random variable X_i.

In addition, the diagonal matrix of standard deviations, $\mathbf{D}_X$, and the correlation coefficient matrix, $\mathbf{R}_{XX}$, is defined as

$$\mathbf{D}_X = \begin{bmatrix} \sigma_1 & 0 & \cdots & 0 \\ 0 & \sigma_2 & & \vdots \\ \vdots & & \ddots & 0 \\ 0 & 0 & \cdots & \sigma_n \end{bmatrix} \qquad \mathbf{R}_{XX} = \begin{bmatrix} 1 & & & sym \\ \rho_{2,1} & 1 & & \\ \vdots & \vdots & \ddots & \\ \rho_{n,1} & \rho_{n,2} & \cdots & 1 \end{bmatrix} \tag{A.32}$$

where $\rho_{i,j}$ is the correlation coefficient between random variable X_i and X_j. Using the identifying $\rho_{XY} = \dfrac{Cov[X,Y]}{\sigma_X \sigma_Y}$, one can easily verify that

$$\Sigma_{XX} = \mathbf{D}_X \mathbf{R}_{XX} \mathbf{D}_X \tag{A.33}$$

A.5 FUNCTIONS OF RANDOM VARIABLES

Sections A.3 and A.4 demonstrate the concept of random variables where their probability distribution is known. However in earthquake-engineering-related problems, the probability distribution of the random variable of interest may not always be easily accessible. For example, the stress level of a component in a building during an earthquake may not be easily accessible but can be determined in terms of the applied load and building deformation. This section will illustrate the concept of functions of random variables where the probability distribution of the dependent random variable can be identified or estimated from independent variables which are accessible.

Let X be a random variable whose probability distribution is known. Let Y be a dependent random variable whose probability distribution depends on the probability distributions of X. If random variable Y can be related to random variable X by a transfer function $Y=g_1(X)$. The n^th^ moment of random variable Y can be calculated using Equation (A.34).

$$
\begin{aligned}
E\{g_1^n(X)\} &= \sum_i g_1^n(x_i)\, p_X(x_i) \quad \text{(discrete random variable)} \\
&= \int_{-\infty}^{\infty} g_1^n(x) f_X(x)\, dx \quad \text{(continuous random variable)}
\end{aligned}
\tag{A.34}
$$

where $p_X(x)$ and $f_X(x)$ are the PMF and PDF of random variable X.

Since $g_1^n(X)$ is just another function of $g(X)$, Equation (A.34) can be written as

$$
\begin{aligned}
E\{g(X)\} &= \sum_i g(x_i)\, p_X(x_i) \quad \text{(discrete random variable)} \\
&= \int_{-\infty}^{\infty} g(x) f_X(x)\, dx \quad \text{(continuous random variable)}
\end{aligned}
\tag{A.35}
$$

Equation (A.35) is known as *expectation* of $g(X)$. It should be noted that the partial descriptors shown in Tables A.2 and A.3 are just some special cases of $g(X)$. For example, when $g(X)=X$, the expectation of $g(X)$ reduces to mean of X and when $g(X)=(X-\ _X)^2$, the expectation of $g(X)$ reduces to $Var[X]$.

If the function depends on more than one random variable, for example $g(\mathbf{X})=g(X_1 X_2 \cdots X_m)$, the expectation of $g(\mathbf{X})$ can be calculated using Equation (A.36).

$$
\begin{aligned}
E\{g(\mathbf{X})\} &= \sum_{X_1}\cdots\sum_{X_m} g(x_1,\cdots,x_m)\, p_{X_1,\cdots,X_m}(x_1,\cdots,x_m) \quad \text{(discrete rv)} \\
&= \int_{-\infty}^{\infty}\cdots\int_{-\infty}^{\infty} g(x_1,\cdots,x_m)\, f_{X_1,\cdots,X_m}(x_1,\cdots,x_m)\, d_{X1}\cdots d_{Xm} \quad \text{(continuous rv)}
\end{aligned}
\tag{A.36}
$$

Where $g(x_1,\cdots,x_m)$ represents the value of the function when $\mathbf{X}=\mathbf{x}$ and $p_{X_1,\cdots,X_m}(x_1,\cdots,x_m)$ and $f_{X_1,\cdots,X_m}(x_1,\cdots,x_m)$ are the joint PMF and PDF of the random variables $X_1 X_2 \cdots X_m$. The series of summations and integrations shown in Equation (A.36) indicate the summation or integrations of all possible outcomes of $\mathbf{X}$. For example, $Y=X_1+2X_2$ and X_1 have two possible outcomes ($x_{1,1}$ and $x_{1,2}$), while X_2 has three possible outcomes ($x_{2,1}$, $x_{2,2}$ and $x_{2,3}$). Equation (A.37) shows the expectation of random variable Y.

$$
\begin{aligned}
E\{Y\} = &\left(x_{1,1} + 2x_{2,1}\right) p\left(x_{1,1}, x_{2,1}\right) + \left(x_{1,1} + 2x_{2,2}\right) p\left(x_{1,1}, x_{2,2}\right) \\
&+ \left(x_{1,1} + 2x_{2,3}\right) p\left(x_{1,1}, x_{2,3}\right) + \left(x_{1,2} + 2x_{2,1}\right) p\left(x_{1,2}, x_{2,1}\right) \\
&+ \left(x_{1,2} + 2x_{2,2}\right) p\left(x_{1,2}, x_{2,2}\right) + \left(x_{1,2} + 2x_{2,3}\right) p\left(x_{1,2}, x_{2,3}\right)
\end{aligned}
\tag{A.37}
$$

Some basic property of the expectation operator is shown in Equation (A.38):

$$
\begin{aligned}
&E\{c\} = c \\
&E\{cg(\mathbf{X})\} = cE\{g(\mathbf{X})\} \\
&E\{g(\mathbf{X}) + h(\mathbf{X})\} = E\{g(\mathbf{X})\} + E\{h(\mathbf{X})\}
\end{aligned}
\tag{A.38}
$$

where c is a constant and $g(\mathbf{X})$ and $h(\mathbf{X})$ are two real value function.

With the definition of expectation, some unique property of functions of random variables can be derived. Consider a system of affine functions

$$
Y_k = \sum_{i=1}^{n} a_{ki} X_i + b_k \qquad k = 1, \mathrm{L}\ , m
\tag{A.39}
$$

where a_{ki} for $i = 1\mathrm{L}\ n$ and b_k are constant coefficients.

Taking expectation of v,

$$
{}_{Y_k} = \sum_{i=1}^{n} a_{ki}\ {}_{X_i} + b_k \qquad k = 1, \mathrm{L}\ , m
\tag{A.40}
$$

Subtract Equation (A.40) from Equation (A.39),

$$
Y_k - \ {}_{Y_k} = \sum_{i=1}^{n} a_{ki} \left(X_i - \ {}_{X_i}\right) \qquad k = 1, \mathrm{L}\ , m
\tag{A.41}
$$

Take expectation of function $\left(Y_k - \ {}_{Y_k}\right)\left(Y_l - \ {}_{Y_l}\right)$

$$
E\left[\left(Y_k - \ {}_{Y_k}\right)\left(Y_l - \ {}_{Y_l}\right)\right] = Cov\left[Y_k, Y_l\right]
\tag{A.42}
$$

$$
\begin{aligned}
Cov[Y_k, Y_l] &= E\left[\sum_{i=1}^{n} a_{ki}\left(X_i - {}_{X_i}\right)\sum_{j=1}^{n} a_{lj}\left(X_j - {}_{X_j}\right)\right] \\
&= \sum_{i=1}^{n}\sum_{j=1}^{n} a_{ki}a_{lj}E\left[\left(X_i - {}_{X_i}\right)\left(X_j - {}_{X_j}\right)\right] \\
&= \sum_{i=1}^{n}\sum_{j=1}^{n} a_{ki}a_{lj}Cov\left[X_i, X_j\right] \\
&= \sum_{i=1}^{n}\sum_{j=1}^{n} a_{ki}a_{lj}\rho_{X_i X_j}\sigma_{X_i}\sigma_{X_j}
\end{aligned}
$$

In matrix notation, Equation (A.39), Equation (A.40), and Equation (A.42) can be written as

$$\mathbf{Y} = \mathbf{AX} + \mathbf{B} \tag{A.43}$$

$$\mathbf{M_Y} = \mathbf{AM_X} + \mathbf{B} \tag{A.44}$$

$$\sum\nolimits_{\mathbf{YY}} = \mathbf{A}\sum\nolimits_{\mathbf{XX}}\mathbf{A}^t \tag{A.45}$$

Equation(A.43), Equation (A.44), and Equation (A.45) show that the mean vector and covariance matrix of random variables, $\mathbf{Y}$, can be calculated from the mean vector and covariance matrix of random variables, $\mathbf{X}$, if the transformation from $\mathbf{X}$ to $\mathbf{Y}$ is affine or linear.

A.6 PROBABILISTIC MODELS

Sections A.3–A.5 deal with random variables and their probability distributions. Table A.4 summarizes some of the probabilistic models that are commonly used in engineering-related problems.

Table A.4 Commonly used probability distributions.

Name (parameters)	Description	PMF $p_X(x)$ (Discrete) PDF $f_X(x)$ (Continuous)	Mean = ${}_X$, Std Dev = σ_x
Binomial distribution (p,n)	Discrete probability distribution representing the probability of having exactly x success in n Bernoulli* trials (independent of the sequence).	$p_X(x)=\binom{n}{x}p^x(1-p)^{n-x}$ for $x=0,\ldots,n$ $\binom{n}{x}=\frac{n!}{x!(n-x)!}$	np, $\sqrt{np(1-p)}$
Geometric distribution (p)	Discrete probability distribution representing the probability of having exactly x Bernoulli* trials until the first success occurs.	$p_X(x)=(1-p)^{x-1}p$ for $x=1,2,\ldots$	$\frac{1}{p}$, $\frac{\sqrt{1-p}}{p}$
Negative binomial distribution (p,k)	Discrete probability distribution representing the probability of having at least x number of Bernoulli* trials to have the k^{th} success to occur.	$p_X(x)=\binom{x-1}{k-1}p^k(1-p)^{x-k}$ for $x=k,k+1,\ldots$	$\frac{k}{p}$, $\frac{\sqrt{k(1-p)}}{p}$

*Note: Bernoulli trials are defined as a sequence of independent trials, where each trial has only two possible outcomes and the probability of each trial remains the same throughout the trials.

Table A.4—*Continued.*

Name (parameters)	Description	PMF $p_X(x)$ (Discrete) PDF $f_X(x)$ (Continuous)	Mean = $_X$, Std Dev = σ_x
Poisson distribution (ν)	Discrete probability distribution representing the probability of having x number of arrivals in the time interval [0,t).	$p_X(x,t)=\dfrac{\nu^x e^{-\nu}}{x!}$ for $x=0,1,\mathrm{L}$ $\nu>0$ represents the average number of arrival in time interval [0,t).	$\nu,\sqrt{\nu}$
Uniform distribution (a,b)	Continuous probability distribution representing the probability of having equally likely probability in the interval (a,b)	$f_X(x)=\dfrac{1}{b-a}$ $\quad a\le x\le b$ $=0$ $\quad$ elsewhere	$\dfrac{a+b}{2},\dfrac{b-a}{2\sqrt{3}}$
Normal distribution $(\ _X,\sigma_X)$	Also known as Gaussian distribution. The probability distribution is represented by the bell shape curve and is symmetric about its mean.	$f_X(x)$ $=\dfrac{1}{\sqrt{2\pi}\sigma_X}\exp\left[-\dfrac{1}{2}\left(\dfrac{x-\ _X}{\sigma_X}\right)^2\right],$ for $-\infty<x<\infty$	$_X,\sigma_X$
Lognormal distribution (λ,ζ)	Exponential of the normal distribution. Taking natural log of lognormal distribution returns the normal distribution. Random variable x takes only positive entry ($x\ge 0$).	$f_X(x)$ $=\dfrac{1}{x\sqrt{2\pi}\zeta}\exp\left[-\dfrac{1}{2}\left(\dfrac{\ln x-\lambda}{\zeta}\right)^2\right]$ for $x\ge 0$ $=0$ $\quad$ elsewhere	$\exp\left(\lambda+\dfrac{\zeta^2}{2}\right),$ $e^{\left(\lambda+\frac{\zeta^2}{2}\right)}\sqrt{e^{\left(\zeta^2\right)}-1}$

Appendix B: Design of Idealized Building

B.1 INTRODUCTION

In order to compare the performance of the suspended zipper braced frame with the inverted-V braced frame, the idealized building as shown in Figure 6.1 has been designed according to the International Building Code (ICC 2000) and the AISC LRFD and seismic provisions (American Inst. of Steel Construction 2002). The detail design calculations are presented in this appendix.

B.2 LOADINGS

B.2.1 Gravity Load and Seismic Weights

The gravity load and seismic weight of the idealized building at the roof, third, and second, floors have been summarized in Tables 6.6–6.8. The dead load (DL) consisted of an area load uniformly distributed on the floor area and a perimeter load to represent the facade. The live load (LL) is uniformly distributed on the floor area. The seismic weight of the building is calculated to be 8586 kips.

B.2.2 Site Seismicity

To calculate the design base shear contributed by the earthquake loading, the spectral accelerations are located from USGS seismic hazard maps (USGS 2002). Based on the reading, the maximum considered spectral acceleration at short period is S_S = 1.9 g, and at 1-sec period, S_1 = 0.82 g. With soil condition classified as site C, the design earthquake spectral acceleration at the short period and the 1-sec period was calculated to be S_{DS} = 1.27 g and S_{D1} = 0.71 g, respectively. Figure B.1 shows the design response spectrum calculated according to the procedure presented in IBC2000 (ICC 2000).

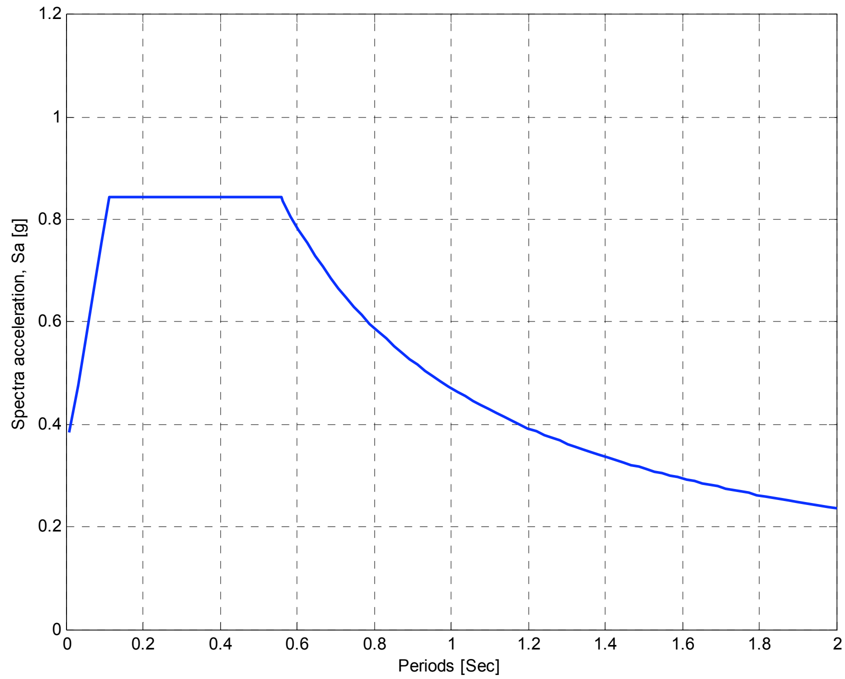

Fig. B.1 Design response spectrum.

B.2.3 System Parameters

Table B.1 summarizes the system parameters that are used for the base shear calculation.

Table B.1 System parameters.

Parameters	Value	References
Occupancy category	I	ASCE 7-02 Table 1.1
Seismic use group	I	ASCE 7-02 Table 9.1.3
Important factor, I	1.0	ASCE 7-02 Table 9.4.2.1a
Response modification factor, R	6	ASCE 7-02 Table 9.5.2.2
Overstrength factor, Ω	2	ASCE 7-02 Table 9.5.2.2
Deflection amplification factor, Cd	2	ASCE 7-02 Table 9.5.2.2
Building height limitation	160 ft	ASCE 7-02 Table 9.5.2.2
Allowable story drift ratio	2%	ASCE 7-02 Table 9.5.2.8

B.2.4 Fundamental Period of Structure

To calculate the seismic base shear, the fundamental period of the structure is estimated using a finite element program (OpenSees) but checked with the provision specified in the ASCE 7-02 Section 9.5.5.3. Table B.2 shows the coefficient used in estimating the fundamental period of the structure.

Table B.2 Parameters used in estimating fundamental period of structure.

Parameters	Value	References
Coefficient for upper limit on calculated period, C_u	1.4	ASCE 7-02 Table 9.5.5.3.1
Coefficient for approximating the period, C_t	0.02	ASCE 7-02 Table 9.5.5.3.2
Coefficient for approximating the period, x	0.75	ASCE 7-02 Table 9.5.5.3.2
Total height of the structure in ft	42	

Approximate fundamental period of the structure

$$T_a = C_t h_n^{\ x} = 0.33 \text{ sec} \qquad \text{(ASCE 7-02 Equation 9.5.5.3.2-1)}$$

Upper limit on calculated period

$$T_{\max} = C_u T_a = 0.462 \text{ sec} \qquad \text{(ASCE 7-02 Section 9.5.5.3.1)}$$

Period calculated from structural analysis

$$T = 0.45 \text{ sec} \qquad \text{(OpenSees analysis)}$$

Select T = 0.45 sec in the calculation of the design base shear

B.2.5 Seismic Base Shear

The seismic design base shear is calculated according to ASCE 7-02 Section 9.5.5.2.

$$C_s = \frac{S_{DS}}{R/I} = \frac{1.267}{6/1} = 0.211\,\mathrm{g} \qquad \text{(ASCE 7-02 Eq. 9.5.5.2.1-1)}$$

$$C_s \leq \frac{S_{D1}}{T(R/I)} = \frac{0.707}{0.45(6/1)} = 0.262\,\mathrm{g} \qquad \text{(ASCE 7-02 Eq.9.5.5.2.1-2)}$$

$$C_s \geq 0.044 S_{Ds} I = 0.044(1.267)1 = 0.056\,\mathrm{g} \qquad \text{(ASCE 7-02 Eq.9.5.5.2.1-3)}$$

$$C_s \geq \frac{0.5 S_1}{R/I} = \frac{0.5(0.816)}{6} = 0.068\,\mathrm{g} \qquad \text{(ASCE 7-02 Eq.9.5.5.2.1-4)}$$

$$\boxed{V = C_S W = \mathbf{1811\ kips}} \qquad \text{(ASCE 7-02 Eq. 9.5.5.2-1)}$$

B.2.6 Vertical Distribution of Base Shear

The vertical distribution of the base shear is calculated according to ASCE 7-02 Section 9.5.5.4. Table B.3 shows the summary of the vertical distribution of the seismic base shear. Since the idealized building has two symmetrical axes along each principal axis of the structure and there are six lateral-load-resisting systems in each principal axis, each lateral-load-resisting system is designed to resist one sixth of the total design seismic base shear.

$$F_x = C_{vx} V \qquad \text{(ASCE 7-02 Eq. 9.5.5.4-1)}$$

$$C_{vx} = \frac{w_x h_x^{\,k}}{\sum_{i=1}^{n} w_i h_i^{\,k}} \qquad \text{(ASCE 7-02 Eq. 9.5.5.4-2)}$$

$$k = 1 \qquad \text{(ASCE 7-02 Eq. 9.5.5.4-2)}$$

Table B.3 Vertical distribution of seismic base shear.

Level	w_i [kips]	h_i [ft]	$w_i h_i^k$ [k-ft]	C_{vx}	$F_{x,\text{total}}$ [kips]	$F_{x/\text{frame}}$ [kips]	Story shear [kips]
Roof	2,899	42.00	121,761	0.50	900	150	150
Third floor	3,122	28.00	87,419	0.36	646	108	258
Second floor	2,565	14.00	35,911	0.15	265	44	302
First floor							
Total	8,586		245,092	1.00	1,812	302	

B.2.7 Distribution of Gravity and Seismic Forces

To simplify the design procedure, all the element connections are assumed to be pinned. With the tributary width of 14 ft, the gravity load is assigned to the lateral-load-resisting system as distributed loads along the beams. Table B.3 summarizes the gravity load value assigned to the lateral-load-resisting system. Figure B.2 shows the distribution of the gravity load and seismic base shear assigned to the lateral-load-resisting system.

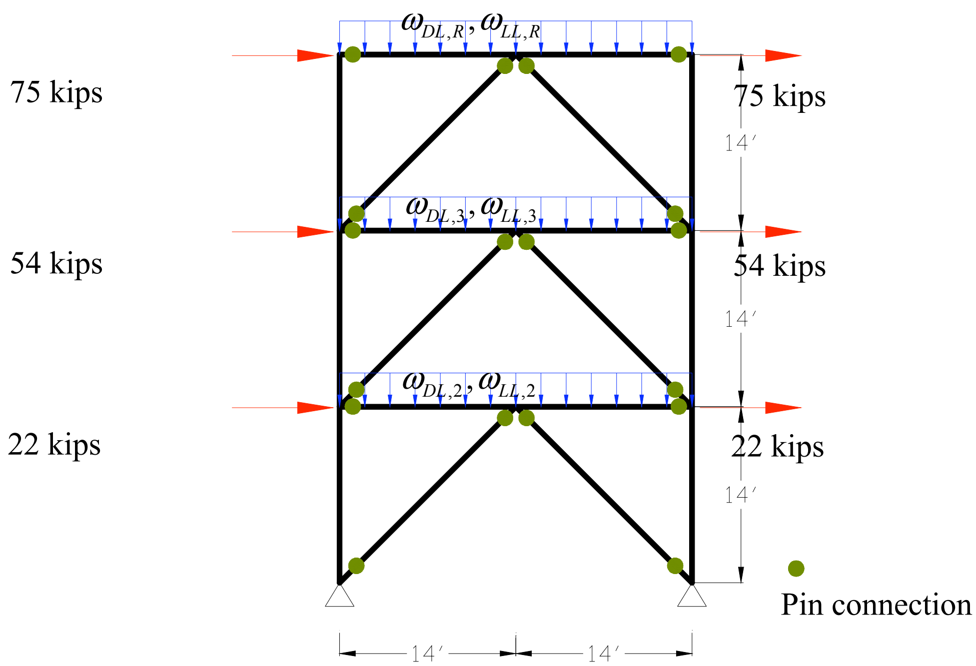

Fig. B.2 Loads applied on lateral-load-resisting systems.

Table B.4 Gravity load assigned to lateral-load-resisting systems.

i	$\omega_{DL,i}$ (kips/ft)	$\omega_{LL,i}$ (kips/ft)
Roof, R	1.91	0.28
Third floor	2.29	1.40
Second floor	2.30	1.12

B.2.8 Load Combinations

The load combination used in designing the lateral-load-resisting system is calculated according to IBC2000 (ICC 2000) Section 1605.2.

1. 1.4 DL
2. 1.2 DL + 1.6 LL + 0.5 Lr
3. 1.2 DL + 0.5 Lr + 1.6 LL
4. 1.2 DL ± 1.0 E + 0.5 LL
5. 0.9 DL ± 1.0 E

Where $E = \rho Q_E + 0.2 S_{DS} DL$ (ASCE 7-02 Section 9.5.2.7) and

$$\rho = \text{reliability factor} = \max(\rho_x),\ 1.0 \le \rho < 1.5$$

$$\rho_x = 2 - \frac{20}{r_{\max}\sqrt{A_x}} \qquad \text{(ASCE 7-02 Section 9.5.2.4.2-1)}$$

$r_{\max_X}$ = ratio of story shear resistance by the most heavily loaded element in story x. Assume all the story shear is resisted by the brace only, since there are a total of 12 braces in a story $\Rightarrow r_{\max_X} = 1/12$.

A_x = floor area = 22736 $ft^2 \Rightarrow \rho_x = 2 - \frac{20}{r_{\max}\sqrt{A_x}} = 0.4 \Rightarrow \rho = 1.0 \Rightarrow E = Q_E + 0.253DL$

Hence the final load combinations used are

1. 1.2 DL + 1.6 LL + 0.5 Lr
2. 1.2 DL + 1.6 Lr + 0.5 LL
3. 1.453 DL + Q_E + 0.5 LL
4. 0.647 DL - Q_E

Note: Live load reduction factor was not applied (IBC2000 Section 4.8 and 4.9).

B.3 DESIGN OF INVERTED-V BRACED FRAME

B.3.1 Design of First-Story Braces

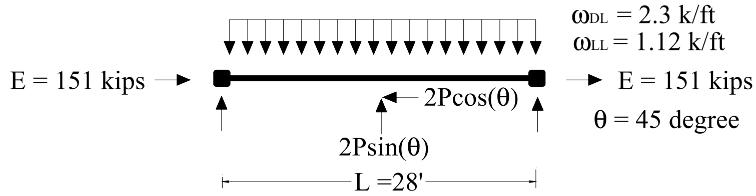

Unfactored load

$$P_{DL} = \frac{0.625 \times \omega_{DL} \times L}{2 \times \sin(\theta)} = -28.5\,kips\ ;\ P_{LL} = \frac{0.625 \times \omega_{LL} \times L}{2 \times \sin(\theta)} = -13.9\,kips\ ;$$

$$P_{Q_E} = \frac{E}{2 \times \cos(\theta)} = \pm 213.5\,kips\ ;$$

Design forces in the braces (factored load)

$P_u =$ 1.2 DL + 1.6 LL = -56.3 kips

$P_u =$ 1.453 DL + Q_E + 0.5 LL = -261.9 kips ⟵ govern compression load

$T_u =$ 0.647 DL - Q_E = 195.1 kips ⟵ govern tension load

⇒ pick HSS7x7x5/8

L_{br} = $19.8\,ft$, $A_g = 14\,in^2$, $F_y = 46\,ksi$, $E_s = 29000\,ksi$,

K = 1 (out-of-plan buckling), $r_x = r_y = 2.58\,in$.

AISC LRFD check

Compression strength: $\phi P_n = 309.4\,kips > P_u$ (ok)

Tension strength: $\phi P_n = 0.9 A_g F_y = 579.6\,kips > P_u$ (ok)

Slenderness: $KL_{br}/r = 92.1 < 5.87\sqrt{E_s/F_y} = 147$

(2002 AISC seismic provision section 13.2a) (ok)

Compactness: $b/t = h/t = 9.05 < 0.64\sqrt{E_s/F_y} = 16$

(2002 AISC seismic provision T-I-8-1) (ok)

Select HSS7x7x5/8 for the first-story braces

B.3.2 Design of Second-Story Braces

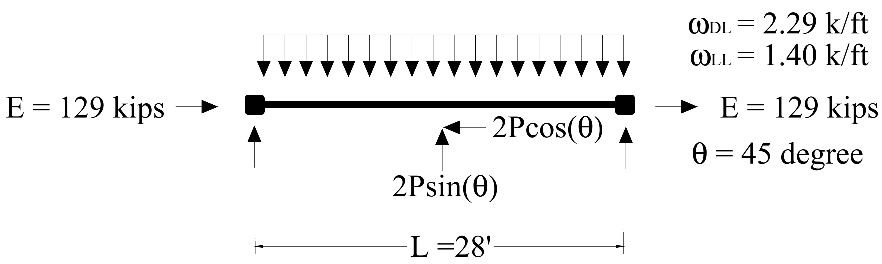

Unfactored load

$$P_{DL} = \frac{0.625 \times \omega_{DL} \times L}{2 \times \sin(\theta)} = -28.3\,kips\,;\; P_{LL} = \frac{0.625 \times \omega_{LL} \times L}{2 \times \sin(\theta)} = -17.3\,kips\,;$$

$$P_{Q_E} = \frac{E}{2 \times \cos(\theta)} = \pm 182.4\,kips\,;$$

Design forces in the braces (factored load)

P_u = 1.2 DL + 1.6 LL = -61.7 kips

P_u = 1.453 DL + Q_E + 0.5 LL = -232.2 kips ← govern compression load

T_u = 0.647 DL - Q_E = 164.1 kips ← govern tension load

⇒ pick HSS7x7x1/2

L_{br} = $19.8\,ft$, $A_g = 11.6 in^2$, $F_y = 46\,ksi$, $E_s = 29000\,ksi$,

K = 1 (out-of-plan buckling), $r_x = r_y = 2.63\,in$.

AISC LRFD check

Compression strength: $\phi P_n = 262.0\,kips > P_u$ (ok)

Tension strength: $\phi P_n = 0.9 A_g F_y = 480\,kips > P_u$ (ok)

Slenderness: $KL_{br} / r = 90.3 < 5.87\sqrt{E_s / F_y} = 147$

(2002 AISC seismic provision section 13.2a) (ok)

Compactness: $\frac{b}{t} = \frac{h}{t} = 12.1 < 0.64\sqrt{E_s / F_y} = 16$

(2002 AISC seismic provision T-I-8-1) (ok)

Select HSS7x7x1/2 for the second-story braces

B.3.3 Design of Third-Story Braces

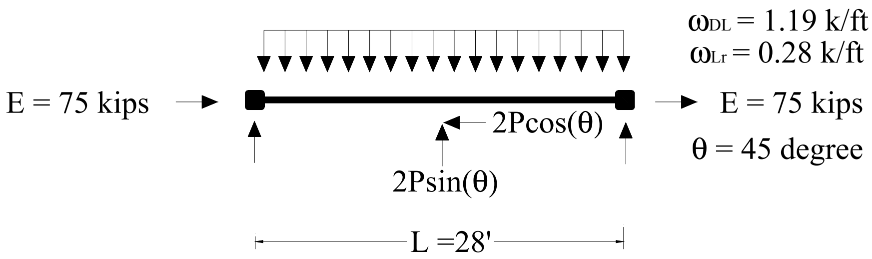

Unfactored load

$$P_{DL} = \frac{0.625 \times \omega_{DL} \times L}{2 \times \sin(\theta)} = -14.7\,kips\,;\; P_{Lr} = \frac{0.625 \times \omega_{Lr} \times L}{2 \times \sin(\theta)} = -3.5\,kips\,;$$

$$P_{Q_E} = \frac{E}{2 \times \cos(\theta)} = \pm 106\,kips\,;$$

Design forces in the braces (factored load)

P_u = 1.2 DL + 1.6 Lr = -23.2 kips.

P_u = 1.453 DL + Q_E = -129.2 kips ⟵ govern compression load

T_u = 0.647 DL - Q_E = 96.5 kips ⟵ govern tension load

⟹ pick HSS6x6x1/2

L_{br} = $19.8\,ft$, $A_g = 9.74 in^2$, $F_y = 46\,ksi$, $E_s = 29000\,ksi$,

K = 1 (out-of-plan buckling), $r_x = r_y = 2.23\,in$.

AISC LRFD check

Compression strength: $\phi P_n = 177.5\,kips > P_u$ (ok)

Tension strength: $\phi P_n = 0.9 A_g F_y = 403.2\,kips > P_u$ (ok)

Slenderness: $KL_{br} / r = 107 < 5.87\sqrt{E_s / F_y} = 147$

(2002 AISC seismic provision section 13.2a) (ok)

Compactness: $\frac{b}{t} = \frac{h}{t} = 9.9 < 0.64\sqrt{E_s / F_y} = 16$

(2002 AISC seismic provision T-I-8-1) (ok)

Select HSS6x6x1/2 for the third-story braces

B.3.4 Design of Second-Floor Beam

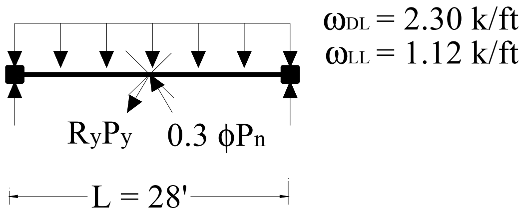

The beams of the IVBF are designed according to the 2002 AISC seismic provision (American Inst. of Steel Construction 2000) Section 13.4 a, where the beams are continuous between columns. The beams are designed to resist the gravity load and unbalanced vertical force when the compression brace buckled. The unbalanced vertical force is calculated based on the assumption that the tension brace yield and reached the capacity of $R_y P_y$ and that the compression brace has a capacity of $0.3\phi P_n$. The following sections show the procedures used to design the beams of the IVBF.

Gravity load (assume the brace is not present)

$V_{DL} = \omega_{DL} \times L/2 = 32.2\,kips$; $M_{DL} = \omega_{DL} \times L^2/8 = 225.4\,k-ft$;

$V_{LL} = \omega_{LL} \times L/2 = 15.7\,kips$; $M_{LL} = \omega_{LL} \times L^2/8 = 109.8\,k-ft$;

Earthquake load (assume with brace buckled)

First-story brace forces (HSS7x7x5/8):

$R_y P_y = R_y A_g F_y = 837.2\,kips$; ($R_y = 1.3$ 2002 AISC seismic provision T-I-6-1);

$0.3\phi P_n = 92.8\,kips$

$V_E = \left(R_y P_y - 0.3\phi P_n\right)\sin\left(45\right) = 526.4\,kips$;

$M_E = \dfrac{V_E L}{4} = 3684.5\,k-ft$;

$P_E = \left(R_y P_y + 0.3\phi P_n\right)\cos\left(45\right)/2 = \pm 328.8\,kips$ (assume the unbalanced horizontal force is distributed to both left and right part of the beam).

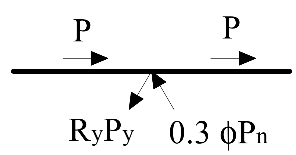

Design forces in the beam (factored load)

$P_u =$ E = -328.8 kips ← govern compression load

$P_u =$ - E = 328.8 kips ← govern tension load

$V_u =$ 1.4 DL = 45.1 kips. $V_u =$ 1.2 DL + 1.6 LL = 63.7 kips

$V_u =$ 1.2 DL + E + 0.5 LL = 572.8 kips $\leftarrow$ govern shear

$M_u =$ 1.4 DL = 315.6 k-ft. $M_u =$ 1.2 DL + 1.6 LL = 446.1 k-ft

$M_u =$ 1.2 DL + E + 0.5 LL = 4010 k-ft $\leftarrow$ govern moment

$\Rightarrow$ pick W33x291

$A_g = 85.7 in^2$, $I_X = 17700 \text{ in}^4$, $kL_x = 28 ft$, $kL_y = 14 ft$, $F_y = 50 ksi$, $E_s = 29000 ksi$,

Lateral braced @ ½ point ($L_b = 14 ft$)

AISC LRFD check

Compression strength: $\phi P_n = 3127.4 kips$

Tension strength: $\phi P_n = 0.9 A_g F_y = 3856.5 kips > P_u$ (ok)

Moment strength: $\phi M_n = 4350 \text{k-ft}$ ($\phi = 0.9$, Cb = 1.3)

Shear strength: $\phi V_n = 902 \text{kips}$ ($\phi = 0.9$, without stiffener) $> V_u$ (ok)

Compactness: $$\frac{b}{2t_f} = 4.6 < 0.3\sqrt{\frac{E_s}{F_y}} = 7.23$$

(2002 AISC seismic provision T-I-8-1 [d]) (ok)

$$\frac{P_u}{\phi P_y} = 0.08 \Rightarrow \frac{h}{tw} = 31 < 3.14\sqrt{\frac{E_s}{F_y}}\left(1 - \frac{1.54 P_u}{\phi P_y}\right) = 65.7$$

(2002 AISC seismic provision T-I-8-1 [d]) (ok)

Combine axial and moment interaction (AISC section H1):

$P_{el} = \pi^2 EI / kL_x^{\ 2} = 44874 kips$;

$C_m = 1.0$ (AISC Chapter C.2 pg 16.1-18, member subject to transverse

load and without end restraint) $\Rightarrow B_1 = \dfrac{C_m}{1 - P_u / P_{el}} = 1.0$

Since $P_u / \phi_c P_n = 0.1 < 0.2$, safety check was analyzed against

$$\frac{P_u}{2\phi_c P_n} + \frac{M_{ux}}{\phi M_n} = 0.97 < 1.0 \text{ (ok)}$$

Select W33x291 for the second-floor beam

B.3.5 Design of Third-Floor Beam

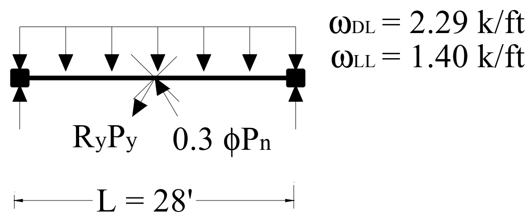

Gravity load (assume the brace is not present)

$$V_{DL} = \omega_{DL} \times L/2 = 32.1\,kips\,;\;\; M_{DL} = \omega_{DL} \times L^2/8 = 224.42\,k-ft\,;$$

$$V_{LL} = \omega_{LL} \times L/2 = 19.6\,kips\,;\;\; M_{LL} = \omega_{LL} \times L^2/8 = 137.2\,k-ft\,;$$

Earthquake load (assume with brace buckled)

Second-story brace forces (HSS7x7x5/8)

$R_yP_y = R_yA_gF_y = 693.7\,kips$; ($R_y = 1.3$ 2002 AISC seismic provision T-I-6-1);

$0.3\phi P_n = 78.6\,kips$

$$V_E = \left(R_yP_y - 0.3\phi P_n\right)\sin(45) = 434.9\,kips\,;$$

$$M_E = \frac{V_E L}{4} = 3044.6\,k-ft\,;$$

$P_E = \left(R_yP_y + 0.3\phi P_n\right)\cos(45)/2 = \pm 273\,kips$ (assume the unbalanced horizontal force is distributed to both left and right part of the beam).

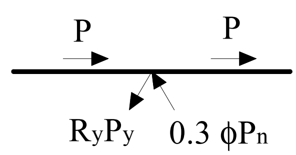

Design forces in the braces (factored load)

$P_u =$ E = -273 kips ← govern compression load

$P_u =$ - E = 273 kips ← govern tension load

$V_u =$ 1.4 DL = 44.9 kips

$V_u =$ 1.2 DL + 1.6 LL = 69.8 kips

$V_u =$ 1.2 DL + E + 0.5 LL = 483.2 kips ← govern shear

$M_u =$ 1.4 DL = 314.2 k-ft

$M_u =$ 1.2 DL + 1.6 LL = 488.8 k-ft

$M_u =$ 1.2 DL + E + 0.5 LL = 3382.5 k-ft ← govern moment

$\Rightarrow$ pick W30x261

$A_g = 76.9\,in^2$, $I_X = 13100\ \text{in}^4$, $kL_x = 28\,ft$, $kL_y = 14\,ft$, $F_y = 50\,ksi$, $E_s = 29000\,ksi$,

Lateral braced @ ½ point ($L_b = 14\,ft$)

AISC LRFD check

Compression strength: $\phi P_n = 2769.4\,kips$

Tension strength: $\phi P_n = 0.9 A_g F_y = 3460.5\,kips > P_u$ (ok)

Moment strength: $\phi M_n = 3536.3\,\text{k-ft}$ ($\phi = 0.9$, Cb = 1.3)

Shear strength: $\phi V_n = 793.5\,\text{kips}$ ($\phi = 0.9$, without stiffener) $> V_u$ (ok)

Compactness: $$\frac{b}{2t_f} = 4.6 < 0.3\sqrt{\frac{E_s}{F_y}} = 7.23$$

(2002 AISC seismic provision T-I-8-1 [d]) (ok)

$$\frac{P_u}{\phi P_y} = 0.08 \Rightarrow \frac{h}{tw} = 28.7 < 3.14\sqrt{\frac{E_s}{F_y}}\left(1 - \frac{1.54\,P_u}{\phi P_y}\right) = 66.4$$

(2002 AISC seismic provision T-I-8-1 [d]) (ok)

Combine axial and moment interaction (AISC section H1):

$P_{el} = \pi^2 EI / kL_x^{\;2} = 33212\,kips$;

$C_m = 1.0$ (AISC Chapter C.2 pg 16.1-18, member subject to transverse

load and without end restraint) $\Rightarrow B_1 = \dfrac{C_m}{1 - P_u / P_{el}} = 1.0$

Since $P_u / \phi_c P_n = 0.10 < 0.2$, safety check was analyzed against

$$\frac{P_u}{2\phi_c P_n} + \frac{M_{ux}}{\phi M_n} = 1 \le 1.0 \text{ (ok)}$$

Select W30x261 for the third-floor beam

B.3.6 Design of Roof Beam

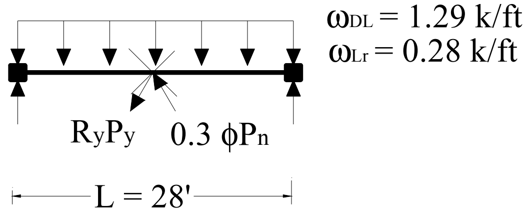

Note: According to the AISC Seismic 2002 section 13.4a exception provision, the top-story beam does not require to design for the unbalanced vertical force when the compression brace buckles. However from the computer simulation, the roof beam has excessive deflection when the third-story braces buckled, and so this exception was removed in the 2005 AISC seismic provision. Hence, the roof beam will be designed to sustain the unbalanced vertical load when the third-story brace buckled.

Gravity load (assume the brace is not present)

$V_{DL} = \omega_{DL} \times L/2 = 26.7\,kips$; $M_{DL} = \omega_{DL} \times L^2/8 = 187.2\,k-ft$;

$V_{Lr} = \omega_{Lr} \times L/2 = 3.9\,kips$; $M_{Lr} = \omega_{Lr} \times L^2/8 = 27.4\,k-ft$;

Earthquake load (assume with brace buckled)

Third-story brace forces (HSS6x6x1/2)

$R_yP_y = R_yA_gF_y = 582.5\,kips$; ($R_y = 1.3$ 2002 AISC seismic provision T-I-6-1);

$0.3\phi P_n = 53.2\,kips$

$V_E = \left(R_yP_y - 0.3\phi P_n\right)\sin(45) = 374.2\,kips$;

$M_E = \dfrac{V_E L}{4} = 2619.5\,k-ft$;

$P_E = \left(R_yP_y + 0.3\phi P_n\right)\cos(45)/2 = 224.7\,kips$ (assume the unbalanced horizontal force is distributed to both left and right part of the beam).

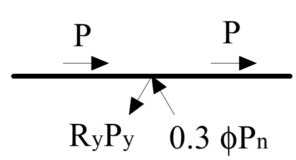

Design forces in the braces (factored load)

P_u = E = -224.7 kips ⟵ govern compression load

P_u = - E = 224.7 kips ⟵ govern tension load

V_u = 1.4 DL = 37.4 kips

$V_u = $ 1.2 DL + 1.6 Lr = 38.4 kips

$V_u = $ 1.2 DL + E = 406.3 kips $\leftarrow$ govern shear

$M_u = $ 1.4 DL = 262.1 k-ft

$M_u = $ 1.2 DL + 1.6 Lr = 268.5 k-ft

$M_u = $ 1.2 DL + E = 2844.1 k-ft $\leftarrow$ govern moment

$\Rightarrow$ pick W30x235

$A_g = 69.2\,in^2$, $I_X = 11700\ \text{in}^4$, $kL_x = 28\,ft$, $kL_y = 14\,ft$, $F_y = 50\,ksi$, $E_s = 29000\,ksi$,

Lateral braced @ ½ point ($L_b = 14\,ft$)

AISC LRFD check

Compression strength: $\phi P_n = 2487.4\ kips$

Tension strength: $\phi P_n = 0.9 A_g F_y = 3114\,kips > P_u$ (ok)

Moment strength: $\phi M_n = 3176.3\,\text{k-ft}$ ($\phi = 0.9$, Cb = 1.3)

Shear strength: $\phi V_n = 701.4\,\text{kips}$ ($\phi = 0.9$, without stiffener) $> V_u$ (ok)

Compactness: $\dfrac{b}{2t_f} = 5 < 0.3\sqrt{\dfrac{E_s}{F_y}} = 7.23$

(2002 AISC seismic provision T-I-8-1 [d]) (ok)

$P_u / \phi P_y = 0.07 \Rightarrow\ h/tw = 32.2 < 1.12\sqrt{E_s / F_y}\left(2.33 - P_u / \phi P_y\right) = 60.7$

(2002 AISC seismic provision T-I-8-1 [d]) (ok)

Combine axial and moment interaction (AISC section H1):

$P_{el} = \pi^2 EI / kL_x^{\ 2} = 29662\,kips$;

$C_m = 1.0$ (AISC Chapter C.2 pg 16.1-18, member subject to transverse load and without end restraint) $\Rightarrow B_1 = \dfrac{C_m}{1 - P_u / P_{el}} = 1.0$

Since $P_u / \phi_c P_n = 0.09 < 0.2$, safety check was analyzed against

$$\frac{P_u}{2\phi_c P_n} + \frac{M_{ux}}{\phi M_n} = 0.94 < 1.0 \text{ (ok)}$$

Select W30x235 for the third-floor beam

B.3.7 Design of Columns

Since the lateral forces are designed to be transfer to the ground by the braces, and the column is pinned at the base, the column will be designed to carry the axial forces caused from the overturning moment from the lateral loads and the resultant forces from the gravity load. According to the 2002 AISC seismic provision (American Inst. of Steel Construction 2002) Section 8.3, when $P_u / \phi P_n > 0.4$ without the amplified seismic load, the amplified seismic load needs to be considered in the load combination. However, the required strength is not required to be greater than 1.1 x Ry times the nominal strength of the connecting brace nor the capacity of the foundation to resist uplifting.

Unfactored load

$$P_{DL} = \left(\omega_{DL,R} + \omega_{DL,3} + \omega_{DL,2}\right) \times 14 = -91\,kips\,;\; P_{LL} = \left(\omega_{LL,2} + \omega_{LL,2}\right) \times 14 = -35.28\,kips\,;$$

$$P_{Lr} = \omega_{LL,R} \times 14 = -3.92\,kips\,;\; Q_E = \frac{44 \times 14 + 108 \times 28 + 150 \times 42}{28} = \pm 355\,kips$$

Design forces in the column (factored load)

$P_u =$ 1.2 DL + 1.6 LL + 0.5 Lr = -167.61 kips

$P_u =$ 1.2 DL + 1.6 Lr + 0.5 LL = -133.11 kips

$P_u =$ 1.453 DL + Ω_0 Q_E + 0.5 LL

= 1.453 DL + 2 Q_E + 0.5 LL = -860 kips ⟵ govern compression load

$P_u =$ 0.647 DL – Ω_0 Q_E = 651.1 kips ⟵ govern tension load

According to 2002 AISC seismic provision section 8.3, $P_u < P_{u,\max}$

$$P_{u,\max} = 1.1 R_y\, F_y \left(A_{g,b3} + A_{g,b2} + A_{g,b1}\right) \sin(45) = 1643.8\,kips\,,$$

where $R_y = 1.3$ (2002 AISC seismic provision, T-I-6-1)

⇒ pick W14x159

$kL_x = 14\,ft$, $kL_y = 14\,ft$, $A_g = 46.7\,in^2$, $F_y = 50\,ksi$, $E_s = 29000\,ksi$, $r_x = 6.38\,in$, $r_y = 4\,in$.

AISC LRFD check

Compression strength: $\phi P_n = 1744.58\,kips > P_u$ (ok)

Tension strength: $\phi P_n = 0.9 A_g F_y = 2101.5\,kips > P_u$ (ok)

Slenderness: $\left(\frac{KL}{r}\right) = 42 < 5.87\sqrt{E_s / F_y} = 141$

(2002 AISC seismic provision section 13.2a) (ok)

Flange compactness: $\frac{b_f}{2t_f} = 6.54 < 0.3\sqrt{E_s / F_y} = 7.22$

(2002 AISC seismic provision, T-I-8-1) (ok)

Web compactness: $\frac{h}{t_w} = 15 < 1.12\sqrt{E_s / F_y}\left(2.33 - \frac{P_u}{\phi_b P_y}\right) = 41$

(2002 AISC seismic provision, T-I-8-1) (ok)

Select W14x159 for the columns. (Use the same column section for all stories.)

B.3 DESIGN OF SUSPENDED ZIPPER BRACED FRAME

Since the suspended zipper braced frame is a novel configuration that is still under evaluation, the suspended zipper braced frame is designed according to the procedure proposed by Yang (2006).

B.4.1 Design of First- and Second-Story Braces

Following the design procedure proposed by Yang (2006), the lower-story braces (except the roof brace) are designed using the same methodology as the invert-V braced frame. Hence the first- and second-story braces are identical to the inverted-V braced frame.

First-story brace forces (HSS7x7x5/8)

$R_y P_{y_1} = 837.2\,kips$; $R_y = 1.3$. 2002 AISC seismic provision T-I-6-1;

$0.3\phi P_{n1} = 92.8\,kips$

Second-story brace (HSS7x7x1/2)

$R_y P_{y2} = 693.7\,kips$; $R_y = 1.3$. 2002 AISC seismic provision T-I-6-1;

$0.3\phi P_{n2} = 78.6\,kips$

B.4.2 Design of Second-Story Zipper Column

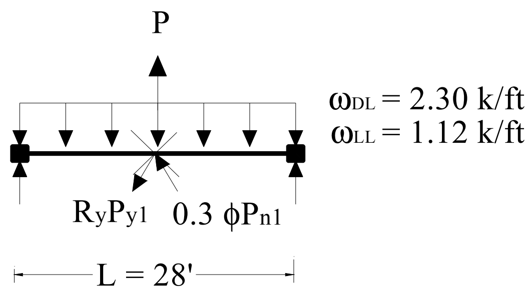

The second-story zipper column is designed to provide a vertical support at mid span of the second-floor beam. Hence the second-story beam does not need to be designed to resist the unbalanced vertical forces when the first-story compression brace buckle.

Gravity load

$$P_{DL} = 0.625\omega_{DL} \times L = 40.3\,kips\,;\;\; P_{LL} = 0.625\omega_{LL} \times L = 19.6\,kips\,;$$

Earthquake load (assume with brace buckled)

$$P_E = \left(R_y P_{y1} - 0.3\phi P_{n1}\right)\sin(45) = 526.4\,kips\,;$$

Design forces in the braces (factored load)

$P_u =$ 1.4 DL = 56.4 kips

$P_u =$ 1.2 DL + 1.6 LL = 79.7 kips

$P_u =$ 1.2 DL + E + 0.5 LL = 584.5 kips $\leftarrow$ govern tension load

$\Rightarrow$ pick W12x50

$$A_g = 14.6 in^2,\; kL_x = 14\,ft,\; kL_y = 14\,ft,\; F_y = 50\,ksi,\; E_s = 29000\,ksi.$$

AISC LRFD check

Tension strength: $\phi P_n = 0.9 A_g F_y = 657\,kips > P_u$ (ok)

Select W12x50 for the second-story zipper column.

B.4.3 Design of Third-Story Zipper Column

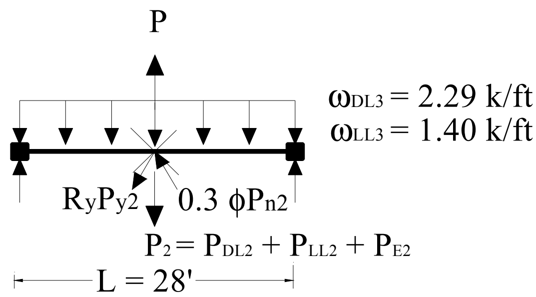

The third-story zipper column is designed to provide a vertical support at mid span of the third-floor beam. It is designed to resist the gravity load at the second and third stories and the unbalanced vertical forces when the first- and second-story compression braces buckle.

Gravity load

$$P_{DL2} = 0.625\omega_{DL2} \times L = 40.3\,kips\,;\;\; P_{LL2} = 0.625\omega_{LL2} \times L = 19.6\,kips\,;$$

$$P_{DL3} = 0.625\omega_{DL3} \times L = 40.1\,kips\,;\;\; P_{LL3} = 0.625\omega_{LL3} \times L = 24.5\,kips\,;$$

Earthquake load

First-story braces forces: (HSS7x7x5/8)

$$P_{E1} = \left(R_y P_{y1} - 0.3\phi P_{n1}\right)\sin\left(45\right) = 526.4\,kips\,;$$

Second-story brace forces: (HSS7x7x1/2)

$$P_{E2} = \left(R_y P_{y2} - 0.3\phi P_{n2}\right)\sin\left(45\right) = 434.9\,kips\,;$$

Design forces in the braces (factored load)

$P_u =$ 1.4 DL = 112.5 kips

$P_u =$ 1.2 DL + 1.6 LL = 167 kips

$P_u =$ 1.2 DL + E + 0.5 LL = 1079.7 kips ← govern tension

⇒ pick W14x90

$$A_g = 26.5\,in^2,\; kL_x = 14\,ft,\; kL_y = 14\,ft,\; F_y = 50\,ksi,\; E_s = 29000\,ksi\,.$$

AISC LRFD check

Tension strength: $\phi P_n = 0.9 A_g F_y = 1192.5\,kips > P_u$ (ok)

Select W14x90 for the third-story zipper column.

B.4.4 Design of Third-Story Braces

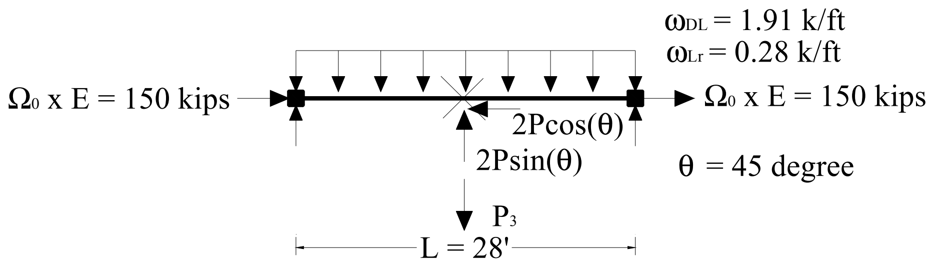

The third-story braces are designed to resist the gravity load from the second, third, and roof stories, lateral shear force at the roof level (assume that the structure reached ultimate capacity, $\Omega_0 = 2$) and the unbalanced vertical forces when the first- and second-story compression braces buckle.

Gravity load

$$P_{DL2} = 0.625\omega_{DL2} \times L = -40.3\,kips\,; \quad P_{LL2} = 0.625\omega_{LL2} \times L = -19.6\,kips\,;$$

$$P_{DL3} = 0.625\omega_{DL3} \times L = -40.1\,kips\,; \quad P_{LL3} = 0.625\omega_{LL3} \times L = -24.5\,kips\,;$$

$$P_{DLr} = 0.625\omega_{DLr} \times L = -20.8\,kips\,; \quad P_{Lr} = 0.625\omega_{LLr} \times L = -4.9\,kips\,;$$

Earthquake load

First-story brace forces (HSS7x7x5/8)

$$P_{E1} = \frac{\left(R_y P_{y1} - 0.3\phi P_{n1}\right)\sin\left(45\right)}{2\,\sin\left(45\right)} = -372.2\,kips\,;$$

Second-story brace forces (HSS7x7x1/2)

$$P_{E2} = \frac{\left(R_y P_{y2} - 0.3\phi P_{n2}\right)\,\sin\left(45\right)}{2\,\sin\left(45\right)} = -307.5\,kips\,;$$

Story shear at the roof floor

$$P_{E3} = \frac{2\Omega_0 E}{2\cos\left(45\right)} = \pm 212.1\,kips\,;$$

Design forces in the braces (factored load)

$P_u =$ 1.4 DL = -141.6 kips

$P_u =$ 1.2 DL + 1.6 LL + 0.5 Lr = -194.4 kips

$P_u =$ 1.2 DL + 0.5 LL + 1.6 Lr = -151.3 kips

P_u = 1.2 DL + E + 0.5 LL = -1035.3 kips $\leftarrow$ govern compression

P_u = 0.9 DL - E = 376.6 kips $\leftarrow$ govern tension

$\Rightarrow$ pick W14x132

L_{br} = $19.8\,ft$, $A_g = 38.8 in^2$, $F_y = 50\,ksi$, $E_s = 29000\,ksi$,

K = 1 (out-of-plan buckling), $r_x = 6.28\,in$, $r_y = 3.76\,in$

AISC LRFD check

Compression strength: $\phi P_n = 1231.5\,kips > P_u$ (ok)

Tension strength: $\phi P_n = 0.9 A_g F_y = 1746.0\,kips > P_u$ (ok)

Slenderness: $\left(\frac{KL}{r}\right) = 63.2 < 5.87\sqrt{E_s / F_y} = 141$

(2002 AISC seismic provision section 13.2a) (ok)

Flange compactness: $\frac{b_f}{2t_f} = 7.2 < 0.3\sqrt{E_s / F_y} = 7.22$

(2002 AISC seismic provision, T-I-8-1) (ok)

Web compactness: $\frac{h}{t_w} = 18 < 1.12\sqrt{E_s / F_y}\left(2.33 - \frac{P_u}{\phi_b P_y}\right) = 69$

(2002 AISC seismic provision, T-I-8-1) (ok)

Select W14x132 for the third-story braces

B.4.5 Design of Third-Floor Beam

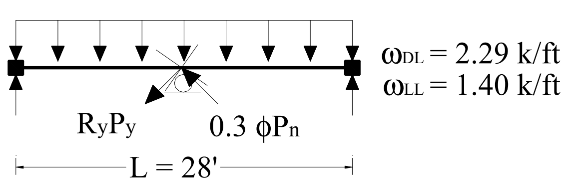

The third-floor beam will be designed to resist the unbalanced horizontal load when the second-story compression brace buckles. It is assumed that the unbalanced brace force is distributed to both the left and right parts of the brace. In addition, since the third-story zipper column is designed to provide vertical support at the mid span of the third-floor beam, the third-floor beam will be designed as a continuous beam with a third support at the mid span.

Gravity load

$$V_{DL} = 0.3125\omega_{DL} \times L = 20.0\,kips\,;\ V_{LL} = 0.3125\omega_{LL} \times L = 12.3\,kips\,;$$

$$M_{DL} = \frac{\omega_{DL} \times L^2}{32} = 56.1\,k-ft\,;\ M_{LL} = \frac{\omega_{LL} \times L^2}{32} = 34.3\,k-ft\,;$$

Earthquake load

$$P_E = \frac{\left(R_y P_y + 0.3\phi P_n\right)\cos(45)}{2} = \pm 273\,kips\,;$$

Design forces in the braces (factored load)

$P_u =$ E = -273 kips $\leftarrow$ govern compression load

$P_u =$ - E = 273 kips $\leftarrow$ govern tension load

$V_u =$ 1.4 DL = 28.1 kips

$V_u =$ 1.2 DL + 1.6 LL = 43.6 kips $\leftarrow$ govern shear

$M_u =$ 1.4 DL = 78.5 k-ft

$M_u =$ 1.2 DL + 1.6 LL = 122.2 k-ft $\leftarrow$ govern moment

$\Rightarrow$ pick W24x76

$A_g = 22.4in^2$, $I_X = 2100\ \text{in}^4$, $kL_x = kL_y = 14\,ft$, $F_y = 50\,ksi$, $E_s = 29000\,ksi$,

Lateral braced @ ½ point ($L_b = 14\,ft$)

AISC LRFD check

Compression strength: $\phi P_n = 480.5\ kips$

Tension strength: $\phi P_n = 0.9 A_g F_y = 1008\,kips > P_u$ (ok)

Moment strength: $\phi M_n = 750\,\text{k-ft}$ ($\phi = 0.9$, Cb = 1.3)

Shear strength: $\phi V_n = 283.9\ \text{kips}$ ($\phi = 0.9$, without stiffener) $> V_u$ (ok)

Compactness: $$\frac{b}{2t_f} = 6.6 < 0.3\sqrt{\frac{E_s}{F_y}} = 7.23$$

(2002 AISC seismic provision T-I-8-1 [d]) (ok)

$$\frac{P_u}{\phi P_y} = 0.27 \Rightarrow \frac{h}{tw} = 49 < 1.12\sqrt{\frac{E_s}{F_y}}\left(2.33 - \frac{P_u}{\phi P_y}\right) = 55.5$$

(2002 AISC seismic provision T-I-8-1 [d]) (ok)

Combine axial and moment interaction (AISC section H1):

$P_{el} = \pi^2 EI / kL_x^{\ 2} = 5324\, kips$;

$C_m = 1.0$ (AISC Chapter C.2 pg 16.1-18, member subject to transverse

load and without end restraint) $\Rightarrow B_1 = \dfrac{C_m}{1 - P_u / P_{el}} = 1.0$

Since $P_u / \phi_c P_n = 0.57 > 0.2$, safety check was analyzed against

$$\frac{P_u}{\phi_c P_n} + \frac{8}{9}\frac{M_{ux}}{\phi M_n} = 0.71 < 1.0 \text{ (ok)}$$

Select W24x76 for the third-floor beam

B.4.6 Design of Second-Floor Beam

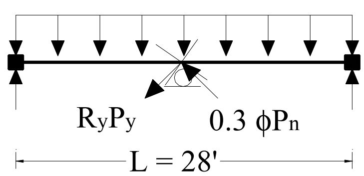

The second-floor beam will be designed to resist the unbalanced horizontal load when the first-story compression brace buckles. It is assumed that the unbalanced brace force is distributed to both the left and right parts of the brace. In addition, since the third-story zipper column is designed to provide vertical support at the mid span of the third-floor beam, the third-floor beam will be designed as a continuous beam with a third support at the mid span.

Gravity load

$V_{DL} = 0.3125\omega_{DL} \times L = 20.1 kips$; $V_{LL} = 0.3125\omega_{LL} \times L = 9.8 kips$;

$M_{DL} = \dfrac{\omega_{DL} \times L^2}{32} = 56.4 k - ft$; $M_{LL} = \dfrac{\omega_{LL} \times L^2}{32} = 27.4 k - ft$;

Earthquake load

$$P_E = \frac{\left(R_y P_y + 0.3\phi P_n\right)\cos(45)}{2} = \pm 328.8\,kips\ ;$$

Design forces in the braces (factored load)

$P_u =$ E = -328.8 kips $\leftarrow$ govern compression load

$P_u =$ - E = 328.8 kips $\leftarrow$ govern tension load

$V_u =$ 1.4 DL = 28.2 kips

$V_u =$ 1.2 DL + 1.6 LL = 39.8 kips $\leftarrow$ govern shear

$M_u =$ 1.4 DL = 78.9 k-ft

$M_u =$ 1.2 DL + 1.6 LL = 111.5 k-ft $\leftarrow$ govern moment

$\Rightarrow$ pick W24x76

$A_g = 22.4 in^2$, $I_X = 2100 \text{ in}^4$, $kL_x = kL_y = 14\ ft$, $F_y = 50\,ksi$, $E_s = 29000\,ksi$, Lateral braced @ ½ point ($L_b = 14\ ft$)

AISC LRFD check

Compression strength: $\phi P_n = 480.5\ kips$

Tension strength: $\phi P_n = 0.9 A_g F_y = 1008\,kips > P_u$ (ok)

Moment strength: $\phi M_n = 750\,\text{k-ft}$ ($\phi = 0.9$, Cb = 1.3)

Shear strength: $\phi V_n = 283.9 \text{ kips}$ ($\phi = 0.9$, without stiffener) $> V_u$ (ok)

Compactness: $$\frac{b}{2t_f} = 6.6 < 0.3\sqrt{\frac{E_s}{F_y}} = 7.23$$

(2002 AISC seismic provision T-I-8-1 [d]) (ok)

$$\frac{P_u}{\phi P_y} = 0.33 \Rightarrow \frac{h}{tw} = 49 < 1.12\sqrt{\frac{E_s}{F_y}}\left(2.33 - \frac{P_u}{\phi P_y}\right) = 54$$

(2002 AISC seismic provision T-I-8-1 [d]) (ok)

Combine axial and moment interaction (AISC section H1):

$$P_{el} = \pi^2 EI / kL_x^{\ 2} = 5324\,kips\ ;$$

$C_m = 1.0$ (AISC Chapter C.2 pg 16.1-18, member subject to transverse

load and without end restraint) $\Rightarrow B_1 = \dfrac{C_m}{1 - P_u / P_{el}} = 1.0$

Since $P_u / \phi_c P_n = 0.68 > 0.2$, safety check was analyzed against

$$\frac{P_u}{\phi_c P_n} + \frac{8}{9}\frac{M_{ux}}{\phi M_n} = 0.81 < 1.0 \text{ (ok)}$$

Select W24x76 for the second-floor beam

B.4.7 Design of Roof Beam

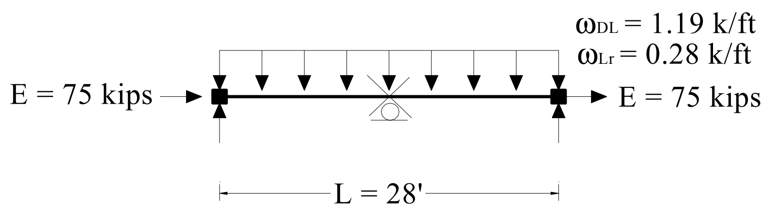

The roof beam will be designed to resist the story shear and gravity load at the roof level. Since the third-story braces were designed to provide vertical support at the mid span of the roof beam, the roof beam will be designed as a continuous beam with a third support at the mid span.

Gravity load

$$V_{DL} = 0.3125\omega_{DL} \times L = 10.4\,kips;\ V_{LL} = 0.3125\omega_{LL} \times L = 2.5\,kips;$$

$$M_{DL} = \frac{\omega_{DL} \times L^2}{32} = 29.2\,k - ft;\ M_{LL} = \frac{\omega_{LL} \times L^2}{32} = 6.9\,k - ft;$$

Earthquake load

$$P_E \pm 75\,kips;$$

Design forces in the braces (factored load)

$P_u =$ E = -75 kips $\leftarrow$ govern compression load

$P_u =$- E = 75 kips $\leftarrow$ govern tension

$V_u =$ 1.4 DL = 14.6 kips

$V_u =$ 1.2 DL + 1.6 Lr = 16.4 kips $\leftarrow$ govern shear

$M_u =$ 1.4 DL = 40.8 k-ft

$M_u =$ 1.2 DL + 1.6 Lr = 46 k-ft $\leftarrow$ govern moment

$\Rightarrow$ pick W24x55

$A_g = 16.3 in^2$, $I_X = 1360 \text{ in}^4$, $kL_x = kL_y = 14\, ft$, $F_y = 50\, ksi$, $E_s = 29000\, ksi$, Lateral braced @ ½ point ($L_b = 14\, ft$)

AISC LRFD check

Compression strength: $\phi P_n = 218.1\ kips$

Tension strength: $\phi P_n = 0.9 A_g F_y = 733.5\, kips > P_u$ (ok)

Moment strength: $\phi M_n = 390.2\, \text{k-ft}$ ($\phi = 0.9$, Cb = 1.3)

Shear strength: $\phi V_n = 251.7 \text{ kips}$ ($\phi = 0.9$, without stiffener) $> V_u$ (ok)

Compactness: $\dfrac{b}{2t_f} = 6.64 < 0.3\sqrt{\dfrac{E_s}{F_y}} = 7.23$

(2002 AISC seismic provision T-I-8-1 [d]) (ok)

$$\frac{P_u}{\phi P_y} = 0.1 \Rightarrow \frac{h}{tw} = 54.1 < 3.14\sqrt{\frac{E_s}{F_y}}\left(1 - 1.54\frac{P_u}{\phi P_y}\right) = 63.7$$

(2002 AISC seismic provision T-I-8-1 [d]) (ok)

Combine axial and moment interaction (AISC section H1):

$P_{el} = \pi^2 EI / kL_x^{\ 2} =\ 3447.9\, kips$;

$C_m = 1.0$ (AISC Chapter C.2 pg 16.1-18, member subject to transverse load and without end restraint) $\Rightarrow B_1 = \dfrac{C_m}{1 - P_u / P_{el}} = 1.0$

Since $P_u / \phi_c P_n = 0.34 > 0.2$, safety check was analyzed against

$$\frac{P_u}{\phi_c P_n} + \frac{8}{9}\frac{M_{ux}}{\phi M_n} = 0.49 < 1.0 \text{ (ok)}$$

Select W24x55 for the roof beam

B.4.8 Design of Columns

Because the lateral forces are transferred to the foundation by the axial forces in the braces and the columns are pinned at the base, columns are designed with axial forces created from the overturning moment from the lateral loads and the gravity loads. According to 2002 AISC seismic provision Section 8.3, when $P_u / \phi P_n > 0.4$ without the amplified seismic load, the amplified seismic load needs to be considered in the load combination. However, the required strength is not required to be greater than 1.1 x Ry times the nominal strength of the connecting brace nor the capacity of the foundation to resist uplifting.

Unfactored load

$$P_{DL} = \left(\omega_{DL,R} + \omega_{DL,3} + \omega_{DL,2}\right) \times 14 = -91\,kips;$$

$$P_{LL} = \left(\omega_{LL,2} + \omega_{LL,2}\right) \times 14 = -35.28\,kips;$$

$$P_{Lr} = \omega_{LL,R} \times 14 = -3.92\,kips$$

$$Q_E = \frac{44 \times 14 + 108 \times 28 + 150 \times 42}{28} = \pm 355\,kips$$

Design forces in the column (factored load)

P_u = 1.2 DL + 1.6 LL + 0.5 Lr = -167.61 kips

P_u = 1.2 DL + 1.6 Lr + 0.5 LL = -133.11 kips

P_u = 1.453 DL + Ω_0 Q_E + 0.5 LL = 1.453 DL + 2 Q_E + 0.5 LL = -860 kips

P_u = 0.647 DL – Ω_0 Q_E = 651.1 kips

Force calculated from the brace capacity

1. Assume the first- and second-story braces buckled and the third-story braces reaches compression capacity.

$$P_u = \left(0.3\phi P_{n1} + 0.3\phi P_{n2} + \phi P_{n3}\right)\sin(45)$$

$P_u = -992\,kips$ ← govern compression load

2. Maximum tension force in the column when second- and third-story braces yielded

$P_u = R_y F_y \left(A_{g,b2} + A_{g,b1}\right)\sin(45) = 1643.8\,kips$,

$P_u = 1643.8\,kips$ ← govern tension load

It is conservative to ignore the axial forces contributed from the third-story braces, since third-story braces are always in compression.

⇒ pick W14x159

$kL_x = 14\,ft$, $kL_y = 14\,ft$, $A_g = 46.7\,in^2$, $F_y = 50\,ksi$, $E_s = 29000\,ksi$, $r_x = 6.38\,in$, $r_y = 4\,in$.

AISC LRFD check

Compression strength: $\phi P_n = 1744.58\,kips > P_u$ (ok)

Tension strength: $\phi P_n = 0.9 A_g F_y = 2101.5\,kips > P_u$ (ok)

Slenderness: $\left(\frac{KL}{r}\right) = 42 < 5.87\sqrt{E_s / F_y} = 141$

(2002 AISC seismic provision section 13.2a) (ok)

Flange compactness: $\frac{b_f}{2t_f} = 6.54 < 0.3\sqrt{E_s / F_y} = 7.22$

(2002 AISC seismic provision, T-I-8-1) (ok)

Web compactness: $\frac{h}{t_w} = 15 < 1.12\sqrt{E_s / F_y}\left(2.33 - \frac{P_u}{\phi_b P_y}\right) = 41$

(2002 AISC seismic provision, T-I-8-1) (ok)

Select W14x159 for the columns. (Use the same column section for all stories.)

Appendix C: Tracking a Point in Space Using Three Independent Displacement Measurements

C.1 INTRODUCTION

In order to monitor the three-dimensional buckling behavior of the brace, selected points along the brace (Fig. 2.11) have been instrumented such that the motion of each point is tracked using three independent displacement transducers. This calculation assumes that the cross section of the brace remains plane and the cross section does not rotate. Hence, the buckling behavior of the brace can be monitored by tracking displacement at the selected points along the brace.

Figure C.1 shows an example of position, P, which the displacement in the global coordinate system can be calculated using the measurement from three independent displacement transducers.

Points 1, 2 and 3 are the locations of the displacement transducers. Distances L_4, L_5, and L_6 are the absolute distance from point 1, 2, and 3 to the point, P, respectively. Axes X, Y, and Z are the global coordinate system, and axes x, y, and z are the local coordinate system. The position of the displacement transducer 1 in the global coordinate system is [0,0,0], the position of displacement transducer 2 in the global coordinate system is [X_2, Y_2, Z_2], and the position of displacement transducer 3 in the global coordinate system is [X_3, Y_3, Z_3]. Therefore, the distances L_1, L_2, and L_3 can be calculated using Equation (C1)

$$L_1 = norm(XYZN_3);\ L_2 = norm(XYZN_2);\ L_3 = norm(XYZN_3 - XYZN_2) \qquad \text{(C.1)}$$

where $XYZN_2 = [X_2, Y_2, Z_2]$ and $XYZN_3 = [X_3, Y_3, Z_3]$.

Positions of point 2 and 3 in local coordinates are [x_2, y_2 ,0], and [0, y_3 ,0], respectively. They can be calculated using Equation (C.2):

$$\alpha_1 = \cos^{-1}\left(\frac{L_3^2 - L_1^2 - L_2^2}{-2L_1L_2}\right);\ x_2 = L_2 \sin\alpha_1;\ y_2 = L_2 \cos\alpha_1;\ y_3 = L_1; \tag{C.2}$$

The position of point P in the local coordinate system $[x, y, z]$ can be solved using Equation (C.3).

$$\begin{gathered} x = \frac{x_2^2 y_3 - y_2 y_3^2 - y_2 L_4^2 + y_2 L_6^2 + y_3 y_2^2 + y_3 L_4^2 - y_3 L_5^2}{2x_2 y_3}; \\ y = \frac{L_6^2 - L_4^2 - L_3^2}{-2y_3};\ z = \sqrt{L_4^2 - x^2 - y^2} \end{gathered} \tag{C.3}$$

Finally, the position of point P in the global coordinate system can be calculated using the transformation matrix, M, that consists of unit vectors of the local coordinate system expressed in term of the global coordinate system. Equation (C.4) shows the transformation from the local coordinate system to the global coordinate system.

$$M = \left[\{x\},\{y\},\{z\}\right];\ [X,Y,Z] = M[x,y,z] \tag{C.4}$$

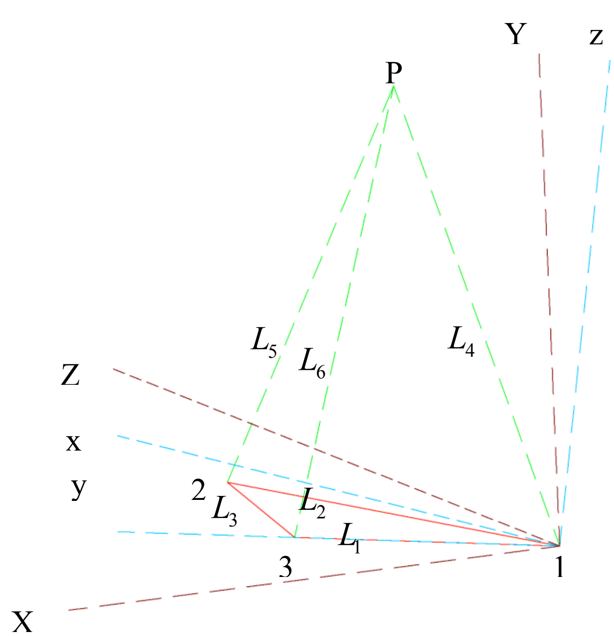

Fig. C.1 Global and local coordinate system.

C.2 MATLAB CODE

The above mathematical derivation has been implemented in the following MATLAB code.

```
function [XYZ] = WirePotDsp3D(XYZN2,XYZN3,L4,L5,L6)
% [XYZ] = WirePotDsp3D(XYZN2,XYZN3,L4,L5,L6)
% Calculate the measured Dsp of a point in 3D from 3 wire pot reading
% XYZ   = location of the node in Global coordinate
% XYZN1 = reference node. Global coordinate of node 1 = [0 0 0]
% XYZN2 = relative Global coordinate from node 2 to node 1 = [X2,Y2,Z2]
% XYZN3 = relative Global coordinate from node 3 to node 1 = [X3,Y3,Z3]
% L4    = absolute distance from node 1 to the point in space (scalar or column vector)
% L5    = absolute distance from node 2 to the point in space (scalar or column vector)
% L6    = absolute distance from node 3 to the point in space (scalar or column vector)
%
% Location of the node is specific!!!
% node 1 2 3 form the base of a Pyramid. Node number at the base must be
% assigned counter clockwise when viewing from the top of the Pyramid.
% Quick check: draw a line from node 1 to node 3 (positive local y axis).
% With right hand rule, thumb pointing the positive local y axis, the Pyramid
% must be on the side of index finger (pointing the positive local z axis)
%
% Written by T.Y.Yang (4/24/05)

% locate the absolute distance (base of the Pyramid)
L1 = norm(XYZN3);
L2 = norm(XYZN2);
L3 = norm(XYZN3-XYZN2);

% some constants (local coordinate for the base of the Pyramid)
alpha1 = acos((L3^2-L1^2-L2^2)/(-2*L1*L2));
x2 = L2*sin(alpha1);
y2 = L2*cos(alpha1);
y3 = L1;
```

```
% calculate the node in space in local coordinate
x = 1/(2*x2*y3)*(repmat(x2^2*y3-y2*y3^2+ y2^2*y3,size(L4,1),size(L4,2))-y2*L4.^2+y2*L6.^2
+L4.^2*y3-L5.^2*y3);
y = 1/(2*y3)*(repmat(y3^2,size(L4,1),size(L4,2))+L4.^2-L6.^2);
z = sqrt(L4.^2-x.^2-y.^2);

% locate the transformation matrix from local axis to global axis
vector_y = XYZN3/norm(XYZN3);
vector_2 = XYZN2/norm(XYZN2);
vector_z = cross(vector_2,vector_y);
vector_z = vector_z/norm(vector_z);
vector_x = cross(vector_y,vector_z);
vector_x = vector_x/norm(vector_x);
Matrix = [vector_x', vector_y', vector_z'];

% calculate the global coordinate of the node in space
XYZ = [x,y,z]*Matrix';
```

PEER REPORTS

PEER reports are available individually or by yearly subscription. PEER reports can be ordered at http://peer.berkeley.edu/publications/peer_reports.html or by contacting the Pacific Earthquake Engineering Research Center, 1301 South 46th Street, Richmond, CA 94804-4698. Tel.: (510) 665-3448; Fax: (510) 665-3456; Email: peer_editor@berkeley.edu

PEER 2009/01 *Evaluation of Ground Motion Selection and Modification Methods: Predicting Median Interstory Drift Response of Buildings.* Curt B. Haselton, Ed. June 2009.

PEER 2008/10 *Technical Manual for Strata.* Albert R. Kottke and Ellen M. Rathje. February 2009.

PEER 2008/09 *NGA Model for Average Horizontal Component of Peak Ground Motion and Response Spectra.* Brian S.-J. Chiou and Robert R. Youngs. November 2008.

PEER 2008/08 *Toward Earthquake-Resistant Design of Concentrically Braced Steel Structures.* Patxi Uriz and Stephen A. Mahin. November 2008.

PEER 2008/07 *Using OpenSees for Performance-Based Evaluation of Bridges on Liquefiable Soils.* Stephen L. Kramer, Pedro Arduino, and HyungSuk Shin. November 2008.

PEER 2008/06 *Shaking Table Tests and Numerical Investigation of Self-Centering Reinforced Concrete Bridge Columns.* Hyung IL Jeong, Junichi Sakai, and Stephen A. Mahin. September 2008.

PEER 2008/05 *Performance-Based Earthquake Engineering Design Evaluation Procedure for Bridge Foundations Undergoing Liquefaction-Induced Lateral Ground Displacement.* Christian A. Ledezma and Jonathan D. Bray. August 2008.

PEER 2008/04 *Benchmarking of Nonlinear Geotechnical Ground Response Analysis Procedures.* Jonathan P. Stewart, Annie On-Lei Kwok, Yousseff M. A. Hashash, Neven Matasovic, Robert Pyke, Zhiliang Wang, and Zhaohui Yang. August 2008.

PEER 2008/03 *Guidelines for Nonlinear Analysis of Bridge Structures in California.* Ady Aviram, Kevin R. Mackie, and Božidar Stojadinović. August 2008.

PEER 2008/02 *Treatment of Uncertainties in Seismic-Risk Analysis of Transportation Systems.* Evangelos Stergiou and Anne S. Kiremidjian. July 2008.

PEER 2008/01 *Seismic Performance Objectives for Tall Buildings.* William T. Holmes, Charles Kircher, William Petak, and Nabih Youssef. August 2008.

PEER 2007/12 *An Assessment to Benchmark the Seismic Performance of a Code-Conforming Reinforced Concrete Moment-Frame Building.* Curt Haselton, Christine A. Goulet, Judith Mitrani-Reiser, James L. Beck, Gregory G. Deierlein, Keith A. Porter, Jonathan P. Stewart, and Ertugrul Taciroglu. August 2008.

PEER 2007/11 *Bar Buckling in Reinforced Concrete Bridge Columns.* Wayne A. Brown, Dawn E. Lehman, and John F. Stanton. February 2008.

PEER 2007/10 *Computational Modeling of Progressive Collapse in Reinforced Concrete Frame Structures.* Mohamed M. Talaat and Khalid M. Mosalam. May 2008.

PEER 2007/09 *Integrated Probabilistic Performance-Based Evaluation of Benchmark Reinforced Concrete Bridges.* Kevin R. Mackie, John-Michael Wong, and Božidar Stojadinović. January 2008.

PEER 2007/08 *Assessing Seismic Collapse Safety of Modern Reinforced Concrete Moment-Frame Buildings.* Curt B. Haselton and Gregory G. Deierlein. February 2008.

PEER 2007/07 *Performance Modeling Strategies for Modern Reinforced Concrete Bridge Columns.* Michael P. Berry and Marc O. Eberhard. April 2008.

PEER 2007/06 *Development of Improved Procedures for Seismic Design of Buried and Partially Buried Structures.* Linda Al Atik and Nicholas Sitar. June 2007.

PEER 2007/05 *Uncertainty and Correlation in Seismic Risk Assessment of Transportation Systems.* Renee G. Lee and Anne S. Kiremidjian. July 2007.

PEER 2007/04 *Numerical Models for Analysis and Performance-Based Design of Shallow Foundations Subjected to Seismic Loading.* Sivapalan Gajan, Tara C. Hutchinson, Bruce L. Kutter, Prishati Raychowdhury, José A. Ugalde, and Jonathan P. Stewart. May 2008.

PEER 2007/03 *Beam-Column Element Model Calibrated for Predicting Flexural Response Leading to Global Collapse of RC Frame Buildings.* Curt B. Haselton, Abbie B. Liel, Sarah Taylor Lange, and Gregory G. Deierlein. May 2008.

PEER 2007/02 *Campbell-Bozorgnia NGA Ground Motion Relations for the Geometric Mean Horizontal Component of Peak and Spectral Ground Motion Parameters.* Kenneth W. Campbell and Yousef Bozorgnia. May 2007.

PEER 2007/01 *Boore-Atkinson NGA Ground Motion Relations for the Geometric Mean Horizontal Component of Peak and Spectral Ground Motion Parameters.* David M. Boore and Gail M. Atkinson. May. May 2007.

PEER 2006/12 *Societal Implications of Performance-Based Earthquake Engineering.* Peter J. May. May 2007.

PEER 2006/11 *Probabilistic Seismic Demand Analysis Using Advanced Ground Motion Intensity Measures, Attenuation Relationships, and Near-Fault Effects.* Polsak Tothong and C. Allin Cornell. March 2007.

PEER 2006/10 *Application of the PEER PBEE Methodology to the I-880 Viaduct.* Sashi Kunnath. February 2007.

PEER 2006/09 *Quantifying Economic Losses from Travel Forgone Following a Large Metropolitan Earthquake.* James Moore, Sungbin Cho, Yue Yue Fan, and Stuart Werner. November 2006.

PEER 2006/08 *Vector-Valued Ground Motion Intensity Measures for Probabilistic Seismic Demand Analysis*. Jack W. Baker and C. Allin Cornell. October 2006.

PEER 2006/07 *Analytical Modeling of Reinforced Concrete Walls for Predicting Flexural and Coupled–Shear-Flexural Responses*. Kutay Orakcal, Leonardo M. Massone, and John W. Wallace. October 2006.

PEER 2006/06 *Nonlinear Analysis of a Soil-Drilled Pier System under Static and Dynamic Axial Loading.* Gang Wang and Nicholas Sitar. November 2006.

PEER 2006/05 *Advanced Seismic Assessment Guidelines.* Paolo Bazzurro, C. Allin Cornell, Charles Menun, Maziar Motahari, and Nicolas Luco. September 2006.

PEER 2006/04 *Probabilistic Seismic Evaluation of Reinforced Concrete Structural Components and Systems.* Tae Hyung Lee and Khalid M. Mosalam. August 2006.

PEER 2006/03 *Performance of Lifelines Subjected to Lateral Spreading.* Scott A. Ashford and Teerawut Juirnarongrit. July 2006.

PEER 2006/02 *Pacific Earthquake Engineering Research Center Highway Demonstration Project.* Anne Kiremidjian, James Moore, Yue Yue Fan, Nesrin Basoz, Ozgur Yazali, and Meredith Williams. April 2006.

PEER 2006/01 *Bracing Berkeley. A Guide to Seismic Safety on the UC Berkeley Campus.* Mary C. Comerio, Stephen Tobriner, and Ariane Fehrenkamp. January 2006.

PEER 2005/16 *Seismic Response and Reliability of Electrical Substation Equipment and Systems.* Junho Song, Armen Der Kiureghian, and Jerome L. Sackman. April 2006.

PEER 2005/15 *CPT-Based Probabilistic Assessment of Seismic Soil Liquefaction Initiation.* R. E. S. Moss, R. B. Seed, R. E. Kayen, J. P. Stewart, and A. Der Kiureghian. April 2006.

PEER 2005/14 *Workshop on Modeling of Nonlinear Cyclic Load-Deformation Behavior of Shallow Foundations.* Bruce L. Kutter, Geoffrey Martin, Tara Hutchinson, Chad Harden, Sivapalan Gajan, and Justin Phalen. March 2006.

PEER 2005/13 *Stochastic Characterization and Decision Bases under Time-Dependent Aftershock Risk in Performance-Based Earthquake Engineering.* Gee Liek Yeo and C. Allin Cornell. July 2005.

PEER 2005/12 *PEER Testbed Study on a Laboratory Building: Exercising Seismic Performance Assessment.* Mary C. Comerio, editor. November 2005.

PEER 2005/11 *Van Nuys Hotel Building Testbed Report: Exercising Seismic Performance Assessment.* Helmut Krawinkler, editor. October 2005.

PEER 2005/10 *First NEES/E-Defense Workshop on Collapse Simulation of Reinforced Concrete Building Structures.* September 2005.

PEER 2005/09 *Test Applications of Advanced Seismic Assessment Guidelines.* Joe Maffei, Karl Telleen, Danya Mohr, William Holmes, and Yuki Nakayama. August 2006.

PEER 2005/08 *Damage Accumulation in Lightly Confined Reinforced Concrete Bridge Columns.* R. Tyler Ranf, Jared M. Nelson, Zach Price, Marc O. Eberhard, and John F. Stanton. April 2006.

PEER 2005/07 *Experimental and Analytical Studies on the Seismic Response of Freestanding and Anchored Laboratory Equipment.* Dimitrios Konstantinidis and Nicos Makris. January 2005.

PEER 2005/06 *Global Collapse of Frame Structures under Seismic Excitations*. Luis F. Ibarra and Helmut Krawinkler. September 2005.

PEER 2005//05 *Performance Characterization of Bench- and Shelf-Mounted Equipment.* Samit Ray Chaudhuri and Tara C. Hutchinson. May 2006.

PEER 2005/04 *Numerical Modeling of the Nonlinear Cyclic Response of Shallow Foundations.* Chad Harden, Tara Hutchinson, Geoffrey R. Martin, and Bruce L. Kutter. August 2005.

PEER 2005/03 *A Taxonomy of Building Components for Performance-Based Earthquake Engineering.* Keith A. Porter. September 2005.

PEER 2005/02 *Fragility Basis for California Highway Overpass Bridge Seismic Decision Making*. Kevin R. Mackie and Božidar Stojadinović. June 2005.

PEER 2005/01 *Empirical Characterization of Site Conditions on Strong Ground Motion.* Jonathan P. Stewart, Yoojoong Choi, and Robert W. Graves. June 2005.

PEER 2004/09 *Electrical Substation Equipment Interaction: Experimental Rigid Conductor Studies.* Christopher Stearns and André Filiatrault. February 2005.

PEER 2004/08 *Seismic Qualification and Fragility Testing of Line Break 550-kV Disconnect Switches.* Shakhzod M. Takhirov, Gregory L. Fenves, and Eric Fujisaki. January 2005.

PEER 2004/07 *Ground Motions for Earthquake Simulator Qualification of Electrical Substation Equipment.* Shakhzod M. Takhirov, Gregory L. Fenves, Eric Fujisaki, and Don Clyde. January 2005.

PEER 2004/06 *Performance-Based Regulation and Regulatory Regimes.* Peter J. May and Chris Koski. September 2004.

PEER 2004/05 *Performance-Based Seismic Design Concepts and Implementation: Proceedings of an International Workshop.* Peter Fajfar and Helmut Krawinkler, editors. September 2004.

PEER 2004/04 *Seismic Performance of an Instrumented Tilt-up Wall Building.* James C. Anderson and Vitelmo V. Bertero. July 2004.

PEER 2004/03 *Evaluation and Application of Concrete Tilt-up Assessment Methodologies.* Timothy Graf and James O. Malley. October 2004.

PEER 2004/02 *Analytical Investigations of New Methods for Reducing Residual Displacements of Reinforced Concrete Bridge Columns.* Junichi Sakai and Stephen A. Mahin. August 2004.

PEER 2004/01 *Seismic Performance of Masonry Buildings and Design Implications.* Kerri Anne Taeko Tokoro, James C. Anderson, and Vitelmo V. Bertero. February 2004.

PEER 2003/18 *Performance Models for Flexural Damage in Reinforced Concrete Columns.* Michael Berry and Marc Eberhard. August 2003.

PEER 2003/17 *Predicting Earthquake Damage in Older Reinforced Concrete Beam-Column Joints.* Catherine Pagni and Laura Lowes. October 2004.

PEER 2003/16 *Seismic Demands for Performance-Based Design of Bridges.* Kevin Mackie and Božidar Stojadinović. August 2003.

PEER 2003/15 *Seismic Demands for Nondeteriorating Frame Structures and Their Dependence on Ground Motions.* Ricardo Antonio Medina and Helmut Krawinkler. May 2004.

PEER 2003/14 *Finite Element Reliability and Sensitivity Methods for Performance-Based Earthquake Engineering.* Terje Haukaas and Armen Der Kiureghian. April 2004.

PEER 2003/13 *Effects of Connection Hysteretic Degradation on the Seismic Behavior of Steel Moment-Resisting Frames.* Janise E. Rodgers and Stephen A. Mahin. March 2004.

PEER 2003/12 *Implementation Manual for the Seismic Protection of Laboratory Contents: Format and Case Studies.* William T. Holmes and Mary C. Comerio. October 2003.

PEER 2003/11 *Fifth U.S.-Japan Workshop on Performance-Based Earthquake Engineering Methodology for Reinforced Concrete Building Structures.* February 2004.

PEER 2003/10 *A Beam-Column Joint Model for Simulating the Earthquake Response of Reinforced Concrete Frames.* Laura N. Lowes, Nilanjan Mitra, and Arash Altoontash. February 2004.

PEER 2003/09 *Sequencing Repairs after an Earthquake: An Economic Approach.* Marco Casari and Simon J. Wilkie. April 2004.

PEER 2003/08 *A Technical Framework for Probability-Based Demand and Capacity Factor Design (DCFD) Seismic Formats*. Fatemeh Jalayer and C. Allin Cornell. November 2003.

PEER 2003/07 *Uncertainty Specification and Propagation for Loss Estimation Using FOSM Methods.* Jack W. Baker and C. Allin Cornell. September 2003.

PEER 2003/06 *Performance of Circular Reinforced Concrete Bridge Columns under Bidirectional Earthquake Loading*. Mahmoud M. Hachem, Stephen A. Mahin, and Jack P. Moehle. February 2003.

PEER 2003/05 *Response Assessment for Building-Specific Loss Estimation.* Eduardo Miranda and Shahram Taghavi. September 2003.

PEER 2003/04 *Experimental Assessment of Columns with Short Lap Splices Subjected to Cyclic Loads*. Murat Melek, John W. Wallace, and Joel Conte. April 2003.

PEER 2003/03 *Probabilistic Response Assessment for Building-Specific Loss Estimation.* Eduardo Miranda and Hesameddin Aslani. September 2003.

PEER 2003/02 *Software Framework for Collaborative Development of Nonlinear Dynamic Analysis Program.* Jun Peng and Kincho H. Law. September 2003.

PEER 2003/01 *Shake Table Tests and Analytical Studies on the Gravity Load Collapse of Reinforced Concrete Frames.* Kenneth John Elwood and Jack P. Moehle. November 2003.

PEER 2002/24 *Performance of Beam to Column Bridge Joints Subjected to a Large Velocity Pulse.* Natalie Gibson, André Filiatrault, and Scott A. Ashford. April 2002.

PEER 2002/23 *Effects of Large Velocity Pulses on Reinforced Concrete Bridge Columns.* Greg L. Orozco and Scott A. Ashford. April 2002.

PEER 2002/22 *Characterization of Large Velocity Pulses for Laboratory Testing.* Kenneth E. Cox and Scott A. Ashford. April 2002.

PEER 2002/21 *Fourth U.S.-Japan Workshop on Performance-Based Earthquake Engineering Methodology for Reinforced Concrete Building Structures*. December 2002.

PEER 2002/20 *Barriers to Adoption and Implementation of PBEE Innovations.* Peter J. May. August 2002.

PEER 2002/19 *Economic-Engineered Integrated Models for Earthquakes: Socioeconomic Impacts.* Peter Gordon, James E. Moore II, and Harry W. Richardson. July 2002.

PEER 2002/18 *Assessment of Reinforced Concrete Building Exterior Joints with Substandard Details.* Chris P. Pantelides, Jon Hansen, Justin Nadauld, and Lawrence D. Reaveley. May 2002.

PEER 2002/17 *Structural Characterization and Seismic Response Analysis of a Highway Overcrossing Equipped with Elastomeric Bearings and Fluid Dampers: A Case Study.* Nicos Makris and Jian Zhang. November 2002.

PEER 2002/16 *Estimation of Uncertainty in Geotechnical Properties for Performance-Based Earthquake Engineering.* Allen L. Jones, Steven L. Kramer, and Pedro Arduino. December 2002.

PEER 2002/15 *Seismic Behavior of Bridge Columns Subjected to Various Loading Patterns.* Asadollah Esmaeily-Gh. and Yan Xiao. December 2002.

PEER 2002/14 *Inelastic Seismic Response of Extended Pile Shaft Supported Bridge Structures.* T.C. Hutchinson, R.W. Boulanger, Y.H. Chai, and I.M. Idriss. December 2002.

PEER 2002/13 *Probabilistic Models and Fragility Estimates for Bridge Components and Systems.* Paolo Gardoni, Armen Der Kiureghian, and Khalid M. Mosalam. June 2002.

PEER 2002/12 *Effects of Fault Dip and Slip Rake on Near-Source Ground Motions: Why Chi-Chi Was a Relatively Mild M7.6 Earthquake.* Brad T. Aagaard, John F. Hall, and Thomas H. Heaton. December 2002.

PEER 2002/11 *Analytical and Experimental Study of Fiber-Reinforced Strip Isolators*. James M. Kelly and Shakhzod M. Takhirov. September 2002.

PEER 2002/10 *Centrifuge Modeling of Settlement and Lateral Spreading with Comparisons to Numerical Analyses***.** Sivapalan Gajan and Bruce L. Kutter. January 2003.

PEER 2002/09 *Documentation and Analysis of Field Case Histories of Seismic Compression during the 1994 Northridge, California, Earthquake.* Jonathan P. Stewart, Patrick M. Smith, Daniel H. Whang, and Jonathan D. Bray. October 2002.

PEER 2002/08 *Component Testing, Stability Analysis and Characterization of Buckling-Restrained Unbonded Braces™.* Cameron Black, Nicos Makris, and Ian Aiken. September 2002.

PEER 2002/07 *Seismic Performance of Pile-Wharf Connections.* Charles W. Roeder, Robert Graff, Jennifer Soderstrom, and Jun Han Yoo. December 2001.

PEER 2002/06 *The Use of Benefit-Cost Analysis for Evaluation of Performance-Based Earthquake Engineering Decisions*. Richard O. Zerbe and Anthony Falit-Baiamonte. September 2001.

PEER 2002/05 *Guidelines, Specifications, and Seismic Performance Characterization of Nonstructural Building Components and Equipment*. André Filiatrault, Constantin Christopoulos, and Christopher Stearns. September 2001.

PEER 2002/04 *Consortium of Organizations for Strong-Motion Observation Systems and the Pacific Earthquake Engineering Research Center Lifelines Program: Invited Workshop on Archiving and Web Dissemination of Geotechnical Data, 4–5 October 2001*. September 2002.

PEER 2002/03 *Investigation of Sensitivity of Building Loss Estimates to Major Uncertain Variables for the Van Nuys Testbed.* Keith A. Porter, James L. Beck, and Rustem V. Shaikhutdinov. August 2002.

PEER 2002/02 *The Third U.S.-Japan Workshop on Performance-Based Earthquake Engineering Methodology for Reinforced Concrete Building Structures*. July 2002.

PEER 2002/01 *Nonstructural Loss Estimation: The UC Berkeley Case Study.* Mary C. Comerio and John C. Stallmeyer. December 2001.

PEER 2001/16 *Statistics of SDF-System Estimate of Roof Displacement for Pushover Analysis of Buildings.* Anil K. Chopra, Rakesh K. Goel, and Chatpan Chintanapakdee. December 2001.

PEER 2001/15 *Damage to Bridges during the 2001 Nisqually Earthquake.* R. Tyler Ranf, Marc O. Eberhard, and Michael P. Berry. November 2001.

PEER 2001/14 *Rocking Response of Equipment Anchored to a Base Foundation.* Nicos Makris and Cameron J. Black. September 2001.

PEER 2001/13 *Modeling Soil Liquefaction Hazards for Performance-Based Earthquake Engineering.* Steven L. Kramer and Ahmed-W. Elgamal. February 2001.

PEER 2001/12 *Development of Geotechnical Capabilities in OpenSees.* Boris Jeremić. September 2001.

PEER 2001/11 *Analytical and Experimental Study of Fiber-Reinforced Elastomeric Isolators*. James M. Kelly and Shakhzod M. Takhirov. September 2001.

PEER 2001/10 *Amplification Factors for Spectral Acceleration in Active Regions.* Jonathan P. Stewart, Andrew H. Liu, Yoojoong Choi, and Mehmet B. Baturay. December 2001.

PEER 2001/09 *Ground Motion Evaluation Procedures for Performance-Based Design.* Jonathan P. Stewart, Shyh-Jeng Chiou, Jonathan D. Bray, Robert W. Graves, Paul G. Somerville, and Norman A. Abrahamson. September 2001.

PEER 2001/08 *Experimental and Computational Evaluation of Reinforced Concrete Bridge Beam-Column Connections for Seismic Performance*. Clay J. Naito, Jack P. Moehle, and Khalid M. Mosalam. November 2001.

PEER 2001/07 *The Rocking Spectrum and the Shortcomings of Design Guidelines.* Nicos Makris and Dimitrios Konstantinidis. August 2001.

PEER 2001/06 *Development of an Electrical Substation Equipment Performance Database for Evaluation of Equipment Fragilities*. Thalia Agnanos. April 1999.

PEER 2001/05 *Stiffness Analysis of Fiber-Reinforced Elastomeric Isolators.* Hsiang-Chuan Tsai and James M. Kelly. May 2001.

PEER 2001/04 *Organizational and Societal Considerations for Performance-Based Earthquake Engineering.* Peter J. May. April 2001.

PEER 2001/03 *A Modal Pushover Analysis Procedure to Estimate Seismic Demands for Buildings: Theory and Preliminary Evaluation.* Anil K. Chopra and Rakesh K. Goel. January 2001.

PEER 2001/02 *Seismic Response Analysis of Highway Overcrossings Including Soil-Structure Interaction.* Jian Zhang and Nicos Makris. March 2001.

PEER 2001/01 *Experimental Study of Large Seismic Steel Beam-to-Column Connections.* Egor P. Popov and Shakhzod M. Takhirov. November 2000.

PEER 2000/10 *The Second U.S.-Japan Workshop on Performance-Based Earthquake Engineering Methodology for Reinforced Concrete Building Structures.* March 2000.

PEER 2000/09 *Structural Engineering Reconnaissance of the August 17, 1999 Earthquake: Kocaeli (Izmit), Turkey.* Halil Sezen, Kenneth J. Elwood, Andrew S. Whittaker, Khalid Mosalam, John J. Wallace, and John F. Stanton. December 2000.

PEER 2000/08 *Behavior of Reinforced Concrete Bridge Columns Having Varying Aspect Ratios and Varying Lengths of Confinement.* Anthony J. Calderone, Dawn E. Lehman, and Jack P. Moehle. January 2001.

PEER 2000/07 *Cover-Plate and Flange-Plate Reinforced Steel Moment-Resisting Connections.* Taejin Kim, Andrew S. Whittaker, Amir S. Gilani, Vitelmo V. Bertero, and Shakhzod M. Takhirov. September 2000.

PEER 2000/06 *Seismic Evaluation and Analysis of 230-kV Disconnect Switches.* Amir S. J. Gilani, Andrew S. Whittaker, Gregory L. Fenves, Chun-Hao Chen, Henry Ho, and Eric Fujisaki. July 2000.

PEER 2000/05 *Performance-Based Evaluation of Exterior Reinforced Concrete Building Joints for Seismic Excitation.* Chandra Clyde, Chris P. Pantelides, and Lawrence D. Reaveley. July 2000.

PEER 2000/04 *An Evaluation of Seismic Energy Demand: An Attenuation Approach.* Chung-Che Chou and Chia-Ming Uang. July 1999.

PEER 2000/03 *Framing Earthquake Retrofitting Decisions: The Case of Hillside Homes in Los Angeles.* Detlof von Winterfeldt, Nels Roselund, and Alicia Kitsuse. March 2000.

PEER 2000/02 *U.S.-Japan Workshop on the Effects of Near-Field Earthquake Shaking.* Andrew Whittaker, ed. July 2000.

PEER 2000/01 *Further Studies on Seismic Interaction in Interconnected Electrical Substation Equipment.* Armen Der Kiureghian, Kee-Jeung Hong, and Jerome L. Sackman. November 1999.

PEER 1999/14 *Seismic Evaluation and Retrofit of 230-kV Porcelain Transformer Bushings*. Amir S. Gilani, Andrew S. Whittaker, Gregory L. Fenves, and Eric Fujisaki. December 1999.

PEER 1999/13 *Building Vulnerability Studies: Modeling and Evaluation of Tilt-up and Steel Reinforced Concrete Buildings.* John W. Wallace, Jonathan P. Stewart, and Andrew S. Whittaker, editors. December 1999.

PEER 1999/12 *Rehabilitation of Nonductile RC Frame Building Using Encasement Plates and Energy-Dissipating Devices.* Mehrdad Sasani, Vitelmo V. Bertero, James C. Anderson. December 1999.

PEER 1999/11 *Performance Evaluation Database for Concrete Bridge Components and Systems under Simulated Seismic Loads.* Yael D. Hose and Frieder Seible. November 1999.

PEER 1999/10 *U.S.-Japan Workshop on Performance-Based Earthquake Engineering Methodology for Reinforced Concrete Building Structures.* December 1999.

PEER 1999/09 *Performance Improvement of Long Period Building Structures Subjected to Severe Pulse-Type Ground Motions*. James C. Anderson, Vitelmo V. Bertero, and Raul Bertero. October 1999.

PEER 1999/08 *Envelopes for Seismic Response Vectors.* Charles Menun and Armen Der Kiureghian. July 1999.

PEER 1999/07 *Documentation of Strengths and Weaknesses of Current Computer Analysis Methods for Seismic Performance of Reinforced Concrete Members.* William F. Cofer. November 1999.

PEER 1999/06 *Rocking Response and Overturning of Anchored Equipment under Seismic Excitations.* Nicos Makris and Jian Zhang. November 1999.

PEER 1999/05 *Seismic Evaluation of 550 kV Porcelain Transformer Bushings.* Amir S. Gilani, Andrew S. Whittaker, Gregory L. Fenves, and Eric Fujisaki. October 1999.

PEER 1999/04 *Adoption and Enforcement of Earthquake Risk-Reduction Measures*. Peter J. May, Raymond J. Burby, T. Jens Feeley, and Robert Wood.

PEER 1999/03 *Task 3 Characterization of Site Response General Site Categories*. Adrian Rodriguez-Marek, Jonathan D. Bray, and Norman Abrahamson. February 1999.

PEER 1999/02 *Capacity-Demand-Diagram Methods for Estimating Seismic Deformation of Inelastic Structures: SDF Systems*. Anil K. Chopra and Rakesh Goel. April 1999.

PEER 1999/01 *Interaction in Interconnected Electrical Substation Equipment Subjected to Earthquake Ground Motions.* Armen Der Kiureghian, Jerome L. Sackman, and Kee-Jeung Hong. February 1999.

PEER 1998/08 *Behavior and Failure Analysis of a Multiple-Frame Highway Bridge in the 1994 Northridge Earthquake.* Gregory L. Fenves and Michael Ellery. December 1998.

PEER 1998/07 *Empirical Evaluation of Inertial Soil-Structure Interaction Effects.* Jonathan P. Stewart, Raymond B. Seed, and Gregory L. Fenves. November 1998.

PEER 1998/06 *Effect of Damping Mechanisms on the Response of Seismic Isolated Structures.* Nicos Makris and Shih-Po Chang. November 1998.

PEER 1998/05 *Rocking Response and Overturning of Equipment under Horizontal Pulse-Type Motions.* Nicos Makris and Yiannis Roussos. October 1998.

PEER 1998/04 *Pacific Earthquake Engineering Research Invitational Workshop Proceedings, May 14–15, 1998: Defining the Links between Planning, Policy Analysis, Economics and Earthquake Engineering.* Mary Comerio and Peter Gordon. September 1998.

PEER 1998/03 *Repair/Upgrade Procedures for Welded Beam to Column Connections.* James C. Anderson and Xiaojing Duan. May 1998.

PEER 1998/02 *Seismic Evaluation of 196 kV Porcelain Transformer Bushings.* Amir S. Gilani, Juan W. Chavez, Gregory L. Fenves, and Andrew S. Whittaker. May 1998.

PEER 1998/01 *Seismic Performance of Well-Confined Concrete Bridge Columns.* Dawn E. Lehman and Jack P. Moehle. December 2000.

ONLINE REPORTS

The following PEER reports are available by Internet only at http://peer.berkeley.edu/publications/peer_reports.html

PEER 2009/103 *Performance Evaluation of Innovative Steel Braced Frames.* T. Y. Yang, Jack P. Moehle, and Božidar Stojadinović. August 2009.

PEER 2009/102 *Reinvestigation of Liquefaction and Nonliquefaction Case Histories from the 1976 Tangshan Earthquake.* Robb Eric Moss, Robert E. Kayen, Liyuan Tong, Songyu Liu, Guojun Cai, and Jiaer Wu. August 2009.

PEER 2009/101 *Report of the First Joint Planning Meeting for the Second Phase of NEES/E-Defense Collaborative Research on Earthquake Engineering.* Stephen A. Mahin et al. July 2009.

PEER 2008/104 *Experimental and Analytical Study of the Seismic Performance of Retaining Structures.* Linda Al Atik and Nicholas Sitar. January 2009.

PEER 2008/103 *Experimental and Computational Evaluation of Current and Innovative In-Span Hinge Details in Reinforced Concrete Box-Girder Bridges. Part 1: Experimental Findings and Pre-Test Analysis.* Matias A. Hube and Khalid M. Mosalam. January 2009.

PEER 2008/102 *Modeling of Unreinforced Masonry Infill Walls Considering In-Plane and Out-of-Plane Interaction.* Stephen Kadysiewski and Khalid M. Mosalam. January 2009.

PEER 2008/101 *Seismic Performance Objectives for Tall Buildings.* William T. Holmes, Charles Kircher, William Petak, and Nabih Youssef. August 2008.

PEER 2007/101 *Generalized Hybrid Simulation Framework for Structural Systems Subjected to Seismic Loading.* Tarek Elkhoraibi and Khalid M. Mosalam. July 2007.

PEER 2007/100 *Seismic Evaluation of Reinforced Concrete Buildings Including Effects of Masonry Infill Walls.* Alidad Hashemi and Khalid M. Mosalam. July 2007.